Improving the dynamical model of the Moon using lunar laser ranging (LLR) and spacecraft data

Vishnu Viswanathan

THÈSE DE DOCTORAT

de l'Université de recherche Paris Sciences et Lettres
PSL Research University

Préparée à l'Observatoire de la Côte d'Azur
CNRS-UMR Géoazur

Improving the dynamical model of the Moon using lunar laser ranging and spacecraft data

École doctorale nº127

OBSERVATOIRE DE PARIS

Spécialité ASTRONOMIE ET ASTROPHYSIQUE

COMPOSITION DU JURY :

Françoise Roques
Observatoire de Paris, Président

Tom Murphy
University of San Diego, Rapporteur

Yves Rogister
EOST-Strasbourg, Rapporteur

François Mignard
Lagrange-Nice, Examinateur

Mark Wieczorek
Lagrange-Nice, Examinateur

Tim Van Hoolst
ROB, Examinateur

Nicolas Rambaux
IMCCE-Paris, Invité

Soutenue par **Vishnu Viswanathan**
le 10 Novembre 2017

Dirigée par **Agnès Fienga**
et par **Jacques Laskar**

l'Observatoire de Paris | PSL RESEARCH UNIVERSITY PARIS

ABSTRACT

The main goal of this Ph.D thesis was to improve the dynamical model of the Moon within the numerically integrated ephemeris (INPOP) and to derive results of scientific value from this improvement through the characterization of the lunar internal structure and tests of general relativity.

At first, raw binaries of LLR echoes obtained from the Grasse ILRS station were used to analyze the algorithm used by the facility, for the computation of a normal point from the full-rate data. Further analysis shows the dependence of the algorithm on the reported uncertainty contained within the distributed LLR normal points from Grasse. The importance of the normal point uncertainty is reflected in the weighted least square procedure used for parameter estimation, especially in the absence of a standardized algorithm between different LLR ground stations. The thesis also benefitted in terms of a more dense dataset due to technical improvements and the switch of operational wavelength to infrared at the Grasse LLR facility (Courde et al., 2017).

The reduction of the LLR observations was implemented within GINS — the orbit determination software from CNES. The modeling follows the IERS 2010 recommendations for the correction of all known effects on the light-time computation. The subroutines were verified through a step by step comparison study using simulated data, with LLR analysis groups in Paris and Hannover, maintaining any discrepancies in the Earth-Moon distance below 1 mm. Additionally, correction of the effect due to hydrology loading observed at the Grasse station was implemented (Mémin et al., 2016). An improved version of the LLR reduction model was submitted to the space geodesy team of CNES (GRGS).

The lunar dynamical model of INPOP was first developed by Manche (2011). However, due to the absence of the fluid core within the previous version of INPOP (13c), the residuals obtained after a least-square fit were in the level of 5 cm for the modern day period (2006 onwards). A detailed comparison of the dynamical equations with DE430 JPL ephemeris helped to identify required changes within INPOP for the activation of the lunar fluid core. Other modifications allowed the use of a spacecraft determined lunar gravity field within the dynamical model. The use of a bounded value least square algorithm during the regression procedure accounted for variability to well-known parameters from their reported uncertainties. The resulting iteratively fit solution of INPOP ephemeris then produces a residual of 1.4-1.8 cm, on par with that reported by Folkner et al. (2014); Pavlov et al. (2016). The new INPOP ephemeris (INPOP17a) is distributed through the IMCCE website (`www.imcce.fr/inpop`) with a published documentation (Viswanathan et al., 2017) in the scientific notes of IMCCE.

Furthermore, on providing tighter constraints on the lunar gravity field from GRAIL-data analysis within the dynamical model, a characteristic lunar libration signature with a period of 6 years was revealed with an amplitude of ± 5 cm. Several tracks were investigated for the identification of the unmodeled effect, involving higher degree tidal terms and torque components, and a new modeling is proposed. A publication is under revision on this subject.

Residuals at the level of a centimeter allow precision tests of the principle of equivalence in the solar system. The fitted value of the parameter characterizing the differential acceleration of the Earth and the Moon towards the Sun was obtained with numerically integrated partial derivatives. The results are consistent with the previous work by Williams et al. (2009, 2012b); Hofmann et al. (2010); Hofmann and Müller (2016). An article on this work is accepted for

publication in MNRAS (Viswanathan et al., 2018).

RÉSUMÉ

L'objectif principal de ce travail était d'améliorer le modèle dynamique de la Lune dans les éphémérides numériques INPOP et d'exploiter cette amélioration en vu d'une meilleure caractérisation de la structure interne de la Lune et d'effectuer des tests de la relativité générale.

Dans un premier temps, un travail d'analyse des algorithmes nécessaires aux calculs des points normaux utilisés pour la construction des éphémérides lunaires a été effectué. L'importance de l'incertitude du point normal se reflète dans la méthode du moindre carré pondéré utilisée pour l'estimation des paramètres lors de la construction des éphémérides. En particulier, l'absence d'un algorithme standardisé entre les différentes stations LLR introduit des biais dans l'estimation des incertitudes qu'il est important de prendre en compte. La thèse a également bénéficié d'un ensemble de données plus dense en raison des améliorations techniques et du passage de la longueur d'onde à l'infrarouge à la station de Grasse (Courde et al., 2017).

Dans un second temps, afin de permettre des analyses multi-techniques combinant mesures SLR et LLR, la réduction des observations LLR a été introduite dans le logiciel de détermination d'orbites GINS du CNES, suite aux recommandations de IERS 2010. En outre, la correction des effets dus au chargement hydrologique observé à la station Grasse a été mise en œuvre et a fait l'objet d'une première communication poster en 2016 (Mémin et al., 2016). Une version améliorée du modèle de réduction LLR a été intégrée à la dernière version distribuée du logiciel GINS par l'équipe de géodésie spatiale (GRGS) du CNES.

Le modèle dynamique lunaire d'INPOP a d'abord été développé par Manche (2011). Cependant, sans doute en raison de l'absence du noyau fluide dans la version précédente (INPOP13c), les résidus obtenus après ajustement étaient au niveau de 5 cm pour la période moderne (2006). Une comparaison détaillée des équations dynamiques avec les éphémérides JPL DE430 a permis d'identifier les changements requis dans INPOP pour l'activation du noyau liquide lunaire. D'autres modifications ont permis l'utilisation d'un champ de gravité lunaire déterminé par la mission spatiale GRAIL. Un algorithme de moindres carrés sous contraintes a aussi été utilisé afin de maintenir les paramètres connus dans des bornes compatibles avec leurs incertitudes. La solution de l'éphéméride INPOP résultante (INPOP17a) produit alors un résidu de 1,4 à 1,8 cm, compatible avec ceux publiés par Folkner et al. (2014); Pavlov et al. (2016). L'éphéméride INPOP17a est distribuée sur le site de l'imcce (www.imcce.fr/inpop) et une documentation a été publiée (Viswanathan et al., 2017) dans les notes scientifiques de l'IMCCE.

En outre, en fournissant des contraintes plus sévères dans le modèle dynamique sur le champ de gravité lunaire à partir de l'analyse des données GRAIL, une signature caractéristique de libration lunaire avec une période de 6 ans a été révélée avec une amplitude de ± 5 cm. Plusieurs pistes ont été étudiées pour l'identification de cet effet, impliquant des termes de marée et des composants de couple à plus haut degré. Une publication est en cours de révision à ce sujet.

Les résidus au niveau d'un centimètre permettent des tests précis du principe d'équivalence dans le système solaire. La valeur ajustée du paramètre caractérisant l'accélération différentielle de la Terre et de la Lune vers le Soleil a été obtenue. Les résultats sont conformes aux travaux antérieurs de Williams et al. (2009, 2012b); Hofmann et al. (2010); Hofmann and Müller (2016) en améliorant la précision de la détermination. Une interprétation en terme de théorie du dilaton est proposée. Un article sur ce travail est accepté pour publication dans MNRAS (Viswanathan et al., 2018).

ACKNOWLEDGEMENTS

This dissertation would not have been possible without the continuous support of my advisors, fellow researchers, family and friends.

I would like to express my sincere gratitude to my thesis advisor, Dr. Agnès Fienga. I am extremely privileged to have worked under her over the past three years. Her support, availability, patience and encouragement have been critical to understand and solve problems I encountered during my research. I am indebted to her guidance through my transition from an engineering background to a researcher in physics. I thank her for her confidence in me from start to finish.

I would like to thank my co-advisor, Dr. Jacques Laskar, for all the guidance, support and opportunities that he provided me with. I thank his support for continuing my thesis research as a post-doctoral position at the ASD-IMCCE, Paris.

During the course of my research at OCA-Géoazur, I had the opportunity to discuss with several experienced researchers, including Anthony Mémin, Gilles Métris, Pierre Exertier, Clement Courde, Jean-Marie Torre, Olivier Minazzoli and Mark Wieczorek. They have been very supportive and I thank and appreciate each of them for their willingness to go that extra mile.

I thank Hervé Manche, Yves Rogister and Nicolas Rambaux for their time and effort to answer each of my frequent questions on the Earth-Moon dynamics. Jean-Charles Marty, Sylvain Loyer and Olivier Laurain for providing the support with GINS setup and development.

To my fellow researchers, Borhan Tavakoli, Alexandre Belli, Dung Luong, Huyen Tran, Monica Segovia, Edouard Palis and many others with whom I have shared time and space, I appreciate your friendship.

I thank all my friends for their support. Muscateers for the brotherhood. Shruti for her positivity. Karthik for being a partner in crime. Navnina for being my partner for life. A big thank you to my parents and my brother who have stood through thick and thin to support and encourage my life decisions, and I hope to continue to make them proud.

To all of them, I owe this thesis.

Contents

List of Tables xi

List of Figures xiii

List of Abbreviations xix

1 Introduction 1
- 1.1 Physics of the Earth-Moon system . . . 1
  - 1.1.1 Formation and evolution mechanism . . . 2
  - 1.1.2 Lunar interior structure . . . 4
- 1.2 Tests of general relativity . . . 8
- 1.3 Ephemerides and its applications . . . 10
- 1.4 Outline of the thesis . . . 12

2 Observation: Lunar Laser Ranging 13
- 2.1 Introduction . . . 13
- 2.2 Normal Point . . . 15
  - 2.2.1 Introduction . . . 15
  - 2.2.2 Data format . . . 16
  - 2.2.3 Existing algorithm at Grasse station . . . 16
  - 2.2.4 Alternate algorithm . . . 23
  - 2.2.5 Results . . . 26
  - 2.2.6 Inference . . . 31
- 2.3 Comparisons between IR and Green LLR data sample . . . 32
  - 2.3.1 Temporal distribution . . . 36
  - 2.3.2 Spatial distribution . . . 37
- 2.4 LLR accuracy . . . 39

3 Data reduction 43
- 3.1 Light-time computation . . . 44
- 3.2 Reference frame transformation . . . 46

3.3 Displacement of reference points . . . 50
3.3.1 Solid tides . . . 50
3.3.2 Ocean tide loading . . . 51
3.3.3 Atmospheric pressure loading . . . 52
3.3.4 Rotational deformation due to polar motion . . . 53
3.3.5 Ocean pole tide loading . . . 54
3.3.6 Hydrological mass loading . . . 55
3.4 Corrections to light-time . . . 56
3.4.1 Atmospheric delay . . . 56
3.4.2 Relativistic correction . . . 57

4 Dynamical model 59
4.1 Improvement from INPOP13c . . . 59
4.2 Lunar orbit interactions . . . 61
4.3 Lunar orientation and extended figure . . . 61
4.3.1 Lunar frame definition . . . 61
4.3.2 Time variation of lunar orientation . . . 62
4.3.3 Lunar moment of inertia tensor . . . 62
4.3.4 Lunar angular momentum and torques . . . 63
4.3.5 Triaxiality of the lunar fluid core . . . 64
4.3.6 External point mass interaction on extended figure of the fluid core . . . 65

5 Construction of a lunar ephemeris: INPOP17a 69
5.1 Fitting procedure . . . 69
5.1.1 Linearity and convergence . . . 70
5.1.2 Weighting adjustments and biases . . . 71
5.1.3 Bounded-value least square . . . 74
5.1.4 Uncertainty . . . 76
5.2 List of fitted parameters . . . 77
5.2.1 Constraints . . . 80
5.2.2 Correlation . . . 80
5.3 Results . . . 84
5.3.1 INPOP13c vs INPOP17a . . . 84
5.3.2 INPOP17a vs INPOP_{G} . . . 90
5.3.3 INPOP17a vs DE430 and EPM2016 . . . 93

6 Applications 101
6.1 Lunar interior . . . 101
6.1.1 Discussion about INPOP17a model . . . 102
6.1.2 Investigation attempts . . . 103

6.1.3 Degree-3 shape of the lunar fluid core . . . 106
6.2 Test of the principle of equivalence . . . 110
6.2.1 Context . . . 110
6.2.2 Method . . . 111
6.2.3 Results . . . 111
6.2.4 Discussion . . . 114
6.2.5 Perspectives . . . 115

7 Conclusion and Perspectives **117**

Appendices **121**

A Adjustments to reference points **123**
A.1 Estimation of coordinates . . . 123
A.1.1 LLR Station coordinates . . . 123
A.1.2 LLR retroreflector coordinates . . . 123
A.2 Station biases . . . 123

B Supplementary materials **127**
B.1 Correlation matrix and partial derivatives . . . 127
B.2 Topographic coupling at CMB . . . 135

C Article submitted to A&A: under revision **137**

D Article submitted to MNRAS **147**

Bibliography **161**

List of Tables

2.1 Comparison of the performance of the Grasse station correlation algorithm and the Expectation Maximization algorithm (EM) using simulated LLR observations and noise, under the cases described in the text (Section 2.2.5). 28

5.1 Fixed parameters for the Earth-Moon system. 83

5.2 Comparison of extended body parameters of solution: INPOP13c vs INPOP17a. Fitted parameters are indicated with their corresponding formal uncertainties (1-σ) 85

5.3 Comparison of post-fit residuals of LLR observations from ground stations with corresponding time span, number of normal points available, number of normal points used in each solution after a 3-σ rejection filter. The WRMS (in cm) is obtained with solutions INPOP13c (1969-2013) and INPOP17a (1969-2017). ‡: Statistics drawn from Fienga et al. (2014) 89

5.4 Reflector-wise statistics computed using residuals obtained with INPOP_G and INPOP17a, within the fit intervals 01/01/2015 to 01/01/2017 (with a 3-σ filter), with the WRMS in m (RMS weighted by number of observation from each reflector). Refer to Section (5.3.2) for the description of the solutions. 92

5.5 Extended body parameters for the Earth and the Moon. Uncertainties for INPOP_G and INPOP17a (1-σ) are obtained from a 5% jackknife (JK). DE430 uncertainties seem to be inflated (unknown scaling) formal uncertainties and EPM solutions provide the 1-σ formal uncertainties. †: C_{32}, S_{32} and C_{33} are reference values from the GRAIL analysis by Konopliv et al. (2013). ‡: h_2 reference value from LRO-LOLA analysis by Mazarico et al. (2014). * : derived quantity. Refer to Section 5.3.2 for the description of the solution INPOP_G 96

6.1 Comparison between solutions: Extended body parameters for the Moon. Uncertainties are obtained from a 5% jackknife (JK) test, the least squares 1-σ uncertainties being either consistent or smaller than the JK estimations. * stands for values fixed to model (GL0660b) values from GRAIL. 17a refers to the INPOP17a solution and S2 refers to an internal version of INPOP with the dynamical model described in Section (6.1.3). ‡ indicates that the h_2 reference value is extracted from Mazarico et al. (2014). 108
6.2 Comparison of results for the ratio Δ_{ESM} (Column 4) estimated with the solution INPOP17A with LLR dataset between: 1) 1969-2011 (for comparison with (Williams et al., 2012b; Müller et al., 2012)); 2) 1969-2017 with data obtain only in Green wavelength, 3) 1969-2017 with data obtained with both Green and IR wavelength. Column 5 contains the converted $\cos D$ coefficient expressed in mm (see Eqn. 6.2). Column 6 empirically corrects the radial perturbation for effects related to solar radiation pressure and thermal expansion. Column 7 contains the ratio Δ_{ESM} derived from Eqn. 6.2 and values of Column 6. 113
6.3 Results of the SEP estimates obtained from the LLR EP numerical estimates, after removing the WEP component provided by the laboratory experiments from Adelberger (2001); Williams et al. (2009). 114

A.1 Fitted values of LLR station coordinates and velocities (expressed in meters and meters per year respectively), at J2000.0, for different solutions. The reference values correspond to ITRF2005. * indicates fixed parameters. 124
A.2 Fitted values of selenocentric coordinates of reflectors (in meters). The reference values are from a previous release of INPOP (Fienga et al., 2014, p. 27). 125
A.3 Estimated values of station biases over different periods (2-way light time in cm) 126

List of Figures

1.1 The Earth-Moon system: The angle between the Earth's equator and the ecliptic, or the plane of the Earth's orbit around the Sun, is 23.5 degrees, and this tilt produces the seasons. The Moon provides a steadying influence for the Earth's tilt, keeping it from varying widely and producing dramatic climate variations. Also note that the plane of the lunar orbit falls neither in the Earth's orbital plane nor in the ecliptic. Source: Kenneth R Lang (2011, p. 184) 3

1.2 According to the fission hypothesis (left), the rotational speed of the young Earth was great enough for its equatorial bulge to separate from the Earth and become the Moon. In the capture hypothesis (middle), a vagabond Moon-sized object once passed close enough to be captured by the Earth's gravitational embrace. We have pictured disruptive capture, with subsequent accretion, but the Moon might have been captured intact. The accretion hypothesis (right) asserts that the Moon formed from a disk near the young Earth. Source: Kenneth R Lang (2011, p. 197) 4

1.3 Massive projectile (A) striking the young, still forming Earth (B) nearly 4.6 billion years ago. Some of the ejected mass fraction remained in Earth orbit (C). A proto-Moon began to form from the orbiting material (D), accreting neighborhood matter, and finally became the Moon (E). Source: Kenneth R Lang (2011, p. 198) . . . 5

2.1 Lunar return pulses over a ranging session at Grasse station using 532 nm laser. File reference: 14121704.09b 14

2.2 Example of calibration profile (measured) from the Grasse station . $\mu_{cal} = 100.29$ ns and $\sigma_{cal} = 60$ ps (with FWHM ≈ 150 ps). File reference: 13010303.08b 17

2.3 Fixed shape of a correlation kernal (simulated) used within the normal point algorithm at the Grasse station, for peak determination of return pulse using the correlation method. Correlation kernal width is chosen so as to match the binning used for the observations. 18

2.4 Lunar return pulses over two ranging session at Grasse station using 532 nm laser. Equal number of photon count is detected between multiple binning intervals, due to which the automatic peak detection algorithm fails to resolve the peaks within the histogram. File reference: 14121705.47b (top), 13010402.33b (bottom). 19
2.5 Filtered lunar return pulses over a ranging session at the Grasse station using 532 nm laser. The distribution is clearly asymmetric due to the combined effect of photo-diodes and timing electronics. The reflector orientation would not contribute to this asymmetry, as the array is considered to be uniform. File reference: 15032717.44b 21
2.6 Improvement in normal point sigma by replacing LLR residuals within the Grasse station full rate data (original), with DE430 ephemeris and GINS reduction model processed residuals (replaced). An improvement of 5% on the standard deviation is noticed. The offset from zero is due to the uncorrected calibration value. 22
2.7 Cumulative distribution function of photon count/session obtained with the 532 nm (Green) wavelength (2014-2017) and the 1064 nm (IR) wavelength (2015-2017) at the Grasse LLR station. 33
2.8 Histogram of annual frequency of LLR data from LLR stations (with the percentage contributions indicated above) with relative contribution from each LRR array including Grasse IR (1064 nm) observations. Points indicate the annual mean of post-fit residuals (in cm) obtained with INPOP17a. The dominance of range observations to Apollo reflectors is evident. A change can be noticed after 2014 due to the contribution from IR at Grasse. 35
2.9 Grasse reflector wise distribution at 532 nm and 1064 nm from 2015 to 2017. 36
2.10 Spatial distribution of retro-reflectors on the lunar surface. 38
2.11 APOLLO and Grasse LLR observations in terms of i) observational accuracy as given by the annual mean of normal point uncertainty (converted from ps to 1-way light time (LT) in cm) and ii) annual weighted root mean square of post-fit residuals (1-way LT in cm) obtained with INPOP17a. 39
2.12 Distribution of IR wavelength LLR observations over 2 years from Grasse vs lunar phase. 40
2.13 Distribution of Green wavelength LLR observations over 2 years from Grasse vs lunar phase. 40
2.14 Distribution of Green wavelength LLR observations over 2 years from APOLLO vs lunar phase. 41

3.1 Schematic of the movement of the Earth-Moon system. The light-time computation involves the state vectors (position (P) and velocity (V)) of the Earth and the Moon at a given time (T), in the ICRF reference frame, at: emission of the laser pulse from the station on the Earth, reflection of the laser pulse off the lunar retro-reflectors, and reception of the reflected pulse at the Earth station. 45

3.2 θ is the angle of nutation between $\vec{K}$ and $\vec{k}$, ϕ is the angle of precession between $\vec{i}$ and $\vec{O\Omega}$, ψ is the rotation angle between $\vec{O\Omega}$ and $\vec{I}$. Ω is the ascending node. Courtesy: Manche (2011, Fig. 3.1) . . . 49

3.3 Multi-geodetic characterization of the seasonal signal at the Grasse geodetic reference station, France. Strong correlation between GPS observations and non-tidal loading predicted deformation due to hydrology. LLR observations agree reasonably well with GPS and hydrology loading predictions in the U component. The estimated amplitude of the effect is (8.5 ± 0.5) mm in the Up component. LLR observations lack sensitivity in the other directions and hence are not provided. Grasse observations are stacked and averaged by month over 13 years. Used with permission from Mémin et al. (2016). 56

5.1 Bias correction and weight scaling requirement for LLR observations from APOLLO (top) and Grasse (bottom) stations. Points in orange and black indicate the post-fit residuals [1-way LT in cm] before and after the correction of estimated bias through LLR analysis. Bias numbering corresponds to that provided in Table (A.3). Points in red indicate the normal point uncertainty from the LLR observation after scaling. Uncertainties from Grasse station are divided by the square root of the number of echoes of each LLR normal point (as recommended), to allow comparison with the uncertainties from the APOLLO station. 72

5.2 Unscaled uncertainties of LLR observations from APOLLO (top) and Grasse (bottom) stations. All the marked regions for APOLLO correspond to logged changes at the station. For Grasse station, regions - A1, A2 and C have unrealistic (near-zero) uncertainties due to suspected rejection filter scaling issues within the normal point algorithm as addressed in Section (2.2.3). 73

5.3 Annual mean of weights from different LLR stations after scaling the uncertainties present within LLR observation (converted to 1-way LT [cm]). The observations obtained from Grasse during 2010-2017 have an accuracy at nearly the same level as of APOLLO station. . 75

5.4 Jackknife (JK) data re-sampling with 5% of total observations removed for variance estimation. The selection is performed from a uniform random distribution (points in red). 77
5.5 Comparison of differences in geocentric distance of the Moon (in m) with DE430 using a) INPOP13c (in black) and b) INPOP17a (in red). The reduction in the radial differences is due to the reduction of the estimated parameter GM_{EMB}, indicating a more consistent estimate with DE430 (Williams et al., 2013). 86
5.6 Comparison of differences in lunar Euler angle rates (where $\dot{\phi}$: rate of precession angle, $\dot{\theta}$: rate of nutation angle and $\dot{\psi}$: rate of rotation angle) with DE430 using a) INPOP13c (in black) and b) INPOP17a (in red). 87
5.7 Post-fit residuals in (cm) vs time (year) obtained with INPOP17a for : a) GRASSE station with the 532 nm wavelength, b) GRASSE station with the 1064 nm wavelength, c) McDonald, MLRS1, MLRS2, Haleakala and Matera stations, d) APOLLO station. Post-fit residuals here are filtered at 5-σ. 98

6.1 Longitude libration signature of ±1 mm over 48 years on the 1-way light time range (0.33 mas on longitude libration) with a period of about 3 years (weak) arising from the introduction of higher order figure-figure interaction (fourth degree torque) between the Moon and the Earth, as provided by $\vec{N}_{22}$ torque in Bois et al. (1992, p. 197).104
6.2 Longitude libration signature of ±3 mm over 48 years on the 1-way light time range (1 mas on longitude libration) with a period of about 3 years arising from the introduction of higher order inter figure-figure interaction (fifth degree torque) between the Moon and the Earth, as provided by $\vec{N}_{23}$ torque in Bois et al. (1992, p. 198). . 105
6.3 Contribution of degree-3 love number on the 1-way light time range. 106
6.4 Longitude libration signature arising from unmodeled effects within the dynamical model, with a period of 6 year and amplitude 5 cm on the range. Post-fit residuals (in 1-way light time [cm]) obtained with APOLLO station data vs time (in years) from solution with : (left) GRAIL-derived degree-3 lunar gravity field coefficients, (center) LLR-derived degree-3 lunar gravity field coefficients ($C_{3,2}$, $S_{3,2}$ and $C_{3,3}$), (right) GRAIL-derived degree-3 lunar gravity field coefficients with the model described in Section (6.1.3). 109

B.1 Correlation between the parameters of the dynamical model and reduction model. 128

B.2 Reflector-wise plot of partial derivatives of dynamical model parameters: A15 (Blue), A14 (Green), A11 (Black), L2 (Cyan), L1 (Red). δ indicates the amplitude of the deviation from the central value used for the respective parameter. Label X_c represents the parameter X with the subscript (c) indicating the lunar fluid core. . 129
B.8 Correlation between core degree-3 spherical harmonics arising from the topographic coupling at the core-mantle boundary of the Moon. 135

List of Abbreviations

AIRS	Atmospheric Infrared Sounder
APOLLO	Apache Point Observatory Lunar Laser-ranging Operation
BCRS	Barycentric Celestial Reference System
BVLS	Bounded-Value Least-Square
CCD	Charge-Coupled Device
CDF	Cumulative Distribution Function
CERGA	CEntre de Recherches en Géodynamique et Astrométrie
CIO	Celestial Intermediate Origin
CIP	Celestial Intermediate Pole
CMB	Core-Mantle Boundary
CMP	Conventional Mean Pole
CNES	Centre National d'Etudes Spatiales
CRD	Consolidated Range Data
DE	Developmental Ephemeris
DGP	Dvali-Gabadadze-Porrati theory
EGM	Earth Gravitational Model
EM	Earth-Moon
EM	Expectation Maximization
EOP	Earth Orientation Parameter
EOST	Ecole et Observatoire des Sciences de la Terre
EP	Equivalence Principle
EPM	Ephemerides of Planets and the Moon
ESA	European Space Agency
FCN	Free Core Nutation
FES	Finite Element Solution
GCRF	Geocentric Celestial Reference Frame
GGM	Global Gravity Model
GINS	Géodésie par Intégrations Numériques Simultanées
GLDAS	Global Land Data Assimilation System
GPS	Global Positioning System

GRACE	Gravity Recovery And Climate Experiment
GRAIL	Gravity Recovery and Interior Laboratory
GRGS	Groupe de Recherche de Géodésie Spatiale
GRT	General Relativity Theory
GSFC	Goddard Space Flight Center
IAA	Institute of Applied Astronomy
IAU	International Astronomical Union
ICRF	International Celestial Reference Frame
IERS	International Earth Rotation and Reference Systems
IfE	Institut für Erdmessung
ILRS	International Laser Ranging Service
IMCCE	Institut de Mécanique Céleste et de Calcul des Éphémérides
INPOP	Intégrateur Planétaire de l'Observatoire de Paris
IR	Infra-Red
ITRF	International Terrestrial Reference Frame
ITRS	International Terrestrial Reference System
JD	Julian Day
JK	Jack-Knife
JPL	Jet Propulsion Laboratory
KEOF	Kalman Earth Orientation Filter
KREEP	potassium (K), rare earth elements (REE), phosphorous (P)
LCRF	Lunar-Centric Reference Frame
LLR	Lunar Laser Ranging
LOLA	Lunar Orbiter Laser Altimeter
LP	Lunar Prospector
LPSC	Lunar and Planetary Science Conference
LRO	Lunar Reconnaissance Orbiter
LRRR	Lunar Ranging Retro Reflector
LS	Least-Square
LT	Light time
MERRA	Modern-Era Retrospective analysis for Research and Applications
MICROSCOPE	MICROSatellite à traînée Compensée pour l'Observation du Principe d'Equivalence
MIT	Massachusetts Institute of Technology
MLE	Maximum Likelihood Estimation
MLRS	McDonald Laser Ranging System
MNRAS	Monthly Notices of the Royal Astronomical Society
NASA	National Aeronautics and Space Administration
Nd:YAG	Neodymium-Doped Yttrium Aluminium Garnet
NNLS	Non-Negative Least-Square

OCA	Observatoire de la Côte d'Azur
PA	Principal Axis
PDF	Probability Distribution Function
PEP	Planetary Ephemeris Program
PKT	Procellarum KREEP Terrane
POLAC	Paris Observatory Lunar Analysis Center
RAS	Russian Academy of Sciences
RMS	Root Mean Squares
SEP	Strong Equivalence Principle
SLR	Satellite Laser Ranging
SOFA	Standards of Fundamental Astronomy
SSB	Solar-System Barycenter
SVD	Singular Value Decomposition
TAI	Temps Atomique International
TCB	Temps Coordonnée Barycentrique
TCG	Geocentric Coordinate Time
TDB	Temps Dynamique Barycentrique
TT	Terrestrial Time
UFF	Universality of Free Fall
UT	Universal Time
UTC	Universal Coordinated Time
VLBI	Very-Long-Baseline Interferometry
WEP	Weak Equivalence Principle
WLS	Weighted Least-Square
WRMS	Weighted Root Mean Squares

Chapter 1

Introduction

The Moon (*in Malayalam:* ചന്ദ്രൻ), is the brightest and the largest object in our night sky. It makes Earth a more livable planet by moderating Earth's wobble on its axis, leading to a relatively stable climate (Laskar et al., 1993). The Moon plays a crucial role to understand the evolutionary history (Section 1.1.1) of the terrestrial planets, as it is the most accessible planetary body that preserves a record spanning most of solar system history. Understanding the evolution of a planetary body requires an in-depth knowledge of its interior structure (Section 1.1.2), involving the information on its composition, differentiation and heat flow.

1.1 Physics of the Earth-Moon system

The gravitational forcing arising from the pull of external objects varies from one part of a body to another, producing differential tugs also known as tidal force (e.g., Avsyuk, 1977). Tidal forces can deform a body and produce torques that alter its rotation state, hence they are important to many aspects of the structure and evolution of planetary bodies (Darwin, 1892).

The Moon pulls the Earth's oceans and the oceans pull back, in accord with Newton's third law of motion that every action has an equal and opposite reaction. Since the gravitational force decreases with distance, the Moon pulls hardest on the ocean facing it and least on the opposite ocean, thus creating two tidal bulges. As the Earth's rotation carries the continents past these tidal bulges, we experience the rise and fall of oceanic water level. The Sun also contributes to the formation of tides in a similar manner. The friction of the continents and the rapid rotation of the Earth carry the ocean's bulge forward so it precedes the Earth-Moon line by about 3 degrees. As the ocean tides flood and ebb, they create eddies in the water producing friction and dissipating energy at the expense of the Earth's rotation.

As a result of this tidal friction the rotation of the Earth is slowing down at a

rate of about 2-3 ms per century. One of the fundamental laws of physics is the law of conservation of momentum. A loss in the rotational angular momentum equals the gain in the orbital angular momentum. Hence as the Earth slows down, the momentum lost is transferred to the Moon's orbit. This gain results in the increase of the distance between the Earth and the Moon, as their masses remain constant. The rate of this outward motion of the Moon amounts to about 3.8 cm/yr. This value is also measurable with the analysis of laser ranging from the Earth (Williams et al., 2014c), to the lunar retro-reflectors placed on the Moon by Apollo astronauts during the Cold War inspired Space Race era.

If this outward motion is extrapolated into the past, we see that the Moon was closer to the Earth, 4.6 billion years ago, when the Earth and Moon were formed. This suggests the formation of the Moon near or even out of the Earth in the distant past, considering stronger tidal interaction propelling the Moon outward at a quicker rate.

1.1.1 Formation and evolution mechanism

How did the Moon form? What theory best explains the origin of the moon? Any theory of the Moon's origin, must explain, the Moon's relatively large mass with respect to its planet Earth. Mars is the only other terrestrial planet to have a moon, however its two satellites are relatively very small. The giant planets have extensive satellite systems, but their moons are usually composed of low-density rock-ice mixtures unlike our high-density rocky Moon.

A satisfactory theory must also explain the Moon's peculiar orbit which lies at 5 degrees to the ecliptic plane (plane of the Earth's orbit around the Sun) which is itself tilted 23.5 degrees with respect to the Earth's equatorial plane (see Fig. 1.1). Furthermore, its mean mass density of about 3344 kg/m^3 is much lower than the Earth's mean mass density of 5513 kg/m^3.

Comparison of the lunar rocks returned from the lunar sample return missions provides further constraints on the Moon's history. The oldest rocks on the Moon solidified about 4.5 billion years ago, which means that the Moon is about as old as the Earth. An important distinction comes from the similar quantities of oxygen isotopes in both Moon and Earth rocks, suggesting common ancestry, instead of the Moon forming elsewhere and then being captured by the Earth's gravity. Another key constraint is the compositional differences, with Moon rocks lacking any detectable water-bearing minerals, or other kinds of volatile elements with low melting points. Yet when compared to the Earth, the Moon is enriched in non-volatile substances having high melting points that require high temperatures and extraordinary heat to vaporize into space.

Fission, capture and co-accretion models (see Fig. 1.2) of lunar origin have all been studied in great detail for more than a century, but none satisfies both the

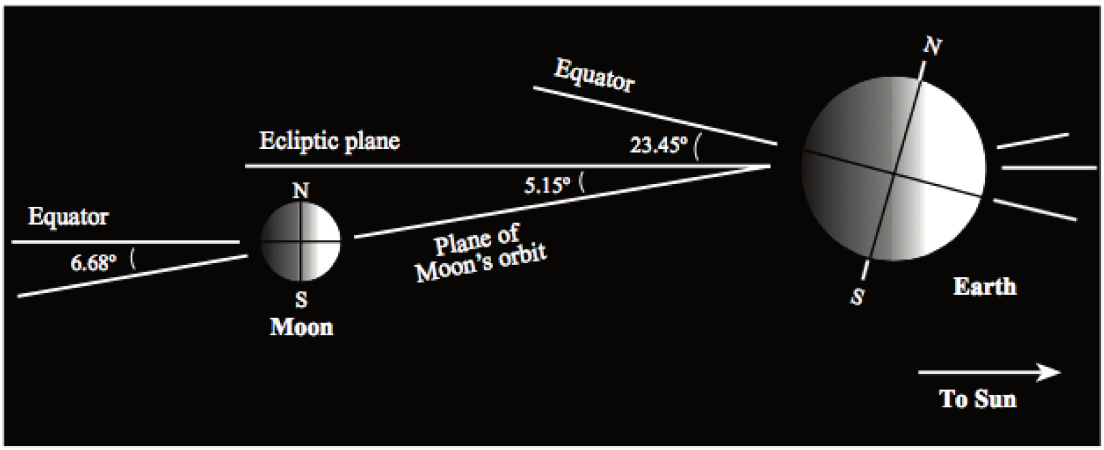

Figure 1.1: The Earth-Moon system: The angle between the Earth's equator and the ecliptic, or the plane of the Earth's orbit around the Sun, is 23.5 degrees, and this tilt produces the seasons. The Moon provides a steadying influence for the Earth's tilt, keeping it from varying widely and producing dramatic climate variations. Also note that the plane of the lunar orbit falls neither in the Earth's orbital plane nor in the ecliptic. Source: Kenneth R Lang (2011, p. 184)

dynamical and chemical constraints in a straightforward manner.

The favored hypothesis is the giant impact model, in which a collision between the Earth and a Mars-sized or larger planetary embryo ejects a lunar mass (or more) of material into Earth's orbit (see Fig. 1.3). Assuming both bodies were differentiated prior to the impact, this model would explain the apparent similarities between the lunar composition and that of the Earth's mantle and at the same time the lack of volatile material on the Moon. Volatile material would have vaporized completely by the impact, and it would have remained in a gaseous state within the circumterrestrial disk, allowing most of the volatiles to escape into interplanetary space. A range of impactor and impact parameters can place roughly one lunar mass of material primarily from the mantle of the impactor and/or Earth, into terrestrial orbit beyond Roche's limit[1]. Once this material is cool enough to form condensed bodies, it can quickly accumulate into a single large moon.

However, the current lunar orbital inclination of five degrees requires a subsequent dynamical process that is still unclear (Touma and Wisdom, 1998; Ward and Canup, 2000; Pahlevan and Morbidelli, 2015). Giant impact simulations find that the lunar disk is predominantly [>60 weight percent (wt %)] composed of material originating from the impactor, which is expected to have a different iso-

[1]The Roche limit is the distance from a planet at which tidal effects would cause an object to disintegrate because the differential force of gravity from the planet overcomes the attraction of the parts of the object for one another.

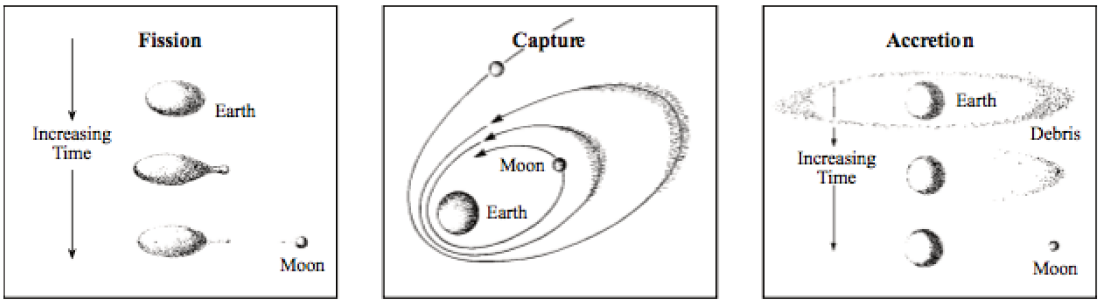

Figure 1.2: According to the fission hypothesis (left), the rotational speed of the young Earth was great enough for its equatorial bulge to separate from the Earth and become the Moon. In the capture hypothesis (middle), a vagabond Moon-sized object once passed close enough to be captured by the Earth's gravitational embrace. We have pictured disruptive capture, with subsequent accretion, but the Moon might have been captured intact. The accretion hypothesis (right) asserts that the Moon formed from a disk near the young Earth. Source: Kenneth R Lang (2011, p. 197)

topic signature than the Earth (Canup and Asphaug, 2001; Canup, 2004, 2008). This has been challenged by the Moon's unexpectedly Earth-like isotopic composition (Melosh, 2014; Burkhardt, 2014; Young et al., 2016) as well as the discovery that the angular momentum could have been transferred away from the Earth-Moon system since the last giant impact (Ćuk and Stewart, 2012; Wisdom and Tian, 2015; Ćuk et al., 2016; Tian et al., 2017). New theories that support a multiple-large impact origin for the Moon emerge due to the difficultly to reconcile giant-impact models with the compositional similarity of the Earth and Moon without violating angular momentum constraints (Rufu et al., 2017).

So how do we arrive at an improved theory? What additional constraints do we have that could support a better hypothesis? For this, we deduce the internal structure of the Moon, which gives us clues to it its evolutionary history.

1.1.2 Lunar interior structure

The lunar interior is hidden from direct inspection, so it must be investigated by measurements on and above the surface. During the Apollo (US) and Luna (Russia) Moon missions, many samples were returned to the Earth. The Apollo missions were also involved in the deployment of seismometers, heat-flow probes, magnetometers, laser retro-reflectors and collection of data from orbit. The information brought by these missions revealed that the evolution of the Moon was drastically different from that of the Earth.

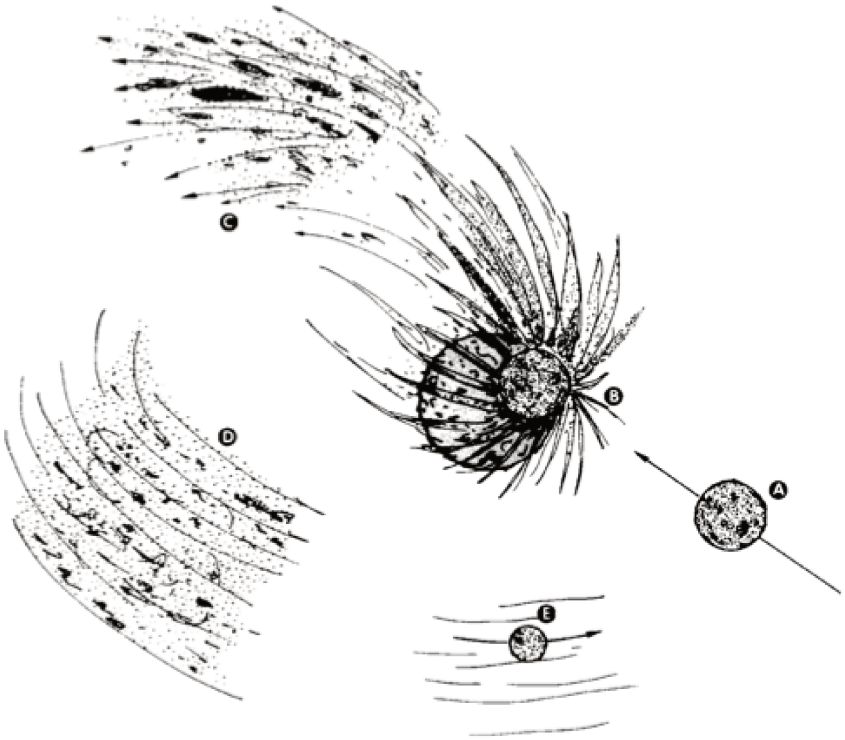

Figure 1.3: Massive projectile (A) striking the young, still forming Earth (B) nearly 4.6 billion years ago. Some of the ejected mass fraction remained in Earth orbit (C). A proto-Moon began to form from the orbiting material (D), accreting neighborhood matter, and finally became the Moon (E). Source: Kenneth R Lang (2011, p. 198)

Observations from the Apollo data hinted that a dichotomy in the geologic processes may have existed between the lunar nearside and far-side. Topographic data obtained from the laser altimeter on the Apollo 15 probe, showed that there was a 2-km displacement between the Moon's center of mass and center of figure roughly along the Earth-Moon axis (Kaula et al., 1972), suggesting far-side crust was thicker than that of the nearside.

Electromagnetic-sounding data placed an upper limit of about 500 km on the core radius (Hood, 1986). The measurement of a weak, induced dipolar magnetic field as the Moon passes through the Earth's geomagnetic tail implies the existence of a high-electrical-conductivity core with a radius of about 340 ± 90 km (Hood et al., 1999), whereas Shimizu et al. (2013) found a radius of 290 km with an upper bound of 400 km. Additionally, the analyses of small rotational signatures obtained from the lunar laser ranging experiment indicate that the energy is currently being dissipated at the boundary between a molten core and a solid mantle (Williams et al., 2001), providing an upper limit of 374 km for a Fe-FeS eutectic fluid core and a 352 km upper limit for a pure Fe composition.

While the available evidence indicates that the Moon possess a small molten core, the geophysical data could not unambiguously constrain its composition as none of the well-determined seismic ray paths, collected by the small network of lunar seismometers, pass through the deepest portion of the lunar interior (Wieczorek, 2009).

Reanalysis of the Apollo-era seismic data using array-processing methods suggests the presence of a solid inner and fluid outer core, with a partially molten boundary layer (Weber et al., 2011). However, analysis by another group Garcia et al. (2011), reports the remaining inconsistencies within Weber et al. (2011) and concludes with a lunar model without a solid inner core due to the strong uncertainties of the different parameters used.

Many of the samples returned contained high concentration of KREEP (potassium (K), rare earth elements (REE) and phosphorous (P)). Lawrence (1998) provides the surface thorium concentrations obtained from the Lunar Prospector gamma-ray spectrometer, showing high concentration of heat sources on the nearside region called Procellarum KREEP Terrane (PKT). A more recent study by Laneuville et al. (2013), show with the help of thermo-chemical convection models, that the impact of such localized heat sources in the crust leaves a present-day temperature anomaly within the nearside mantle with its influence down to the core-mantle boundary (CMB).

Contributions from GRAIL and LLR

The gravity field of a planet provides a view of its interior and thermal history by revealing areas of different density. The Gravity Recovery and Interior Laboratory

(GRAIL) mission placed a pair of satellites in an orbit around the Moon, acting as a highly sensitive gravimeter, and began mapping the Moon's gravity in early 2012. Zuber et al. (2013) provide the lunar gravity field to spherical harmonic degree and order 420, obtained from the spacecraft-to-spacecraft tracking observations from the GRAIL mission. The study revealed several new tectonic and geologic features of the Moon. Impacts have worked to homogenize the density structure of the Moon's upper crust while fracturing it extensively. Wieczorek et al. (2013) show that the upper crust is 35 to 40 kilometers thick and less dense and thus more porous than previously thought. Andrews-Hanna et al. (2013) show that the crust is cut by widespread magmatic dikes that may reflect a period of expansion early in the Moon's history.

From the 3 months of data collected over the primary mission, two independent groups at the Jet Propulsion Laboratory (JPL) and Goddard Space Flight Center (GSFC) determined the lunar gravity field (Konopliv et al., 2013; Lemoine et al., 2013) up to degree and order 660, with comparable estimates and uncertainties between the groups.

While the high-degree coefficients are very well determined, the solutions for the low-degree coefficients are very sensitive to the libration model (obtained from the fit of lunar ephemerides to lunar laser ranging (LLR) data) and to the models of the non-gravitational acceleration on the GRAIL spacecraft including the empirical periodic acceleration model (Konopliv et al., 2013). The physical libration model of the Moon from Williams et al. (2013) consists of a solid crust and mantle plus a uniform fluid core, without a solid inner core. Williams et al. (2014b) introduced variations on the models of Weber et al. (2011) and Garcia et al. (2011) to satisfy the lunar mean density, mean solid moment of inertia, love number and a deep low-velocity zone constraints to account for a solid inner core surrounded by an outer fluid core (see Williams et al. (2014b, Table 7-8)) to give a family of lunar interior models.

A detection of the solid inner core is feasible from very precise measurements of the lunar gravity field. The axis of rotation of a solid inner core within a liquid outer core can be different from the axis of the mantle. With an axis of rotation tilted by a different amount than the mantle, the inner core degree-2 spherical harmonics would produce variable gravity field as the core rotates. This causes a time varying C_{21} and S_{21} harmonics (when viewed in a mantle-fixed frame) with a period of 27.212 days (Williams, 2007). The search for variable C_{21} and S_{21} harmonics was one of the goals of the GRAIL mission. Though the mission goals were met, the search for the inner core periodicities did not find results above the noise level (Williams and Watkins, 2015). The detection of the solid inner core would provide further constraints to the models of lunar origin and evolution and answer key questions related to the possible existence of a now-extinct lunar

dynamo (Wieczorek, 2006; Laneuville et al., 2014).

Combining gravity field with other observational techniques provides synergistic advantage to the problem. Laser-altimeter data from a lunar orbiting spacecraft (e.g. LRO-LOLA) provides constraints on the body tides (Mazarico et al., 2014) and LLR provides rotational signatures (Rambaux and Williams, 2011). A study that combines these constraints (Matsuyama et al., 2016) provide probability distribution curves to the lunar solid inner core size and liquid core density. This can then be used to provide constraints on the thermal evolution of the lunar core and hence providing a link to its evolution. However, Matsuyama et al. (2016) did not consider the hemispheric asymmetry found by Laneuville et al. (2013); Zhang et al. (2013), which could influence the estimates of the lunar interior structure due to the tidal forcing brought by the asymmetry (Qin, 2015).

Thermal evolution models suggest that a portion of the core should have crystallized to form a solid inner core at its center (Zhang et al., 2013; Laneuville et al., 2013; Scheinberg et al., 2015). Hence, similar to the gravitational torques of the Earth acting on the lunar mantle, the Earth should also drive a tilt of the elliptical figure of the solid inner core, forcing it to precess with the 18.6 year period lunar mantle precession (Dumberry and Wieczorek, 2016). Furthermore, the gravitational torques exerted by the inner core on the lunar mantle may affect the Cassini state of the lunar mantle, similar to that expected for Mercury (Peale et al., 2016). This would in turn be detectable by LLR, provided the accuracy and time span of the LLR observations permit.

LLR observations continue to bring critical information in terms of libration sensitive low-degree gravity field coefficients due to its long time span and high accuracy, which would complement the low-degree coefficients of the GRAIL-derived gravity field models for the detection of the solid inner core of the Moon.

1.2 Tests of general relativity

The year 2015 marked the 100th anniversary of General Relativity Theory (GRT) (Einstein, 2015). Up to now, GRT successfully described all available observations and no clear observational evidence against General Relativity was identified. However, the discovery of Dark Energy that challenges GRT as a complete model for the macroscopic universe and the continuing failure to merge GRT and quantum physics indicate that new physical ideas should be searched for. To streamline this search it is indispensable to test GRT in all accessible regimes and to highest possible accuracy.

Violations of the Equivalence Principle (EP) are predicted by a number of modifications of GRT aimed to suggest a solution for the problem of Dark Energy and/or to merge GRT with quantum physics (Damour and Polyakov, 1994;

Damour and Donoghue, 2010; Damour, 2012). The Universality of Free Fall (UFF), an important part of the Equivalence Principle, is currently tested at a level of about 10^{-13} with torsion balances (Adelberger et al., 2003) and the LLR (Williams et al., 2012a; Müller et al., 2012). EP violations and time variations in the fundamental coupling constants could also be a result of the effects of a scalar field coupling with the gravitational field (Damour, 1996; Damour and Vokrouhlický, 1996). Therefore, tests of EP and $\dot{G}$ have great importance due to its wide reach as sensitive probes towards new physics (Murphy, 2013).

Some other formalisms often used to test gravity in the solar system and to solve some questions raised by the Dark Matter and the expending universe can also be tested with the LLR measurements: the modification of the inverse square law of gravity (Falcon, 2011), additional force represented by Yukawa-type expression (Adelberger et al., 2003; Müller et al., 2005).

> "Measurement of the precession rate can also probe a recent idea (called Dvali, Gabadadze, Porrati (DGP) gravity) in which the accelerated expansion of the universe arises not from a non-zero cosmological constant but rather from a long-range modification of the gravitational coupling, brought about by higher-dimensional effects (Lue and Starkman, 2003; Dvali et al., 2003; Dvali et al., 2003). Even though the lunar orbit is far smaller than the Gigaparsec length-scale characteristic of the anomalous coupling, there would be a measurable signature of this new physics, manifesting itself as an anomalous precession rate at about 5 μarcsec.yr^{-1}, roughly a factor of 10 below current LLR limits, and potentially reachable by millimeter quality LLR." – (Murphy, 2013, p. 8)

Tests of GRT remains as an important tool to streamline the theoretical development. While a number of space missions are planned to improve these tests (MICROSCOPE to test the UFF with the level of 10^{-15} (Bergé et al., 2015), Gaia (Hees et al., 2015) and BepiColombo (de Marchi and Congedo, 2017) to provide a number of high accuracy tests of GRT, EUCLID (Laureijs et al., 2011) to study the distribution of Dark Matter in our Galaxy and the Universe, etc.), the instrumentation proposed here will lead to study the solar system dynamics for aiming at a set of advanced GRT tests that are complementary to the planned space-mission tests.

Finally, direct measurement of Dark matter in the solar system is also proposed by Nordtvedt et al. (1995) with the detection of its gravitational influence on the most accurately measured quantity in the solar system, the Earth-Moon distances (Merkowitz, 2010).

1.3 Ephemerides and its applications

The 1960's were a turning point for the generation of ephemerides, before which analytical models were used for describing the state of the solar system bodies as a function of time. A team from the Lincoln Laboratory, MIT (Ash, 1965) introduced the planetary ephemeris program (PEP) on a computer software using FORTRAN IV language, to improve the planetary and lunar ephemerides using the results of radar and optical observations. The first laser ranges to the lunar retro-reflectors were obtained in 1969 after the Apollo landing (Faller et al., 1969). The change from lunar angular measurements to laser ranges marked a great improvement to the observational accuracy driving comparable improvements to the lunar ephemerides (Bender et al., 1973). Opportunities to test the theory of general relativity also surfaced (Shapiro, 1964; Nordtvedt, 1968; Williams et al., 1976; Anderson et al., 1978).

While the fitting of optical data was long accomplished with analytical theories for the Moon and planets, the improved data required the development of numerical integration techniques and more comprehensive physical models. In the late 1970's the numerically integrated planetary ephemerides were built by the Jet Propulsion Laboratory (JPL), called the developmental ephemeris (DE96) (Standish et al., 1976). Since then, there have been many versions of the JPL DE ephemerides through the present (Newhall et al., 1983; Standish Jr, 1990; Standish, 1998, 2006; Folkner et al., 2009; Folkner et al., 2014). These ephemerides are continuously fitted to the data gathered from tracking space probes (radar ranging, flybys and VLBI), optical data (transit, photographic plates and CCD observations for outer planets) and direct range measurements (LLR). Semi-analytical theories also emerged to take advantage from both the worlds (Chapront-Touze and Chapront, 1983), however they lack accuracy when compared with numerically integrated ephemerides.

Simultaneously, with the growing interest in space sciences, the European Space Agency (ESA) was actively involved in interplanetary missions and collaborated with other national space administrations. With these developments, the "Intégrateur Planétaire de l'Observatoire de Paris" (INPOP) project was initiated in 2003 to build the first European planetary ephemeris independently from JPL. The INPOP project evolved over the years with the first official release in 2008: INPOP06 (Fienga et al., 2008) followed by versions 08-15 (Fienga et al., 2009; Fienga et al., 2011; Fienga et al., 2014, 2015, 2016a). Through the official website[2] of the"Institut de Mécanique Céleste et de Calcul des Éphémérides" (IMCCE), these ephemerides are freely distributed to the users. With the help of ephemerides, the users can have access to the positions and the velocities of the

[2]Available at: www.imcce.fr/inpop

major planets, Moon and asteroids of our solar system, the libration angles of the Moon as well as the differences between the terrestrial time TT (time scale used to date the observations) and the solar system barycentric times (TDB/TCB) (time scales used in the equations of motion). The ephemerides can be accessed using CALCEPH (Gastineau et al., 2015) or SPICE (Acton, 1996) toolkit libraries.

In addition to INPOP and DE, another numerical ephemeris are those developed by the teams at the Institute of Applied Astronomy (IAA) of the Russian Academy of Sciences (RAS), called the Ephemerides of Planets and the Moon (EPM) (Pitjeva, 2005, 2013). These ephemerides are based on the same modeling as the JPL DE ephemerides. The most recent version being EPM2016 (Pavlov et al., 2016).

As numerical ephemerides are fitted to real observations, the mathematical model backing the ephemerides follow closely with the real-world processes. This enables a more realistic simulation of the natural processes allowing comparison of the real observations with simulated observations. Any remaining differences (post-fit residuals) between the simulated and the real observations indicate unmodeled effects within the numerical model provided the amplitude of the differences are greater than the level of the known accuracy of the real observations and also considering the absence of modeling errors at the same level. Introducing model additions/changes based on the detected unmodeled effects continuously improve the quality of the simulation as well as provide best-fit estimates of the model parameters.

Traditionally, numerical ephemerides are used to satisfy high accuracy requirements for spacecraft navigation and mission planning. Other scientific applications include (but are not limited to) orbit determination and localization (Fienga et al., 2016a), reference frame ties (Folkner et al., 1994), gravity field determination (Iess et al., 2014; Folkner et al., 2017) asteroid mass determination (Kuchynka et al., 2010), fundamental physics (Bertotti et al., 2003; Williams et al., 2004; Fienga et al., 2011; Fienga et al., 2016b), solar corona studies (Verma et al., 2013) and paleoclimate studies (Laskar et al., 2004, 2011).

For this study, we develop on the INPOP planetary and lunar ephemeris, as a laboratory to perform tests relevant to two of the interests described in the previous sections: lunar interior structure (Section 1.1) and test of the violation of the universality of free fall using the principle of equivalence (Section 1.2), in using LLR observations and a GRAIL-derived gravity field model (Konopliv et al., 2013).

1.4 Outline of the thesis

The following describes a brief outline of this thesis:

Chapter (2) discusses the observations used for this study, consisting of lunar laser ranging (LLR) data acquired between 1969 to 2017 from various LLR stations. The existing normal point algorithm at the Grasse LLR station is evaluated and an alternative algorithm is proposed. New LLR observations from the Grasse station obtained using the IR (1064 nm) wavelength are also included and its benefits are discussed.

The numerical model for the Earth-Moon system consists of two components: the reduction model (Chapter 3) and the dynamical model (Chapter 4). The geophysical and relativistic effects implemented within the reduction model (GINS software) are discussed with its impact on the Earth-Moon distance. The dynamical model consists of the INPOP planetary and lunar ephemeris. The lunar part of the ephemeris is described with the improvement from the previous model (INPOP13c).

Chapter (5) describes the processes behind the construction of a lunar ephemeris followed by the analysis of the post-fit residuals and comparison of the model parameter estimates with previous LLR analyses. A technical report on the new INPOP solution (INPOP17a) is published within the "Notes Scientifiques et Techniques de l'Institut de Mécanique Céleste", Viswanathan et al. (2017).

Chapter (6) applies the results to the study of lunar interior structure and a strong longitude libration signature of 6 years is detected. Investigation attempts to correct this signature are discussed and a model is provided. An article on the study of the lunar interior structure is submitted to the Astronomy & Astrophysics journal provided in Appendix (C). Chapter (6) also describes a test of the theory of general relativity with respect to the universality of free fall in the Earth-Moon system. A discussion on the results obtained is provided. An article on this work is accepted to the Monthly Notices of the Royal Astronomical Society (MNRAS) and provided in Appendix (D).

Chapter (7) summaries the achieved goals of this thesis, followed by the conclusion and future perspectives.

Chapter 2

Observation: Lunar Laser Ranging

2.1 Introduction

Lunar Ranging Retro Reflector (LRRR) arrays were part of the scientific payloads on the three US Manned (APOLLO XI, XIV, XV) and on-board two Soviet Rover (Lunakhod 1, 2) Lunar missions (hereby referred to as A11, A14, A15, L1 and L2 respectively). These arrays were installed by each respective mission, resulting in five distinct positions on the near-side of the Moon.

Ground-based telescopes were used to precisely point to the array location on the lunar near-side, and high energy laser pulses were fired. Initial attempts to acquire the return pulses were made at the Lick Observatory in California, US (Faller et al., 1969) with an outgoing beam, approximately 2 seconds of arc, corresponding to a spot diameter of 3.2 km on the lunar surface. Over the next decades, other ground-based telescopes from various sites joined the list of lunar laser ranging stations, namely, McDonald (Texas) (Bender et al., 1973), MLRS1 and MLRS2 (Texas) (Shelus, 1985), Haleakala (Hawaii) (Berg et al., 1978), Grasse (France) (Veillet et al., 1993; Samain et al., 1998; Torre, 2013), Matera (Italy) (Varghese et al., 1993) and APOLLO (New Mexico) (Murphy et al., 2008). The accuracy of observations improved over time with improvements in detector electronics, aided by larger ground-based telescopes, and improved normal point computation algorithms. The most accurate observations are provided by APOLLO station with a 3.5 m telescope (Murphy et al., 2012; Murphy, 2013) and to some extent the Grasse station with recently improved detection capabilities in infrared wavelength (Courde et al., 2017).

Retro-reflectors have the ability to reflect waves in the same direction as the incident waves, arising from the arrangement of the optical mirrors as a corner

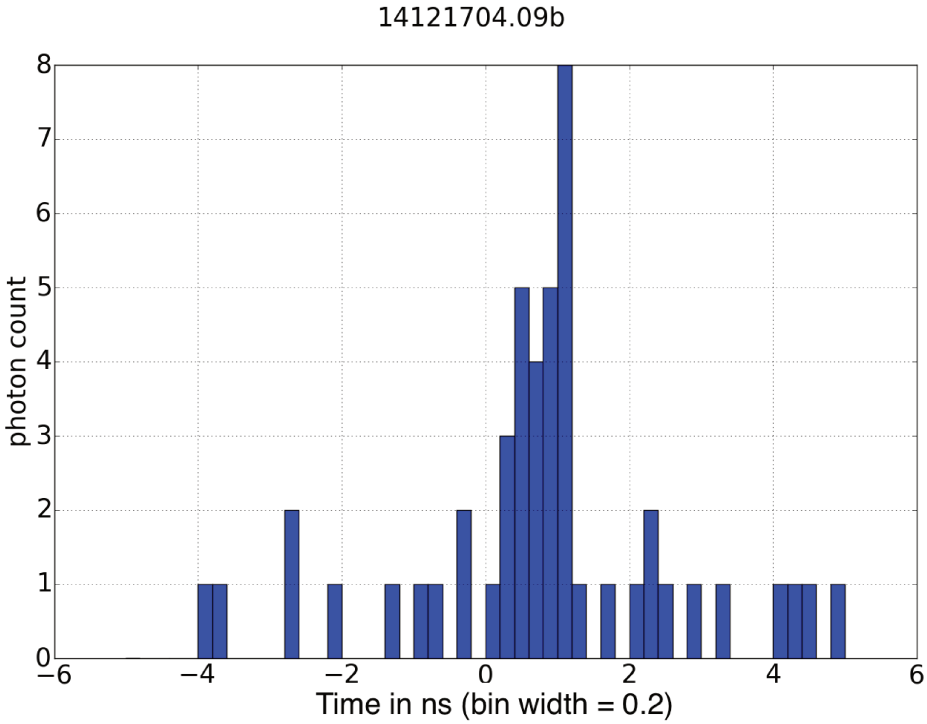

Figure 2.1: Lunar return pulses over a ranging session at Grasse station using 532 nm laser. File reference: 14121704.09b

cube within the retro-reflector arrays. The return laser pulses along with the noise from the scattered sunlight from the lunar surface are accumulated at the ground-station during the ranging sessions. The firing of the laser initiates a time-delay generator. With the help of a lunar ephemeris, the predicted delay (round-trip light-time of around 2.5s) of the pulses are known with some accuracy ($\approx$ 1ns). This helps to reduce the accumulation of noise by enabling a shorter time-window for the detection of the reflected laser pulse. Each acquired pulse is time stamped and compared with the predicted arrival time. This difference between the observed arrival time and the expected arrival time are stacked using a histogram. A statistically significant peak within the histogram differentiates the return pulses from the noise floor over the successive ranging attempts within a session. This dataset, comprising of all the return pulses along with the noise within the temporal window of a ranging session, is refered to as the full rate data.

2.2 Normal Point

2.2.1 Introduction

A normal point is a reduced observation containing the round trip time of the light pulse at a given time from the spatial reference of the Lunar Laser Ranging (LLR) station on the Earth to the retro-reflector array on the surface of the Moon, computed from many individual echoes. A normal point is computed from full-rate data. The idea is to reduce the data collected from one ranging session (consisting of several echoes) to one single time delay value, the 2-way light time at some specific epoch.

The primary advantage of using a normal point over the full-rate data is the reduction of the computational complexity achieved through a reduced data volume. Unlike satellite laser ranging (SLR) where the motion of the artificial satellite is rapid within each ranging session, high frequency variations (of a few hundred Hz) within lunar laser ranging are mostly associated with turbulent fluctuations within the Earth's upper atmosphere and local pressure-temperature gradients. Using a single normal point to represent the full-rate LLR data averages out most of these variations over the 10 minute ranging session. A study on the processes involved for the identification, filtering and reduction of the full-rate LLR data from the McDonald LLR station can be found in Abbot et al. (1973).

In order that the normal point well represents the full-rate data, the algorithm used for the computation of the former must well characterize the distribution of the latter.

In the case of laser ranging to the lunar retro-reflector arrays from ground-based stations, the mean of the detection time distribution comprising of the accumulated return pulses, indicates the average difference between the predicted and observed round-trip time taken by the photon. The photons traverse the sum of the total calibration path of the set-up and twice the Earth-Moon distance (up-leg and down-leg). The standard deviation of the detection time distribution is primarily due to the contributions from the orientation of the retro-reflector array or target and the response function of the detector and timing electronics, while the shape of the laser pulse fired defines the theoretical minimum (with contributions from the detector and timing electronics). The contribution from the atmospheric turbulences become dominant at low elevation angles (around 10°) while LLR is typically performed at higher elevation angles (30° to 40°) (Currie and Prochazka, 2014).

The International Laser Ranging Service (ILRS) Herstmonceux Normal Point algorithm (Pearlman et al., 2002) recommends a tight rejection limit of 2.5-σ for first photo-electron detection systems. This is because such detection systems often involve a photo-diode which is highly sensitive to the first-photon that arrives to

the detector. This arrival triggers an avalanche multiplication phenomenon which causes the signature of the detector to influence the skew of the expected return pulse distribution. A scheme for the normal point generation and first-photo bias at the APOLLO LLR station can be found in Michelsen (2010).

2.2.2 Data format

The historical LLR data spanning over 1969-2016 from all stations is available publicly in the "MINI" format at http://polac.obspm.fr/llrdatae.html. Recent LLR observations (both in Green and IR wavelength) from Grasse station (2015-2017) is made available at http://www.geoazur.fr/astrogeo/?href=observations/donnees/lune/brutes.

Each LLR normal point contains information about the ground station (ITRF code), targets (lunar reflectors), time of flight of photons (s), observation epoch (UTC), meteorological measurements at the ground station such as atmospheric pressure (0.01 $mbar$), ground temperature (0.1 $°C$) and relative humidity (%), wavelength of the laser used (0.1 nm) and data quality information through the number of echoes received, signal to noise ratio and the estimated uncertainties (0.1 ps).

This study uses the MINI format for the normal points. Another format available is the Consolidated Range Data (CRD) useful for kilohertz ranging applications, whose description can be found at the ILRS website[1].

2.2.3 Existing algorithm at Grasse station

The original code employed at the Grasse station uses a Visual Basic program allowing a user interface for the control of laser pulse firing, telescope pointing adjustments and normal point computation based on the Herstmonceux Normal Point Recommendation (Pearlman et al., 2002).

At the Grasse ILRS station, a fixed temporal detection window of ±50 ns is used for acquiring the incoming reflected photons after laser firing to the retro-reflectors. The arrival times of the reflected photons are compared with a semi-analytical lunar ephemeris provided by the Paris Observatory Lunar Analysis Center (POLAC), accurate to a few centimeters on the lunar orbit[2]. These differences are then stacked in time to form an histogram as shown in Fig. (2.1).

This is followed by the determination of the peak of the accumulated return pulses, identified using a correlation method. The accumulated return pulses are correlated with a fixed laser pulse shape. The histogram (Fig. 2.3) is intended to

[1] Available at https://ilrs.cddis.eosdis.nasa.gov/data_and_products/formats/crd.html

[2] Available at: http://polac.obspm.fr/lune.html

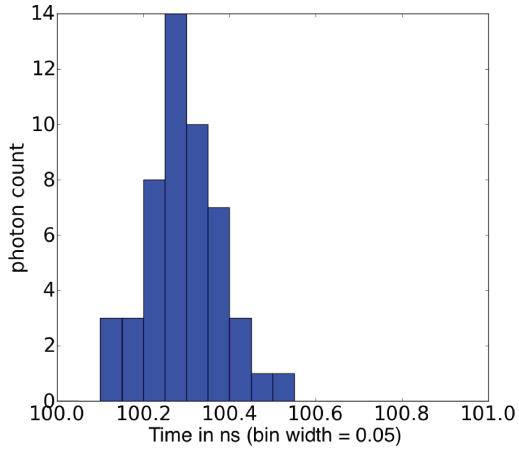

Figure 2.2: Example of calibration profile (measured) from the Grasse station . μ_{cal} = 100.29 ns and σ_{cal} = 60 ps (with FWHM ≈ 150 ps). File reference: 13010303.08b

represent the shape of the laser pulse fired (containing contributions from the electronic equipments). The bin with the maximum correlation coefficient is selected as the bin with the expected mean residual.

A rejection filter of 2.5-σ_r is then applied around the expected mean residual. The value of σ_r here is dependent on the reflectors onto which the ranging is performed, attributed by the array dimensions. The σ_r values are taken from Abbot et al. (1973) and rounded-off to one decimal place (σ_r = 0.3 ns for A15 and 0.2 ns for other LRRR, which in their study includes an average contribution due to the lunar librations).

After filtering, the mean of the corresponding date of the residuals is obtained (d_m). The nearest date of a real echo to this mean date is selected as the date of the observation (d_i) with a corresponding light time (LT_i) and residual (r_i).

The difference Δr between the mean of the filtered residuals (r_m) and the residual (r_i) is then added to the light time (LT_i). Every ranging session has a calibration light time to account for excess path length from the optical cables and electronics which must be removed from LT_i. The calibration procedure is performed before each ranging attempt and the mean of the calibration profile (see Fig. 2.2) is used to remove from the LT_i. When the calibration is performed for a longer time interval one can obtain a better determination of its profile (see Courde et al. (2017, Fig.3)).

The normal point corresponding to a ranging session is obtained by adding Δr to the light time LT_i. The standard deviation of the filtered residuals from the average residual r_m gives the observational uncertainty (σ_i).

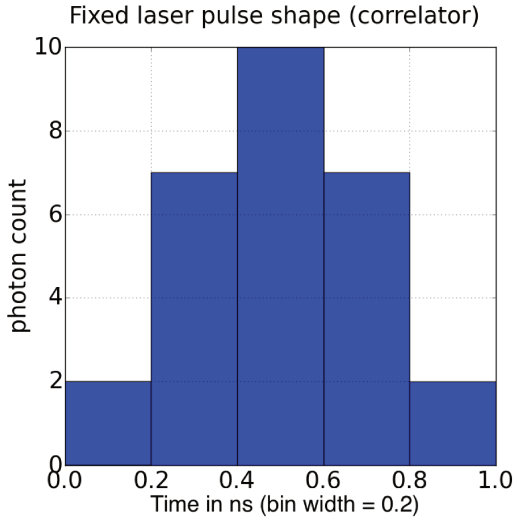

Figure 2.3: Fixed shape of a correlation kernal (simulated) used within the normal point algorithm at the Grasse station, for peak determination of return pulse using the correlation method. Correlation kernal width is chosen so as to match the binning used for the observations.

Challenges with the existing algorithm

- Grasse station algorithm recovery
  The original code employed at the Grasse station uses a Visual Basic program allowing a user interface for the control of laser pulse firing, telescope pointing adjustments and normal point computation based on the Herstmonceux Normal Point Recommendation (Pearlman et al., 2002).

  A Python implementation of this algorithm is made independently to recover the normal point computation at the Grasse station. Although the new implementation is able to recover most (about 90%) of the normal points, it is noticed that the remaining normal points were offset by a few tens of picoseconds in light time from that distributed publicly.

  These offsets were present in those ranging sessions where the algorithm failed to resolve between two similar peaks in the histogram. Examples of two such instances are made available in Fig. (2.4). In such cases, the automatic peak selection of the Grasse station algorithm is overridden by mean of a user selection of the histogram peak for the normal point computation. This introduces unaccounted for biases of about few millimeters within the normal point computation, while introducing reproducibility issues to normal points from such ranging sessions. Since the uncertainty in the choice of the user input is not taken into account during the normal point uncer-

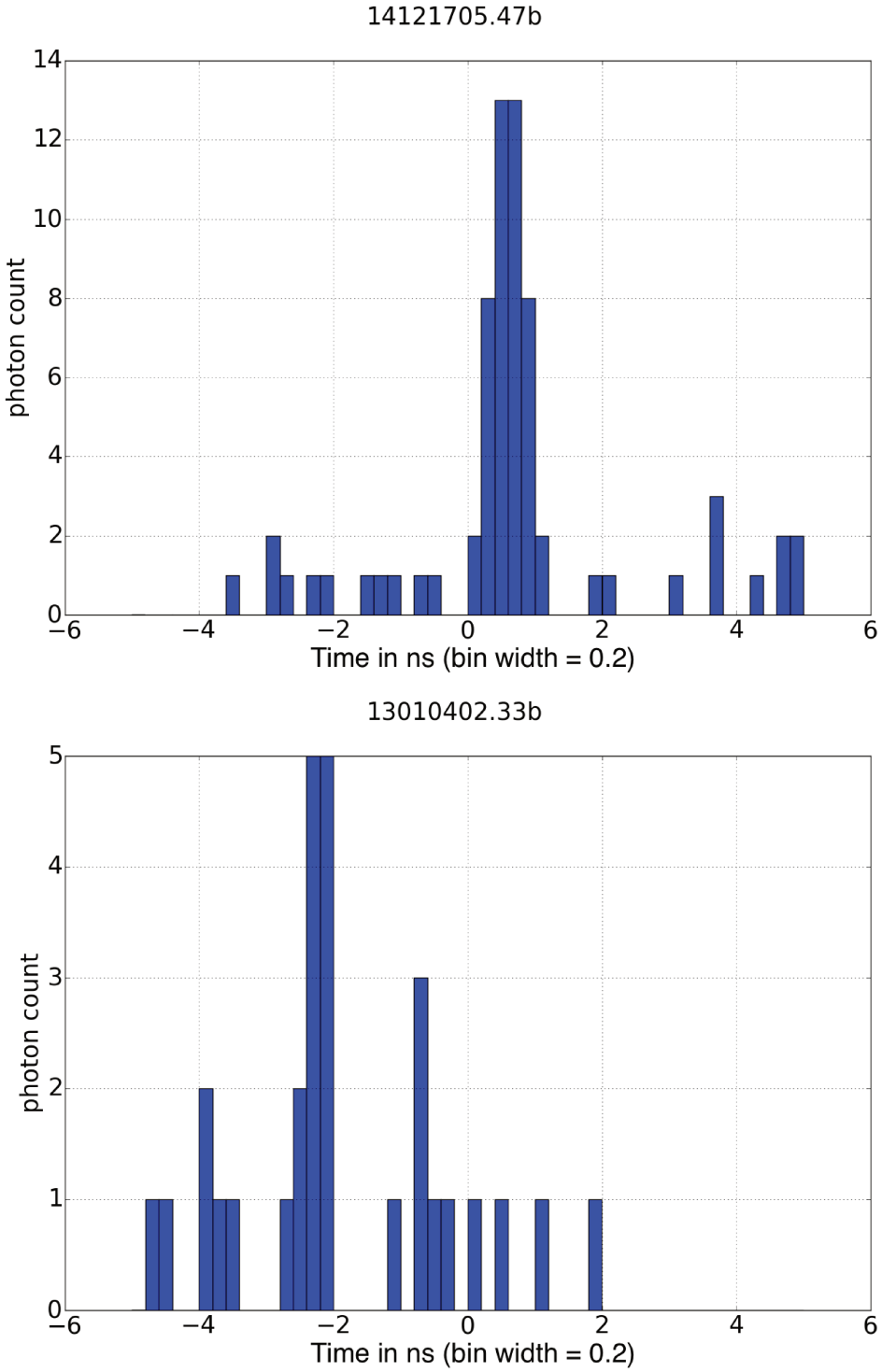

Figure 2.4: Lunar return pulses over two ranging session at Grasse station using 532 nm laser. Equal number of photon count is detected between multiple binning intervals, due to which the automatic peak detection algorithm fails to resolve the peaks within the histogram. File reference: 14121705.47b (top), 13010402.33b (bottom).

tainty computation, the public distribution of the normal points from such instances, impact the regression procedures used by LLR analyses groups (see Section 5.1.2).

As a better practice it is recommended by this study to remove such observations from the distributed list of normal points.

- Rejection filter scaling
  The ILRS recommends a scaling factor of 2.5 for the rejection filter with systems that detect the first photo-electron. A change in the rejection filter will directly impact the standard deviation of the filtered residuals (and therefore the construction of lunar ephemerides as shown in Section 5.1.2) stored in the normal point, especially when outliers are involved.

  Within different versions of the original code available through internal repositories at the Grasse station, variations of this scaling factor is noticed from 2.2 to 2.5 prior to year 2000. Such changes made at the Grasse station are often internal and the information is not logged for public access.

  As a result, one can notice scaling factors being applied independently by LLR analyses groups (Manche, 2011; Williams et al., 2014a; Pavlov et al., 2016) while weighting observations during regression, using normal point uncertainties (see Fig. 5.1.2).

  As a better practice it is recommended by this study to:

  1. Log changes to algorithm through a publicly accessible domain;
  2. Suggested use of a version control tool for all codes impacting publicly released data.

- Fixed shape of correlator
  The Grasse station algorithm uses a fixed shape (see Fig. 2.3) within the correlation method for separating the return pulse distribution from accumulated noise within the histogram. While this fixed shape approximates to an ideal laser pulse, return pulse distribution from LLR involves other dependencies such as that from photo-diodes, timing electronics and retro-reflector orientation (Michelsen, 2010).

  Although the current LLR photon detection rate (typically below 100 photons over 10 minutes ranging session) at the Grasse station is not sufficient to fully characterize lunar reflector orientation signatures (trapezoidal), the detected photon distributions are seldom symmetric (see Fig. 2.5). Hence, employing a fixed symmetric Gaussian distribution is only an approximation to the expected pulse distribution. An alternative is to use the calibration profile of the laser pulse at the Grasse station (see Fig. 2.2) obtained by

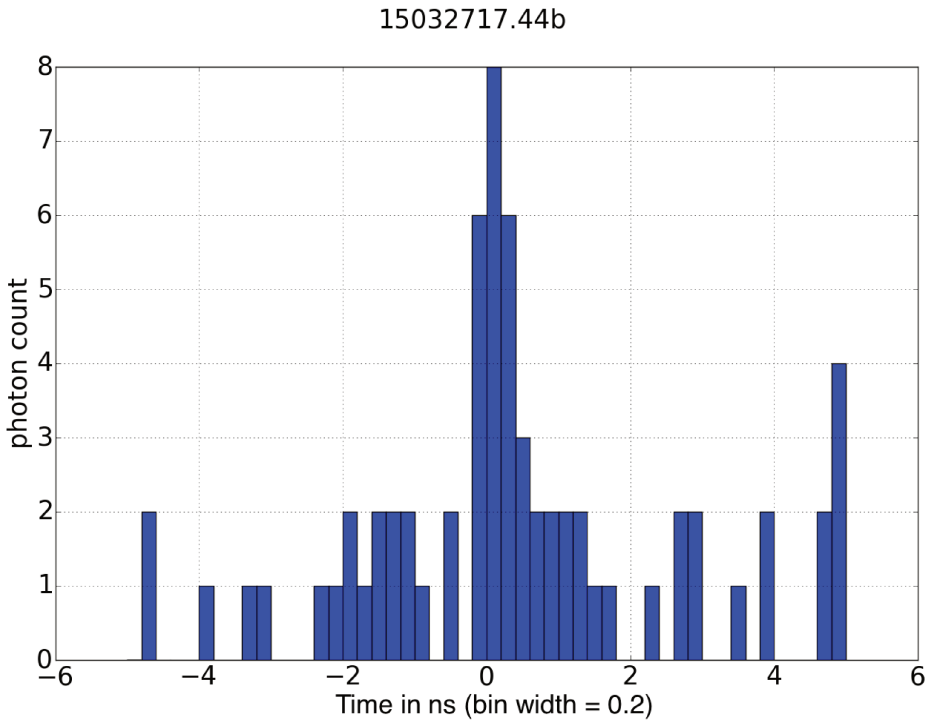

Figure 2.5: Filtered lunar return pulses over a ranging session at the Grasse station using 532 nm laser. The distribution is clearly asymmetric due to the combined effect of photo-diodes and timing electronics. The reflector orientation would not contribute to this asymmetry, as the array is considered to be uniform. File reference: 15032717.44b

.

ranging to a corner cube mounted at the telescope output (Samain et al., 1998; Courde et al., 2017).

- Choice of ephemerides used for prediction
  The Grasse station LLR facility uses light time predictions provided by the Paris Observatory Lunar Analysis Center (POLAC) website[3]. The predictions were previously obtained with the ELP96 (Chapront et al., 2002), an analytical lunar ephemeris, with numerical complements from DE245 (Williams et al., 1993) and re-adjusted to the LLR data till 2010. A more recent version from POLAC, ELPMPP02 uses numerical components from DE405 (Standish, 1998) adjusted to the LLR data till 2013, based on model recommendation from IERS2003 (McCarthy and Petit, 2004).

[3] ftp://polac.obspm.fr/pub/llr_repository/PaVb3/TPF_REPOSITORY/GRASSE

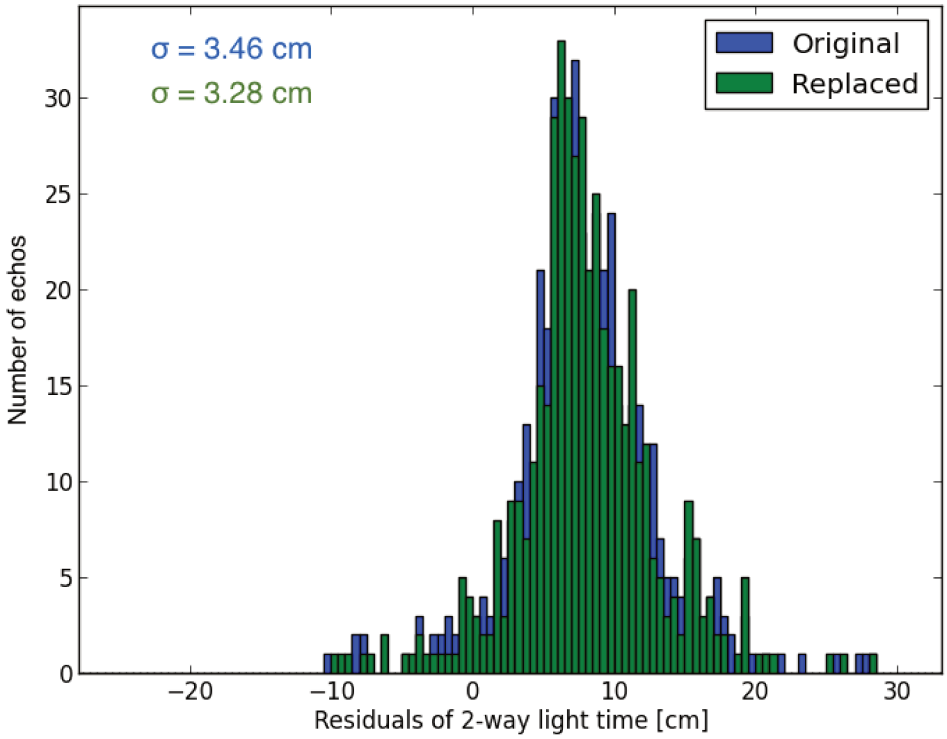

Figure 2.6: Improvement in normal point sigma by replacing LLR residuals within the Grasse station full rate data (original), with DE430 ephemeris and GINS reduction model processed residuals (replaced). An improvement of 5% on the standard deviation is noticed. The offset from zero is due to the uncorrected calibration value.

.

The spread of echoes within the histogram represents the deviations of the detected photons to the predictions from POLAC. The predictions involve both an ephemeris and a reduction model. Hence with the help of a more accurate ephemeris and updated reduction models, one can expect a tighter spread of the echoes, owing to the accuracy of the prediction.

The full rate data were used here to illustrate the impact of an improved prediction. Each echo within the full rate data has a light-time associated with it. These light-times with the corresponding datation were analyzed using the GINS software with a higher accuracy numerical ephemeris (such as DE430). The LLR post-fit residuals obtained with ELPMPP02 give about 5 cm (at 1-σ) for the observations from the APOLLO station over the period

2006-2012 (Bouquillon et al., 2013), while those from DE430 give about 2 cm (Folkner et al., 2014). The resulting residuals obtained with DE430 is converted to 2-way light time and compared with that obtained with the original predictions present within the LLR full rate data. As one can notice on Fig. (2.6), a 5% improvement of the residual dispersion (σ) is noticed on the replaced light-times due to the accuracy of the underlying ephemeris and improved reduction software, used for the prediction.

This study recommends the use of an updated numerical planetary and lunar ephemerides as the prediction model for LLR observations to obtain a tighter spread of LLR residuals during the normal point computation.

2.2.4 Alternate algorithm

Improvements to the normal point algorithm must be effective to remove unwanted signatures within the full rate data. These may include biases introduced by the detection electronics or from the asymmetry of the projection of the ranging object to the plane wave of laser light. Michelsen (2010) shows the impact of such effects on normal point algorithm for APOLLO LLR data and Kucharski et al. (2015) proposes methods to remove satellite (Ajisai) signatures in high-repetition rate (few kHz) SLR normal points for millimeter-level applications in geodesy.

For LLR, although the retro-reflectors are aligned to nominally face the earth center at zero libration (variation in the apparent orientation of the Moon), for any given observation, the reflectors are tilted with respect to the plane wave of laser light. This tilt spreads out the return pulse over the time it takes the wave front to pass from the nearest point on the retro-reflector to the farthest. This has a direct impact on the spread of the core of the Gaussian distribution present in the histogram of the residuals. In addition, the characteristics of the background noise (zero mean or non-zero mean) can cause the histogram to skew towards the mean of the noise. Hence it becomes important to completely characterize the components present in this LLR dataset, rightly called as a mixture model.

In this method of normal point calculation we used the Expectation Maximization Approach (Gupta and Chen, 2011) in order to decipher the characteristics of the skewed normal components present in the LLR return pulses with background noise, and thereafter computed the normal point for the corresponding LLR dataset.

A Python implementation[4] is used for the Mixture Model Fitting and adapted to a three-component mixture sample (returns from IR and/or Green wavelengths and background noise). The Expectation Maximization (EM) algorithm is implemented, for estimating the maximum likelihood of the model parameters (mean

[4]Available at https://github.com/tritemio

and variance). In addition we also include the skewness estimate by combining another Python implementation[5] based on the study by Azzalini and Capitanio (1999) for the generation of skewed normal distribution in the maximum likelihood step.

We assume that the mixture model consists of the linear combination of three Gaussian distributions corresponding to the residuals for Green and/or Infrared lasers, along with the background noise (with the sigma of the background noise chosen to be very large when compared to the residuals to represent a near uniform noise). The EM method allows to fit a statistical model in the case where the experimental data has unknown variables. These variables provided us the information about which component has generated each sample in our dataset.

With the EM method, we first assigned each sample to each component of the distribution. After which, we computed MLE estimators of parameters of each component of the mixture. Apart from the mean and variance estimates we also introduced a skewness parameter for our study. For each sample s_i we have three coefficients $\gamma(i,1)$, $\gamma(i,2)$ and $\gamma(i,3)$ that represent the fraction of s_i that belong to the respective components green, IR or noise.

And,

$$\gamma(i,1) + \gamma(i,2) + \gamma(i,3) = 1 \tag{2.1}$$

where γ is the responsibility function.

The probability distribution function (PDF) f corresponding to the components in the mixture model follow a Gaussian distribution given by:

$$f\left(x|p\right) = \frac{1}{\sigma\sqrt{2\pi}} e^{-\frac{(x-\mu)^2}{2\sigma^2}} \tag{2.2}$$

The PDF of the mixture becomes:

$$f\left(x|p\right) = \sum_{k=1}^{3} \pi_k f_k\left(x|p\right) \tag{2.3}$$

If we know the parameters p (from our initial guess), we can compute for each sample and each component the responsibility function defined as:

$$\gamma(i,k) = \frac{\pi_k f_k\left(s_i|p\right)}{f\left(s_i|p\right)} \tag{2.4}$$

where, π_k is the probability that the sample belongs to the distribution k described by:

$$\pi_k = \frac{N_k}{N} \tag{2.5}$$

[5] Available at http://azzalini.stat.unipd.it/SN/skew_normal-py.zip

and starting from the effective number of samples for each category (N_k) we can compute the new estimation of parameters:

$$N_k = \sum_{i=1}^{N} \gamma(i,k) \tag{2.6}$$

where, $k = 1, 2, 3$

$$N_1 + N_2 + N_3 = N \tag{2.7}$$

The new mean corresponding to the component k is computed as:

$$\mu_k^{new} = \frac{1}{N_k} \sum_{i=1}^{N} \gamma(i,k) \cdot s_i \tag{2.8}$$

Followed by the new variance corresponding to the component k is computed as:

$$\sigma_k^{2\ new} = \frac{1}{N_k} \sum_{i=1}^{N} \gamma(i,k) \cdot \left(s_i - \mu_k^{new}\right)^2 \tag{2.9}$$

And the new values of skew are computed as:

$$\xi_k^{new} = \frac{1}{N_k} \sum_{i=1}^{N} \gamma(i,k) \cdot \left(\frac{4-\pi}{2} \cdot \frac{E\{X\}^3}{var\{X\}^{\frac{3}{2}}} \right) \tag{2.10}$$

where,

$$\delta = \frac{\alpha}{\sqrt{1+\alpha^2}} \tag{2.11}$$

$$E\{X\} = \sqrt{\frac{2}{\pi}}\delta \tag{2.12}$$

$$var\{X\} = 1 - \frac{2\delta^2}{\pi} \tag{2.13}$$

where, α is the shape parameter, which regulates the shape of the density function of the skewed normal distribution.

The skewness is introduced into the Eqn. (2.2) through the shape parameter α with the help of the complementary gauss error function (erfc), as:

$$f^{new}(x|p) = \frac{e^{-\frac{(x-\mu)^2}{2\sigma^2}} erfc\left(-\frac{\alpha(x-\mu)}{\sigma\sqrt{2}}\right)}{\sigma\sqrt{2\pi}} \tag{2.14}$$

The following steps are iterated until the convergence criteria is achieved:

1. Recomputation of $\gamma(i,k)$;

2. Estimation of the updated moments.

The maximum variation of the computed moments of the distribution between the i^{th} and $(i-1)^{th}$ iteration to a specified tolerance ϵ forms the basis for the convergence.

The apriori selection for the mean of the distribution is controlled by the calibration setup allowing a good separation in time with different wavelength. The following values were set as the initial conditions for the moments during iterations:

- The mean for the green laser residuals (μ_G) can be expected within ±3 ns from the predicted value.
- The mean for the IR laser residuals (μ_{IR}) are offset from μ_G by +5 ns (set by the Grasse station technical team for ease of separation of the two detection paths).
- The expected standard deviation for Apollo 15 reflector is about 300 ps whereas for all the other reflectors it is about 200 ps.
- The noise variance is expected to be as large as the window of reception, which is about 25 ns.

The algorithm was implemented in parallel to the technical developments and tests conducted at the Grasse station in 2015, when both IR and Green distributions were collected on the same datafile with a 5 ns separation between them. At the time of writing however, LLR ranging at the Grasse station using the two wavelengths are separated into two independent observations. This reduces the number of distribution pertaining to an observation set to two components (observation and noise). The results obtained with the EM algorithm described in the following section considers this update.

2.2.5 Results

Methodology

Observations were simulated as a Gaussian distribution with initialized values of mean (about 0.5 ns) and standard deviation (about 0.3 ns) corresponding to a typical observation from the Grasse LLR station. Noise was introduced as a zero-mean Gaussian distribution with a standard deviation of 25 ns with 10 times the number of samples as the observation. Simulations were run over 100 iterations and the average recovery error (% difference between the recovered and simulated mean/standard deviation) in the estimation of the mean and standard deviation obtained from the two algorithms are considered. In each iteration the mean and

the standard deviation of the simulated observation was allowed to vary by 50% (from a uniform random distribution), so that a realistic estimation of the recovery error is obtained. To favor comparison between the results obtained with the two algorithms, the same set of seeds are used to initialize the pseudo-random number generator. These simulations were implemented in Python and are made publicly available[6].

[6]Available at: https://github.com/viswanat/NPT

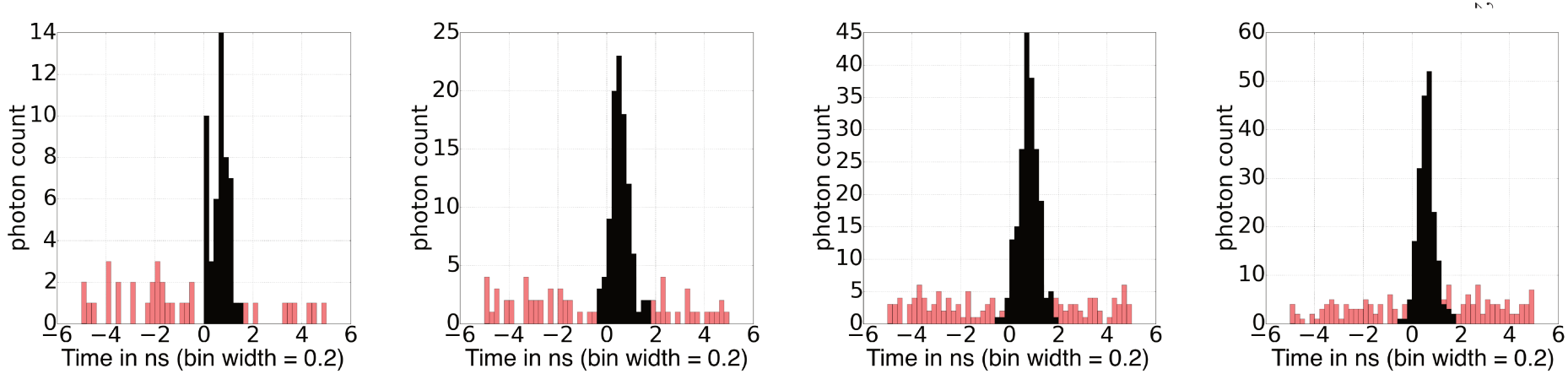

1.a & 1.b 2 3.a 3.b & 3.c

Case no.	Photons/session	Rejection filter scaling - Grasse station	Skew on simulated data	Recovery error in [%]			
				Grasse station		EM	
				μ	σ	μ	σ
1.a.	50	2.5-σ	-	2	4	5	7
b.	50	2.2-σ	-	1	1	5	7
2.	100	2.5-σ	-	2	3	3	4
3.a.	200	2.5-σ	-	2	6	1	0.5
b.	200	2.5-σ	0.2	3	7	0.1	0.5
c.	200	2.2-σ	0.2	4	12	0.1	0.5

Table 2.1: Comparison of the performance of the Grasse station correlation algorithm and the Expectation Maximization algorithm (EM) using simulated LLR observations and noise, under the cases described in the text (Section 2.2.5).

Evaluation criteria

The two algorithms: the Grasse station correlation method (Section 2.2.3) and the Expectation Maximization method (Section 2.2.4), are analyzed with the help of different simulated datasets, similar to that encountered with the real observations. A total of six cases are considered for the simulated dataset for the purpose of evaluation. They are as follows:

1. Low photon count (50 photons/session) corresponding to Grasse station operation in 532 nm wavelength
   (a) 2.5-σ rejection filer (Case 1.a in Table 2.1)
   (b) 2.2-σ rejection filter (Case 1.b in Table 2.1)
2. Medium photon count (100 photons/session) corresponding to Grasse station operation in 1064 nm wavelength
   (a) 2.5-σ rejection filer (Case 2 in Table 2.1)
3. High photon count (200 photons/session) considering future improvements to photon detection.
   (a) 2.5-σ rejection filer with zero skew (Case 3.a in Table 2.1)
   (b) 2.5-σ rejection filer with 0.2 skew (Case 3.b in Table 2.1)
   (c) 2.2-σ rejection filer with 0.2 skew (Case 3.c in Table 2.1)

Each of the above cases are grouped into the following evaluation criteria, so as to compare the performance of the two algorithms (Grasse station and EM algorithms) used for the normal point computation. They are as follows:

- Photon count and rejection filter
  A tight rejection filter at 2.2-σ to 2.5-σ eliminates the tail of the Gaussian distribution. If a symmetric distribution is expected from the return pulses, the scaling factor in the rejection filter would play no role on the mean value of the distribution, but a significant role on the estimation of the standard deviation.

  For low photon count LLR ranging (below 100 detected photons - cases 1.a and 1.b in Table 2.1), it is recommended to set a tight rejection filter in order that outliers are not taken into account for the computation of the normal point, which otherwise would lead to a bias on the average residual and the standard deviation. Hence, with a tight rejection and low photon count, the Grasse station algorithm performs better in recovering both the

mean and the standard deviation of the simulated distribution compared to the alternate algorithm, by 5 % and 7 % respectively. This is due to the combined effect of the limited number of photon counts and a tight rejection filter, as employed at the Grasse station algorithm. The limited number of photons degrade the quality of the EM fit.

On the other hand, when the photon counts are greater (200 detected photons and above), the alternative algorithm performs better as it is able to characterize the distribution well above the noise floor. The improvement in % error is 2 times on the mean and an order magnitude on the standard deviation as given by the case 3.a within Table (2.1). With the introduction of skew and tighter rejection, the current algorithm used at the Grasse station becomes significantly degraded as indicated by the case 3.c. Currently, at the Grasse LLR station, on an average, about 50 photons/session are obtained with 532 nm laser and about 100 photons/session using 1064 nm laser corresponding to cases 1 and 2 (respectively) within Table (2.1).

- Background noise
  The background noise is simulated as a near uniform distribution (simulated with a Gaussian distribution with a large standard deviation of 25ns as compared with the observations) with 10 times more samples than the detected photons. The performance of the algorithm at the Grasse station under background noise is at the expense of strong sample rejection filter, while all samples are retained with the alternate EM algorithm. Moreover, since the rejection filter within the Grasse station is subject to user adjustments, the EM algorithm allows a more autonomous approach with both high or low background noise. When comparing a fixed scaled (2.2-σ) rejection filter of the algorithm used at the Grasse station and a 2 Gaussian EM algorithm, the latter recovers the mean and the standard deviation marginally better ($\leq 2\%$) under strong background noise. The improvement becomes more significant with the EM algorithm when a 3-σ filter is assigned to the Grasse station method.

- Binning effect
  The effect of binning arises typically in a sparse distribution (for example, but not limited to case 1 in Fig. 2.1), giving rise to gaps and multiple peaks within the histogram of the distribution. About 5-10 % of data obtained from the Grasse station is susceptible to these effects. In the presence of such artifacts, the correlation algorithm fails to distinguish (2-6 % error) between two identical peaks. The EM algorithm does not require binning and hence is not susceptible to this effect.

  Gaps within the histogram raises a problem for correlation method, as it

suggests a weak correlation due to missing data. However, on adjustment of the bin width, one may notice a strong correlation. This directly affects the peak detection using maximum point of correlation under a fixed bin width, and the rejection scheme employed around the peak thereafter. The EM normal point algorithm is not affected by small data gaps (at few hundreds of ps) which arise as a result of bin width.

- Initial conditions
  The EM algorithm requires the initialization of the moments of the Gaussian distributions. The selection of these initial conditions do not affect the outcome of the algorithm due to the inherent iterative approach. The algorithm used by the Grasse station on the other hand relies vastly on the correlation peak (initialized for the application of the rejection filter) which is susceptible to the above mentioned binning effects.

- Symmetry
  The current algorithm used at the Grasse station assumes a strong symmetry both in the correlation method and the application of the rejection filter. The EM algorithm allows the estimation of higher order moments such as skew and kurtosis to be included as parameters within the normal point computation. With increased photon count, the asymmetry of the distribution becomes significant to an extent that the simple average does not coincide with the Gaussian core i.e. for a positive skew, the mean becomes greater than the Gaussian core as one can see in cases 3.b and 3.c within Table (2.1). When the symmetric correlation method used at the Grasse station is applied on these cases, the error on the moments become significant (up to 12% in case 3.c of Table (2.1)). The skewness is neglected for the low photon count case, as its estimation is found to be uncertain at the chosen low sampling rate.

2.2.6 Inference

The two algorithms are weighted statistically by their performance under different scenarios (Section 2.2.5). The Grasse station algorithm performs well with observations constituting a low photon count under the application of a strong rejection filter though it assumes a strong symmetry through the correlator method and relies heavily on the selection of the scale of the rejection filter. The optimal rejection filter is currently set to 2.2-σ but this value has varied in the past and have affected the uncertainties reported in the distributed normal points.

As a first step towards the standardization of normal point computation it is required that the normal point be recoverable from the full rate data by another

user. Hence, through the EM algorithm, the user variables within the currently employed normal point algorithm at the Grasse station are minimized. The alternative algorithm is independent from:

- Selection of rejection filter scaling
- User inputs to overcome binning effects
- Symmetry assumptions

The EM algorithm here assumes that the expected distribution follows a Gaussian distribution, with skewness as an optional variable. Though other distributions were not explored for a better fit, under such an event, the EM algorithm can be easily adapted to follow the required distribution. The choice of a functional distribution can be chosen based on the expected response function of the underlying instruments.

Fig. (2.7) shows the cumulative distribution of the photon count obtained at the Grasse station in 532 nm (2014-2017) and 1064 nm (2015-2017) wavelengths. With a photon count of below 100 photons/session, the Grasse algorithm is preferred, while with the remaining higher photon count (constituting about 6% of Green and 18% of IR LLR data from Grasse) the EM algorithm is optimal.

With increased number of detected photons, some of the issues associated with the Grasse station algorithm (Section 2.2.3) can be avoided with the help of the EM algorithm. With the constant technological advancements and tests conducted by the technical team at the Grasse LLR station one can expect a greater photon count in the near future. Fig. (2.7) also shows the recent (August 2017) high photon count sessions obtained from the IR detection at Grasse station. In addition, an effort is in place to study the prospects of LLR pulse train accumulation for increased photon count. Moreover, as the number of detections increases, the asymmetry of the distribution of detected photons become evident and appropriate compensation within the normal point algorithm will be required for millimeter level LLR accuracy.

2.3 Comparisons between IR and Green LLR data sample

Non-uniform distributions in the dataset are one contributor to correlations between solution parameters (Williams et al., 2009). Like one can see on Fig. (2.8), Fig. (2.9) and Fig. (2.13), about 70% of the data are obtained after reflection on Apollo XV reflector and on average 40% of the data are acquired at 30° apart from the quarter moons.

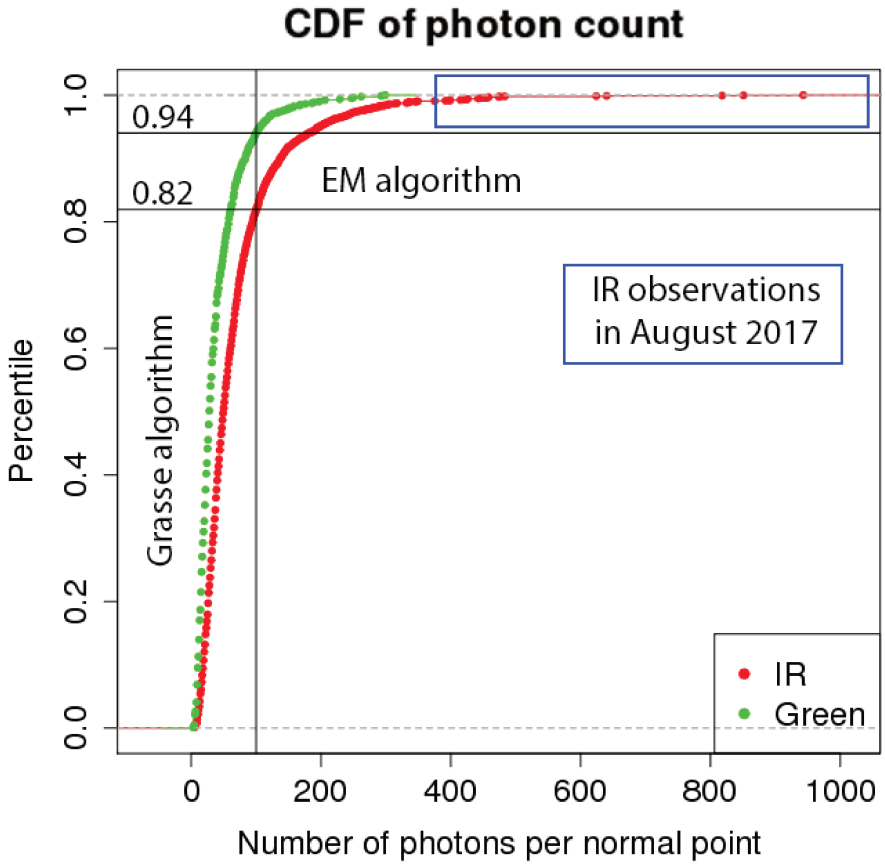

Figure 2.7: Cumulative distribution function of photon count/session obtained with the 532 nm (Green) wavelength (2014-2017) and the 1064 nm (IR) wavelength (2015-2017) at the Grasse LLR station.

In this work, we show how the IR LLR observations acquired at the Grasse station during 2015-2017 (corresponding to 7% of the total LLR observations obtained between 1969-2017 from all known ILRS ground stations) can help for the reduction of such heterogeneity.

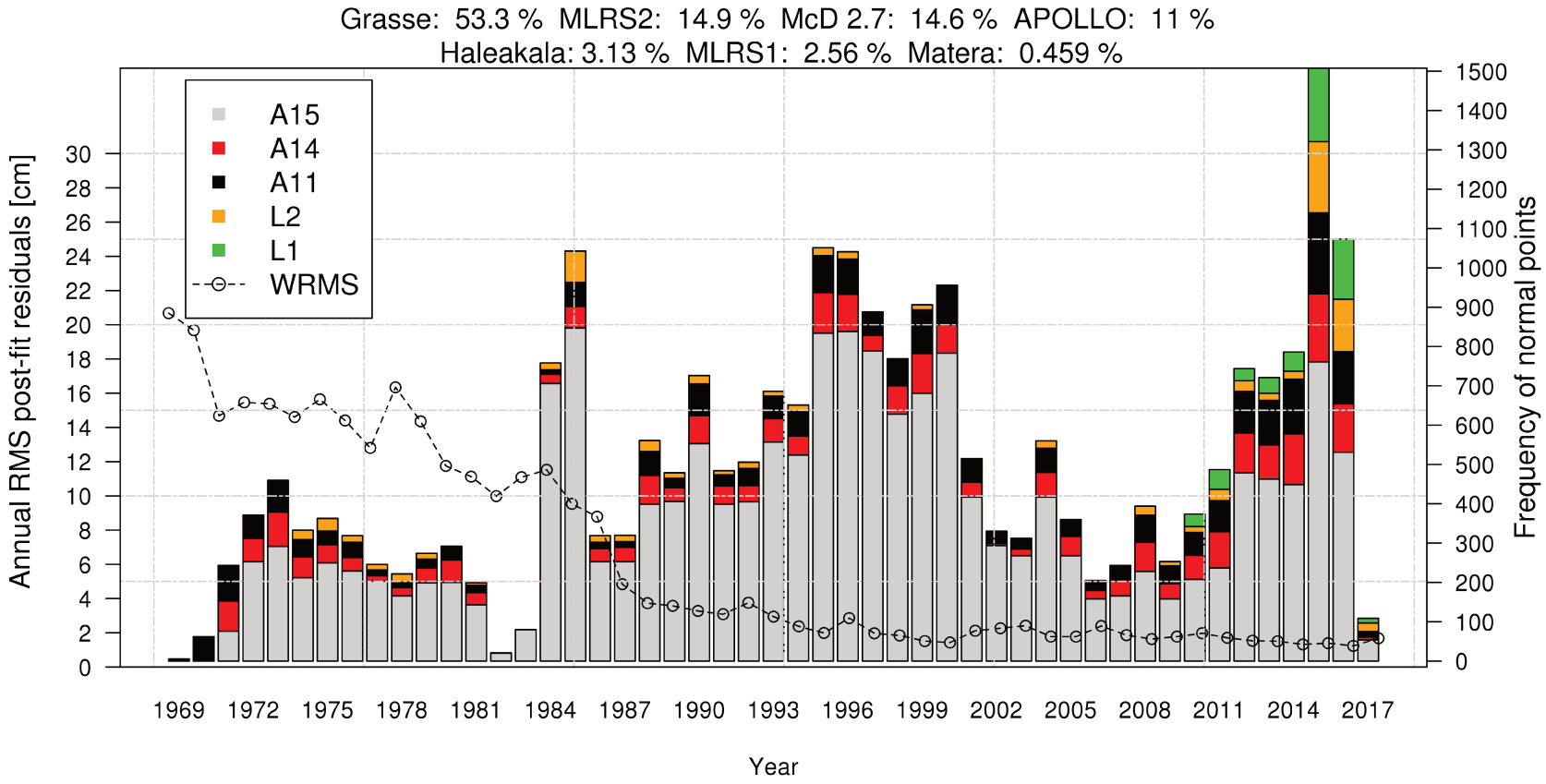

Figure 2.8: Histogram of annual frequency of LLR data from LLR stations (with the percentage contributions indicated above) with relative contribution from each LRR array including Grasse IR (1064 nm) observations. Points indicate the annual mean of post-fit residuals (in cm) obtained with INPOP17a. The dominance of range observations to Apollo reflectors is evident. A change can be noticed after 2014 due to the contribution from IR at Grasse.

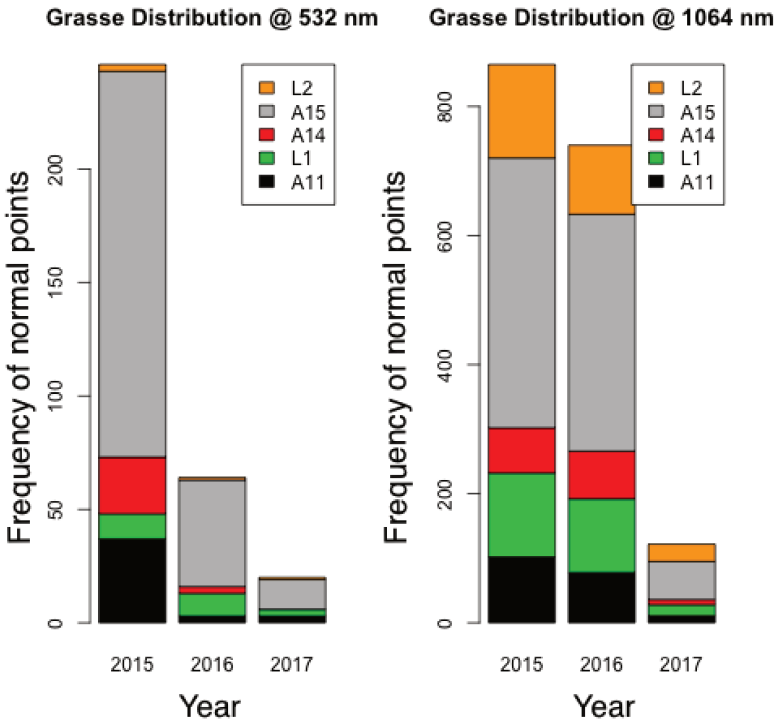

Figure 2.9: Grasse reflector wise distribution at 532 nm and 1064 nm from 2015 to 2017.

2.3.1 Temporal distribution

As demonstrated by Nordtvedt (1998), the full and new moon periods are the most favorable for testing gravity as the gravitational and tidal effects are maximum.

In Fig. (2.12, 2.13 and 2.14) are plotted the distributions of normal points relative to the synodic angle for Grasse station obtained at 1064 nm and 532 nm and APOLLO station, respectively. When for the APOLLO data sets the distribution of normal point around quarter moons (15° before and after 90° and 270°) correspond to about 25% of the full data sample, almost 45% of the Grasse station 532 nm data sample is obtained away from the full and new moon periods. This can be explained by two factors:

a. New Moon phase: As the pointing of the telescope onto the reflectors is calibrated with respect to a nearby topographical feature on the surface of the Moon, the pointing itself becomes a challenge when the reference points lie in the unlit areas of the Moon. Also, as the New Moon phase occurs in the daylight sky, the noise floor increases and the detector electronics become vulnerable due

to ranging at a very close angle to the Sun (Williams et al., 2009; Courde et al., 2017).

b. Full Moon phase: During this phase, thermal distortions remain as the primary challenge, arising due to the over-head Sun heating of the retro-reflector arrays. This induces refractive index gradients within each corner cube causing a spread in the return beam, which makes detection more difficult (see Goodrow and Murphy (2012)). The proportion of this effect is partially linked to the thermal stability of the arrays. Since the A11, A14 and A15 arrays have a better thermal stability compared to the L1 and L2 arrays (Murphy et al., 2014), observations to the latter become sparse during the full Moon phase.

Despite these challenges, LLR observations during the above mentioned phases of the Moon have been acquired with the IR detection. For the first two years of 1064 nm detection path at the Grasse station, about 32% of observations were indeed obtained at 30° apart from the moon quarters, increasing by 10% the portion of data sample close from the most favorable periods for tides and EP studies.

This is primarily achieved due to the improved signal to noise ratio resulting from an improved transmission efficiency of the atmosphere at the IR wavelength of 1064 nm. In addition, high precision data have also been acquired on the two Lunakhod reflector arrays during full moon phase.

2.3.2 Spatial distribution

Statistics drawn from the historical LLR dataset (1969-2015) show an observer bias to range to the larger Apollo reflector arrays (mainly A15). This trend (see Fig. 2.8) is also present on statistics taken during time periods after the re-discovery of Lunakhod 1 by Murphy et al. (2011).

This is due to the higher return rate and thermal stability over a lunar day on the Apollo reflectors, thereby contributing to the higher likelihood of success.

With the installation of the 1064 nm detection path (see Fig. 2.9), as explained in Courde et al. (2017), the detection of photon reflected on all reflectors is facilitated, especially for Lunakhod 2 (L2): about 17% of IR data are obtained with L2 when only 2% were detected at 532 nm.

Owing to the spatial distribution of the reflectors on the Moon (see Fig. 2.10), A11 and A14 give sensitivity to longitude librations, A15 gives sensitivity to latitude librations and the Lunokhod reflectors (L1 and L2) give sensitivity both in the latitude and longitude libration of the Moon. The heterogeneity in the reflector-wise distribution of LLR data affects then the sensitivity of the lunar modeling adjustment (Viswanathan et al., 2016) (discussed in Section 5.3.2).

By acquiring a better reflector-wise sample, IR contributes to improve the adjustment of the Moon dynamical and rotational modeling.

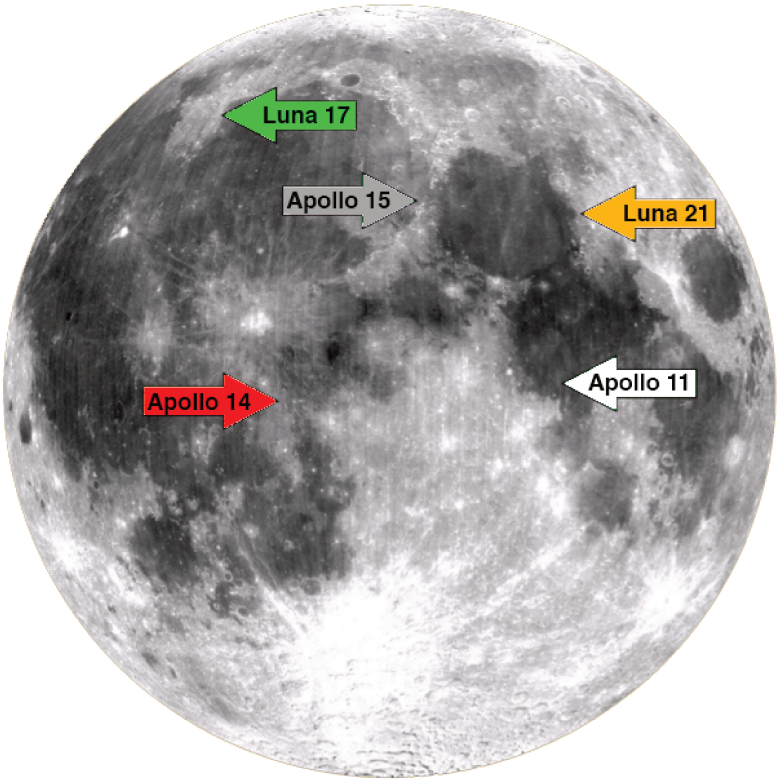

Figure 2.10: Spatial distribution of retro-reflectors on the lunar surface.

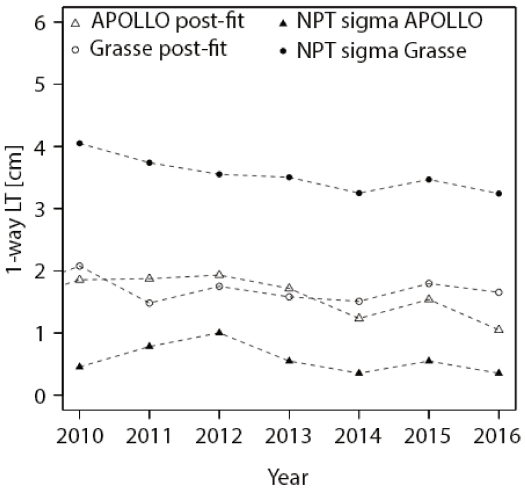

Figure 2.11: APOLLO and Grasse LLR observations in terms of i) observational accuracy as given by the annual mean of normal point uncertainty (converted from ps to 1-way light time (LT) in cm) and ii) annual weighted root mean square of post-fit residuals (1-way LT in cm) obtained with INPOP17a.

2.4 LLR accuracy

APOLLO observations are obtained with a 3.5 m telescope (under time sharing) at the Apache Point Observatory, while Grasse observations are obtained with a 1.5 m (MeO) telescope dedicated for LLR. A larger aperture is beneficial for statistically reducing the uncertainty of the observation by accumulating more photons (Murphy et al., 2008), which translates to millimeter level accuracies as shown in Fig. (2.11) for APOLLO. For the Grasse station, LLR ranging in IR (1064 nm) procures three times more photons and lesser noise compared to Green (532 nm). This allows a better one-way range uncertainty at 1064 nm than at 532 nm (Courde et al., 2017). The impact of IR LLR data on the current dynamical model of INPOP17a is discussed in Section (5.3.2).

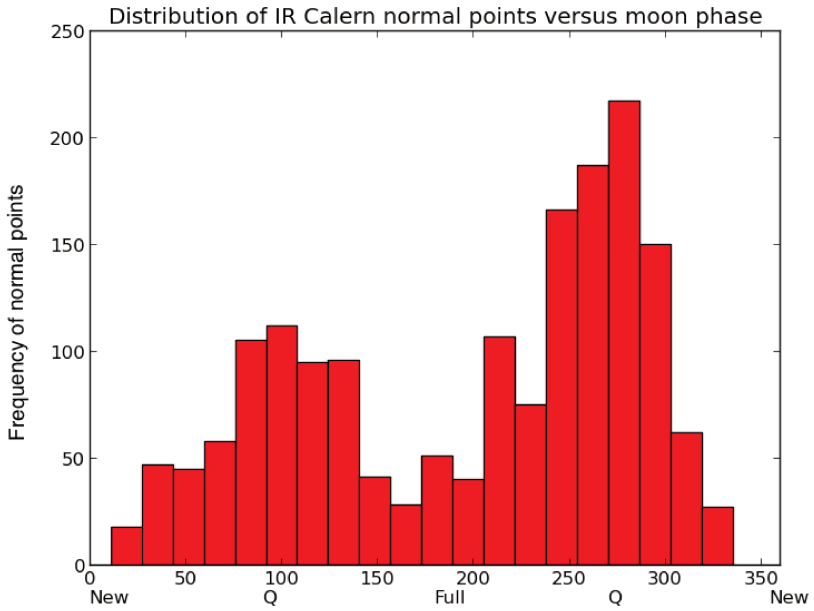

Figure 2.12: Distribution of IR wavelength LLR observations over 2 years from Grasse vs lunar phase.

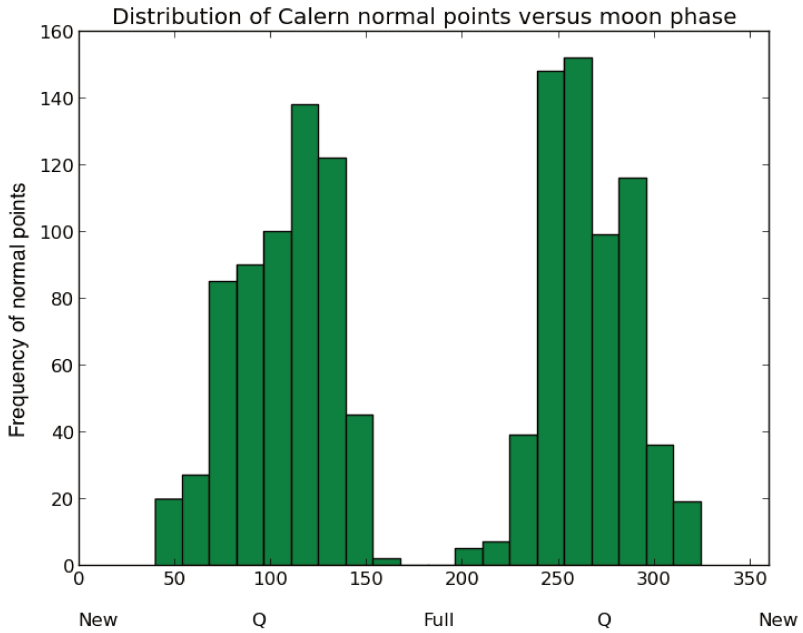

Figure 2.13: Distribution of Green wavelength LLR observations over 2 years from Grasse vs lunar phase.

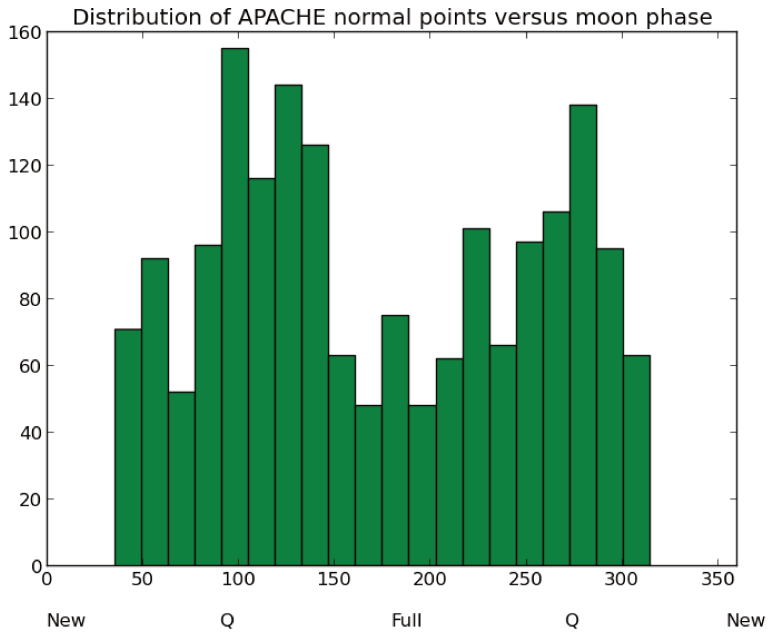

Figure 2.14: Distribution of Green wavelength LLR observations over 2 years from APOLLO vs lunar phase.

Chapter summary

The existing algorithm used for the normal point computation at the Grasse LLR station is implemented independently and analyzed. The key points of the analysis are: reproducibility issues due to experience-based user inputs at the point of failure (binning effects) of the correlation algorithm, adjustments on the rejection filter scale, pattern search independent of calibration profile, choice of mediocre prediction ephemeris. The use of high accuracy numerical ephemeris such as DE430/INPOP17a/EPM2016 is recommended for prediction over less accurate semi-analytical solutions. An alternate algorithm is provided to overcome most of these limitations and recommended for use when a high photon detection is available. A shift in photon count regime is observed for most recent IR LLR observations from Grasse. A statistical analysis on the normal point data distribution shows a considerable improvement in terms of temporal and spatial homogeneity. A statistical reduction of the normal point uncertainty is observed for Grasse IR LLR observations due to the high photon detection. The following chapter (Chapter 3) focuses on the removal of geophysical and relativistic effects from the LLR observation for the purpose of light-time computation.

Chapter 3

Data reduction

During Lunar Laser Ranging (LLR), the observed time of flight (or the equivalent distance traveled by light) includes inherent signatures resulting from the orbital dynamics, geophysical and relativistic phenomena present in the Earth-Moon system, in addition to the absolute Earth-Moon distance measurement. The well-known effects on the Earth-Moon system are modeled within a data analysis program (called the reduction model) and a simulated station-reflector distance is computed. The difference of the observed and the computed light-time includes all the unmodeled and unknown dynamics (and/or measurement error) present within the observation, the magnitude of which relates inversely to the accuracy of the model (currently less than 2 cm wrms in one-way light-time (Viswanathan et al., 2017)). Here after this difference is referred to as the LLR residual.

The reduction model for the LLR data analysis is implemented within a precise orbit determination and geodetic software - Géodésie par Intégrations Numériques Simultanées (GINS) (Marty et al., 2011; Viswanathan et al., 2015) maintained by space geodesy teams at GRGS/OCA[1]/CNES and written in Fortran90. The GINS software was chosen as it allows to compare various types of observation techniques used for geodesy at the OCA station i.e. SLR, LLR, GPS, etc. The subroutines for the LLR data reduction within GINS are vetted through a step-wise comparison study conducted among the LLR analysis teams in OCA-Sophia Antipolis (this study), IMCCE-Paris and IfE-Hannover, by using simulated LLR data and DE421 (Folkner et al., 2009) as the planetary and lunar ephemeris. The modeling follows the recommendations of IERS 2010 (Petit and Luzum, 2010). To avoid any systematics in the reduction model, the upper-limit on the discrepancy between the teams was set to a 1 mm threshold in one-way light time.

The following sections describe the procedure behind the iterative computation of the light-time (Section 3.1), the reference frame transformations required during

[1]Available at : https://www.geoazur.fr/svn/web/gins

this computation (Section 3.2), the displacements that occur at the two reference points - Earth station and LLR retro-reflector (Section 3.3) and the necessary correction to the light-time (Section 3.4) .

3.1 Light-time computation

The major statistical quality of a model requires that the difference between the model prediction and the observed quantity be minimum. In LLR analysis, the light-time solution of the observed quantity (i.e. two-way observed light time) provides the computed or the model prediction (i.e two-way computed light time).

The light-time computation involves iteratively determining the time of reflection of the laser pulse from the lunar retro-reflectors, with the help of the time of emission (T_e) and the round-trip time, both contained within the observation. This procedure is split into two legs (or paths) identified by the direction of travel of light. The up-leg consists of the path traveled by light from the station on the Earth to the reflector on the Moon, while the down-leg follows the reflected path in the opposite direction. A schematic is provided in Fig. (3.1).

The station code present within the LLR data files identifies the Earth-based ground station from which the laser was fired, providing the link to the International Terrestrial Reference Frame (ITRF) coordinates of the Earth station. The time-stamp of emission (in UTC) allows the interpolation of the station position from the reference epoch of the ITRF model used. This interpolation is linear and it accounts for the correction of tectonic plate motion at the Earth station. At this stage, additional corrections on the station position follow from the effect of tides and spin, described further in Section (3.3).

The station positions are then transformed from the International Terrestrial Reference System (ITRS) to the Barycentric Celestial Reference System (BCRS) and its realization, the International Celestial Reference Frame (ICRF). This is carried out by a series of both time and coordinate transformations described in Section (3.2), by the use of Earth Orientation Parameters (EOPs). The EOPs take into account the irregularities of the Earth's rotation as a function of time.

The lunar reflector code to which the ranging was performed is provided through the observation. Fits of LLR data to lunar ephemerides allows the determination of the reflector coordinates in the seleno-centric reference frame. The Moon's mantle unlike Earth's, is cooler and does not convect to cause an active tectonic plate motion. Hence, the reflector coordinates are fixed with respect to the seleno-centric reference frame. The seleno-centric reference frame is transformed to the inertial (ICRF) reference frame using the Euler angles, estimated with the help of lunar ephemerides, and in considering the motion of the Moon relative to the Earth and the position of the Earth relative to the solar-system barycenter (SSB).

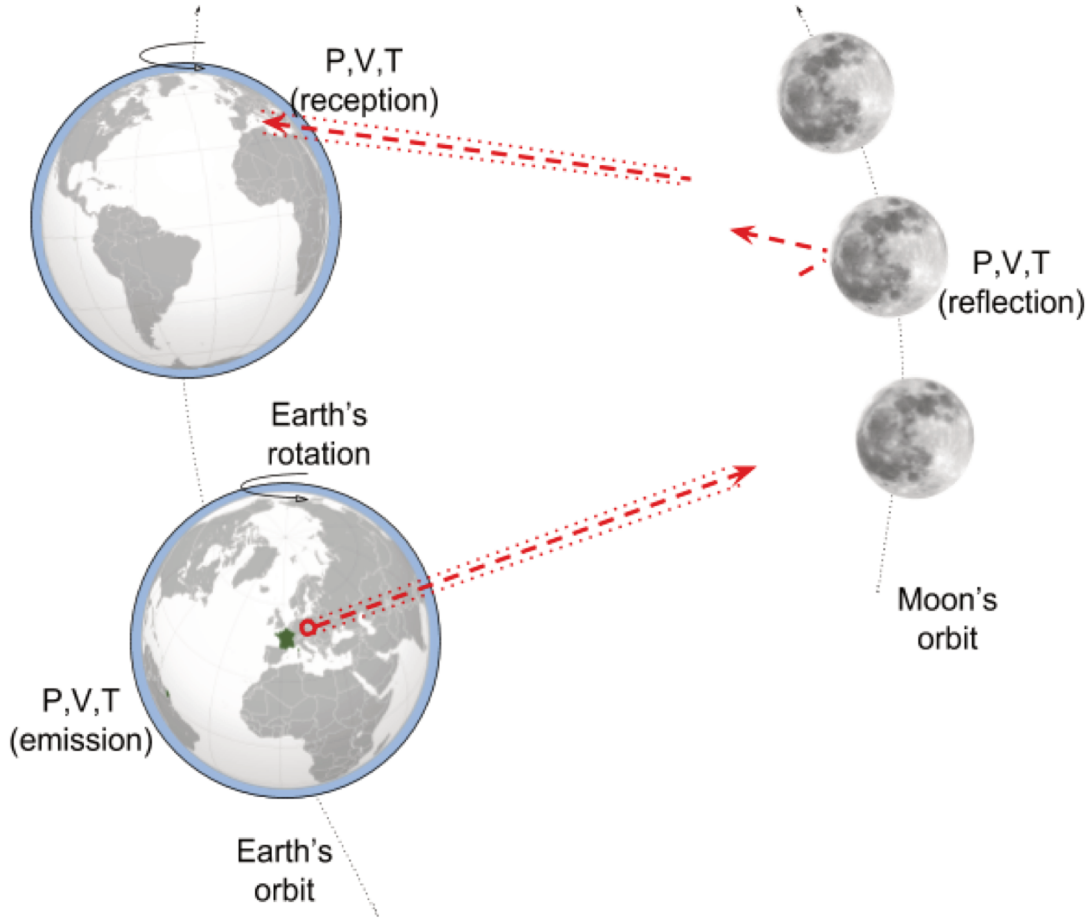

Figure 3.1: Schematic of the movement of the Earth-Moon system. The light-time computation involves the state vectors (position (P) and velocity (V)) of the Earth and the Moon at a given time (T), in the ICRF reference frame, at: emission of the laser pulse from the station on the Earth, reflection of the laser pulse off the lunar retro-reflectors, and reception of the reflected pulse at the Earth station.

3.2 Reference frame transformation

The light-time solution for LLR analysis and the INPOP planetary and lunar ephemeris, uses the Solar-System barycentric space-time frame of reference (the ICRF), a realization of the Barycentric Celestial Reference System (BCRS). The BCRS is a system of barycentric space-time coordinates for the solar system within the framework of General Relativity (GR) with metric tensor specified by the IAU 2000 Resolution B1.3. The BCRS is assumed to be oriented according to the ICRS axes (Petit and Luzum, 2010). The coordinate time scale used for INPOP ephemeris is Barycentric Dynamical Time (TDB), defined in terms of the Barycentric Coordinate Time (TCB) as per the IAU Resolution B2 (1991) and B1.3 (2000). State vectors of the Sun, the Earth, the Moon and other planets defined in the BCRS can be extracted from the numerically integrated planetary and lunar ephemeris (e.g., INPOP or DE) using an ephemeris access library - CALCEPH (Gastineau et al., 2015).

For the LLR analysis, two coordinate transformations are involved. The transformation of geocentric station coordinates (ITRF) to the Solar-System barycentric coordinates (ICRF), and, the transformation of the lunar reflector coordinates from the seleno-centric coordinates (LCRF) to the ICRF.

1. ITRF to ICRF transformation
   A vector in the ITRF (station coordinates) is first converted to a geocentric celestial reference frame (GCRF). GCRF has its origin at the geocenter with its axes aligned with the ICRF.

   A detailed description of the transformation between ITRS and GCRS is given in Petit and Luzum (2010, p. 69) and Manche (2011, p. 103). For this study, the CIO-based transformation (Petit and Luzum, 2010, p. 71) was implemented using SOFA subroutines (an example can be found in IAU SOFA Board, p. 25). The transformation requires input parameters such as, the terrestrial time (TT), $UT1$, Celestial Intermediate Pole offsets ($\Delta X, \Delta Y$) and the coordinates of the pole (x_p, y_p).

   These input parameters are obtained with the help of Earth Orientation Parameters (EOP), available publicly through the Earth Orientation Center website[2] in accordance with the IAU2006/2000A precession-nutation model. Alternatively, the Kalman Earth Orientation Filter (KEOF) EOPs can be used (Ratcliff and Gross, 2015). For LLR analysis, the latter is preferred as it includes the LLR observations during the determination of the variation in latitude (VOL) and UT0 (Pavlov et al., 2016). The EOPs correspond to 0

[2] http://hpiers.obspm.fr/iers/eop/eopc04/eopc04_IAU2000.62-now

h UTC of each date. A 4-point Lagrangian interpolation was used to obtain the corresponding input parameters at the observation times.

The effect of tidal variations in the Earth's rotation can either be corrected directly from the EOP website[2] or through the IERS recommended subroutines[3]. Other corrections to EOPs involve diurnal luni-solar effect on polar motion, sub-diurnal librations in UT1 and corrections to CIP coordinates to account for Free Core Nutation (FCN), subroutines for which are publicly available[4]. These models were implemented within the software using the IERS subroutines.

The time coordinate of GCRS is TCG (Geocentric Coordinate Time), which differs from TT at a constant rate (Petit and Luzum, 2010, Eqn. 10.1). This transformation was implemented using the SOFA subroutine ($TTTCG.F$).

The difference between the Terrestrial Time (TT) to the Barycentric Dynamical Time (TDB) is obtained through numerical integration within the ephemeris (Fienga et al., 2011) or through an approximation via the SOFA subroutine ($DTDB.F$) - with differences between the two choices having a maximum effect of 0.01 mm on the Earth-Moon distance. The former is chosen for the implementation within the reduction model. For the purpose of measurement reduction, the difference between International Atomic Time (TAI) and TDB is needed at the point the measurement is made, where $TT = TAI + 32.184s$. The differential equation integrated with the ephemeris concerning the difference $TT - TDB$ can be found in Manche (2011, Eqn. 9.24) for INPOP and Folkner et al. (2014, Eqn. 5). The coordinate time scale used for INPOP ephemeris, describing the equations of motion of solar-system bodies, is TDB. The amplitude of the effect due to the difference $TT - TDB$ on the Earth-Moon distance reaches up to 45 cm between 1969 to 2017.

The transformation from GCRF to BCRF also includes a relativistic transformation in order to consider the effect of gravitational potential in the vicinity due to a change in the coordinate origin. The transformation of a geocentric position vector $\vec{r}_{GCRF}$ to $\vec{r}_{BCRF}$, expressed in the BCRF, is given by the following equation with an uncertainty of about 0.01 mm (Moyer, 2003, p. 4-9):

$$\vec{r}_{BCRF} = \vec{r}_{GCRF}\left(1 - \frac{U}{c^2}\right) - \frac{1}{2}\left(\frac{\vec{V}\cdot\vec{r}_{GCRF}}{c^2}\right)\vec{V} \tag{3.1}$$

[3] http://iers-conventions.obspm.fr/chapter8.php
[4] http://iers-conventions.obspm.fr/chapter5.php

where U is the gravitational potential at the geocenter (excluding the Earth's mass), $\vec{V}$ is the barycentric velocity of the Earth and c is the speed of light.

The first term of Eqn. (3.1) reduces the geocentric radius of the station by about 16 cm, while the second term reduces the component of the station position vector along the Earth's velocity vector by up to 3 cm (Moyer, 2003, p. 4-9).

The transformation of $\vec{r}_{TT}$ (TT-compatible position vector) to $\vec{r}_{TDB}$ (TDB-compatible position vector) is then given, with an uncertainty of about 0.01 mm (Moyer, 2003, p. 4-9), by :

$$\vec{r}_{TDB} = \vec{r}_{TT}\left(1 - \frac{U}{c^2} - L_C\right) - \frac{1}{2}\left(\frac{\vec{V}\cdot\vec{r}_{TT}}{c^2}\right)\vec{V} \tag{3.2}$$

where $L_C = 1.48082686741 \times 10^{-8}$ and c is the speed of light.

The amplitude of the effect due to the relativistic transformation from GCRF to BCRF on the Earth-Moon distance reaches up to 19 cm between 1969 to 2017.

Using the above mentioned reference frame transformations, one can obtain the station position in the BCRF for the light-time solution.

2. LCRF to BCRF transformation
The lunar reflector coordinates are given in the seleno-centric frame of reference (refer to Section (4.3) for lunar frame definitions). The Euler angles (ϕ_m, θ_m and ψ_m) are integrated numerically (along with the positions of the bodies) within the ephemeris, defined here as the precession, nutation and rotation angle, respectively (see Fig. 3.2).

These Euler angles are used to orient the principal axes (PA) of the lunar (crust+mantle) coordinate system to the BCRS. A vector in the LCRS (or PA) frame of reference can be transformed to the BCRS using Euler's rotation theorem as:

$$\vec{r}_{BCRF} = \mathcal{R}_z(-\phi_m)\mathcal{R}_x(-\theta_m)\mathcal{R}_z(-\psi_m)\vec{r}_{PA} \tag{3.3}$$

where,

$$\mathcal{R}_x(\alpha) = \begin{bmatrix} 1 & 0 & 0 \\ 0 & \cos\alpha & \sin\alpha \\ 0 & -\sin\alpha & \cos\alpha \end{bmatrix}$$

$$\mathcal{R}_z(\alpha) = \begin{bmatrix} \cos\alpha & \sin\alpha & 0 \\ -\sin\alpha & \cos\alpha & 0 \\ 0 & 0 & 1 \end{bmatrix}$$

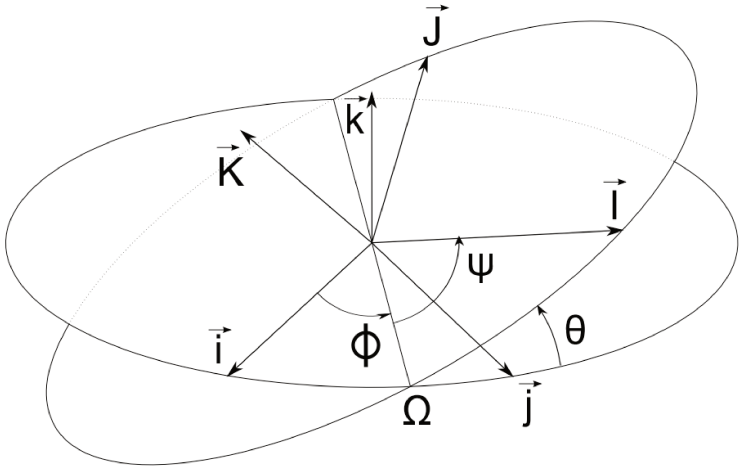

Figure 3.2: θ is the angle of nutation between $\vec{K}$ and $\vec{k}$, ϕ is the angle of precession between $\vec{i}$ and $\vec{O\Omega}$, ψ is the rotation angle between $\vec{O\Omega}$ and $\vec{I}$. Ω is the ascending node. Courtesy: Manche (2011, Fig. 3.1)

Similar to Eqn. (3.1), the transformation LCRF to BCRF also includes a relativistic transformation. The transformation of a seleno-centric position vector $\vec{r}_{LCRF}$ to $\vec{r}_{BCRF}$, expressed in the BCRF, is given by the following equation with an uncertainty of about 0.01 mm :

$$\vec{r}_{BCRF} = \vec{r}_{LCRF}\left(1 - \frac{U}{c^2}\right) - \frac{1}{2}\left(\frac{\vec{V}\cdot\vec{r}_{LCRF}}{c^2}\right)\vec{V} \tag{3.4}$$

where U is the gravitational potential at the lunar center of mass and $\vec{V}$ is the barycentric velocity of the Moon.

The transformation of $\vec{r}_{LCRF}$ to $\vec{r}_{TDB}$ (TDB-compatible position vector) is then given by (similar to Eqn. 3.2) :

$$\vec{r}_{TDB} = \vec{r}_{TT}\left(1 - \frac{U}{c^2} - L_B\right) - \frac{1}{2}\left(\frac{\vec{V}\cdot\vec{r}_{TT}}{c^2}\right)\vec{V} \tag{3.5}$$

where $L_B = 1.48082686741 \times 10^{-8}$ and c is the speed of light.

The amplitude of the effect due to the relativistic transformation from LCRF to BCRF on the Earth-Moon distance reaches up to 2.5 cm between 1969 to 2017.

This transformation (LCRF to BCRF) plays a crucial role in providing constraints to lunar ephemerides using LLR observations. This also means that any unmodeled effect present within the lunar dynamical model in terms of lunar libration will be carried over to the data reduction through this step. Pavlov et al.

(2016) add supplementary periodic correction terms (Λ) to the rotation angle ψ_m to compensate unmodeled effects in the longitude libration of the Moon. We avoid this empirical correction in our model and instead discuss investigation attempts to improve the lunar dynamical model in (Section 6.1.2).

3.3 Displacement of reference points

For LLR observations, the two points of reference are: the station position linked with the geocentric frame of reference (ITRF) at a given epoch, and the lunar retro-reflector coordinates linked with the seleno-centric (LCRF) frame of reference. These two points of reference undergo displacement due to the effect of tides (Solid, Ocean and Atmosphere) and loading effects arising from the mass redistribution due to tides, polar motion, seasonal effects, etc. The following subsections describe the implemented effects within the LLR reduction model.

3.3.1 Solid tides

Solid tides comprise of the crustal movement due to the gravitational forces produced by external bodies, thereby causing a displacement of the position coordinates (Earth station or Lunar reflectors). The solid tides produce both vertical and horizontal displacements in the reference coordinates that can be expressed by the spherical harmonic expansion and characterized by the Love (h) and Shida numbers (l) (Wahr, 1981). The radial component is proportional to the Love number while the components orthogonal to the radial is proportional to the Shida number.

For the Earth-station displacements caused by the lunar and solar gravitational attraction, the IERS Fortran subroutine (DEHANTTIDEINEL.F) is used, complete up to degree-3. The modeling follows the description given in Petit and Luzum (2010, p. 99). The amplitude of the effect due to solid tides on the Earth, results in the variation of the Earth-Moon distance up to 35 cm between 1969 to 2017.

Similarly, for the Lunar-reflector displacements caused by the gravitational attraction of the Earth and the Sun, an adaption of the IERS Solid Earth tides model is used following Petit and Luzum (2010, Eqn. 7.5). The displacement vector of the reflector due to degree-2 tides is given by:

$$\Delta\vec{r} = \sum_{j=2}^{3} \frac{GM_j {R_m}^4}{GM_{Moon} {R_j}^3} \left\{ h_2 \hat{r} \left(\frac{3(\hat{R_j} \cdot \hat{r})^2 - 1}{2} \right) + 3l_2 (\hat{R_j} \cdot \hat{r}) \left[\hat{R_j} - (\hat{R_j} \cdot \hat{r}) \hat{r} \right] \right\} \tag{3.6}$$

where,

GM_j = gravitational parameter for the Earth (j=2) or the Sun (j=3),
GM_{Moon} = gravitational parameter for the Moon,
$\hat{R}_j, R_j$ = seleno-centric unit vector to the Earth/Sun with its magnitude,
R_m = Mean radius of the Moon,
$\hat{r}, r$ = seleno-centric unit vector to the Lunar reflector with its magnitude,
h_2 = Lunar degree-2 Love number,
l_2 = Lunar degree-2 Shida number,

Higher degree displacement due to solid tides weaken by 2 orders of magnitude per degree. The impact of degree-3 displacement love numbers on the Earth-Moon distance for values of h_3=0.0233 and l_3=0.003 (Weber et al., 2011; Williams et al., 2014b) is about 1.4 mm and 0.2 mm, respectively (computed using Petit and Luzum (2010, Eqn. 7.6)). The amplitude of the effect due to solid tides on the Moon (degree-2), result in the variation of the Earth-Moon distance up to 55 cm between 1969 to 2017.

3.3.2 Ocean tide loading

The ocean tides are produced by the gravitational pull of the Moon and Sun. Ocean tides cause a time-variation of the ocean mass distribution. This results in a time-varying load on the the ocean floor. Since the Earth is not completely rigid, it deforms under this load (Farrell, 1972). This time-varying deformation of the Earth is known as ocean tide loading (Schwiderski, 1980). Since the orbits of both the Sun and the Moon have more than one periodicity due to their orbital motion and interaction, the ocean tides can be described as a sum of several ocean tides with each having their own period (Hartmann and Wenzel, 1995).

The 11 main tidal terms usually considered are the semi-diurnal waves M_2, S_2, N_2, K_2, the diurnal waves K_1, O_1, P_1, Q_1 and the long-period waves M_f, M_m and S_{sa}. By inputing the station positions of interest, the amplitude and phase of the loading response for these 11 tidal terms are obtained with the ocean tide loading service[5].

Moreover, when the solid Earth and oceans are considered to be a system without any external forces on it, then the position of its common center of mass will remain fixed in space. Since the ocean tides cause water mass displacements, its center of mass will move periodically and must be compensated by an opposite

[5] http://holt.oso.chalmers.se/loading/

motion of the center of mass of the solid Earth. Stations placed on the solid Earth are subject to this counter-motion. For the analysis of LLR data, this correction is mandatory and can be enabled within the loading service website given above.

The site displacement due to ocean tide loading (Δc) at a given time (t) is given by :

$$\Delta c = \sum_j A_{cj} \cos\left(\chi_j(t) - \phi_{cj}\right) \tag{3.7}$$

where,

Δc = site displacement components (radial, west, south),
A_{cj}, ϕ_{cj} = amplitudes and phases for the loading response at each site,
$\chi_j(t)$ = astronomical argument for the 11 main tidal terms, computed with IERS distributed subroutine ARG2.F

We use the IERS subroutine (HARDISP.F) provided by D. Agnew to compute the ocean tide loading displacements for a site, given the amplitudes A_{cj} and phases $\phi_{cj}, 1 \le j \le 11$. The amplitude of the effect due to ocean tide loading on the Earth-Moon distance is around 20 cm, with a maximum of 70 cm (based on the station location) between 1969 to 2017.

3.3.3 Atmospheric pressure loading

The diurnal heating of the atmosphere by the Sun, causes surface pressure oscillations at the diurnal (S_1), semi-diurnal (S_2) and higher harmonics. The result of which induces periodic motions of the Earth's surface. Petit and Luzum (2010) recommend calculating the station displacement due to atmospheric loading using Ray and Ponte (2003) S_1 and S_2 tidal model.

The displacement grid method was implemented to obtain the surface displacement coefficients (A_{d1}, B_{d1}, A_{d2} and B_{d2}), in order to compute the site displacement due to S_1-S_2 atmospheric loading[6] given by:

$$d(u,e,n)S_1 = A_{d1}(u,e,n) \times \cos(\omega_1 T) + B_{d1}(u,e,n) \times \sin(\omega_1 T) \tag{3.8a}$$
$$d(u,e,n)S_2 = A_{d2}(u,e,n) \times \cos(\omega_2 T) + B_{d2}(u,e,n) \times \sin(\omega_2 T) \tag{3.8b}$$

where,

u, e, n up, east, north components in mm
T = UT1 in days
ω_1, ω_2 = 1 cycle/day, 2 cycle/day corresponding to frequencies of S_1, S_2 atmospheric tides.

[6] http://geophy.uni.lu/ggfc-atmosphere/tide-loading-calculator.html

The amplitude of the effect due to atmospheric pressure loading on the Earth-Moon distance reaches up to 0.8 cm between 1969 to 2017.

3.3.4 Rotational deformation due to polar motion

The centrifugal potential caused by the Earth's rotation is given by:

$$V = \frac{1}{2}\Big[r^2|\vec{\Omega}| - (\vec{r}\cdot\vec{\Omega})^2\Big], \tag{3.9}$$

where,

$\vec{\Omega}$ = $\Omega(m_1\hat{x} + m_2\hat{y} + (1+m_3)\hat{z})$
Ω = mean angular velocity of the Earth's rotation
m_1, m_2 = time-dependent offset of the instantaneous rotation pole from the mean
m_3 = fractional variation in the rotation rate
r = geocentric distance to the station
$\hat{x}, \hat{y}, \hat{z}$ = unit vectors of the station coordinates in the ITRF.

The first order perturbations (neglecting sub-mm level variations due to m_3) in the potential V due to the Earth's rotation is given by Wahr (1985):

$$\Delta V(r,\theta,\lambda) = -\frac{\Omega^2 r^2}{2}\sin 2\theta(m_1\cos\lambda + m_2\sin\lambda) \tag{3.10}$$

with,

$$m_1 = x_p - \overline{x}_p \text{ and } m_2 = -(y_p - \overline{y}_p) \tag{3.11}$$

The Petit and Luzum (2010) mean pole model is given as:

$$\overline{x}_p(t) = \sum_{i=0}^{3}(t-t_0)^i \times \overline{x}_p^i \text{ and } \overline{y}_p(t) = \sum_{i=0}^{3}(t-t_0)^i \times \overline{y}_p^i \tag{3.12}$$

where t_0 is 2000.0, t is the Julian epoch in years and coefficients $\overline{x}_p^i$ and $\overline{y}_p^i$ represent the annual pole position (cubic model until 2010.0 and linear model after 2010.0) are tabulated in (Petit and Luzum, 2010, Table 7.7).

The displacements due to ΔV are obtained using the formulation of tidal Love numbers (h_2 = 0.6207 and l_2 = 0.0836) and $r = a = 6.378 \times 10^6$ m (Munk and MacDonald, 1960), to give:

$$\begin{aligned} S_r &= -33\sin 2\theta(m_1\cos\lambda + m_2\sin\lambda) \\ S_\theta &= -9\cos 2\theta(m_1\cos\lambda + m_2\sin\lambda) \\ S_\lambda &= 9\cos\theta(m_1\sin\lambda - m_2\cos\lambda) \end{aligned} \tag{3.13}$$

where,

S_r, S_θ and S_λ = displacement vectors in mm (positive upwards, south and east, respectively.)
m_1, m_2 = offsets in arc-seconds
θ, λ = latitude and longitude of the station, respectively.

The IERS subroutine (IERS_CMP_2015.F) was used to obtain the conventional mean pole position and the displacements were computed using Eqn. (3.13). The amplitude of the effect due to the rotational deformation from polar motion on the Earth-Moon distance reaches up to 1.6 cm between 1969 to 2017.

3.3.5 Ocean pole tide loading

The displacement of station position due to the centrifugal effect of the polar motion on the oceans is called ocean pole tide loading. The displacement vector is given in terms of radial, north and east components, u_r,u_n and u_e, respectively (Desai, 2002).

$$\begin{bmatrix} u_r(\phi,\lambda) \\ u_n(\phi,\lambda) \\ u_e(\phi,\lambda) \end{bmatrix} = K \left\{ (m_1\gamma_2^R + m_2\gamma_2^I) \begin{bmatrix} u_r^R(\phi,\lambda) \\ u_n^R(\phi,\lambda) \\ u_e^R(\phi,\lambda) \end{bmatrix} + (m_2\gamma_2^R - m_1\gamma_2^I) \begin{bmatrix} u_r^I(\phi,\lambda) \\ u_n^I(\phi,\lambda) \\ u_e^I(\phi,\lambda) \end{bmatrix} \right\} \quad (3.14)$$

where,

ϕ, λ = latitude and longitude
m_1, m_2 = wobble parameters Eqn. (3.11)
$K = \dfrac{4\pi G a_E \rho_w H_p}{3g_e}$
$H_p = \left(\dfrac{8\pi}{15}\right)^{\frac{1}{2}} \cdot \dfrac{\Omega^2 {a_e}^4}{GM}$
ρ_w = density of sea water = 1025 kg m^{-3}
$\gamma = (1 + k_2 - h_2) = \gamma_2^R + i\gamma I_2 = 0.6870 + 0.0036i$
Ω = nominal mean Earth's angular velocity
a_e = equatorial radius of the Earth
GM = geocentric gravitational constant
g_e = mean equatorial gravity
G = constant of gravitation

Coefficients u^R and u^I are the real and imaginary part of the ocean pole tide deformation parameters from the self-consistent equilibrium model of ocean pole tide (Desai, 2002) [7] and they provide the surface deformations with respect to the instantaneous center of mass of the deformed Earth, including the mass of the loading ocean pole tide. The gridded values were first interpolated to the station position and then introduced as displacement vectors as per Eqn. (3.14). The amplitude of the effect due to ocean pole tide loading on the Earth-Moon distance reaches up to 0.1 cm between 1969 to 2017.

3.3.6 Hydrological mass loading

The Earth's surface is deformed in response to temporal variations in the mass distribution of atmospheric, hydrological and oceanic loads imposed on the lithosphere. Apart from the tidal-induced mass variations, non-tidal mass variations with sub-daily to seasonal periods lead to primarily vertical elastic deformations at global, regional and local scales (Blewitt et al., 2001; Fu et al., 2012; Bevis et al., 2005). A perfect understanding of the loading signal observed by geodetic techniques should help in improving terrestrial reference frame (TRF) realizations. Yet, discrepancies between crustal motion estimates from models of surface-mass loading and observations are still too large so that no model is currently recommended by the IERS for reducing the data.

The astronomical and geodetic observatory OCA, located on the karst plateau of Calern (Caussols, France) has been monitoring the Earth deformation. Gilli et al. (2010) show that the deformations induced at the Calern station by the effects of rainfall and snow-melt is non-negligible. The study concludes by identifying two probable components, a surface and a deep component, while the mechanical effect remained unknown.

A recent study (Mémin et al., 2016) aimed at the multi-geodetic characterization of this seasonal signal, shows a strong correlation between GPS observations obtained at the Calern station and non-tidal loading predicted deformation due to atmosphere, ocean and hydrology[8]. Two continental hydrology loading models were used, derived from, Global Land Data Assimilation System (GLDAS) and Modern-Era Retrospective analysis for Research and Applications (MERRA).

For the purpose of comparison, LLR residuals obtained from the Calern station between 2002 to 2015 were stacked and averaged by week (see Fig. 3.3). This was then compared with the other geodetic techniques in operation at Calern station. It was noticed that the impact due to hydrology remained as the main driver of the

[7] interpolated from equally spaced 0.5 by 0.5 degree global grid available at ftp://tai.bipm.org/iers/conv2010/chapter7/opoleloadcoefcmcor.txt.gz

[8] Surface displacement maps were obtained from http://loading.u-strasbg.fr/displ_maps.php

seasonal signal at Calern, with a good correlation of LLR, GPS and the non-tidal loading predictions in the vertical component.

The signal at the Calern station was characterized as seasonal with amplitudes of (8.5 ± 0.5), (1.5 ± 0.5) and (1.5 ± 0.5) in the Up, North and East component, respectively (in mm).

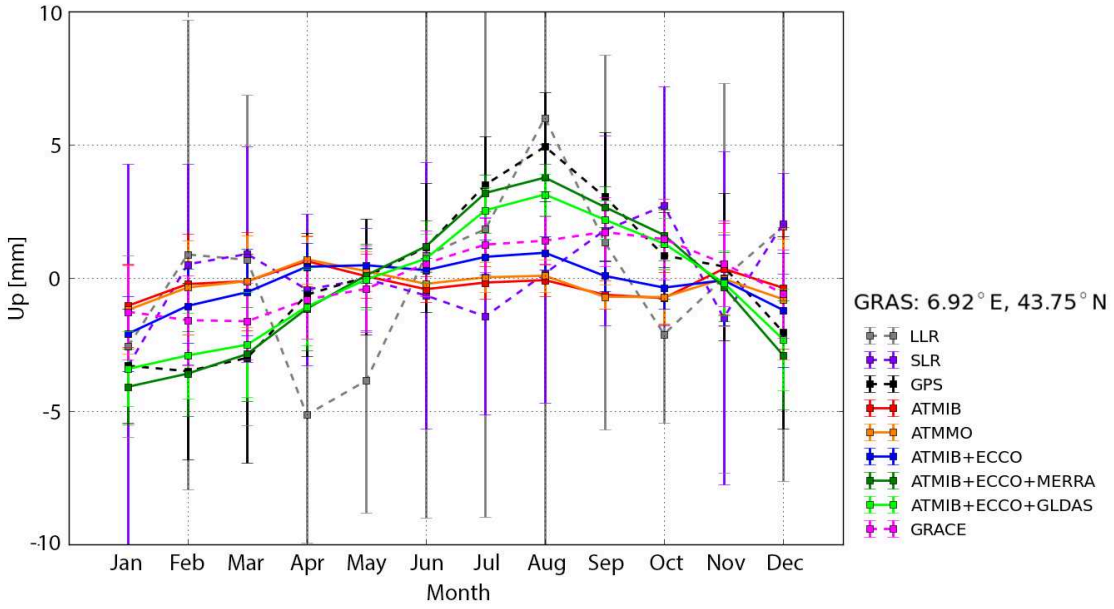

Figure 3.3: Multi-geodetic characterization of the seasonal signal at the Grasse geodetic reference station, France. Strong correlation between GPS observations and non-tidal loading predicted deformation due to hydrology. LLR observations agree reasonably well with GPS and hydrology loading predictions in the U component. The estimated amplitude of the effect is (8.5 ± 0.5) mm in the Up component. LLR observations lack sensitivity in the other directions and hence are not provided. Grasse observations are stacked and averaged by month over 13 years. Used with permission from Mémin et al. (2016).

3.4 Corrections to light-time

3.4.1 Atmospheric delay

The observed round-trip light-time in distance inherently contains the effect of an increased propagation path as the laser pulse traverses through the different layers of varying refractive index within the atmosphere. The propagation effects concerning the optical regime are only subject to delays in the neutral atmosphere

(up to about 100 km). Hence, it must be accounted for within the light-time computation of the observable and along each leg.

The atmospheric delay in the zenith direction is characterized into hydrostatic delay and wet delay. Hydrostatic delay can be accurately determined from surface pressure measurements available within the LLR observations, while the wet delay cannot be estimated accurately from the same information. The elevation dependence of the zenith atmospheric delay is characterized by a mapping function.

This study follows the Petit and Luzum (2010) recommendation with Mendes et al. (2002); Mendes and Pavlis (2004) as the mapping function - zenith delay pair for the correction of tropospheric optical delays. Fortran subroutines are provided by the IERS as an implementation of the recommended models (FCUL_ZTD_HPA.F and FCUL_A.F).

It is to be noted that the mapping function within Mendes et al. (2002) neglects the contribution of horizontal refractivity gradients. Hulley and Pavlis (2007) developed a new technique with the inclusion of horizontal gradients using a three-dimensional atmospheric ray tracing (3D ART) with meteorological data (NS and EW gradients) from the Atmospheric Infrared Sounder (AIRS), improving the SLR range residuals by up to 25% while ranging at low elevation angles (10°). For LLR ranging, the typical elevation angles lie between 30° to 40° where the effect is below 1 mm (Currie and Prochazka, 2014). While this study (Hulley and Pavlis, 2007) can be a future improvement to the LLR data analysis community handling modern-day high accuracy data approaching the millimeter level, the ray-tracing technique would increase the computational time due to the large meteorological gridded datasets and become susceptible to temporal interpolation errors due to the availability of the data for each station.

The amplitude of the correction from atmospheric delay on the Earth-Moon distance reaches up to 10 m between 1969 to 2017. The uncertainty of the atmospheric delay model when compared with ray tracing techniques reaches up to 2 mm for stations with high water vapor content (Mendes and Pavlis, 2004). However, at lower elevation angles (below 10°) the contribution from horizontal gradients dominate, ranging between 7 mm to 14 mm (Hulley and Pavlis, 2007).

3.4.2 Relativistic correction

According to the general theory of relativity, the speed of a light wave depends on the strength of the gravitational potential along its path (Shapiro, 1964). From a geometrical point of view, each of the gravitating bodies curve the space-time fabric in their vicinity. In the solar-system barycentric frame of reference, this is expressed as Moyer (2003, Eqn. 8-25). This correction is included in the up-leg and down-leg iterations, from that due to the Sun and the Earth. The amplitude of the correction from the relativistic deviation of light on the Earth-Moon distance

reaches up to 8 m between 1969 to 2017. The ignored effect of the Moon amounts to about 0.7 mm (Williams et al., 1996).

Chapter summary

The LLR data reduction model within the GINS software was vetted through a step-wise comparison study with two other independent LLR groups in Europe. In addition to the IERS 2010 recommended models, the impact of hydrological mass loading at Grasse station was analyzed through multi-geodetic techniques. A seasonal signature due to hydrology loading is characterized and a correction model is implemented within the reduction software using a model from the EOST Loading Service. The following chapter (Chapter 4) focuses on the dynamical model of the lunar ephemeris which provide critical inputs to the reduction software in terms of lunar orientation and other state vectors.

Chapter 4

Dynamical model

For the LLR analysis, the dynamical model involves the description of the motion and the orientation of the Moon as it moves along its orbit around the Earth. This is described with the help of planetary and lunar ephemerides (such as INPOP, DE and EPM).

This study benefited from the previous work of Fienga et al. (2008); Fienga et al. (2011); Fienga et al. (2014, 2015, 2016a), Gastineau et al. (2015) and Manche (2011) on their respective developments on the numerical solution of INPOP since its inception in 2003. This study develops on the last update of the lunar model within the INPOP ephemeris (Fienga et al., 2014), elaborates on the improvements from INPOP13c in Section (4.1), with the description of the lunar orbital interactions (Section 4.2) and the lunar orientation with its extended figure (Section 4.3).

4.1 Improvement from INPOP13c

The dynamical model backing the lunar part of the INPOP planetary and lunar ephemeris is described within this chapter. The two-layer Moon (solid mantle with a fluid core) was implemented within INPOP by Manche (2011); Fienga et al. (2014). In the last version: INPOP13c (Fienga et al., 2014) the lunar fluid core is not activated, and the LLR post-fit residuals in 1-way light light (LT) did not seem to improve below 4 cm. This is identified as a programming error within the modeling of the differential equation of the lunar fluid core. Following the correction of this error, and iteratively fitting the LLR observations, an improvement is noticed in the post-fit LLR residuals to about 2 cm for the modern day period.

The polar moment of inertia of the Moon was previously implemented as the sum of two separate components; that of the mantle and the fluid core. This required input parameters such as the spherical harmonic coefficients C_{20} and C_{22} of the lunar mantle and the lunar fluid core, to describe the respective moment of

inertia tensor. This is reorganized as that of the total Moon and the fluid core. This modification allowed the use of spacecraft observed gravity field coefficients that monitor the Moon as a whole, hence providing strong constraints on the lunar spherical harmonic coefficients used for the Moon within the dynamical model. The C_{20} (fluid core) is redefined to the flattening of the lunar fluid core f_c through Eqn. (4.1).

$$f_c \cdot \alpha_c = \frac{\left[C_c - \left(\frac{A_c+B_c}{2}\right)\right]}{C_T} \tag{4.1}$$

where, $\alpha_c = \frac{C_c}{C_T}$ is kept as a fixed value to $7{\times}10^{-4}$ (Folkner et al., 2014);
A_c,B_c and C_c are the principle moments of the tensor of inertia of the fluid core;
C_T is the polar moment of inertia of the whole Moon.

This redefinition allows for a better determined value of $f_c \cdot \alpha_c$ implying that the existence of a flattening of the lunar core is strong (Williams et al., 2014b). However, the value of f_c would depend on the fraction of the core polar moment of inertia

Folkner et al. (2014); Pavlov et al. (2016) consider an axisymmetric fluid core with $A_c = B_c = C_c(1-f_c)$, due to the weak sensitivity of LLR to equatorial ellipticity (Goldreich, 1967; Williams et al., 2014b).

To confirm this assertion of low sensitivity, a triaxial fluid core is implemented using Rambaux et al. (2007), discussed through Eqn. (4.9), with $g_c = \frac{B_c - A_c}{2A_c}$. Due to the strong correlation of the polar (f_c) and equatorial (g_c) flattening of the fluid core (correlation coefficient of 0.97) and the above mentioned low sensitivity of the equatorial flattening to LLR observations (arising from the geometry), it is difficult to iteratively fit these two parameters together. As a result, g_c is kept fixed to a theoretical value of 4.10^{-5} (an order small than the value of f_c), computed using a density profile from Dumberry and Wieczorek (2016) and extended to a triaxial fluid core. An undetectable variation of about 0.5 mm is induced on the Earth-Moon distance, below the current LLR data accuracy of about 5 mm.

The time-delay tide model accounts for dissipation in the Earth-Moon system. INPOP13c consisted of three time delays ($\tau_{21,E}$, $\tau_{22,E}$ and τ_M). To account for time delays shifting across the diurnal and semi-diurnal frequency bands (Williams and Boggs, 2015b), the two time delays ($\tau_{2m,E}$) were split to associate them with the Earth's rotation and the lunar orbit (Folkner et al., 2014).

4.2 Lunar orbit interactions

In the INPOP17a model, we include the following accelerations perturbing the Moon's orbit:

1. Point mass mutual interactions from the Sun, planets and asteroids from Folkner et al. (2014, Eqn. 27)

2. Point mass mutual interactions from the extended bodies from Folkner et al. (2014, Eqn. 28) which include :

   - the interaction of the zonal harmonics of the Earth through degree 6;
   - the interaction between zonal, sectoral, and tesseral harmonics of the Moon through degree 6 and the point mass Earth, Sun, Jupiter, Saturn, Venus and Mars;
   - the interaction of degree 2 zonal harmonic of the Sun.

3. Interaction from the Earth tides (Folkner et al., 2014, Eqn. 32)
   The tidal acceleration from the tides due to the Moon and the Sun are separated into three frequency bands (zonal, diurnal and semi-diurnal). Each band is represented by a potential Love number $k_{2m,E}$ with a matching pair of time delays $\tau_{Xm,E}$ (where subscript X is either associated with the daily Earth rotation $\tau_{Rm,E}$ or orbital motion $\tau_{Om,E}$) to account for frequency dependent phase shifts from an anelastic Earth with oceans. Here the time delay represents the phase lag induced by the tidal components. Although the time delay method inherently assumes that the imaginary component of $k_{2m,E}$ varies linearly with frequency, it reduces the complexity of the dynamical model. The diurnal $\tau_{R1,E}$ and semi-diurnal $\tau_{R2,E}$ are included as solution parameters in the LLR analysis, while model values for potential Love numbers for a solid Earth are fixed to that from Petit and Luzum (2010, Table 6.3) followed by corrections from the ocean model FES2004 (Lyard et al., 2006). A detailed explanation about the most influential tides relevant to the Earth-Moon orbit integration can be found in Williams and Boggs (2016, Table 6).

4.3 Lunar orientation and extended figure

4.3.1 Lunar frame definition

The mantle coordinate system is defined by the principal axes of the undistorted mantle, whose moment of inertia matrix is diagonal. The time varying mantle

Euler angles ($\phi_m(t)$,$\theta_m(t)$,$\psi_m(t)$) define the orientation of the principal axis (PA) frame with respect to the inertial ICRF2 frame (Ma et al., 2009) where: ϕ_m is the angle from the X-axis of the inertial frame along the XY plane to the intersection of the mantle equator; θ_m is the inclination of the mantle equator from the inertial XY plane; and ψ_m is the longitude from the intersection of the inertial XY plane with the mantle equator along the mantle equator to the prime meridian.

4.3.2 Time variation of lunar orientation

The angular velocity of the mantle is expressed through the instantaneous rates of the Euler angles as shown in Newhall et al. (1983), repeated here as:

$$\begin{aligned}\omega_x &= \dot{\phi}\sin\theta\sin\psi + \dot{\theta}\cos\psi \\ \omega_y &= \dot{\phi}\sin\theta\cos\psi - \dot{\theta}\sin\psi \\ \omega_z &= \dot{\phi}\cos\theta + \dot{\psi}\end{aligned} \tag{4.2a}$$

The second derivatives of the Euler angles follows Newhall et al. (1983, Eqn. 3):

$$\begin{aligned}\ddot{\phi} &= \frac{\dot{\omega_x}\sin\psi + \dot{\omega_y}\cos\psi + \dot{\theta}(\dot{\psi} - \dot{\phi}\cos\theta)}{\sin\theta} \\ \ddot{\theta} &= \dot{\omega_x}\cos\psi - \dot{\omega_y}\sin\psi - \dot{\phi}\dot{\psi}\sin\theta \\ \ddot{\psi} &= \dot{\omega_z} - \ddot{\phi}\cos\theta + \dot{\phi}\dot{\theta}\sin\theta\end{aligned} \tag{4.2b}$$

4.3.3 Lunar moment of inertia tensor

The undistorted total moment of inertia of the Moon $\tilde{\mathrm{I}}_T$ is expressed in terms of $C_{(2,0),M}$ and $C_{(2,2),M}$ using Manche (2011, Eqn. C.6):

$$\tilde{I}_T = \frac{\tilde{C}_T}{m_M R_M^2}\begin{bmatrix}1 & 0 & 0\\ 0 & 1 & 0\\ 0 & 0 & 1\end{bmatrix} + \begin{bmatrix}\tilde{C}_{2,0,M} - 2\tilde{C}_{2,2,M} & 0 & 0\\ 0 & \tilde{C}_{2,0,M} + 2\tilde{C}_{2,2,M} & 0\\ 0 & 0 & 0\end{bmatrix} \tag{4.3}$$

where $\tilde{\mathrm{C}}_{n,m,M}$ is the unnormalized degree n, order m of the Stokes coefficient $C_{n,m}$ for the spherical harmonic model of the undistorted Moon and $\tilde{C}_T$ is the undistorted polar moment of inertia of the Moon normalized by its mass m_M and radius squared R_M^2. Through Eqn. (4.3), we are able to directly use the undistorted value of C_{22} from GRAIL derived spherical harmonic model of Konopliv et al. (2013).

The moment of inertia of the fluid core I_c is given by:

$$I_c = \alpha_c \tilde{C}_T \begin{bmatrix} 1-f_c & 0 & 0 \\ 0 & 1-f_c & 0 \\ 0 & 0 & 1 \end{bmatrix} = \begin{bmatrix} (A_c+B_c)/2 & 0 & 0 \\ 0 & (A_c+B_c)/2 & 0 \\ 0 & 0 & C_c \end{bmatrix} \tag{4.4a}$$

where α_c is the ratio of the fluid core polar moment of inertia C_c to the undistorted polar moment of inertia of the Moon C_T, f_c is the fluid core polar flattening and, A_c and B_c are the equatorial moments of the fluid core.

Here, Eqn. (4.4a) similar to Folkner et al. (2014, Eqn. 39) and Pavlov et al. (2016, Eqn. 17), assumes an axis-symmetric ($A_c = B_c$) fluid core for the Moon while the triaxial equivalent is given in Eqn. (4.9g).

The moment of inertia of the mantle I_m has a rigid-body contribution $\tilde{I}_m$ and two time varying contributions due to the tidal distortion by the Earth and spin distortion as given in Folkner et al. (2014, Eqn. 41). The single time delay model (characterized by τ_M) allows for dissipation when flexing the Moon (Williams et al., 2001; Standish et al., 2003; Folkner et al., 2014). Although in practice the time delay model fits well the monthly tides, phase shifts at other periods are not realistic (Williams and Boggs, 2015b). We propose some possible improvements in Chapter (7).

Finally we have:

$$\tilde{I}_m = \tilde{I}_T - I_c \tag{4.4b}$$

4.3.4 Lunar angular momentum and torques

The time derivative of the angular momentum vector is equal to the sum of torques ($\vec{N}$) acting on the body. In the rotating mantle frame, the angular momentum differential equation for the mantle is given by:

$$\frac{d}{dt} I_m \vec{\omega}_m + \vec{\omega}_m \times I_m \vec{\omega}_m = \vec{N} \tag{4.5a}$$

where,

$$\vec{N} = \sum_{A \neq M} (\vec{N}_{M,figM-pmA}) + \vec{N}_{M,figM-figE} + \vec{N}_{CMB} \tag{4.5b}$$

and,

$\vec{N}_{M,figM-pmA}$ = net torque on the lunar mantle from the point mass body A;

$\vec{N}_{M,figM-figE}$ = figure-figure interaction between the Moon and the Earth;

$\vec{N}_{CMB}$ = the viscous interaction between the fluid core and the mantle.

The motion of the uniform fluid core is controlled by the mantle interior, with the fluid core moment of inertia (I_c) constant in the frame of the mantle. The angular momentum differential equation of the fluid core in the mantle frame is then given by:

$$\frac{d}{dt} I_c \vec{\omega}_c + \vec{\omega}_m \times I_c \vec{\omega}_c = -\vec{N}_{CMB} \tag{4.6}$$

$$\dot{\vec{\omega}}_c = I_c^{-1} \Big\{ -\vec{N}_{CMB} - \vec{\omega}_m \times I_c \vec{\omega}_c \Big\} \tag{4.7}$$

where $\vec{\omega}_c$ is the angular velocity of fluid core and $\vec{N}_{CMB}$ is the torque arising at the core-mantle boundary (CMB) due to the relative velocity between the fluid core and the solid mantle, expanded as:

$$\vec{N}_{CMB} = k_v \big(\vec{\omega}_c - \vec{\omega}_m\big) + \big(C_c - A_c\big)\big(\hat{z}_m \cdot \vec{\omega}_c\big)\big(\hat{z}_m \times \vec{\omega}_c\big) \tag{4.8}$$

where k_v is the coefficient of viscous friction at the CMB and $\hat{z}_m$ is a unit vector aligned with the polar axis of the mantle frame.

4.3.5 Triaxiality of the lunar fluid core

In Eqn. (4.6), the inertial coupling (second term on the RHS of Eqn. (4.8)) between the fluid core and the mantle is modeled for an axis-symmetric fluid core. Due to a small value of α_c, the additional coupling term arising from a triaxial core carries only a weak effect while integrating the physical librations through the Euler angles. We test the impact of the inclusion of the additional inertial coupling arising from the triaxiality by modifying Eqn. (4.5a) and Eqn. (4.6) to Eqn. (4.9a) and Eqn. (4.9b) respectively, given by:

$$\frac{d}{dt} \vec{L} + \vec{\omega}_m \times \vec{L} = \vec{N} \tag{4.9a}$$

with $\vec{N}$ here, as the sum of torques on the Moon from point mass mutual interactions ($\vec{N}_{M,figM-pmA}$) and from figure-figure interactions $\vec{N}_{M,figM-figE}$.

$$\frac{d}{dt} \vec{L}_c - (\vec{\omega}_c - \vec{\omega}_m) \times \vec{L}_c = -\vec{N}_C \tag{4.9b}$$

where,

$$\vec{L} = I_T \vec{\omega}_m + I_{fgh} (\vec{\omega}_c - \vec{\omega}_m) \tag{4.9c}$$

with,

$$\vec{L}_c = I_{fgh} \vec{\omega}_m + I_c (\vec{\omega}_c - \vec{\omega}_m) \tag{4.9d}$$

$$I_{fgh} = \begin{bmatrix} F_c & 0 & 0 \\ 0 & G_c & 0 \\ 0 & 0 & H_c \end{bmatrix} \tag{4.9e}$$

and,

$$\vec{N}_C = k_v\left(\vec{\omega}_c - \vec{\omega}_m\right) \tag{4.9f}$$

The diagonal elements of I_{fgh} (F_c, G_c and H_c) introduce the triaxial inertial coupling between the fluid core and the mantle into the angular momentum differential equation following Rambaux et al. (2007).

$$\begin{aligned} F_c^2 &= A_c^2 - (C_c - B_c)^2 \\ G_c^2 &= B_c^2 - (A_c - C_c)^2 \\ H_c^2 &= C_c^2 - (B_c - A_c)^2 \end{aligned} \tag{4.9g}$$

A triaxial fluid core modifies I_c in Eqn. (4.4a) to Eqn. (4.9h), with g_c as the fluid core equatorial flattening, given by :

$$I_c = \alpha_c \tilde{C_T} \begin{bmatrix} \dfrac{(1-f_c)}{(1+g_c)} & 0 & 0 \\ 0 & \dfrac{(1-f_c)}{\left(1+\dfrac{g_c}{1+g_c}\right)} & 0 \\ 0 & 0 & 1 \end{bmatrix} \tag{4.9h}$$

where, $f_c\alpha_c = [C_c - \dfrac{A_c + B_c}{2}]/C_T$; $g_c = \dfrac{B_c - A_c}{2A_c}$

The impact of the lunar fluid core equatorial flattening parameter g_c was found to be very weak during the fit to observation. By introducing the triaxial fluid core equation and refitting the lunar solution, an undetectable variation of about 0.5mm is induced on the Earth-Moon distance, which is about 10 times smaller than the most accurate LLR data currently available.

4.3.6 External point mass interaction on extended figure of the fluid core

An additional torque from point mass Earth on the degree-3 figure of the fluid core (only C_{32}, S_{32} and C_{33} spherical harmonics) is modeled through Folkner et al. (2014, Eqn. 28), with a fixed fluid core radius of 330 km (Weber et al., 2011). This is introduced as $\vec{N}_{c,figC-pmA}$, which appears on the right hand side of Eqn. (4.6), repeated here, as:

$$\frac{d\vec{L}_c}{dt} + \vec{\omega}_m \times \vec{L}_c = -\vec{N}_{CMB} + \vec{N}_{c,figC-pmA} \tag{4.10}$$

This additional torque is only computed as coming from the interaction of the point mass Earth (while neglecting other bodies) on the lunar fluid core shape implemented within an internal version of INPOP (S2) to compensate the degree-3 discrepancy (see Section 6.1.2). A detailed discussion on the introduction of this effect is provided within Section (6.1.3). For a complete torque balance on the fluid core, one must also consider the pressure torques generated from the assumed assymetry of the fluid core, which is absent at the time of writing. A submitted article (Appendix C) presents the results obtained with this modeling, and is under revision to consider a complete torque model. INPOP17a (Viswanathan et al., 2017) does not include this interaction, as it is a work in progress.

Chapter summary

The model description of the lunar rotation and orbit (within this chapter) is numerically integrated together with the planet orbits. The obtained orbits are then adjusted to the LLR data, including those parameters describing the lunar interior, such as the flattening of the fluid core, viscous friction at core-mantle boundary, etc. The procedure involved during the adjustment to the model, the comparison of the estimates obtained after iterative fits, and the post-fit residuals obtained, are discussed in the next chapter (Chapter 5).

Chapter 5

Construction of a lunar ephemeris: INPOP17a

This chapter focuses on the fit of the model to the LLR observations. The reduced observations (described in Chapter 3) are compared with a simulated dynamical model (proposed in Chapter 4) that closely follows the motion and orientation of the Moon under the perturbation of other solar system objects. The simulated dynamical model and the reduction procedure are controlled through several parameters that function as model variables (Section 5.2). These variables are then optimized in order to minimize the difference between the simulations and the observations (also known as residuals), achieved through an iterative weighted least-squares fit (Section 5.1). Some observations could be more accurate than the others, in which case they carry more weight during the fit, while few others could be biased (Section 5.1.2). In cases where one or a set of parameter(s) are better determined through a technique different from LLR (e.g. spacecraft derived), bounds can be set using the Bounded-value least-squares (Section 5.1.3) fit to provide tight constraints (Section 5.2.1) to correlated parameters (Section 5.2.2). The resulting post-fit residuals obtained with the newly constructed lunar ephemeris is provided (Fig. 5.7) along with two different uncertainty computation (Section 5.1.4) for each estimated parameter. The estimated parameters are then compared with the previous release of INPOP (version 13c) and that obtained from other LLR analyses groups (Section 5.3).

5.1 Fitting procedure

In this section the algorithm used for the adjustments is described. This algorithm is based on the least-squares (LS) method for which the linearization of the problem is required. Furthermore, because of the inhomogeneity of the LLR data sample,

special attention is taken for building an efficient weighting scheme and for debiasing the adjustment from systematics. Finally, the LS method is combined with an optimization method for keeping well-known values inside realistic bounds.

5.1.1 Linearity and convergence

A weighted least-squares (WLS) regression equation is represented by the linear relation following the Moore-Penrose pseudo-inverse of the matrix A_{ij} (Moore; Penrose and Todd, 1955) in the following form:

$$\hat{\beta}_{j,n} = (A_{ij}^{\top} W_{ii} A_{ij})^{-1} A_{ij}^{\top} W_{ii} X_{i,n-1} \tag{5.1}$$

where partial derivatives (A_{ij}) with respect to each parameter p_j are approximated by using numerical central differencing of the computed one-way light-time ($C(p_j)$). The choice of the magnitude of the variation of the parameter (δp_j) for the computation of A_{ij} is such that a linear region of the function $C(p_j)$ is explored. An investigation for the selection of the appropriate δp_j was made following Manche (2011). $\hat{\beta}_{j,n}$ gives the value of the estimated correction to be added to p_j for the n^{th} iteration and $X_{i,n-1}$ are the post-fit residuals ($O-C(p_j)$) from the $n-1^{th}$ iteration. The WLS procedure (Tapley et al., 2010) (weighted by the matrix W_{ii}, see Section 5.1.2) is iterated until the χ^2 (the goodness of fit, computed as the normalized sum of squared deviations between observed and theoretical values) reaches a minimum value, after which numerical noise dominates.

The sensitivity of the observable to each parameter can be characterized by computing its partial with respect to the computed one-way light-time. Although not the primary objective of these partial derivatives, they also allow the user to make a first-guess of: the order of magnitude of the expected corrections, periodicity, non-linearity and detection limits associated with each parameter over the desired fit interval. The reflector-wise plot of partial derivatives for all the 47 dynamical model parameters are provided within the Appendix (B.2).

The correlation matrix was computed from the partial derivatives of all the parameters (both dynamical and reduction model) using a standard python routine (pandas.dataframe.corr.py) using the Pearson standard correlation coefficient (Pearson, 1895). A heat-map of the correlation matrix is provided within Appendix (B.1). Two or more correlated parameters that exhibit similar signature on the Earth-Moon distance can be hard to be separated in the fit. An instance of correlated parameters are the equivalence principle violation parameter Δr_{EM} and the Earth-Moon barycenter GM_{EMB}, with a correlation coefficient of +0.96 between them. Gravity field coefficients of the Moon also exhibit strong correlation among the different degrees and orders. Hence, we introduced constraints on the gravity field of the Moon from the GRAIL spacecraft-derived model (Konopliv et al., 2013), which are further explained in Section (5.2.1).

The linearity of each parameter was verified about a central value, such that the partial derivative lies within the linear region of the parameter space. Several values of δp_j were chosen and tested for recovery i.e (simulations were performed by introducing δp_j into the model and recovered using the least-squares fit). All parameters except the angular velocity component of the lunar core (ω_y) exhibit strong linearity and recovery (by at-least 99.99%) during the simulations. To solve this problem, the partial derivatives w.r.t the lunar core angular velocity, were computed at multiple initial conditions during the iterative fit (once about zero and then subsequently about the non-zero values obtained from the previous iterations). It was noticed during the LLR iterative fit that, at-least two consequent partial computations were required from a zero initial condition of the lunar core angular velocity, to achieve a converged solution. JPL LLR team uses an approximation method involving a linear combination of the core coefficient of viscous friction and flattening to address this problem (Williams et al., 2013, Eqn. 2).

5.1.2 Weighting adjustments and biases

The diagonal elements of the weighting matrix (W_{ii}) within Eqn. (5.1) are the squares of the inverse of the inherent uncertainties (σ_i) of each observation, computed using the normal point algorithm. LLR station analyses teams continuously attempt to improve existing algorithms, methods and practices, which result in the absence of a standardization in the distributed observational uncertainty (see Section 2.2). Moreover, since the uncertainties are partly tied with the rejection scheme used in the normal point computation employed at each station (as described in Section (2.2.3) for Grasse station), rescaling of the uncertainties becomes necessary in cases where a lack of clean evolution of the uncertainties is noticed (as seen in Fig. 5.1 and 5.2).

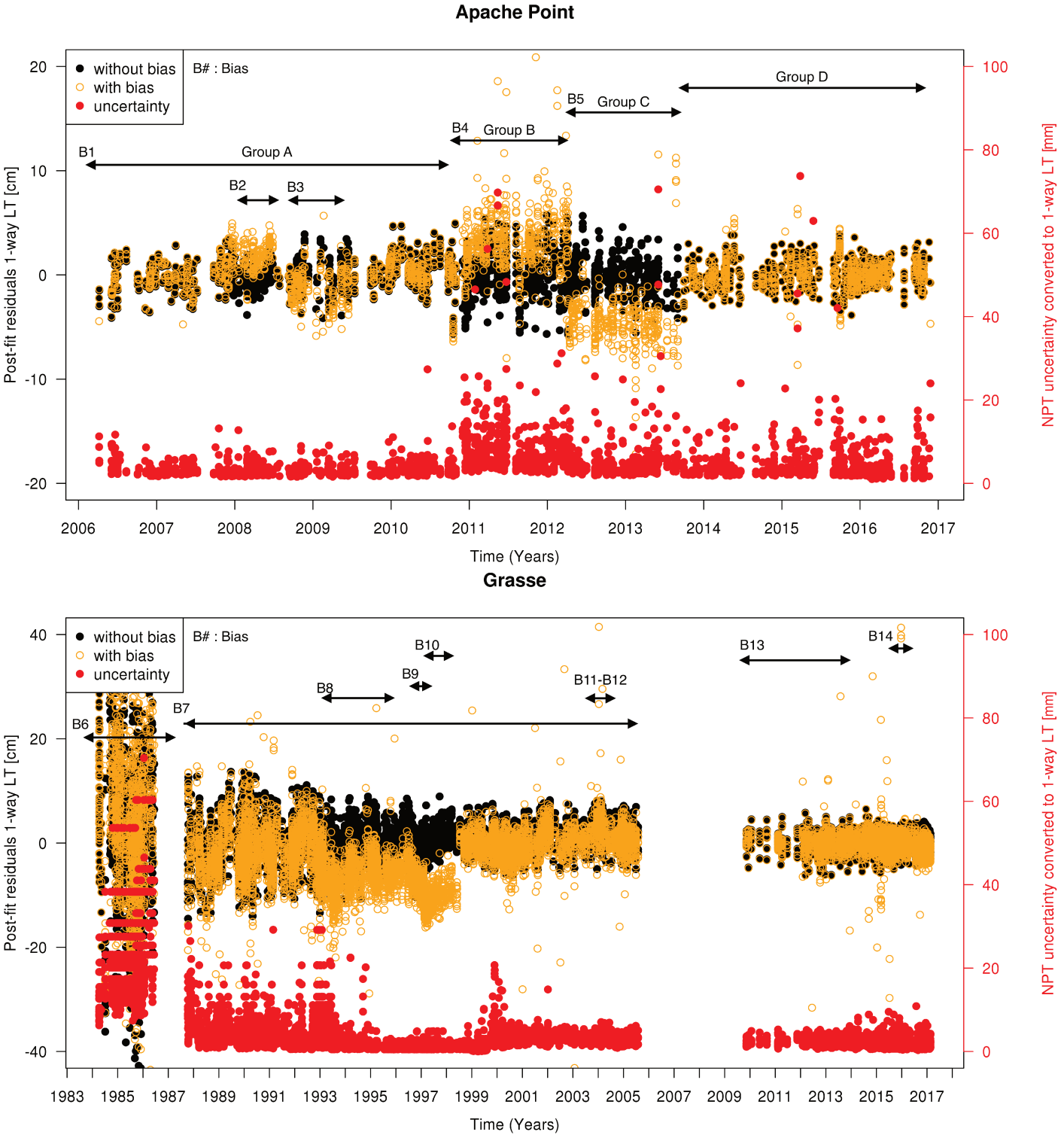

Figure 5.1: Bias correction and weight scaling requirement for LLR observations from APOLLO (top) and Grasse (bottom) stations. Points in orange and black indicate the post-fit residuals [1-way LT in cm] before and after the correction of estimated bias through LLR analysis. Bias numbering corresponds to that provided in Table (A.3). Points in red indicate the normal point uncertainty from the LLR observation after scaling. Uncertainties from Grasse station are divided by the square root of the number of echoes of each LLR normal point (as recommended), to allow comparison with the uncertainties from the APOLLO station.

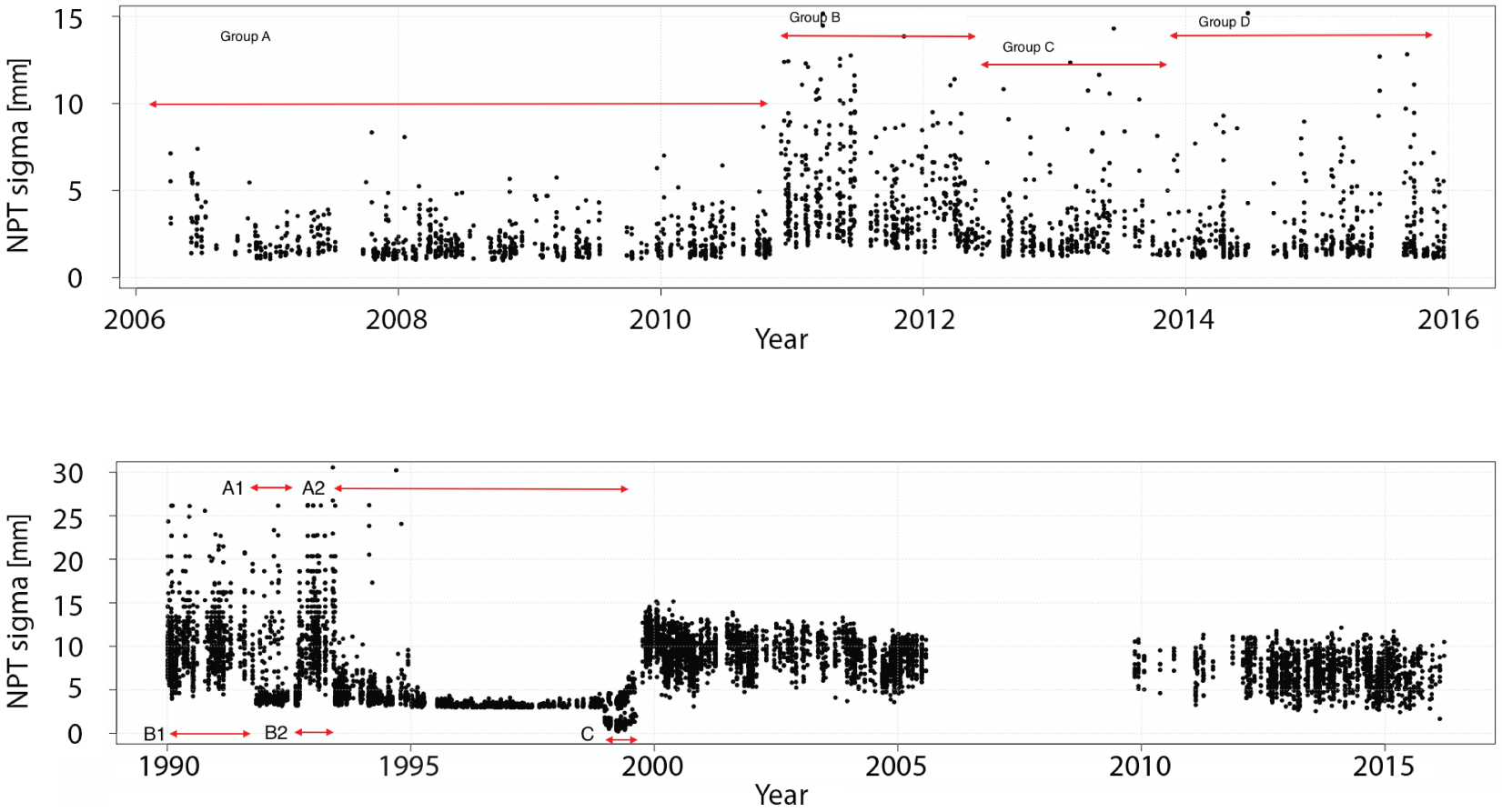

Figure 5.2: Unscaled uncertainties of LLR observations from APOLLO (top) and Grasse (bottom) stations. All the marked regions for APOLLO correspond to logged changes at the station. For Grasse station, regions - A1, A2 and C have unrealistic (near-zero) uncertainties due to suspected rejection filter scaling issues within the normal point algorithm as addressed in Section (2.2.3).

Fig. (5.1) shows the estimated biases and the uncertainties within the LLR observations from APOLLO and Grasse stations. For observations from the APOLLO station, scaling the uncertainties of the normal points depending on the change of equipments, or a change in the normal point computation algorithm, is advised. The recommended scaling of the uncertainties for APOLLO station are distributed into groups (labeled A to D within Fig. 5.1) and are made publicly available[1]. It must be noted that while APOLLO station scales down their LLR uncertainties by the square root of the corresponding number of echoes detected (Murphy et al., 2008), uncertainties from Grasse station are recommended to be manually scaled in the same manner by the user (J.M Torre, personal communication, 2017). LLR uncertainties indicated within Fig. (5.1) have been scaled down for observations from Grasse, to allow comparison. The computation of the LLR normal point and the uncertainty for Grasse station is described in Section (2.2.3).

Unrealistic uncertainties present in observations from Grasse (see Fig. 5.2), McDonald MLRS2 and Matera between time periods 1998-1999, 1996 and 2010-2012 respectively, must be rescaled before using them as weights to fit lunar ephemerides.

Annual mean adjusted weights are given in Fig. (5.3). A sudden dip in the mean weights in 1987 is due to the change of laser (Ruby to Nd:YAG) at Grasse. Mean weights between 2005 to 2010 reach a minimum due to the operation of APOLLO station in the absence of observations from Grasse during the same period. Due to these necessary adjustments, a smooth evolution on the annual mean RMS of the post-fit residuals is noticed in Fig. (2.8).

Changes at the ground station, if not accounted for within the ranging calibration procedure, introduces biases in the observations. These biases (as shown in Fig. 5.1) correspond either with a known technical development at the station (new equipment, change of optical fiber cables) or other systematics. Any estimated bias can be correlated with a corresponding change in the ground station, provided the incidents have been logged. In cases where a station log file indicating equipment changes were not available, station bias recommendations from other LLR analyses groups are followed (Pavlov et al., 2016). A list of known and detected biases are provided in Table (A.3) and shown in Fig. (5.1) for APOLLO and Grasse stations.

5.1.3 Bounded-value least square

The bounded-value least-squares (BVLS) algorithm is a generalization of the non-negative least-squares (NNLS) algorithm, that solves a least squares problem with upper and lower bounds on the variable (Lawson and Hanson, 1995; Stark and

[1] Available at http://physics.ucsd.edu/~tmurphy/apollo/151201_notes.txt

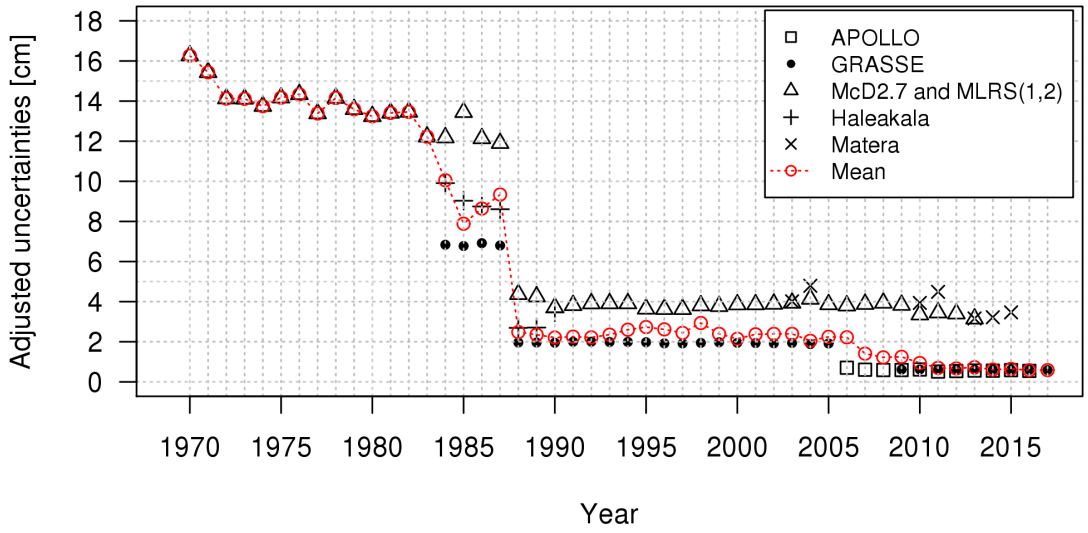

Figure 5.3: Annual mean of weights from different LLR stations after scaling the uncertainties present within LLR observation (converted to 1-way LT [cm]). The observations obtained from Grasse during 2010-2017 have an accuracy at nearly the same level as of APOLLO station.

Parker, 1995).

Given an m by n matrix, A, and a m-vector, B, BVLS computes a n-vector X that solves the least-squares problem:

$$A_{m,n} \times X_{n,1} = B_{m,1} \tag{5.2}$$

with the inequality constraints,

$$BND(1,j) \leq X(j) \leq BND(2,j), \qquad \text{with } 1 \leq j \leq n$$

For this study, a FORTRAN90 implementation of the BVLS algorithm is used. The original source code is available publicly[2].

The BVLS algorithm allows us to set constraints on parameters well-determined through other observational methods while allowing adjustments at the level of the reported uncertainties during the estimation process. The BVLS algorithm was previously used within planetary ephemeris parameter estimation (Fienga et al., 2011). It is now extended to the lunar parameter estimation (Viswanathan et al., 2017) to benefit from spacecraft-derived gravity field constraints for the Moon and the Earth (see Section 5.2.1).

[2] http://www.netlib.org/lawson-hanson/index.html

5.1.4 Uncertainty

Two sets of uncertainties are computed for each of the estimated parameters. The following section describes how the two methods (the least squares method and the re-sampling method) can be used to estimate the uncertainty of the estimated parameters. The main source of error for numerical ephemerides arise from the accuracy and biases of the observational dataset. In the case of LLR, one can notice a gradual shift of the observational accuracy from few meters since its inception to millimeter capabilities. The least-squares method provides the L2-norm as the uncertainty, while the re-sampling method highlights the differences in the goodness of fit (χ^2) to the variances and biases of the observational data set. For the LLR, the L2 norm tends to convey a more optimistic estimate due to the stability of the solution, while the re-sampling method provides realistic estimates for those parameters which have a strong dependency on the data distribution (Busing et al., 1999). These two situations are considered and hence the estimates of the uncertainties provided throughout this manuscript takes the maximum of the two methods as a more realistic uncertainty.

Least-squares method

The term $(A_{ij}^{\top} W_{ii} A_{ij})^{-1}$ in Eqn. (5.1) corresponds to the covariance matrix. For reasons of numerical stability (to avoid problems due to multicollinearity) the matrix inversion is solved by using SVD (singular value decomposition) (Press et al., 2007). In parallel, the QR decomposition (Press et al., 2007) was also tested, giving the same results as the SVD. The square root of the diagonal elements of the covariance matrix gives the standard deviation (1-σ) of each parameter during the least-squares fit.

Re-sampling method

This method of re-sampling the data set, is employed here for determining the dependency of the χ^2 of the fit to the observational accuracies and biases. By removing randomly a part of the observational sample used for the fit (Busing et al., 1999), one can estimate the robustness of the estimated parameters and a more realistic estimation of the post-fit residuals along with its χ^2 (Cook and Weisberg, 1982; Fay, 1985). The number of iterations required for the random re-sampling along with its percentage of removal was tuned manually. The percentage of data set to be re-sampled is then set at 5% (refer Fig. 5.4). A selection is performed from a uniform random distribution and removed from the original data set.

The WLS iterations are then performed on the re-sampled data set. The average deviation of the resulting estimate, away from that obtained with the full data set gives the re-sampling uncertainty.

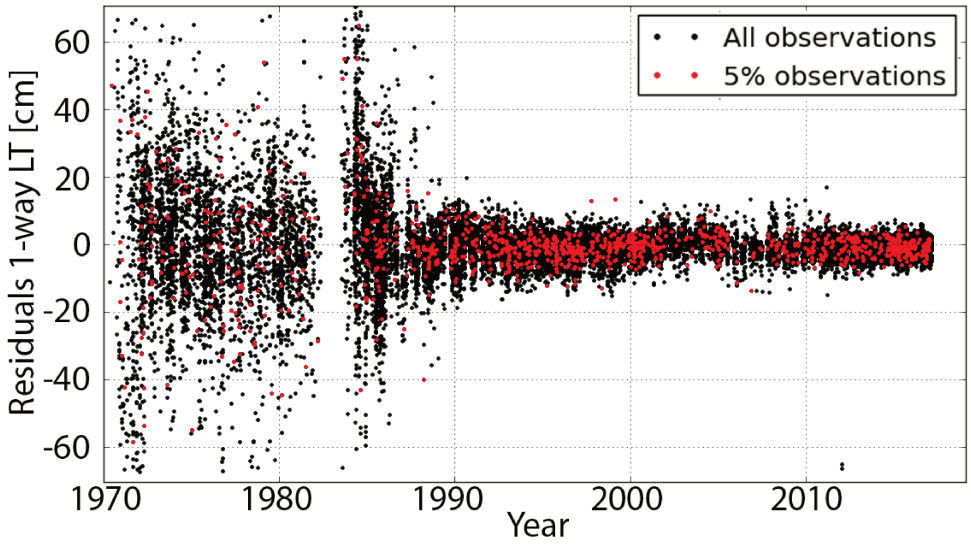

Figure 5.4: Jackknife (JK) data re-sampling with 5% of total observations removed for variance estimation. The selection is performed from a uniform random distribution (points in red).

5.2 List of fitted parameters

The following list of parameters are fitted to the LLR observations within the lunar part of INPOP ephemeris. They are categorized into two: dynamical parameters and reduction parameters.

Dynamical parameters

These parameters determine the dynamics of the Earth-Moon within the numerically integrated ephemeris. They are as follows:

- Gravitational mass of the Earth-Moon barycenter;
  GM_{EMB} determines the barycentric mass of the Earth-Moon system scaled by the gravitational constant G.

- Initial conditions of the Euler angles and the angular velocities for the Moon;
  These angles (ϕ_m, θ_m, ψ_m) correspond to the initial conditions of the time varying mantle Euler angles and their derivatives ($\dot{\phi_m}$,$\dot{\theta_m}$,$\dot{\psi_m}$) at the start of the integration time (JD 2451544.5 in TDB), defined in Section (4.3.2).

- Initial conditions of the position and the velocities for the Moon;
  These vectors correspond to the position of the Moon with respect to the

Earth in the ICRF2 frame of reference, at the start of the integration time (JD 2451544.5 in TDB).

- Initial conditions of the angular velocities for the lunar fluid core;
  This velocity vector $(\omega_{c,x}, \omega_{c,y}, \omega_{c,z})$ correspond to the angular velocity of the lunar fluid core with respect to the mantle frame.

- Polar moment of inertia of the Moon;
  C/MR^2 is the largest component of the inertia tensor of the Moon along the polar axis, defined in Section (4.3).

- Oblateness of the lunar fluid core;
  f_c is the oblateness of the lunar fluid core which characterizes the difference between the equatorial and polar diameters, defined in Section (4.4a).

- Coefficient of viscous friction at the core-mantle boundary;
  k_v is the coefficient of viscous friction that scales the dissipative effect within the Moon, due to the relative motion of the lunar mantle and the lunar fluid core at the lunar core-mantle boundary. This gives rise to a dissipative torque described in Section (4.8).

- Lunar tidal time delay;
  τ_M allows for the dissipative effect of tides by considering a delayed response acting on the Moon from both Earth and the Sun (described in Section 4.2).

- Rotational tidal time delays for the Earth;
  Similar to the lunar tidal time delay, $\tau_{R1,E}$ and $\tau_{R2,E}$ are the diurnal and semi-diurnal time delays that represent the tidal phase lag induced on the daily Earth rotation (described in Section 4.2).

- Gravity field coefficients of the Moon;
  $C_{n,m}$ and $S_{n,m}$ are the Stokes' coefficients representing the integral functions of the mass distribution inside the Moon. Their mean values are obtained from GRAIL-derived GL660b model (Konopliv et al., 2013) and are included as a constrained fit (Section 5.2.1), with the upper and lower bounds (Section 5.1.3) set to the scaled [3] uncertainties from Konopliv et al. (2013).

- Gravity field coefficients of the Earth;
  Similar to the Moon, the Earth's gravity field coefficients are taken from GGM05C Ries et al. (2016) and are included as a constrained fit (Section 5.1.3), with the provided uncertainties. A scaling factor of 20 was applied for the constrained fit (Section 5.2.1).

[3] Konopliv et al. (2013) recommends a scaling factor of 40 to the formal uncertainties.

- Potential Love number for the Moon;
  $k_{2,m}$ is the degree-2 lunar potential Love number which is included as a constrained fit (Section 5.2.1), using the mean value and scaled uncertainty from Konopliv et al. (2013).

- Equivalence principle parameter;
  The parameter $\Delta(m^G/m^I)_{EM}$ introduces an additional acceleration of the Moon with respect to the Earth, in a direction towards the Sun, due to a violation of the equivalence principle (EP). This is included as a fit parameter only for obtaining the sensitivity tests of LLR to EP (Section 6.2). In all other solutions, it is fixed to its general relativity (GR) value of 0.

Reduction parameters

These parameters are relevant to the reduction of the LLR observations. They are as follows:

- Lunar reflector coordinates;
  The coordinates of the five lunar retro-reflectors (A11, A14, A15, L1 and L2) provide their position in the seleno-centric frame of reference. The reflector coordinates are compared with that obtained from a previous release of INPOP (version 13c) in Table (A.2).

- Earth station coordinates and velocities;
  These correspond to the geocentric coordinates and velocities of the LLR stations. For some stations (Haleakala, MLRS1) only the positions are fitted, while their velocities are fixed to ITRF2005 (Altamimi et al., 2007). For Matera station, both positions and velocities are taken from the ITRF2005 values due to sparse data points. One can notice the strong correlation (correlation matrix provided in Appendix B.1) between the coordinates and their velocities for the above mentioned stations due to the lack of data span (further discussed in Section 5.2.2). MLRS2 and Grasse stations with the least correlations, provides the maximum data span, followed by APOLLO station. This enables the coordinates and velocities for these stations to be determined also from LLR analysis. The estimated coordinates and velocities for stations are compared with their ITRF2005 value in Table (A.1).

- Vertical displacement lunar Love number;
  $h_{2,M}$ is the degree-2 vertical displacement Love number for the Moon. LLR observations are sensitive to this vertical displacement, however the uncertainty is large due to only 5 retro-reflector points. Its LLR estimated value is compared with the LRO-LOLA determined value from Mazarico et al. (2014) in Table (5.5).

- Bias parameters; These correspond to station specific parameters intended to absorb the impact of local equipment changes. A list of the station biases estimated is provided with the corresponding time period in Table (A.3).

5.2.1 Constraints

During the LLR estimation process, while some parameters have strong sensitivity (5.2) to LLR observations, others maybe better determined through another technique. The level of sensitivity of a parameter is determined through the impact of the mean-value of the parameter on the Earth-Moon distance. If the amplitude of the effect translates to an uncertainty in the Earth-Moon distance below few mm (at the limit of LLR observational accuracy), the parameter maybe weakly determined due to the current accuracy of the LLR observations. The plot of the partial derivatives given in Appendix (B.1) can be helpful to arrive at this decision. In cases where the parameters fall below this threshold, a constraint is attributed to each weakly determined parameter (for instance, $C_{(4,0),E}$) during the estimation process, from externally derived estimates.

Some other parameters may show high sensitivity (for instance the gravity field of the Earth and Moon). However this is not the only requirement to be well-determined by LLR analysis. This is because they have strong correlation between the different degree/order of the spherical harmonics which is hard to resolve considering only the distance measurement towards the mean-Earth direction used in LLR analyses. Hence, estimates from spacecraft-derived gravity field measurements provides synergy to the LLR analysis in terms of spherical harmonics both for the Earth and the Moon.

For the lunar gravity field model, the study relies on estimates derived from observations by the GRAIL mission, from Konopliv et al. (2013). A variability at the level of the uncertainty of the determined parameters is set with the help of the BVLS algorithm (Section 5.1.3) in the LLR analysis. Due to some unmodeled effects present in the lunar dynamical model, the constraints on few of the degree-3 spherical harmonic coefficients of the lunar gravity field (C_{32},S_{32} and C_{33}) are kept unbounded for improving the LLR post-fit residual (Williams et al., 2014b; Pavlov et al., 2016). Recent JPL LLR model attempts to fit 7 third-degree gravity field coefficients (Williams and Boggs, 2015a). On the other hand, a discussion on the attempts to identify the source of this effect is provided in Section (6.1.1).

5.2.2 Correlation

Signatures from some parameters in the model maybe absorbed by others during the least-squares fit. For instance, the Earth-Moon mass ratio EMRAT and GM_{EMB} have similar signatures on the Earth-Moon distance (see plot of partials

in Appendix B.2). Moreover, these two parameters are difficult to be separated during the fit, using LLR observations alone. This is partly also due to the lesser sensitivity of LLR observations to $EMRAT$. Hence, the estimate of $EMRAT$ is performed routinely during the joint fits of the planetary ephemeris (Fienga, 1999) which rely on a multitude of observations such as, astrometry, space-craft range and doppler, VLBI, etc.

Another example is the fit of extended parameters of the lunar fluid core. C_{20} of the fluid core is expressed in terms of the core flattening (f_c) so as to improve the inversion of the moment of inertia matrix (I_c) in Eqn. (4.7) while solving the differential equation for the angular velocity of fluid core. Moreover, the value of f_c is sensitive to the choice of the ratio of the polar moment of inertia of the fluid core to that of the Moon (α_c) (Section 5.3). Hence, α_c is fixed to a model value (Williams et al., 2014b). And through Eqn. (4.1), $f_c \cdot \alpha$ value is determined better than f_c itself.

Strong correlations between the spherical harmonic coefficients of the lunar gravity field are noticed. This is overcome by either fixing them to known values or by applying constraints (Section 5.2.1) during the least-squares fit. A similar approach is also followed for the zonal harmonic coefficients and ocean tidal time lags for the Earth.

Station coordinates and velocities are well determined with the help of an extensive geodetic technique. Since, LLR falls short of a worldwide network of stations due to the complexity of ranging to the Moon, ITRF solutions do not include LLR observations while resolving station positions (Z. Altamimi, personal communication, 2016). Hence, in cases where a longer time span of LLR data is available, the station positions and velocities are fit to LLR data. Table (A.1) provides the estimated station position and velocities. Resolving the station coordinates using LLR observations requires ranging at very low elevation angles. This is difficult due to the increased dispersion of photons while the laser pulse travels through a greater length of the atmosphere.

The reflector coordinates are fitted to the LLR observations. The estimates for which have been provided in Table (A.2). Strong correlations between the reflector coordinates exist, making the reflector coordinate resolution uncertain to the level of few cm at 1-σ. Observationally, this can be overcome by successive ranging attempts to multiple reflectors, while minimizing the time interval between them.

Fixed-values corresponding to the Earth (Table 5.1) are taken from the recommendations of Petit and Luzum (2010), when available. Potential love numbers ($k_{2m,E}$) are obtained from Petit and Luzum (2010, Table 6.3) followed by corrections from the ocean model FES2004 (Lyard et al., 2006) accounting for most influential tides (Williams and Boggs, 2016, Table 6). The orbital phase lag $\tau_{Om,E}$ values are taken from Pavlov et al. (2016), which were derived by J. Williams (D.

Pavlov, personal communication, 2017). α_C and l_2 are fixed to model recommendations from Williams et al. (2014b). This is due to the strong correlation of α_C with the polar moment of inertia of the Moon, and the inability of LLR to simultaneously resolve l_2 the horizontal displacement love number and the reflector position coordinates in the same plane. The parameter EMRAT is determined through a joint analysis between the lunar and planetary part of the INPOP ephemeris. A list of fixed parameters for the Earth-Moon system is given in Table (5.1).

Table 5.1: Fixed parameters for the Earth-Moon system.

Parameter	**Units**	**INPOP13c** Fienga et al. (2014)	**INPOP17a** Viswanathan et al. (2017)	**DE430** Williams et al. (2013)	**EPM**$^{\square}$ Pavlov et al. (2016)
$(EMRAT^{\dagger} - 81.300570) \times 10^6$		-0.54	1.87	-0.92	-0.92 (fixed)
$(R_E - 6378.1366) \times 10^4$	km	0.0	0.0	-3	-3 (assumed)
$(\dot{J}_{2E} - 2.6 \times 10^{-11})$	year^{-1}	0.4	0.0	0.0	0.0
$(k_{20,E} - 0.335)$		-0.0331	0.0	0.0	0.0
$(k_{21,E} - 0.32)$		-0.0217	0.0	0.0	0.0
$(k_{22,E} - 0.30102)$		0.0	-0.01902	0.01898	-0.01902
$(\tau_{O0,E} - 7.8 \times 10^{-2}) \times 10^2$	day	*	0.0	-1.4	0.0
$(\tau_{O1,E} + 4.4 \times 10^{-2})$	day	*	0.0	0.0‡	0.0
$(\tau_{O2,E} + 1.13 \times 10^{-1}) \times 10^1$	day	*	0.0	0.13	0.0
$(R_M - 1738.0)$	km	0.0	0.0	0.0	0.0
$(\alpha_C - 7.0 \times 10^{-4})$		-	0.0	0.0	0.0
$(k_{2,M} - 0.024059) \times 10^3$		2.2	0.0	0.0	0.0
$(l_2 - 0.0107)$		0.0	0.0	0.0	0.0

†: EMRAT is fit during the joint analysis between the lunar and planetary part.
‡: $\tau_{O1,E}$ in Folkner et al. (2014) given as -0.0044 is a typographical error (J.G. Williams, personal communication, 2017).
* : INPOP13c uses only two time delays (d^{-1}) for the Earth ($\tau_{21,E} = 1.239 \times 10^{-2}$ and $\tau_{22,E} = 6.9768 \times 10^{-3}$)
$\square$: refer to the Solution I in Pavlov et al. (2016)

5.3 Results

In this section we discuss the results obtained with the new lunar dynamical model of the planetary and lunar ephemeris INPOP17a (Viswanathan et al., 2017). The parameter estimates and the post-fit residuals are compared with the results obtained with the previous release - INPOP13c (Fienga et al., 2014), the JPL ephemeris - DE430 (Williams et al., 2013) and the IAA RAS ephemeris - EPM2016 (Pavlov et al., 2016). We also study the impact of not including the IR LLR data taken into account for INPOP17a as a way to monitor the improvement brought by IR wavelength compared to Green data.

5.3.1 INPOP13c vs INPOP17a

This section compares the estimates and the post-fit residuals between the solutions INPOP13c (Fienga et al., 2014) and INPOP17a (Viswanathan et al., 2017). The changes between these two solutions in terms of the dynamical modeling is discussed in Section (4.1). In addition, INPOP17a includes 3 years of LLR data (2014-2016) from APOLLO, Grasse (including Green and IR data sets), Matera and MLRS2 stations. The gravity field of the Moon used within the dynamical model of INPOP17a was updated from the model coefficients of LP150Q (Konopliv et al. (2001)) to that of GL0660b (Konopliv et al. (2013)). The DE430 time delay model for the tides was updated with 5 time delays (Section 4.2) for INPOP17a.

Comparison of estimates: INPOP13c vs INPOP17a

A description of the procedure used to fit the INPOP13c ephemeris can be found in Manche (2011, p. 121). A major difference in the fit procedure between the two independent analyses is that, INPOP17a uses a bounded-value approach (further described in Section 5.1.3) to constrain correlated parameters (Section 5.2.2) without removing parameters from the fit during successive iterations. On the other hand, INPOP13c solution followed several selection criteria to include parameters into the fit during iterations, where the decision is based on the adjustment of the parameter relative to its uncertainty, degradation of residuals and correlated parameters (Manche, 2011, p. 126).

Table (5.2) provides the major differences in estimated parameters from the two solutions (INPOP13c and INPOP17a). With the new solution, a reduction of the parameter GM_{EMB} is noticed. The geocentric distance of the Moon obtained with the two solutions and DE430 (Folkner et al. (2014)) is compared in Fig.5.5, indicating a reduction in the radial difference from ~2.5 m in INPOP13c to ~0.19 m in INPOP17a. The reduction in the bias is a direct consequence of the reduction in the estimate of GM_{EMB}. A radial difference of ~0.25 m is also noticed between

Table 5.2: Comparison of extended body parameters of solution: INPOP13c vs INPOP17a. Fitted parameters are indicated with their corresponding formal uncertainties (1-σ)

Parameter	**Units**	**INPOP13c**	**INPOP17a**
$(GM_{EMB} - 8.997011400 \times 10^{-10}) \times 10^{19}$	AU^3/day^2	173 ± 9	4 ± 2
$(C_T/(m_M R^2) - 0.393140) \times 10^6$		−122.2 ± 26	8.2 ± 0.2
$(C_{32} - 4.8404981 \times 10^{-6}) \times 10^9$		4.7	3.9 ± 0.3
$(S_{32} - 1.6661414 \times 10^{-6}) \times 10^8$		2 ± 0.049	1.666 ± 0.006
$(C_{33} - 1.7116596 \times 10^{-6}) \times 10^8$		0.8 ± 0.59	-2.40 ± 0.04
$(\tau_M - 9 \times 10^{-2}) \times 10^4$	day	1012 ± 12	-35 ± 3
$(\frac{k_v}{C_T} - 1.6 \times 10^{-8}) \times 10^{10}$	day^{-1}	-	15.3 ± 0.5
$(f_c - 2.1 \times 10^{-4}) \times 10^6$		-	42 ± 3
$(h_2 - 3.71 \times 10^{-2}) \times 10^3$		15.5 ± 2.4	6.8± 0.2

solutions DE430 and DE421 (Williams et al., 2013, Fig. 1). This indicates the consistency of the lunar orbit obtained with INPOP17a and other teams (see Section 5.3.3).

With the introduction of the lunar fluid core, the estimate of the total polar moment of inertia of Moon ($C_T/m_M R^2$) has increased. Dissipation at the core-mantle boundary is introduced through the coefficient of viscous friction ($\frac{k_v}{C_T}$) which is now a solution parameter. The estimate of the polar flattening f_c is sensitive to the choice of the term α_c (the ratio of the fluid core polar moment of inertia C_c to the undistorted polar moment of inertia of the Moon C_T) fixed as 7×10^{-4}. The new estimate of the lunar vertical displacement Love number h_2 is closer to estimates from Mazarico et al. (2014). An overall improvement in the estimated uncertainty is also noticed.

With the improved lunar interior modeling, the comparison of the Euler angle rates in Fig. (5.6), becomes closer to the corresponding values from DE430. Small differences of few milliseconds of arc remain due to the absence of empirical periodic correction terms in the longitude libration model of INPOP17a, which is present in DE430 (Williams et al., 2013, p. 9).

Comparison of post-fit residuals: INPOP13c vs INPOP17a

The statistics of the post-fit residuals (in cm of wrms) between the two solutions are provided in Table (5.3). An overall improvement in the post-fit residuals is noticed after the introduction of the lunar fluid core in INPOP17a. The major improvement comes from the correction of a programming error within the implementation of the lunar fluid core angular momentum equation within INPOP13c

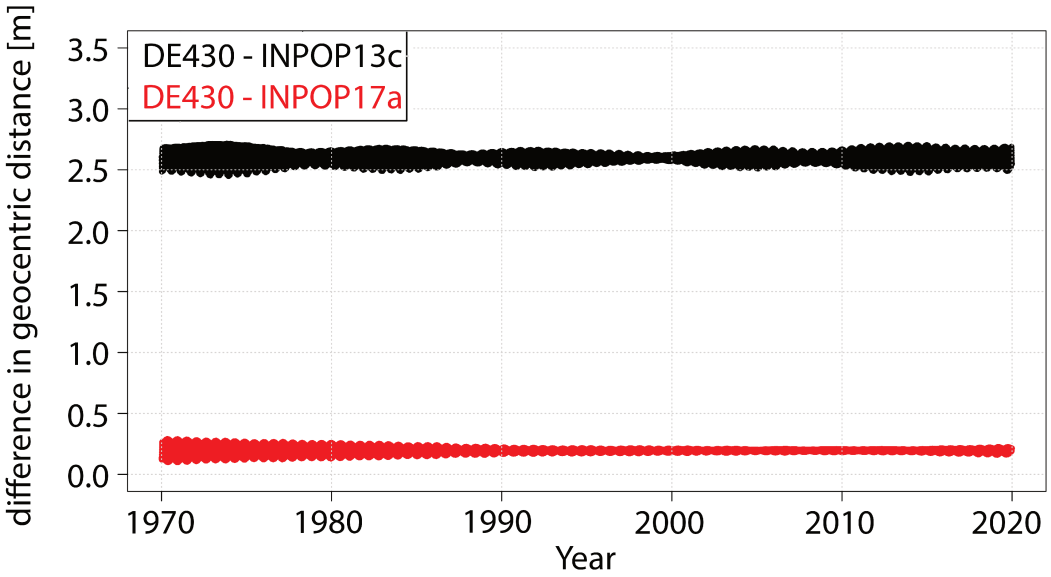

Figure 5.5: Comparison of differences in geocentric distance of the Moon (in m) with DE430 using a) INPOP13c (in black) and b) INPOP17a (in red). The reduction in the radial differences is due to the reduction of the estimated parameter GM_{EMB}, indicating a more consistent estimate with DE430 (Williams et al., 2013).

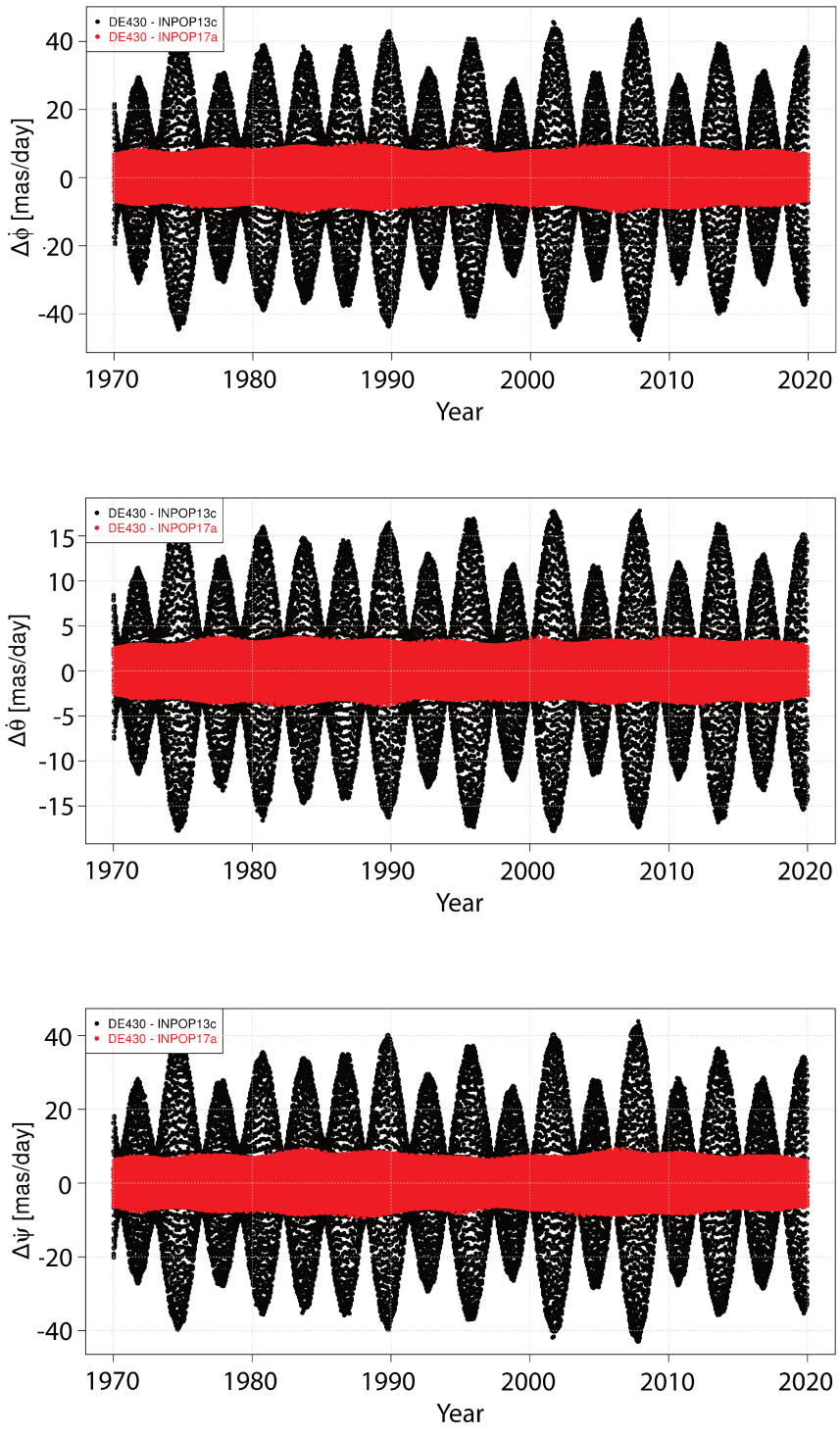

Figure 5.6: Comparison of differences in lunar Euler angle rates (where $\dot{\phi}$: rate of precession angle, $\dot{\theta}$: rate of nutation angle and $\dot{\psi}$: rate of rotation angle) with DE430 using a) INPOP13c (in black) and b) INPOP17a (in red).

(see Section 4.1). A small annual variation is visible across post-fit residuals from all stations in INPOP17a due to the improved residuals (see Fig. 5.7). This signature corresponds to inaccuracies in the longitude libration modeling of the Moon. Williams et al. (2013); Pavlov et al. (2016) empirically correct this signature using supplementary periodic correction terms to the longitude libration of the Moon. None of the INPOP solutions rely on empirical corrections.

For the common dataset used between the two models, the improvements in the post-fit residuals have an average of: a factor 4 for observations from APOLLO , a factor 3 for observations from Matera and a factor 2 for observations from Grasse. The improvement reaches up to a factor 5 and a factor 4 on the post-fit residuals obtained for the recent observations of high accuracy from APOLLO and Grasse stations respectively. Post-fit residuals obtained on older periods prior to 1984 are improved from using the JPL KEOF (Ratcliff and Gross, 2015) EOPs in the reduction model as recommended by Pavlov et al. (2016). Beyond the common fit data span, the post-fit residuals continue to exhibit small residuals at the level of 1.15 cm and 1.47 cm for high quality observations from APOLLO and Grasse stations, respectively.

Table 5.3: Comparison of post-fit residuals of LLR observations from ground stations with corresponding time span, number of normal points available, number of normal points used in each solution after a 3-σ rejection filter. The WRMS (in cm) is obtained with solutions INPOP13c (1969-2013) and INPOP17a (1969-2017). ‡: Statistics drawn from Fienga et al. (2014)

Code	**Station**	**Time span**		**INPOP13c‡**		**INPOP17a**	
			Available	**Used**	**WRMS**	**Used**	**WRMS**
					[cm]		[cm]
70610	APOLLO, NM, USA (group A)	2006 - 2010	941	940	4.92	929	1.27
70610	APOLLO, NM, USA (group B)	2010 - 2012	506	414	6.61	486	1.95
70610	APOLLO, NM, USA (re-group C)	2012 - 2013	361	359	7.62	345	1.52
70610	APOLLO, NM, USA (group D)	2013 - 2016	832	-	-	800	1.15
01910	Grasse, FR	1984 - 1986	1187	1161	16.02	1161	14.01
01910	Grasse, FR	1987 - 1995	3443	3411	6.58	3407	4.11
01910	Grasse, FR	1995 - 2006	4881	4845	3.97	4754	2.86
01910	Grasse, FR	2009 - 2013	999	990	6.08	982	1.41
01910	Grasse, FR	2013 - 2017	2553	-	-	2542	1.47
56610	Haleakala, HI, USA	1984 - 1990	770	739	8.63	728	4.80
07941	Matera, IT	2003 - 2013	83	70	7.62	37	2.37
07941	Matera, IT	2013 - 2015	30	-	-	28	2.93
71110	McDonald, TX, USA	1969 - 1983	3410	3302	31.86	3246	18.87
71110	McDonald, TX, USA	1983 - 1986	194	182	20.60	148	16.77
71111	MLRS1, TX, USA	1983 - 1984	44	44	29.43	44	32.73
71111	MLRS1, TX, USA	1984 - 1985	368	358	77.25	356	62.58
71111	MLRS1, TX, USA	1985 - 1988	219	207	7.79	202	11.07
71112	MLRS2, TX, USA	1988 - 1996	1199	1166	5.36	1162	3.81
71112	MLRS2, TX, USA	1996 - 2012	2454	1972	5.81	1939	3.72
71112	MLRS2, TX, USA	2012 - 2015	17	-	-	15	2.59
	TOTAL			**20160**		**23311**	

5.3.2 INPOP17a vs INPOP$_G$

INPOP$_G$ refers to an internal solution with the same dynamical model specifications as of INPOP17a, but without the addition of two years of the new IR LLR observations (Courde et al., 2017). This allows the separation of the improvements brought by the IR LLR data from the overall improvement noticed in Section (5.3.1).

The IR LLR dataset constitutes 1707 normal points (7% of the total LLR data till date) from 2 years of operation in IR (1064 nm) wavelength at the LLR station in Grasse[4]. A review of the technical developments and accuracy of this new dataset can be found in Courde et al. (2017). The homogeneity in the distribution (both spatial and temporal domains) of IR LLR data is described in Section (2.3). This dataset is weighted at the same level of accuracy as the APOLLO station normal points during the estimation procedure (see Section 5.1.2).

Comparison of estimates: INPOP17a vs INPOP$_G$

The improvement brought by the addition of IR data on the estimated parameters characterizing the Moon and its inner structure is currently not massive (see Table 5.5). This is because of the relatively short time span of IR LLR data (2 years) compared to the remaining (47 years) historical LLR data. However, since the observations have a better temporal distribution in terms of the lunar phase, an improvement in the uncertainty of the parameter $(\Delta(m^G/m^I)_{EM})$ is expected with the prolongation of IR data in the near future. This is because tests of equivalence principle (Section 6.2) have maximum sensitivity during the new and the full Moon, where the past LLR data have been sparse (described in Section 2.3.1). With the help of the 2 years of IR LLR data, the improvement on the uncertainty of the EP parameter is about 15%, as provided in Table (6.2). With a larger time span of IR LLR data, we expect the spatial improvements (Section 2.3.2) to impact the present imperfections of the dynamical model of the lunar interior (Section 6.1.1) under the constraints of a high accuracy lunar gravity field.

Comparison of post-fit residuals: INPOP17a vs INPOP$_G$

With the increase of normal points obtained for the L1 reflector (as discussed in Section 2.3.2), the reflector-wise distribution of LLR data becomes more homogeneous, as shown in Fig. (2.8) and Fig. (2.9). This improves the post-fit residuals obtained for L1 reflector (by 23 % for Grasse) as given in Table (5.4). The effect of reduction in the spatial distribution bias on the model, brought by the new

[4]This data is made publicly available on http://www.geoazur.fr/astrogeo/?href=observations/donnees/luneRG/brutes

IR LLR data from Grasse, can be also seen on the improvement of L1 post-fit residuals from other stations. Table (5.4) highlights this improvement on the L1 post-fit residuals of APOLLO station (by 15%).

Table 5.4: Reflector-wise statistics computed using residuals obtained with INPOP_G and INPOP17a, within the fit intervals 01/01/2015 to 01/01/2017 (with a 3-σ filter), with the WRMS in m (RMS weighted by number of observation from each reflector). Refer to Section (5.3.2) for the description of the solutions.

	Grasse				**APOLLO**			
LRRR	**INPOP_G**	**INPOP17a**	**% change**	**NPTs**	**INPOP_G**	**INPOP17a**	**% change**	**NPTs**
A15	0.0183	0.0181	1.1	1018	0.0127	0.0127	0.2	344
A14	0.0203	0.0177	12.8	172	0.0192	0.0177	7.8	176
A11	0.0267	0.0239	10.5	215	0.0185	0.0169	8.7	164
L1	0.0215	0.0166	**22.8**	265	0.0186	0.0157	**15.6**	89
L2	0.0246	0.0215	12.6	256	0.0136	0.0137	-0.7	64
WRMS	0.0207	0.0189	**TOTAL:**	1926	0.0159	0.0149	**TOTAL:**	837

5.3.3 INPOP17a vs DE430 and EPM2016

This section compares the estimates of INPOP17a (Viswanathan et al., 2017) with that from other independent LLR analyses groups (Williams et al., 2013; Pavlov et al., 2016). The modeling followed by the three groups are similar. However there exist differences between them, which include: number of fitted parameters (102 for INPOP17a, 102 for EPM and about 109 for DE430), constraints applied to the parameters during the fit, independent adjustments to the weighting scheme used for the fit, empirical corrections to longitude librations to absorb unmodeled effects, iterative rejection scheme, etc. Some of these differences are kept internal to the analyses groups and hence requires internal communication for a one to one comparison. (D. Pavlov, personal communication, 2017) provided some of the additions and bug-fixes to the work within Pavlov et al. (2016), involving extended LLR time span, correction of error within ocean loading model, bias additions for Grasse and adjustment of under-weighted Grasse observations.

Comparison of estimates: INPOP17a vs DE430 and EPM2016

Table (5.1) provides few of the fixed parameters of the above mentioned LLR analyses groups relevant to the lunar dynamical modeling. For EPM, the solution used for comparison is Pavlov et al. (2016, Solution I).The parameter EMRAT is a result of the joint iteration between the lunar and planetary parts of the ephemeris. This approach of the joint iteration is also followed by DE430 ephemeris (Williams et al., 2013; Folkner et al., 2014). Pavlov et al. (2016) use the value from DE430 for EMRAT throughout the LLR analysis.

Folkner et al. (2014); Williams et al. (2013) and Pavlov et al. (2016) use EGM2008 (Pavlis et al., 2008) as the Earth's gravity field model. INPOP17a uses a more recent gravity field model GGM05C (Ries et al., 2016) scaled to the equatorial radius (R_E) of the Earth taken from Petit and Luzum (2010, p. 18). R_E from EGM2008/GGM05C is 0.3 m smaller than that given in Petit and Luzum (2010, p. 18). The values of $k_{22,E}$ and $\tau_{O2,E}$ were chosen to be closer to a more recent study (Williams and Boggs, 2016; Pavlov et al., 2016) than Williams et al. (2013).

Table (5.5) provides the estimates of the extended parameters of the Earth-Moon system from the LLR analyses groups under comparison. Overall, the estimates from INPOP17a lie within the error bars from DE430. The value of $\tau_{R1,E}$ is consistent with DE430, but inconsistent with EPM2016, presumably due to the communicated ocean tides modeling error in Pavlov et al. (2016). $\tau_{R2,E}$ is closer to EPM2016 than DE430 due to: the use of recent values of $k_{22,E}$ and $\tau_{O2,E}$ from Williams and Boggs (2016); Pavlov et al. (2016); and, has a smaller impact from the modeling error in Pavlov et al. (2016) on the semi-diurnal tidal time delay

$\tau_{R2,E}$ (from M2 and N2 ocean tides), than on the diurnal tidal time delay $\tau_{R1,E}$ (from O1 and Q1 ocean tides) considering the amplitude of the tidal delays within Williams and Boggs (2016, Table 6).

The uncertainty reported in INPOP17a on the $C_T/(m_m R^2)$ is about 10 times smaller than from DE430 and EPM2016 due to the use of C_{22} from GRAIL (Konopliv et al., 2013) as a constraint with the help of Eqn. (4.3), thereby reducing the degree of freedom from the solution than when using libration β and γ as solution parameters. The result is that the one could separate the annual dissipation component from that induced by the additional degree of freedom of the solution mimicking similar signatures. Although this makes the solution rely strongly on the spacecraft-derived gravity field at degree-2, it also helps to reveal modeling inconsistencies at higher degrees as shown in Section (6.1.1).

Three of the degree-3 coefficients (C_{32}, S_{32} and C_{33}) are included as unconstrained fitted parameters (Section 5.2.1) as a method to absorb modeling inconsistencies (Section 6.1.1). This approach is also followed by Williams et al. (2013); Pavlov et al. (2016). We follow the same approach only to facilitate the comparison of estimates and post-fit residual, while providing a discussion on the attempts to improve the lunar dynamical model (refer Section 6.1.1). The estimated degree-3 coefficient in Table (5.5) are marginally closer to GRAIL solution (Konopliv et al., 2013) than DE430 or EPM2016. This could be due to the constraint applied on degree-2 using Eqn. (4.3). The LLR estimated C_{32} differences found by the different LLR analyses teams from the gravity field provided by Konopliv et al. (2013) have the same magnitude as those between a previous lunar gravity field model (LP150Q: Konopliv et al. (2001)) and GRAIL (GL0660b: Konopliv et al. (2013)). However, differences on other degree-3 gravity field coefficients (S_{32} and C_{33}) are an order greater. The reasons behind these discrepancies are discussed in Section 6.1.1.

Other estimates from INPOP17a, linked to the dissipation (τ and k_v/C_T) and core flattening (f_c) are also within the uncertainties provided by DE430. However, these estimates are linked with the choice of the value of core fraction (α_c), currently fixed to 7×10^{-4} (Folkner et al., 2014).

INPOP17a solution does not fit any additional parameters to empirically correct for unmodeled libration in longitude such as in Williams et al. (2013, Eqn. 1) and Pavlov et al. (2016). Williams et al. (2008) mention that a rotation in longitude would be very sensitive to the gravity field coefficients. Moreover, the absence of higher-degree torques as in the dynamical model, can be masked by small adjustments to gravity field (Cappallo, 1980, Appendix E.2). Hence, we prefer to introduce minimum adjustments to the GRAIL-derived gravity field and to identify the shortcomings of the current lunar model which causes this unmodeled libration. By doing this we open the grounds for further research using LLR by

disentangling similar signatures noticed on the lunar libration arising from the lunar interior. Some of the missing higher-degree torques within the DE430 model (Folkner et al., 2014) were identified and implemented within an internal solution of INPOP. The results of introducing a more complete torque up to degree-3 components of the gravity field (Section 6.1.2) show small improvements in the residuals, while the inconsistencies in the estimates remain.

Table 5.5: Extended body parameters for the Earth and the Moon. Uncertainties for INPOP_G and INPOP17a (1-σ) are obtained from a 5% jackknife (JK). DE430 uncertainties seem to be inflated (unknown scaling) formal uncertainties and EPM solutions provide the 1-σ formal uncertainties. †: C_{32}, S_{32} and C_{33} are reference values from the GRAIL analysis by Konopliv et al. (2013). ‡: h_2 reference value from LRO-LOLA analysis by Mazarico et al. (2014). * : derived quantity. Refer to Section 5.3.2 for the description of the solution INPOP_G

Parameter	**Units**	**INPOP_G**	**INPOP17a**	**DE430**	**EPM**
$(GM_{EMB} - 8.997011400 \times 10^{-10}) \times 10^{19}$	AU^3/day^2	4 ± 2	4 ± 2	-10	10 ± 5
$(\tau_{R1,E} - 7.3 \times 10^{-3}) \times 10^5$	day	0 ± 4	6 ± 3	6 ± 30	57 ± 5
$(\tau_{R2,E} - 2.8 \times 10^{-3}) \times 10^5$	day	9.2 ± 0.4	8.7 ± 0.3	-27 ± 2	5.5 ± 0.4
$(C_T/(m_M R^2) - 0.393140) \times 10^6$		6.9 ± 0.2	8.2 ± 0.2	$2^\star$	$2^\star$
$(C_{32} - 4.8404981 \times 10^{-6\dagger}) \times 10^9$		4.1 ± 0.3	3.9 ± 0.3	4.4	4.4 ± 0.1
$(S_{32} - 1.6661414 \times 10^{-6\dagger}) \times 10^8$		1.707 ± 0.006	1.666 ± 0.006	1.84	1.84 ± 0.02
$(C_{33} - 1.7116596 \times 10^{-6\dagger}) \times 10^8$		-1.19 ± 0.04	-2.40 ± 0.04	-3.6	-4.2 ± 0.2
$(\tau_M - 9 \times 10^{-2}) \times 10^4$	day	-14 ± 5	-35 ± 3	58.0 ± 100	60 ± 10
$(\frac{k_v}{C_T} - 1.6 \times 10^{-8}) \times 10^{10}$	day^{-1}	12.7 ± 0.4	15.3 ± 0.5	4.0 ± 10.0	3.0 ± 2.0
$(f_c - 2.1 \times 10^{-4}) \times 10^6$		37 ± 3	42 ± 3	36 ± 28	37 ± 4
$(h_2 - 3.71 \times 10^{-2\ddagger}) \times 10^3$		6.3 ± 0.2	6.8 ± 0.2	11.0 ± 6	6 ± 1
$Q_{27.212} - 45$ (derived)		3.9 ± 0.5	5.0 ± 0.2	0 ± 5	0 ± 1

Comparison of residuals: INPOP17a vs DE430 and EPM2016

As one can see on Fig. (5.7), the overall post-fit residuals obtained using INPOP17a indicate that its model accuracy is at par with other lunar ephemeris such as DE430 and EPM2016. After a successful fit of the model to the observations, ideally the residuals should only carry the observational uncertainties. Deficiencies in the model, if above the observational uncertainties, would be visible in the post-fit residuals. An annual signature is present on all reflectors arising from inconsistencies of the lunar longitude libration model. Williams et al. (2013) suggest the poor performance of the lunar time delay model for this annual term and recommend the introduction of an empirical term ($\cos l'$). The amplitude of this effect is about 5 mas for longitude libration or about 1.5 cm in range. Another suggested empirical correction term for the lunar rotational dissipation model with a period of 6 years ($F-l$) would be only at about 1 mas or about 3 mm in range (Williams et al., 2001), which is insufficient to explain the 5 cm model inconsistency for degree-3 gravity field discrepancy found in Section (6.1.1).

Figure 5.7: Post-fit residuals in (cm) vs time (year) obtained with INPOP17a for : a) GRASSE station with the 532 nm wavelength, b) GRASSE station with the 1064 nm wavelength, c) McDonald, MLRS1, MLRS2, Haleakala and Matera stations, d) APOLLO station. Post-fit residuals here are filtered at 5-σ.

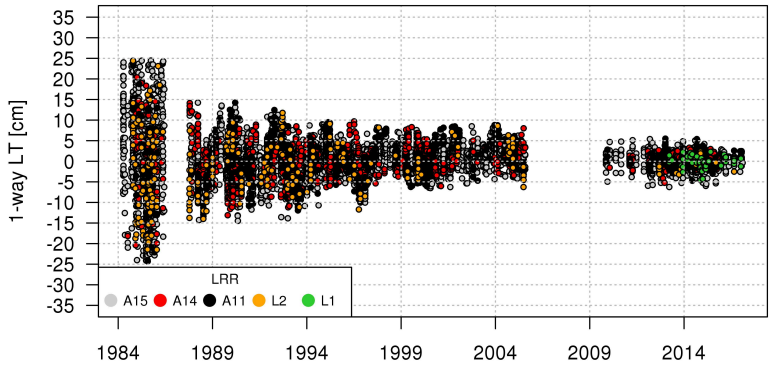

a) GRASSE station with the 532 nm wavelength

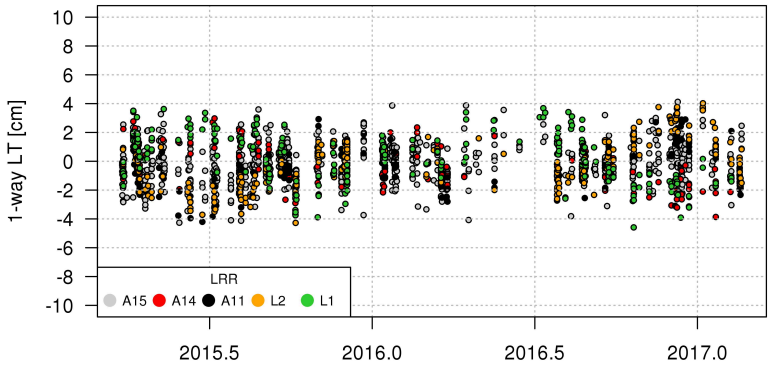

b) GRASSE station with the 1064 nm wavelength

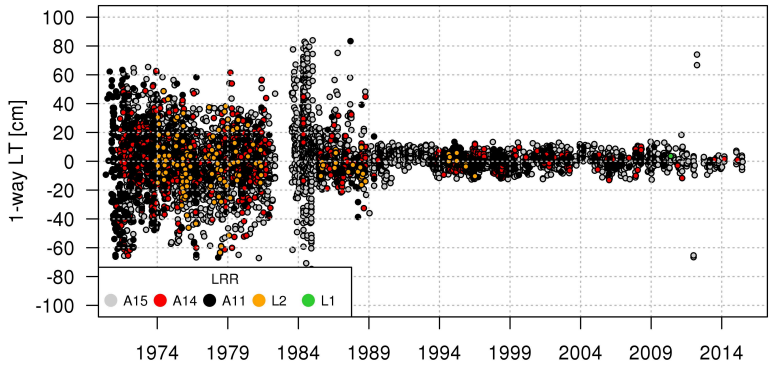

c) McDonald, MLRS1, MLRS2, Haleakala and Matera stations

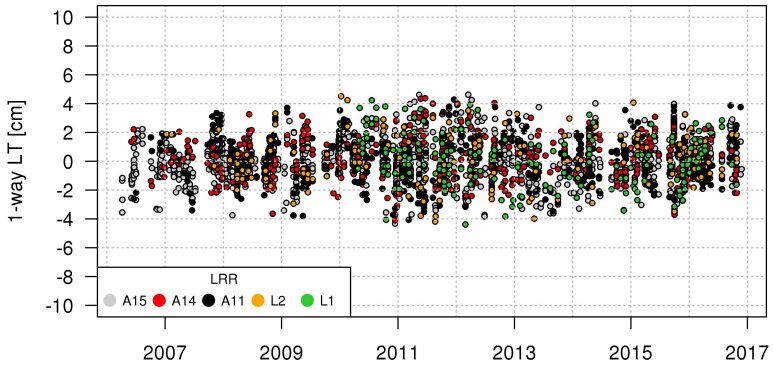

d) APOLLO station

Chapter summary

A successful fit of the lunar ephemeris to LLR observations requires attention to detail from several key points. Few of these points include the identification and correction to: irregularities in the uncertainty of each LLR observation, biases in the observation, regression procedure limitations and parameter uncertainty computation and its interpretation. Constraints to fit parameters are used when a better accurate estimate is available. The new estimates and post-fit residuals are compared with that obtained by other independent LLR analyses groups. The following chapter (Chapter 6) focuses on the extraction of scientific values from the analysis/estimates provided within this chapter.

Chapter 6

Applications

The application of lunar laser ranging observations and its analyses covers a wide range of scientific disciplines like lunar science, gravitation, geophysics and geodesy. After the first seven years of operation, a collection of scientific articles pertaining to these disciplines were put together as proceedings (Ewing, 1976; Mulholland et al., 1977). The Clementine and Lunar Prospector missions returned global data sets of lunar gravity, topography, remanent magnetism, mineralogy, and chemical composition of the surface (Nozette et al., 1994; Binder, 1998). Other lunar missions include SELENE (Kato et al., 2008), Chandrayaan (Goswami and Annadurai, 2009) and Chang'E (Ouyang et al., 2010). Recent developments were brought by the GRAIL mission (Zuber et al., 2013) following which a better understanding of the lunar topography and interior surfaced.

Here we elaborate on the current state-of-the-art in terms of the understanding of the lunar interior, investigation attempts and a new model (work in progress) to correct for degree-3 GRAIL-derived gravity field coefficient incompatibility to the lunar dynamical model, as well as the application of the improved lunar model to the study of fundamental physics.

6.1 Lunar interior

A better understanding of the structure of the interior of the Moon aids to recover information on its past history. Planetary geodesy measurements of global parameters such as the gravity field and variations in rotation gives key information on its interiors. The Gravity Recovery and Interior Laboratory (GRAIL) mission (Zuber et al., 2013), analogous to the GRACE mission in the Earth's orbit, was able to map the global gravity field of the Moon (Konopliv et al., 2013; Lemoine et al., 2014) using differential gravity measurements obtained with a pair of spacecraft with accurately known relative positions.

The use of GRAIL-derived gravity field data provides significant constraints during the analysis of LLR observations, and complements the recovery of information. This is because while the GRAIL-derived gravity field provides a global lunar model with a 6-month observation time span, LLR modeling involves differential equations describing the relative motion of a layered Moon with a larger observational time span (1969-present). Moreover, the synergistic use of the GRAIL-derived gravity field with LLR observations allows the user to study the orbital evolution of the Moon with the help of ephemerides.

6.1.1 Discussion about INPOP17a model

During the iterative fit of the INPOP17A model to the LLR observations, it was noticed that, in order to maintain the post-fit residuals at the level of 2 cm it was necessary for a few degree-3 spherical harmonic coefficients (C_{32}, S_{32} and C_{33}) to deviate by about 1% from the GRAIL-derived gravity field values (Konopliv et al., 2013). This was associated by other LLR analysis groups (Williams et al., 2014b; Pavlov et al., 2016) as unmodeled effects in the physical libration model and an adjustment to these degree-3 coefficients was suggested to obtain a better LLR fit.

The difference between the value of the spherical harmonic coefficient C_{32} derived from the Lunar Prospector Mission LP150Q Konopliv et al. (2001) and that from GRAIL GL0660b Konopliv et al. (2013) is about 4.7×10^{-9}, consistent with the LLR estimates from DE430 (Folkner et al., 2014), EPM2016 (Pavlov et al., 2016) and INPOP17a (Viswanathan et al., 2017). However, differences (LP150Q-GL0660b) on the coefficients S_{32} and C_{33} are one order of magnitude smaller than from LLR estimates. Overall, this indicates that the discrepancies on the degree-3 gravity field of the Moon with the current lunar dynamical models are not mission specific. For GRAIL, the two independent gravity field model from JPL (Konopliv et al., 2013) and GSFC (Lemoine et al., 2013) have 3 orders of magnitude smaller differences, ruling out analysis specific discrepancies in the 1% deviation noticed from LLR estimates. Cappallo (1980, Appendix E.2) comments about the impact of neglecting degree-4 torques, which can be masked by small changes in the degree-3 coefficients. To study the impact of the neglected components of torques within the dynamical model, we constrain the INPOP17a model to a strictly GRAIL-derived lunar gravity field. This is followed by an iterative fit. A strong 6-year longitude libration signature on all reflectors (expect weakly on A15 reflector due to its central position when viewed from the mean-Earth direction) with an amplitude of ±5 cm, is then noticed within the post-fit residuals (see Fig. 6.4). A longitude libration signature can be identified in LLR using the phase of the range signature with respect to the position of the retro-reflector on the surface of the Moon i.e A11 and L2 located along similar longitudes have the same phase in the range compared to A14 and L1.

The following discussion (Section 6.1.2) as well as a new modeling (Section 6.1.3) was proposed for publication to the Astronomy & Astrophysics journal (see submitted manuscript in Appendix C).

6.1.2 Investigation attempts

Here we list some of the additions made to the dynamical model of INPOP (internal version), in order to consider the unmodeled higher-degree components (torque, Love number and CMB topography) that is expected to compensate the longitude libration signature noticed.

Fourth degree torque

Within the torques due to interaction of the figure of the Moon with the figure of the Earth provided by Folkner et al. (2014, p. 18), only the three most significant terms are considered. This is an approximation from the complete expansion of the $\vec{N}_{22}$ torque provided in Bois et al. (1992, p. 197). On introducing this torque component into Eqn. (4.5a) as a higher degree component of $\vec{N}_{M,figM-figE}$, a longitude libration signature with a period of about 3 years with a maximum amplitude of ±1 mm over 48 years on the 1-way light time range (0.33 mas on longitude libration) is noticed (see Fig. 6.1). Since the effect is below the uncertainty of the observations till date, the improvement of the model with the inclusion of this effect is not noticable within the iterative post-fit residuals and the signature (indicated within Fig. 6.1) is absorbed.

Fifth degree torque

The fifth degree torque consists of figure-figure interaction exerted by the Earth (second degree in harmonics) on the Moon (third degree in harmonics). This is expanded as $\vec{N}_{23}$ in Bois et al. (1992, p. 198)[1]. On introducing this torque component into Eqn. (4.5a) as an inter-degree component of $\vec{N}_{M,figM-figE}$, a longitude libration signature with a period of about 3 years with a maximum amplitude of ±3 mm over 48 years on the 1-way light time range (1 mas on longitude libration) is noticed (see Fig. 6.2). Similar to the fourth-degree torque, the signature brought by the inclusion of the fifth-degree torque is also absorbed during an iterative fit, without any noticable improvement on the post-fit residuals.

An internal solution was refitted with the introduction of these two torque components (fourth and fifth degree) with a strictly GRAIL-derived gravity field model. With the GRAIL constraints on the degree-3 components, the solution

[1]The first $\tilde{S}_{52}$ on Bois et al. (1992, p. 198) is assumed to be a typographical error, which should be read as $\tilde{S}_{51}$.

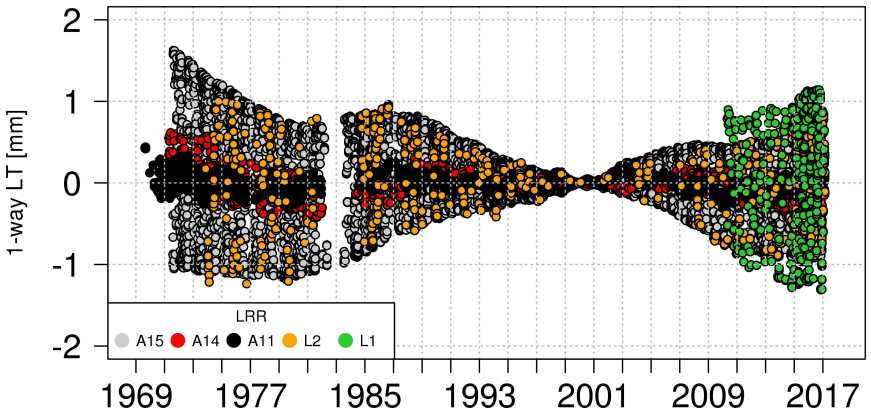

Figure 6.1: Longitude libration signature of ±1 mm over 48 years on the 1-way light time range (0.33 mas on longitude libration) with a period of about 3 years (weak) arising from the introduction of higher order figure-figure interaction (fourth degree torque) between the Moon and the Earth, as provided by $\vec{N}_{22}$ torque in Bois et al. (1992, p. 197).

produces the same 6 year signature as described in Section 6.1.1. And, on relaxing the constraints on the degree-3 components (as described in Section 5.2.1), the resulting solution produced similar post-fit residuals (with differences below 1 mm on 1-way light time range) with the new estimates being within the uncertainty of INPOP17a solution.

This implies that the modeled higher degree components (fourth and fifth degree) of the figure-figure torques are not responsible for the noticed discrepancy.

Degree-3 love number for the Moon

Konopliv et al. (2013) provide the value of degree-3 Love number k_3 as 0.0089 ± 0.0021, from the analysis of the GRAIL Primary Mission. The degree-3 love number estimated by Konopliv et al. (2013) for the Moon, is introduced into the dynamical model using Manche (2011, Eqn. 4.10), inducing time variations on the degree-3 gravity field of the Moon.

It was noticed that the maximum amplitude of this effect is about 0.2 mm over 48 years on the 1-way light time range with a period of 18.6 years. This implies that the introduction of the degree-3 love number is undetectable with the current LLR accuracy, and is easily absorbed during an iterative fit of the solution including this effect.

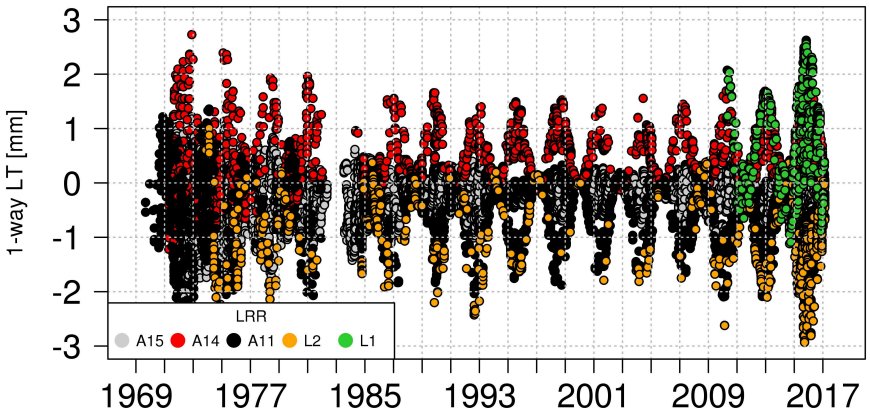

Figure 6.2: Longitude libration signature of ±3 mm over 48 years on the 1-way light time range (1 mas on longitude libration) with a period of about 3 years arising from the introduction of higher order inter figure-figure interaction (fifth degree torque) between the Moon and the Earth, as provided by $\vec{N}_{23}$ torque in Bois et al. (1992, p. 198).

Topographic coupling at the core-mantle boundary

An expression for the topographic coupling up to degree-3 (see Appendix B.2) was derived by (N.Rambaux, personal communication, 2017), developed under the approximation that the flow of the liquid at the core-mantle boundary is mainly controlled by the ellipsoidal shape (i.e without correction on higher harmonics) and conforming with Sasao and Wahr (1981). This extends the lunar core gravity field coefficients up to degree and order 3, thereby introducing 7 additional parameters (without known values) for the lunar core. These parameters are strongly correlated (0.8 to 0.9) and the plot of the partial derivatives of the core degree-3 spherical harmonics are not sensitive at the current level of the LLR accuracy for a given core fraction ($\alpha_c = 7 \times 10^{-4}$). One could expect a higher sensitivity for larger values of α_c, however, the signature of interest (6 year period on longitude libration) was not visible on the plot of the partial derivatives of the core gravity field coefficients.

At the time of writing, the overall impact of this effect (from the degree-3 components) on the 1-way light time remains unknown due to the inability to perform the fit due to the strong correlation among the lunar core gravity field coefficients.

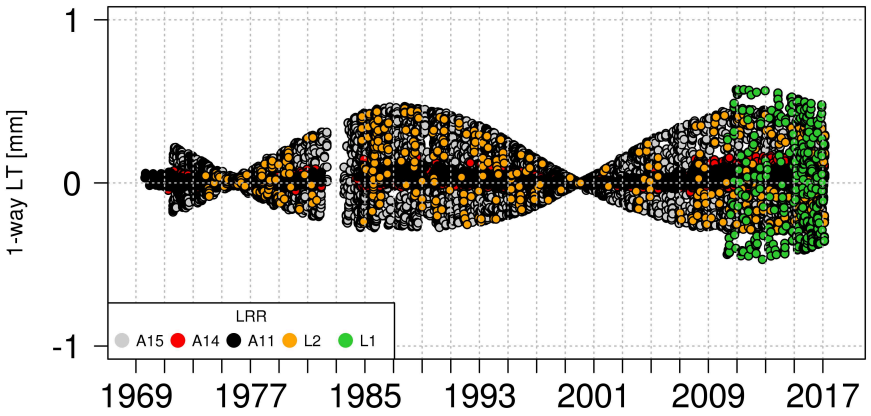

Figure 6.3: Contribution of degree-3 love number on the 1-way light time range.

6.1.3 Degree-3 shape of the lunar fluid core

Folkner et al. (2014); Pavlov et al. (2016) assume that the lunar fluid core rotates like a rigid body and is constrained by the shape of the CMB at the interior of the mantle, with a constant core moment of inertia in the frame of the lunar mantle. Under these assumptions, several constraints to the present lunar ephemerides are introduced.

Fluid core rotation like an rigid body implies, a simplified flow with a homogeneous density distribution. Although the flow is well represented by the model of Poincaré (1910) through the inertial coupling torque (considering a triaxial fluid core following Rambaux et al. (2007)), the homogeneous density distribution restricts the introduction of density variations on the fluid core. Gravitational forcing from external mass anomalies (within the mantle/inner core or CMB-topography) can cause lateral structure inside the fluid core (Wahr and de Vries, 1989; Dai and Song, 2008). Mass anomalies on the Moon were detected by the analysis of Lunar Orbiter data (Muller and Sjogren, 1968) and further studied by GRAIL-derived gravity field (Melosh et al., 2013; Neumann et al., 2015). Hence, the presence of such lateral variations in the fluid core would change the potential when reoriented with respect to the mantle frame and therefore the gravitational torques on the fluid core can no longer be neglected (Williams et al., 2014b). Furthermore, in the presence of a laterally varying structure, degree-2 tidal forces excite gravitational response at non-degree-2 harmonics due to mode coupling effects (Zhong et al., 2012).

To study the impact of the above mentioned assumptions, in addition to the inertial and viscous coupling torques, we introduce an external gravitational torque from the point mass Earth on the lunar fluid core figure (similar to Van

Hoolst (2007, Eqn. 35)), considering the presence of core lateral variations induced by mass anomalies within the lunar mantle. This refers to the introduction of Eqn. (4.10) into the lunar core angular momentum equation provided in Section (4.3.6).

An internal version of INPOP (S2), introduces this model in order to study the effect of this torque on the estimates. This solution additionally solves for lunar core degree-3 components with constraints placed on the lunar gravity field derived from GRAIL (Konopliv et al., 2013). The post-fit residuals obtained with solution S2 show small improvements over the INPOP17a model (see Fig. 6.4) with consistent estimates (see Table 6.1). More importantly, the results indicate strong consistency with the GRAIL-derived gravity field coefficients without requring any adjustments. The estimated value of h_2 is then compatible with the LRO LOLA-derived estimate by Mazarico et al. (2014). Additional test solutions linked to this study can be found in Appendix (C).

It must be noted that the solution S2 does not consider a complete torque balance within the lunar interior and the results shown are only preliminary. The submitted paper is under revision which requires further analysis. The new objective is to consider a three layer (solid mantle, fluid outer core and a solid inner core) lunar model, with a complete gravitational and pressure torque balance between the internal layers. This revision (a work in progress) would allow us to verify if the lunar libration signature absorbed by the torque imbalance (arising from the introduction of the external gravitational torque alone on the fluid core) is similar to that introduced from an additional layer such as the solid inner core.

A constant core moment of inertia does not allow tidal deformations of the lunar fluid core or the core-mantle boundary. Tidal deformations partly affect the lunar orientation through the responding moment of inertia and its time derivative (Williams, 2009; Williams et al., 2012a). Le Bars et al. (2011) show the importance of the tidal distortion of the lunar core-mantle boundary to explain the lunar magnetic anomalies with links to the lunar dynamo for the early Moon. Introducing time variations to the lunar fluid core moment of inertia requires Love numbers for the fluid core, which are obtained through lunar seismic studies (Weber et al., 2011; Garcia et al., 2011) and also provided in Williams et al. (2014b, Table 6). At the time of writing, the impact of the deformations on the fluid core was neglected within the lunar dynamical model, however a work is in progress to address this contribution.

Table 6.1: Comparison between solutions: Extended body parameters for the Moon. Uncertainties are obtained from a 5% jackknife (JK) test, the least squares 1-σ uncertainties being either consistent or smaller than the JK estimations. * stands for values fixed to model (GL0660b) values from GRAIL. 17a refers to the INPOP17a solution and S2 refers to an internal version of INPOP with the dynamical model described in Section (6.1.3). ‡ indicates that the h_2 reference value is extracted from Mazarico et al. (2014).

Parameter	**17a**	**S2**
$(C_T/(m_M R^2) - 0.393140) \times 10^6$	7.3 ± 0.2	5.0 ± 0.2
$(C_{32} - 4.8404981 \times 10^{-6}) \times 10^9$	4.1 ± 0.3	$0.0^\star$
$(S_{32} - 1.6661414 \times 10^{-6}) \times 10^8$	1.704 ± 0.006	$0.0^\star$
$(C_{33} - 1.7116596 \times 10^{-6}) \times 10^8$	-1.19 ± 0.04	$0.0^\star$
$(\tau_M - 9 \times 10^{-2}) \times 10^4$ [d]	-2 ± 5	-56 ± 5
$(\frac{k_v}{C_T} - 1.6 \times 10^{-8}) \times 10^{10}$ [d^{-1}]	10.2 ± 0.4	17.9 ± 0.4
$(f_c - 2.1 \times 10^{-4}) \times 10^6$	41 ± 3	47 ± 3
$(C_{32,core} + 5.6 \times 10^{-8}) \times 10^{10}$	-	-3.0 ± 2
$(S_{32,core} - 5.0 \times 10^{-8}) \times 10^{10}$	-	5 ± 10
$(k_{2,M} - 0.024059) \times 10^3$	$0.0^\star$	$0.0^\star$
$(h_2 - 3.71 \times 10^{-2})^\ddagger \times 10^3$	6.6 ± 0.2	2.3 ± 0.2
$l_{2,m} - 1.07 \times 10^{-2}$	$0.0^\star$	$0.0^\star$
$Q_{27.212} - 45$ (derived)	3.2 ± 0.5	6.6 ± 0.3

Figure 6.4: Longitude libration signature arising from unmodeled effects within the dynamical model, with a period of 6 year and amplitude 5 cm on the range. Post-fit residuals (in 1-way light time [cm]) obtained with APOLLO station data vs time (in years) from solution with : (left) GRAIL-derived degree-3 lunar gravity field coefficients, (center) LLR-derived degree-3 lunar gravity field coefficients ($C_{3,2}$, $S_{3,2}$ and $C_{3,3}$), (right) GRAIL-derived degree-3 lunar gravity field coefficients with the model described in Section (6.1.3).

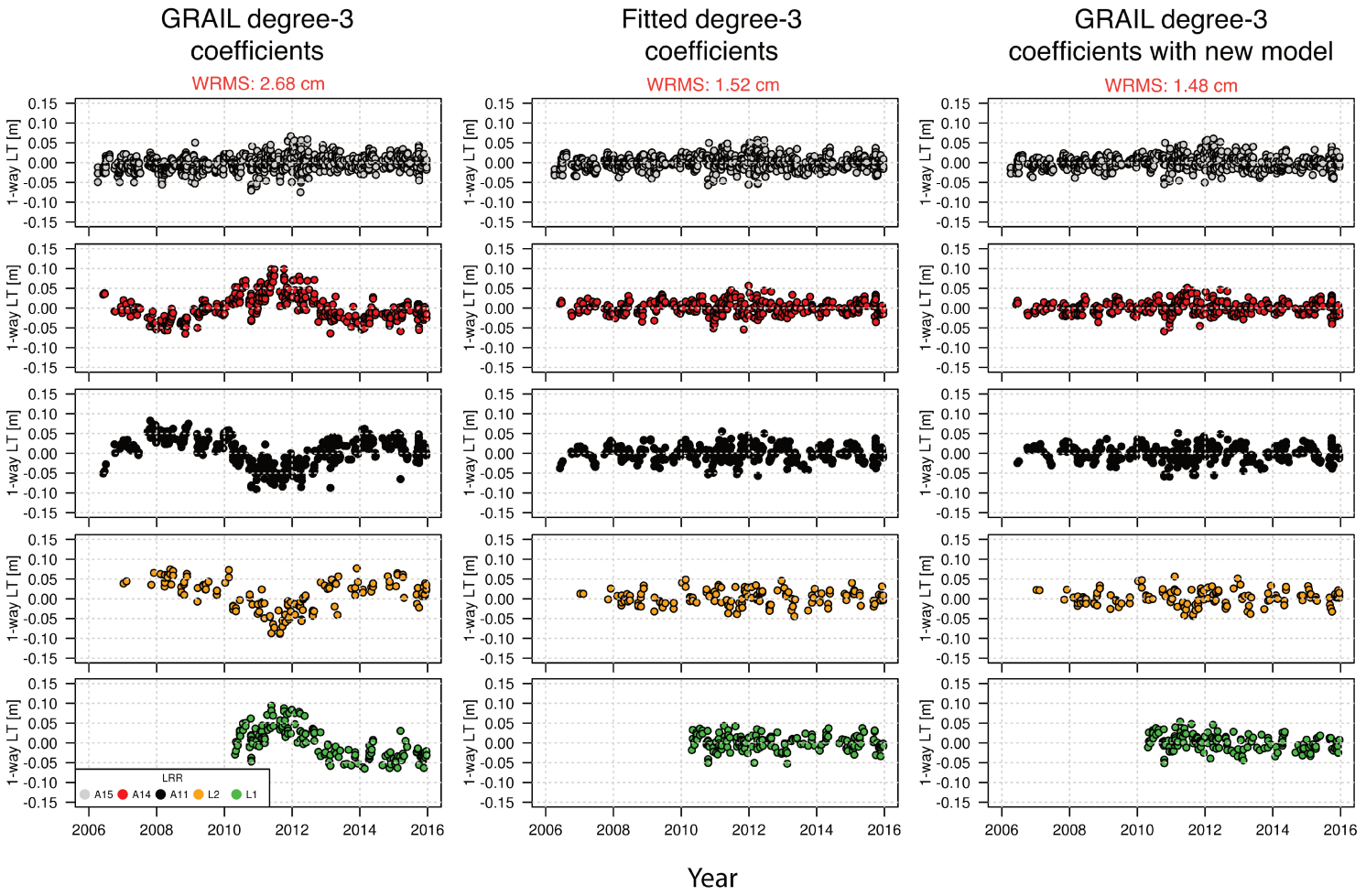

6.2 Test of the principle of equivalence

Towards the end of 16$^{\text{th}}$ century, the Italian scientist Galileo Galilei conceived an experiment in which he dropped two objects of different composition and mass together from the top of the Tower of Pisa. In his theory, as the two objects hit the ground at exactly the same time, he deduced that in vacuum, and under the influence of a gravitational field, all bodies are accelerated equally. This is what we call the Universality of Free Fall (UFF) or the equality of gravitational and inertial mass. This was later stated by Albert Einstein, as the Equivalence Principle (EP) which was the central assumption of the General Relativity Theory (GRT).

In the following section we provide a test of the UFF with the help of INPOP lunar ephemeris, considering the Moon and the Earth as test subjects falling in the gravitational field of the Sun. The results of this test are provided in Section (6.2.3), followed by a discussion (Section 6.2.4) and an interpretation (Section 6.2.3). The results presented here are accepted for publication in the Monthly Notices of the Royal Astronomical Society (see submitted manuscript in Appendix D).

6.2.1 Context

Among all possibilities to test GRT, the tests of the motion and light propagation in the solar system were historically the first ones and still provide the highest accuracies, since the dynamics of the solar system is well understood and supported by a long history of observational data. In general, tests of GRT can be split into two groups: tests of the Equivalence Principle (claiming that gravity can be understood in a geometrical way) and those of the Einstein field equations (describing how the space-time geometry is influenced by matter). Violations of the Equivalence Principle are predicted by a number of modifications of GRT aimed to suggest a solution for the problem of Dark Energy and/or to merge GRT with quantum physics: e.g., string theory (Damour and Polyakov, 1994; Damour et al., 2002) or models where some physical constants are dynamical entities (Damour and Donoghue, 2010; Damour, 2012). The Universality of Free Fall, an important part of the Equivalence Principle, is currently tested at a level of about 10^{-13} with torsion balances (Adelberger et al., 2003) and the LLR (Williams et al., 2012b).

As the Earth and the Moon both fall in the gravitational field of the Sun — and because they neither have the same compositions, nor the same gravitational self-energies — the Earth-Moon system is an ideal probe of both the Weak Equivalence Principle (WEP) and the Strong Equivalence Principle (SEP), while torsion balance (Adelberger et al., 2003) or the MICROSCOPE satellite (Liorzou et al., 2014) are only sensitive to violations of the WEP.

6.2.2 Method

In order to test possible violations of GRT in terms of UFF, a supplementary acceleration is introduced in the geocentric equation of motion of the Moon, such that the UFF violation related difference between the Moon and the Earth accelerations reads (Nordtvedt, 1968):

$$\Delta \boldsymbol{a}^{\overline{UFF}} \equiv (\boldsymbol{a}_M - \boldsymbol{a}_E)^{\overline{UFF}} = \boldsymbol{a}_E \Delta_{ESM} \tag{6.1}$$

Corrections

LLR EP estimates are sensitive to a variety of effects, including (but not limited to), solution parameter correlations, choice of parameters in the fit, reduction model used, artifacts from non-uniform distribution of the data, biases, etc.

In order to estimate Δ_{ESM} with the appropriate accuracy, one should correct for known supplementary effects along the radial component, such as the solar radiation pressure (-3.65 ± 0.08 mm cosD) and the thermal expansion (≈ 0.67 mm cosD) of the retro-reflectors (Vokrouhlický, 1997; Williams et al., 2012b). An empirical correction on the radial perturbation (Δr_{ESM}) induced by the UFF test has to be applied. The UFF additional acceleration would indeed lead to an additional radial perturbation (Δr_{ESM}) of the Moon's orbit towards the direction of the Sun given by:

$$\Delta r_{ESM} = S \Delta_{ESM} \cos D, \tag{6.2}$$

where S is a scaling factor of about -2.93×10^{10} m and D is the synodic angle. A correction $\Delta r = -3.0 \pm 0.5$ mm $\cos D$ (Vokrouhlický, 1997; Williams et al., 2012b) is then applied and a new corrected value of Δ_{ESM} is then deduced.

6.2.3 Results

As described firstly by Nordtvedt (1968), we consider first the quantity Δ_{ESM} such as:

$$\Delta_{ESM} = \left[\left(\frac{m^G}{m^I} \right)_E - \left(\frac{m^G}{m^I} \right)_M \right]. \tag{6.3}$$

where $\left(\frac{m^G}{m^I}\right)_E$ and $\left(\frac{m^G}{m^I}\right)_M$ are the ratios between the gravitational and the inertial masses of the Earth and the Moon respectively.

Following Williams et al. (2012b), we obtain

$$\boldsymbol{a}_M - \boldsymbol{a}_E = -\frac{G\mu}{r_{EM}^3}\boldsymbol{r}_{EM} + Gm_S^G\left[\frac{\boldsymbol{r}_{SE}}{r_{SE}^3} - \frac{\boldsymbol{r}_{SM}}{r_{SM}^3}\right] + \\ +Gm_S^G\left[\frac{\boldsymbol{r}_{SE}}{r_{SE}^3}\left(\left(\frac{m^G}{m^I}\right)_E - 1\right) - \frac{\boldsymbol{r}_{SM}}{r_{SM}^3}\left(\left(\frac{m^G}{m^I}\right)_M - 1\right)\right], \tag{6.4}$$

In recombining the previous equation, one shows that the supplementary acceleration induced by the violation of the universality of free fall $\Delta\boldsymbol{a}^{\overline{UFF}}$, can be written such as:

$$\begin{aligned}\Delta\boldsymbol{a}^{\overline{UFF}} &\equiv (\boldsymbol{a}_M - \boldsymbol{a}_E)^{\overline{UFF}} \\ &\approx Gm_S^G\left[\frac{\boldsymbol{r}_{SE}}{r_{SE}^3}\left(\left(\frac{m^G}{m^I}\right)_E - 1\right) - \frac{\boldsymbol{r}_{SM}}{r_{SM}^3}\left(\left(\frac{m^G}{m^I}\right)_M - 1\right)\right] \\ &\equiv \boldsymbol{a}_E\Delta_{ESM}\end{aligned} \tag{6.5}$$

The results of the estimation of Δ_{ESM} from LLR is provided in Table (6.2).

Supplementary Interpretation

The LLR test of the UFF captures a combined effect of the SEP, from the differences in the gravitational self-energies, and the WEP due to compositional differences, of the Earth-Moon system. In order to separate the effects of WEP, we rely on results from laboratory experiments that simulate the composition of the core and the mantle materials of the Earth-Moon system. One such estimate is provided by (Adelberger, 2001), that translates to a relative acceleration:

$$\left[\left(\frac{m^G}{m^I}\right)_{Earth} - \left(\frac{m^G}{m^I}\right)_{Moon}\right]_{WEP} = (1.0 \pm 1.4) \times 10^{-13} \tag{6.6}$$

The results of the estimation of SEP from LLR is provided in Table (6.3).

Table 6.2: Comparison of results for the ratio Δ_{ESM} (Column 4) estimated with the solution INPOP17A with LLR dataset between: 1) 1969-2011 (for comparison with (Williams et al., 2012b; Müller et al., 2012)); 2) 1969-2017 with data obtain only in Green wavelength, 3) 1969-2017 with data obtained with both Green and IR wavelength. Column 5 contains the converted $\cos D$ coefficient expressed in mm (see Eqn. 6.2). Column 6 empirically corrects the radial perturbation for effects related to solar radiation pressure and thermal expansion. Column 7 contains the ratio Δ_{ESM} derived from Eqn. 6.2 and values of Column 6.

Reference	**Data time span** [Year]	**Uncertainty**	**estimated** $\Delta(m^G/m^I)_{ESM}$ [$\times 10^{-14}$]	**converted** $\cos D$ [mm]	**corrected** $\cos D$ [mm]	**converted** $\Delta(m^G/m^I)_{ESM}$ [$\times 10^{-14}$]
Williams et al. (2009)	1969-2004	N/A	3 ± 14	-0.9 ± 4.2	2.1 ± 4.2	-7.24 ± 14.3
Williams et al. (2012b)	1969-2011	N/A	0.3 ± 12.8	-0.08 ± 3.75	2.92 ± 3.78	-9.94 ± 12.9
Müller et al. (2012)	1969-2011	3-σ	-14 ± 16	4.1 ± 4.69	7.1 ± 4.7	-24.2 ± 16.1
INPOP17A (limited data)	1969-2011	3-σ	-3 ± 18	0.88 ± 5.28	3.88 ± 5.30	-13.23 ± 18.08
Hofmann and Müller (2016)	1969-2017	3-σ	-	-	-	-3.0 ± 6.6 †
INPOP17A (Green only)	1969-2017	3-σ	5 ± 8.7	-1.47 ± 2.55	1.54 ± 2.60	-5.24 ± 8.87
INPOP17A (Green and IR)	1969-2017	3-σ	8 ± 7.5	-2.35 ± 2.20	0.66 ± 2.25	-2.24 ± 7.69

† SRP correction applied within the reduction model. Thermal expansion of reflectors is not taken into account (F.Hofmann, personal communication, 2017)

Table 6.3: Results of the SEP estimates obtained from the LLR EP numerical estimates, after removing the WEP component provided by the laboratory experiments from Adelberger (2001); Williams et al. (2009).

Reference	**Data time span** [Year]	**derived SEP** $\Delta(m^G/m^I)_{ESM}$ [$\times 10^{-13}$]
Williams et al. (2009)	1969-2004	-2.0 ± 2.0
Williams et al. (2012b)	1969-2011	-1.8 ± 1.9
Müller et al. (2012)	1969-2011	-2.4 ± 2.2
INPOP17A (limited data)	1969-2011	-2.3 ± 2.3
INPOP17A (Green only)	1969-2017	-1.5 ± 1.7
INPOP17A (Green and IR)	1969-2017	-1.2 ± 1.6

6.2.4 Discussion

Fits were performed with the difference in accelerations Δ_{ESM} given in Eqn. (6.1) along with the other fitted parameters presented in Table (5.5). Two different fits were considered including the Green and the Infrared data sets: INPOP17A (Green and IR), or just the Green data sets: INPOP17A (Green only). A supplementary fitted solution was obtained for comparisons to the previous determinations by Williams et al. (2012b); Müller et al. (2012) which were limited to LLR data samples up to 2011: INPOP17A (limited data). The results are given in Table (6.2).

The additional acceleration of the Moon's orbit in the direction of the Sun correlates with a coefficient of 0.95 and 0.90 with GM_{EMB} and the Earth-Moon mass ratio (EMRAT), respectively. In all the solutions w.r.t LLR EP estimation, GM_{EMB} remains as a fit parameter due to its high correlation with the EP parameter ($\Delta(m^G/m^I)_{ESM}$). EMRAT was estimated from a joint planetary solution and kept fixed during LLR EP tests due to its weak determination from LLR. This is reassured using a test solution that fitted EMRAT, while keeping GM_{EMB} as a fixed parameter, giving an estimate of $\Delta(m^G/m^I)_{ESM} = (8 \pm 7.0) \times 10^{-14}$. However, the value of EMRAT obtained with this test solution has an uncertainty of one order of magnitude greater than that obtained from the planetary fit, consistent with a similar result by Williams et al. (2009). As a result, EMRAT was not included as a fit parameter for the estimates provided in Table (6.2), as it resulted in a degraded fit of the overall solution.

Williams et al. (2012b) show through solutions labeled EP71 and EP72, that including annual nutation components of the Earth's pole direction in space, to the list of fit parameters during the estimation of LLR EP solution, increases

the uncertainty of the estimated EP parameter ($\Delta(m^G/m^I)_{ESM}$) by 2.5 times. Moreover, it is to be noted that within Table (6.2), reference solutions: Williams et al. (2009, 2012b); Müller et al. (2012) use the IERS2003 (McCarthy and Petit, 2004) recommendations within the reduction model, while all INPOP17 solutions use IERS2010 (Petit and Luzum, 2010) recommendations. The notable difference between the two IERS models impacting the LLR EP estimation is expected to be from the precession-nutation of the celestial intermediate pole (CIP) within the ITRS-GCRS transformation, while other differences can be found within Petit and Luzum (2010, p. 8).

Eqn. (6.2) shows the dependence of Δr_{ESM} w.r.t the cosine of the lunar orbit's synodic angle ($\cos D$), synonymous with the illumination cycle of the lunar phases. Due to the difficulties involved with ranging to the Moon during the lunar phases with the maximum value of $\cos D$ (during the New and Full Moon phases) as described in Section (2.3.1), the LLR observations during these phases remain scarce. The availability of LLR observations from Grasse (in IR) and APOLLO, contributes to the improvement of this situation, as shown in Fig. (2.12 and 2.14) compared to Fig. (2.13). This is reflected in the improvement of the uncertainty of the estimated value of $\Delta(m^G/m^I)_{ESM}$ by 14% for the solution using the complete LLR dataset.

6.2.5 Perspectives

An observable bias in the differential radial perturbation of the lunar orbit w.r.t the Earth, towards the direction of the Sun, if significant and not accounted for within the dynamical model, would result in a false indication of the violation of the principle of equivalence estimated with the LLR observations. Oberst et al. (2012) show the distribution of meteoroid impacts with the lunar phase. Peaks within the histogram in Oberst et al. (2012, p. 186) indicate a non-uniform temporal distribution with a non-negligible increase in both small and large impacts during the New and Full Moon phase. Future improvements to the LLR EP estimation must consider the impact of such a bias that could potentially be absorbed during the fit by the LLR EP parameter Δr_{ESM}.

Chapter summary

The long time span of LLR observations and its ongoing millimeter level accuracy allow LLR analyses to identify subtle changes in the lunar orientation and other state vectors resulting from the dynamics of the lunar interior and/or equations of motion. A longitude libration signature is induced due to the incompatibility of few of the degree-3 spherical harmonics of spacecraft-derived gravity field models. Attempts to investigate the source of the supposed modeling error are provided. A

new model is proposed and it reduces this incompatibility significantly. Additional work is required (and is ongoing) to introduce tidal variations on the lunar core matrix of inertia to model deformations of the fluid core. A test of the universality of free fall using the INPOP17a model of the Earth-Moon system shows no violation of the universality of free fall at 10^{-14}. The following chapter (Chapter 7) concludes this study with the future perspectives.

Chapter 7

Conclusion and Perspectives

The observations used for this study consists of lunar laser ranging (LLR) data (Chapter 2). The study begins with the use of raw observations collected by the Grasse LLR station situated in the Côte d'Azur region of France. The Grasse LLR station has acquired LLR range data for nearly three decades (Veillet, 1987; Veillet et al., 1993; Samain, 1995; Samain et al., 1998; Martinot-Lagarde et al., 2016) and continues to procure high accuracy LLR observations since the change of the operational wavelength to IR (1064 nm) (Courde et al., 2017). The fit of the parameters benefits from the homogeneous distribution of IR in both spatial and temporal domains when compared to the operation in 532 nm wavelength. The existing normal point computation algorithm employed at Grasse station was evaluated under different scenarios describing the various range data obtained, and an alternative algorithm (Section 2.2.4) is proposed to compensate for its limitations (Section 2.2.3). Statistical analyses are performed on the LLR data (subsets and collective) distribution to quantify its temporal and spatial dependencies (Section 2.3). Wavelength dependent response of the Lunokhod retro-reflectors (Courde et al., 2017) requires further study. Internal binaries from Grasse station indicate insufficient echoes for characterization of components in the calibration distribution. Future calibration sessions must acquire more echoes for smoother profiling.

The numerical model consists of two components: the reduction model (Chapter 3) and the dynamical model (Chapter 4). The LLR reduction model computes the simulated time taken by the laser pulse during the LLR experiment during the up-leg (station-reflector) and down-leg (reflector-station) paths of the laser pulse, including all the known geophysical and relativistic effects. This model was implemented within a precise orbit determination and geodetic software: GINS. The frame of reference was changed to the ICRF to facilitate the accuracy of the numerically integrated ephemerides. A step-wise comparison study was conducted (using simulated LLR data) between the LLR analyses groups at IMCCE-Paris (Manche,

2011) and IfE-Hannover (Müller et al., 2005), to identify and correct modeling errors at the 1 mm level using the IERS 2010 (Petit and Luzum, 2010) and DE421 (Folkner et al., 2009) as the reference models. Additionally, the impact of hydrology loading at the Grasse station was analyzed through multi-geodetic techniques (Mémin et al., 2016) and modeled into the reduction software (Section 3.3.6). A report was submitted to CNES containing the LLR reduction model modifications in GINS software and libraries along with the code delivery.

The dynamical model consists of a planetary and lunar ephemeris. The lunar part of the ephemeris describes the motion and orientation of the Moon as it orbits the Earth. A previous version (13c) of the INPOP lunar ephemeris (Fienga et al., 2014) was extensively tested and compared with two other independent lunar ephemerides: DE430 - Folkner et al. (2014) and EPM2016 - Pavlov et al. (2016). Inconsistencies between the models were identified and corrected during the comparison (Section 4.1). The fluid core within the new solution is activated. Additional work is required for alternatives to the time delay model of dissipation used in lunar ephemerides, as the current model requires empirical corrections on the longitude librations to account for dissipation effects for periods away from a month (Williams and Boggs, 2015b). A proposition is to introduce imaginary Love numbers to account for dissipation.

An improved version of the INPOP lunar ephemeris was constructed through an iterative weighted least-squares fit (Chapter 5), providing new independent estimates of the lunar dynamical model. The new post-fit residuals are below 2 cm in wrms, a factor 5 improvement on the latest high accuracy observation compared to that obtained from the previous version of INPOP (Section 5.3). Comparison with the LLR estimates from other analyses groups (Folkner et al., 2014; Pavlov et al., 2016) show strong consistency at the 2 cm level. The INPOP17a ephemeris is publicly distributed through the IMCCE website: `www.imcce.fr/inpop` with a technical report (Viswanathan et al., 2017).

The construction of a high accuracy lunar ephemeris allows us to probe deeper into the questions of the lunar interior structure (Section 6.1) and conduct tests of the universality of free fall (Section 6.2) as described in Chapter (6).

The use of a strictly GRAIL-derived gravity field model (Konopliv et al., 2013) highlights longitude libration signatures well above the LLR noise floor, arising from unmodeled effects in the lunar ephemeris (Section 6.1.1). Other LLR analyses groups (DE421/430 and EPM2016) prefer to fit the degree-3 components away from GRAIL-derived gravity field coefficients. We provide the investigation attempts to this issue to identify the cause of the low-degree spacecraft-derived gravity field inconsistency (Section 6.1.2). Additionally, a model is also provided to compensate this signature (Section 6.1.3). New leads suggest that there may be a small non-spherical response to tidal forcing due to asymmetric elastic properties

between the lunar near-side and far-side. Zhong et al. (2012) propose that this asymmetry would change the degree-2 tides and introduce a mixed-mode degree-3 response due to the lateral density variations. Further development on the introduction of a three-layer Moon (mantle, outer fluid core and solid inner core) in the lunar dynamical model is envisioned in the near future due to the availability of accuracy on the LLR observations. The observational evidence for the presence of a solid inner core within the Moon would answer to several key questions regarding the now-extinct lunar dynamo (Wieczorek, 2006; Laneuville et al., 2014). For LLR, this remains as a near possibility.

Estimates of the principle of equivalence (EP) parameter are obtained (Section 6.2.3) and show no violation at the level of 10^{-14}. Oberst et al. (2012) show the distribution of meteoroid impacts with the lunar phase, indicating a non-uniform temporal distribution during the New and Full Moon phase which could impact the test of EP. The impact of this effect needs to be characterized to be considered as negligible at the present LLR accuracy. Thermal expansion of the retro-reflectors and solar radiation pressure will be included in the reduction model (instead of the currently employed empirical corrections) for future LLR analysis, so as to improve the uncertainty of the EP test.

The last four decades saw LLR accuracy move by 2 order of magnitude, down to a present millimeter level. This was achieved solely through efforts from the technical teams at various LLR stations who continue to produce high accuracy observations and make them available to the public. New LLR stations continue to be commissioned (Munghemezulu et al., 2016; Vasilyev et al., 2016; Dehant et al., 2017) while a class of next-generation laser retro-reflectors await for their launch, to the Moon (Ciocci et al., 2017) as well as to Mars (Dell'Agnello et al., 2017). To this, I recollect a quote by Clive R. Neal from the LPSC (2017) Vision 2050 Workshop: "You can't be a Martian without being a lunatic first".

Appendices

Appendix A

Adjustments to reference points

A.1 Estimation of coordinates

A.1.1 LLR Station coordinates

A.1.2 LLR retroreflector coordinates

A.2 Station biases

Table A.1: Fitted values of LLR station coordinates and velocities (expressed in meters and meters per year respectively), at J2000.0, for different solutions. The reference values correspond to ITRF2005. * indicates fixed parameters.

Station	**Coordinate** [m]	**INPOP$_G$**	**INPOP17a**
APOLLO	x + 1463998.7870	-0.1269 ± 0.0004	-0.1285 ± 0.0004
	y + 5166632.8080	+0.0420 ± 0.0004	+0.0390 ± 0.0004
	z - 3435012.8560	-0.0119 ± 0.0014	+0.0099 ± 0.0014
	$\dot{x}$ + 0.0141	+0.0009 ± 0.0001	+0.0011 ± 0.0001
	$\dot{y}$ + 0.0015	+0.0012 ± 0.0001	+0.0016 ± 0.0001
	$\dot{z}$ + 0.0064	+0.0084 ± 0.0016	+0.0064 ± 0.0016
Grasse	x - 4581692.1420	+0.0014 ± 0.0001	-0.0071 ± 0.0001
	y - 556196.0800	-0.0006 ± 0.0001	-0.0020 ± 0.0001
	z - 4389355.1080	-0.0039 ± 0.0012	-0.0040 ± 0.0012
	$\dot{x}$ + 0.0156	+0.0018 ± 0.0001	+0.0024 ± 0.0001
	$\dot{y}$ - 0.0184	+0.0006 ± 0.0012	+0.0007 ± 0.0012
	$\dot{z}$ - 0.0089	+0.0048 ± 0.0002	+0.0044 ± 0.0001
Haleakala	x + 5466006.6900	+2.9163 ± 0.0019	+2.9168 ± 0.0019
	y + 2404427.2460	+1.2864 ± 0.0031	+1.2882 ± 0.0031
	z - 2242187.8750	+9.9607 ± 0.0078	+9.9610 ± 0.0078
	$\dot{x}$ + 0.0122 *	-	-
	$\dot{y}$ - 0.0622 *	-	-
	$\dot{z}$ - 0.0310 *	-	-
Matera	x - 4641978.8100 *	-	-
	y - 1393067.5310 *	-	-
	z - 4133249.4800 *	-	-
	$\dot{x}$ + 0.0180 *	-	-
	$\dot{y}$ - 0.0192 *	-	-
	$\dot{z}$ - 0.0140 *	-	-
McDonald	x + 1330781.4610	-0.0120 ± 0.0142	-0.0146 ± 0.0142
	y + 5328755.4550	-0.6717 ± 0.0037	-0.6682 ± 0.0037
	z - 3235697.5110	+0.6911 ± 0.0315	+0.6446 ± 0.0315
	$\dot{x}$ + 0.0124	-0.0040 ± 0.0006	-0.0041 ± 0.0006
	$\dot{y}$ - 0.0009	-0.0177 ± 0.0002	-0.0176 ± 0.0002
	$\dot{z}$ + 0.0053	+0.0343 ± 0.0014	+0.0325 ± 0.0014
MLRS1	x + 1330121.1440	+0.0920 ± 0.0234	+0.0875 ± 0.0234
	y + 5328532.2620	+0.0440 ± 0.0204	+0.0369 ± 0.0204
	z - 3236146.6030	-0.4753 ± 0.0213	-0.4798 ± 0.0213
	$\dot{x}$ + 0.0124 *	-	-
	$\dot{y}$ - 0.0009 *	-	-
	$\dot{z}$ + 0.0053 *	-	-
MLRS2	x + 1330021.1090	-0.0119 ± 0.0008	-0.0118 ± 0.0008
	y + 5328401.8580	-0.0171 ± 0.0003	-0.0148 ± 0.0003
	z - 3236480.7680	-0.0098 ± 0.0018	-0.0129 ± 0.0018
	$\dot{x}$ + 0.0124	+0.0004 ± 0.0004	+0.0005 ± 0.0004
	$\dot{y}$ - 0.0009	+0.0014 ± 0.0001	+0.0015 ± 0.0001
	$\dot{z}$ + 0.0053	+0.0003 ± 0.0007	+0.0007 ± 0.0007

Table A.2: Fitted values of selenocentric coordinates of reflectors (in meters). The reference values are from a previous release of INPOP (Fienga et al., 2014, p. 27).

Reflector	**Coordinate** [m]	**INPOP$_G$**	**INPOP17a**
Apollo 11	x - 1591924.5110	+42.2267 ± 0.0181	+42.1831 ± 0.0181
	y - 690802.5820	-103.0306 ± 0.0052	-102.9494 ± 0.0052
	z - 21003.7740	-0.1029 ± 0.0118	-0.1035 ± 0.0118
Apollo 14	x - 1652725.8400	-36.1039 ± 0.0196	-36.0924 ± 0.0196
	y + 520890.3070	-107.1523 ± 0.0140	-107.0555 ± 0.0140
	z + 109730.4800	-0.1173 ± 0.0028	-0.1287 ± 0.0028
Apollo 15	x - 1554674.5700	+3.8976 ± 0.0155	+3.8898 ± 0.0155
	y - 98196.2940	-100.6368 ± 0.0068	-100.5489 ± 0.0068
	z - 765005.6960	-0.5951 ± 0.0067	-0.6184 ± 0.0067
Lunakhod 1	x + 1330021.1090	-53.0291 ± 0.0149	-52.9913 ± 0.0149
	y + 5328401.8580	-71.7348 ± 0.0042	-71.6464 ± 0.0042
	z - 3236480.7680	-0.8370 ± 0.0021	-0.8250 ± 0.0021
Lunakhod 2	x - 1114345.4960	+49.3650 ± 0.0145	+49.3269 ± 0.0145
	y + 781226.5970	-86.7535 ± 0.0015	-86.6622 ± 0.0015
	z - 1076059.3350	-0.6976 ± 0.0083	-0.6982 ± 0.0083

Table A.3: Estimated values of station biases over different periods (2-way light time in cm)

Bias #	**Station**	**Date**	**Bias 2-way light time [cm]**	
			INPOP$_G$	**INPOP17a**
1	APOLLO	2006/04/07 - 2010/11/01	0.24 ± 0.01	-0.24 ± 0.01
2		2007/12/15 - 2008/06/30	-3.86 ± 0.04	-3.90 ± 0.04
3		2008/09/20 - 2009/06/20	2.83 ± 0.07	2.83 ± 0.07
4		2010/11/01 - 2012/04/07	-5.74 ± 0.04	-5.98 ± 0.04
5		2012/04/07 - 2013/09/02	9.18 ± 0.01	9.12 ± 0.01
6	Grasse	1984/06/01 - 1986/06/13	-8.76 ± 0.45	-6.49 ± 0.45
7		1987/10/01 - 2005/08/01	1.32 ± 0.07	2.47 ± 0.07
8		1993/03/01 - 1996/10/01	10.32 ± 0.02	10.38 ± 0.02
9		1996/12/10 - 1997/01/18	17.33 ± 0.06	16.92 ± 0.06
10		1997/02/08 - 1998/06/24	19.49 ± 0.01	19.56 ± 0.01
11		2004/12/04 - 2004/12/07	-5.74 ± 0.31	-7.07 ± 0.31
12		2005/01/03 - 2005/01/06	-5.39 ± 0.01	-6.72 ± 0.01
13		2009/11/01 - 2014/01/01	0.59 ± 0.08	0.34 ± 0.08
14		2015/12/20 - 2015/12/21	-	-88.34 ± 0.03
15		2016/06/01 - 2018/01/01	2.52 ± 0.01	2.46 ± 0.01
16	Haleakala	1984/11/01 - 1990/09/01	2.36 ± 0.29	2.55 ± 0.29
17		1984/11/01 - 1986/04/01	-3.76 ± 0.56	-3.61 ± 0.56
18		1986/04/02 - 1987/07/30	13.60 ± 0.02	13.07 ± 0.02
19		1987/07/31 - 1987/08/14	1.92 ± 0.64	1.83 ± 0.64
20		1985/06/09 - 1985/06/10	-12.25 ± 0.09	-13.18 ± 0.09
21		1987/11/10 - 1988/02/18	20.42 ± 0.42	19.49 ± 0.42
22		1990/02/06 - 1990/09/01	15.26 ± 0.11	14.32 ± 0.11
23	Matera	2003/01/01 - 2016/01/01	0.73 ± 7.24	4.62 ± 7.24
24	McDonald	1969/01/01 - 1985/07/01	-37.98 ± 1.20	-37.88 ± 1.20
25		1971/12/01 - 1972/12/05	28.71 ± 0.88	28.21 ± 0.88
26		1972/04/21 - 1972/04/27	88.17 ± 0.71	88.09 ± 0.71
27		1974/08/18 - 1974/10/16	-112.58 ± 0.37	-112.08 ± 0.37
28		1975/10/05 - 1976/03/01	30.48 ± 0.22	28.44 ± 0.22
29		1983/12/01 - 1984/01/17	10.49 ± 1.69	11.06 ± 1.69
30		1969/01/01 - 1971/12/31	2249.64 ± 0.83	2249.19 ± 0.83
31	MLRS1	1983/08/01 - 1988/01/28	39.99 ± 2.01	38.73 ± 2.01

Appendix B

Supplementary materials

B.1 Correlation matrix and partial derivatives

The correlation matrix (given in Fig. B.1) is obtained from the partial derivatives matrix (A_{ij}) used in Eqn. 5.1 using a standard python routine (pandas.dataframe.corr.py) which uses the Pearson standard correlation coefficient (Pearson, 1895). The partial derivatives of each parameter is obtained by the central differencing method using an appropriate δp_j (see Section 5.1.1). The plot of the partial derivatives w.r.t each retroreflector is given in Fig. B.2.

Figure B.1: Correlation between the parameters of the dynamical model and reduction model.

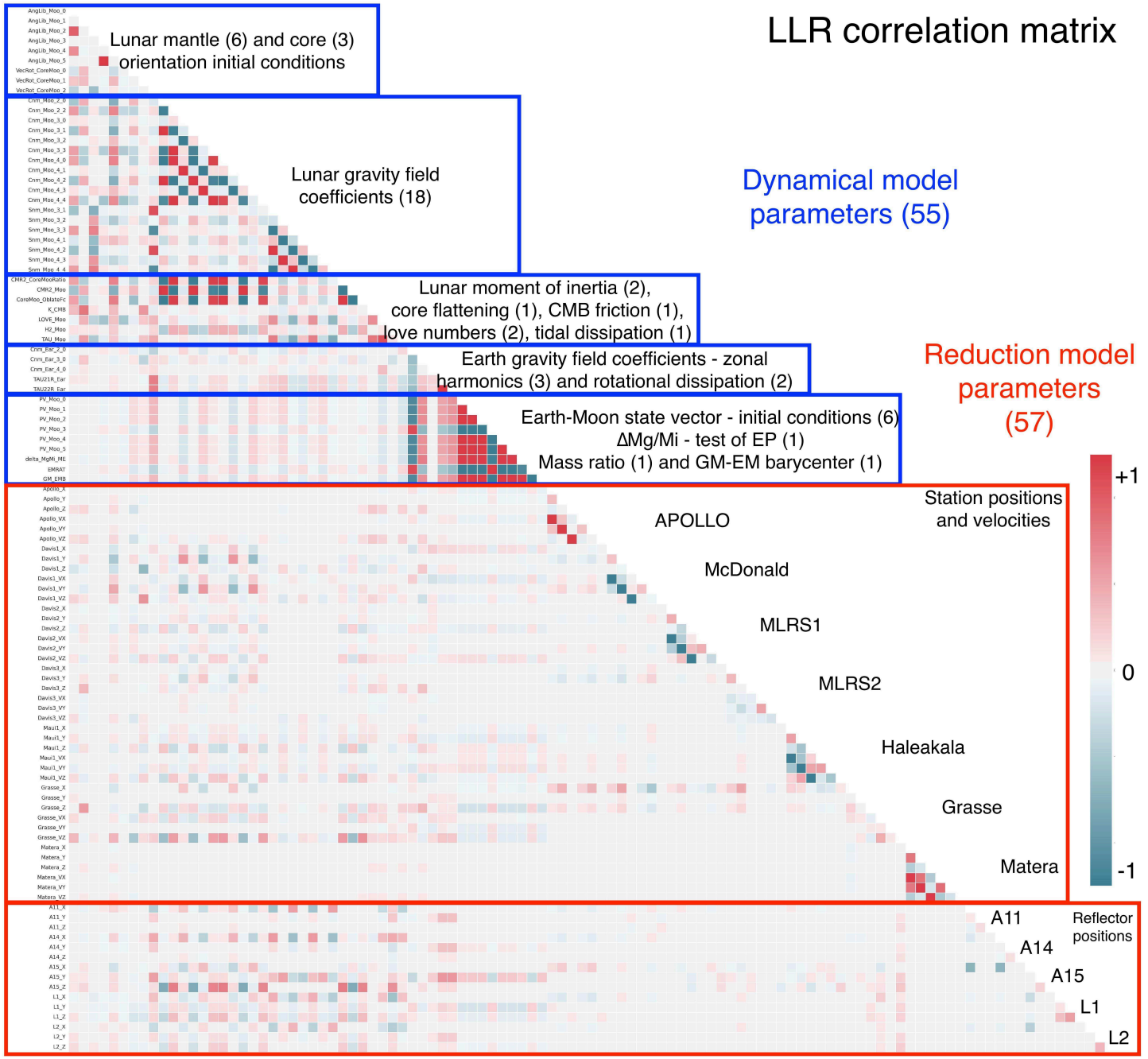

Figure B.2: Reflector-wise plot of partial derivatives of dynamical model parameters: A15 (Blue), A14 (Green), A11 (Black), L2 (Cyan), L1 (Red). δ indicates the amplitude of the deviation from the central value used for the respective parameter. Label X_c represents the parameter X with the subscript (c) indicating the lunar fluid core.

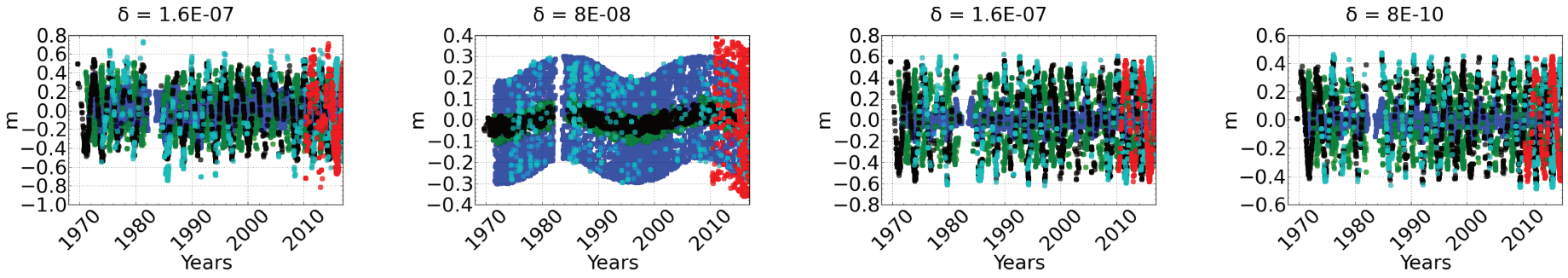

Euler angle ϕ | Euler angle θ | Euler angle ψ | Euler angle $\dot{\phi}$

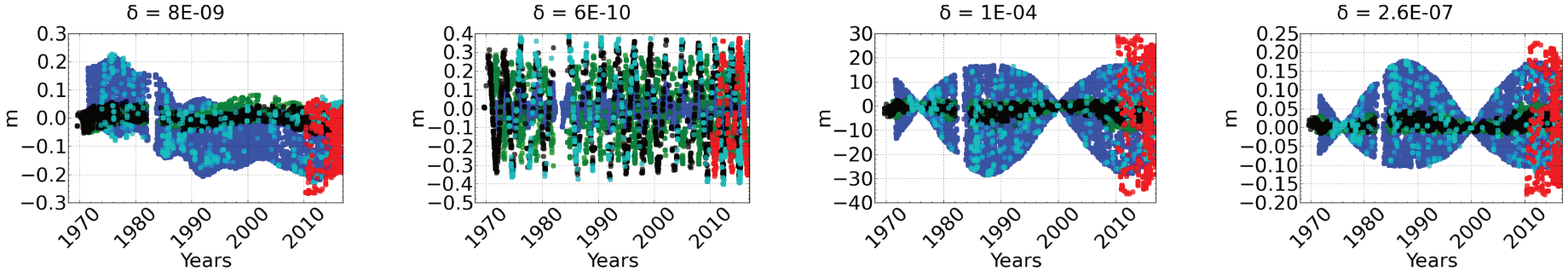

Euler angle $\dot{\theta}$ | Euler angle $\dot{\psi}$ | $\alpha_c = C_f/C_T$ | $\frac{C_T}{MR^2}$

Figure B.2: continued

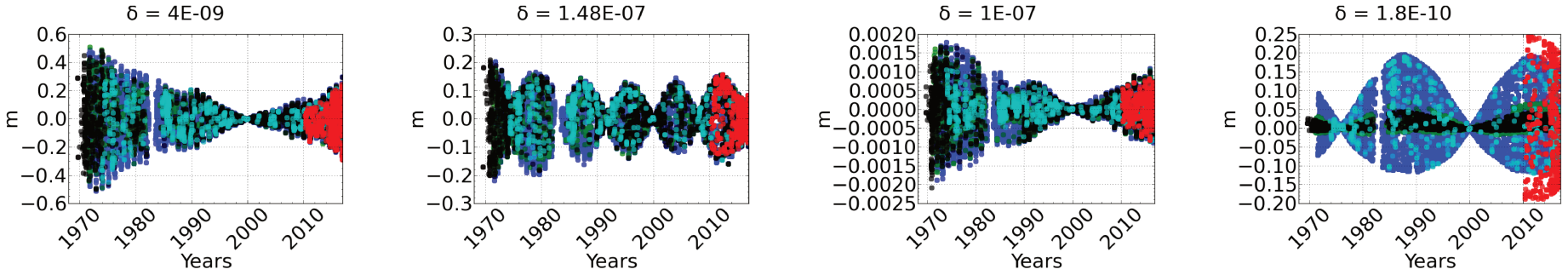

$C_{2,0}, Earth$ $C_{3,0}, Earth$ $C_{4,0}, Earth$ $C_{2,0}, Moon$

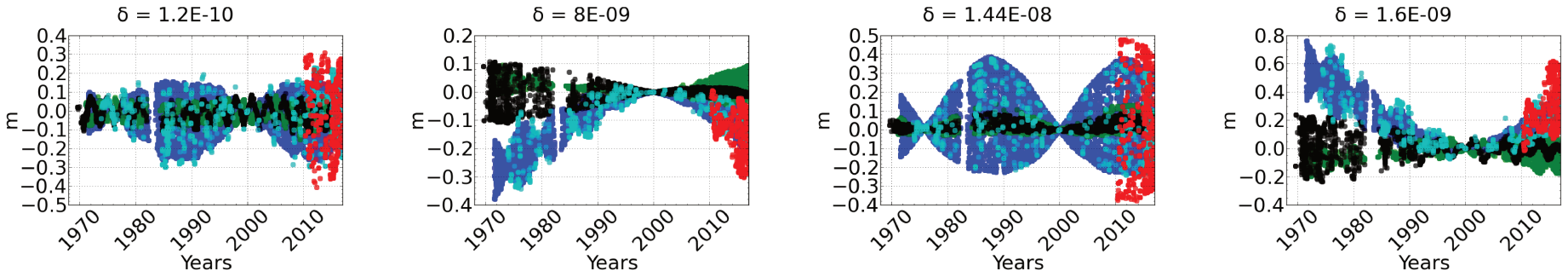

$C_{2,2}, Moon$ $C_{3,0}, Moon$ $C_{3,1}, Moon$ $C_{3,2}, Moon$

Figure B.2: continued

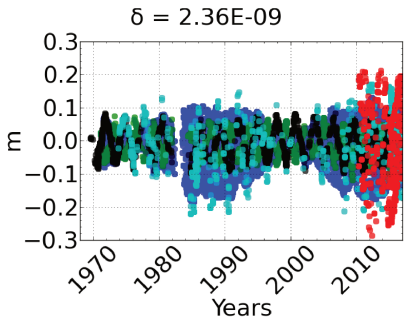

$C_{3,3}, Moon$

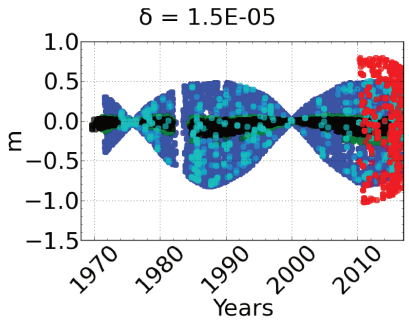

$C_{4,0}, Moon$

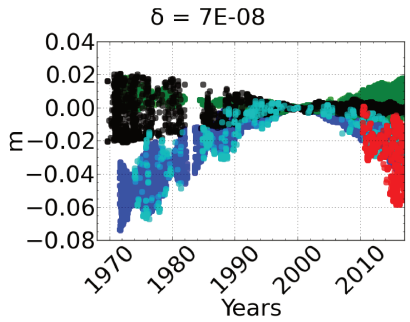

$C_{4,1}, Moon$

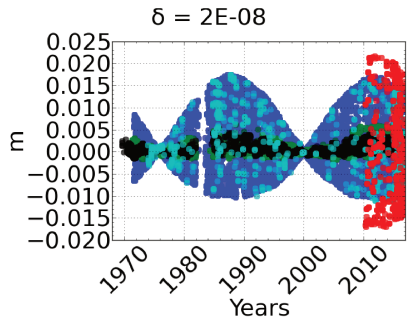

$C_{4,2}, Moon$

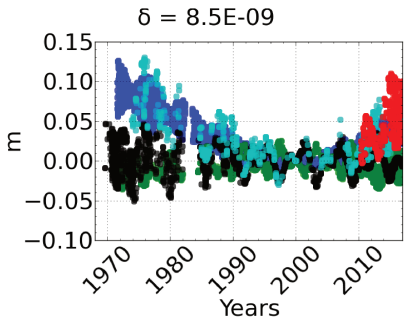

$C_{4,3}, Moon$

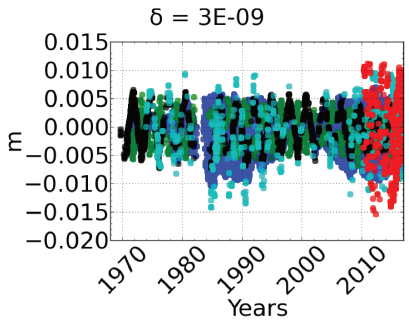

$C_{4,4}, Moon$

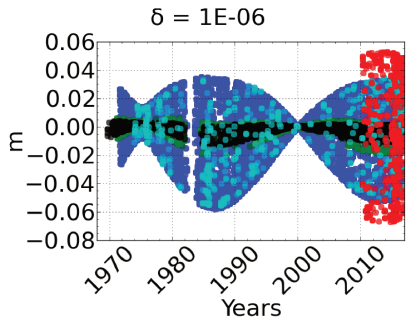

f_c

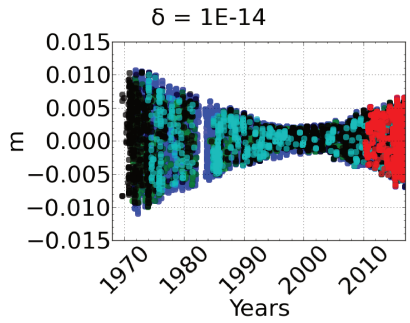

$\Delta(m^G/m^I)_{EM}$

Figure B.2: continued

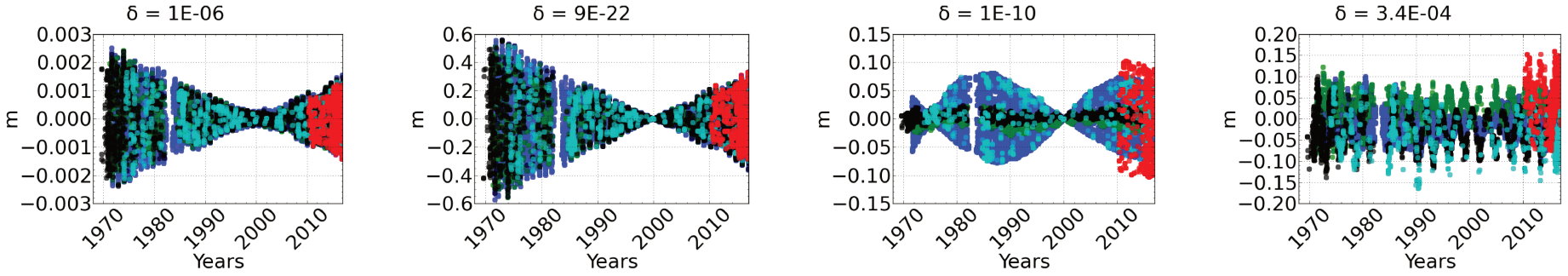

$EMRAT$ GM_{EMB} k_v $k_2, Moon$

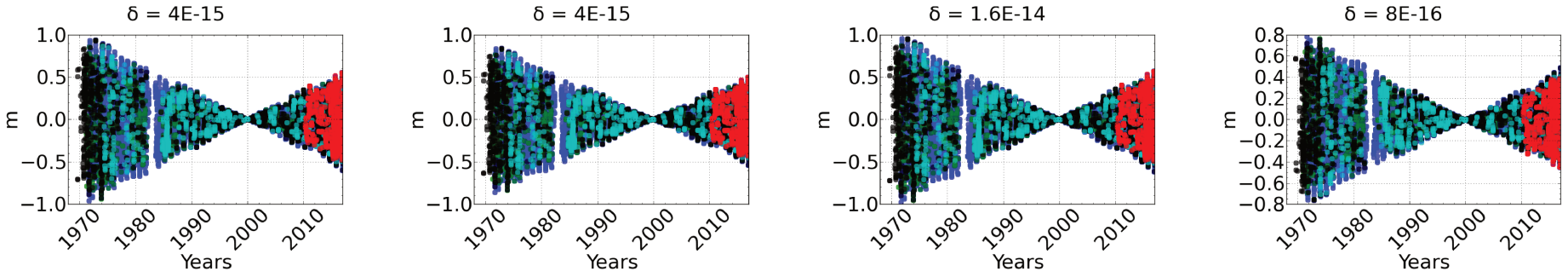

$\vec{r}_x, EM(t=0)$ $\vec{r}_y, EM(t=0)$ $\vec{r}_z, EM(t=0)$ $\vec{\dot{r}}_x, EM(t=0)$

Figure B.2: continued

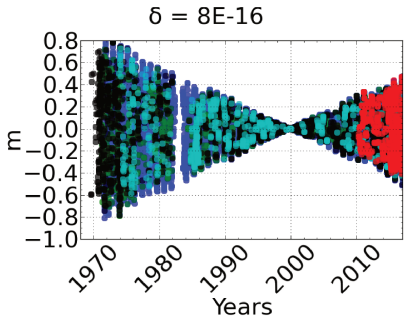

$\dot{\vec{r}}_y, EM(t=0)$

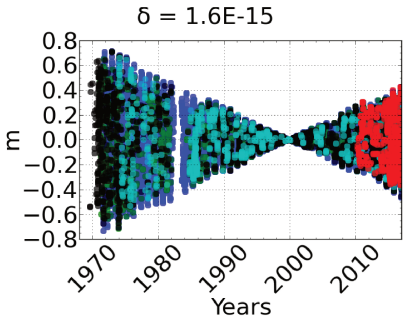

$\dot{\vec{r}}_z, EM(t=0)$

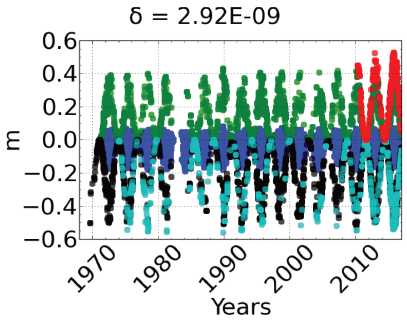

$S_{3,1}, Moon$

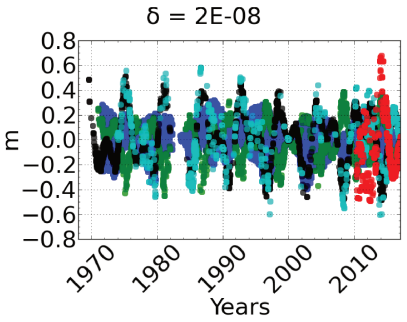

$S_{3,2}, Moon$

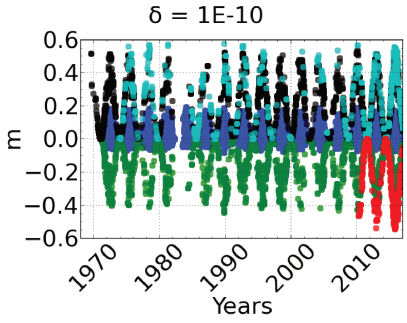

$S_{3,3}, Moon$

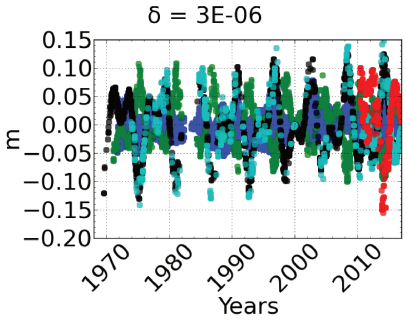

$S_{4,1}, Moon$

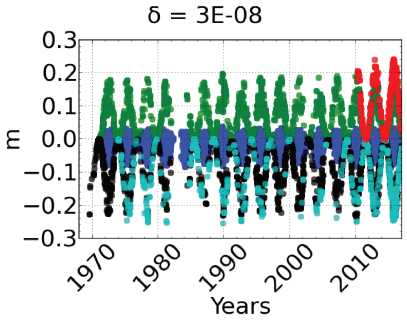

$S_{4,2}, Moon$

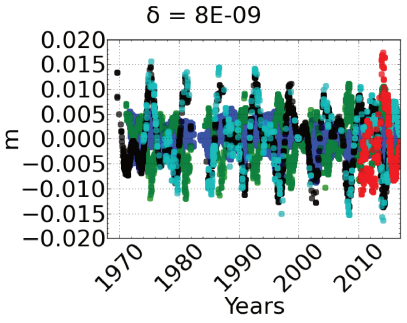

$S_{4,3}, Moon$

Figure B.2: continued

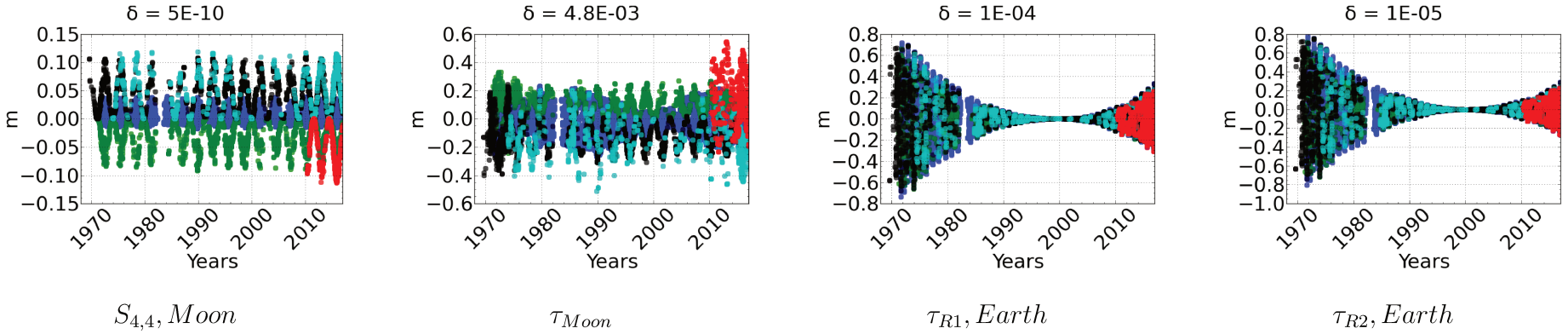

$S_{4,4}, Moon$ τ_{Moon} $\tau_{R1}, Earth$ $\tau_{R2}, Earth$

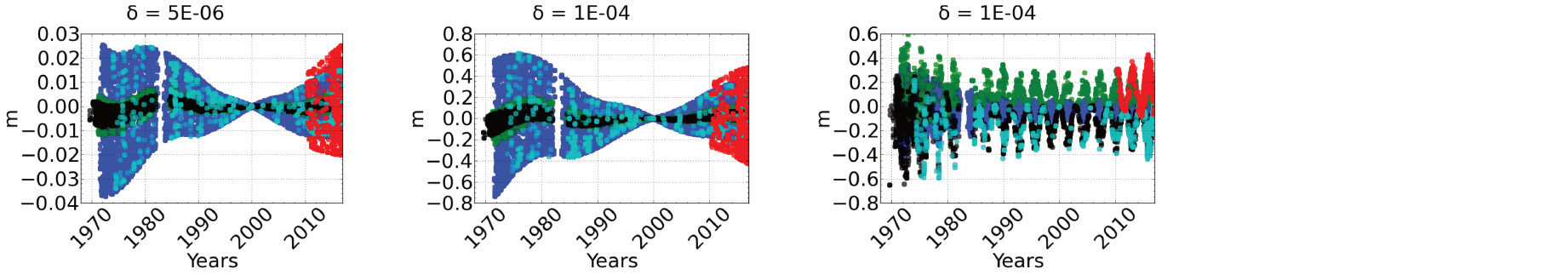

$\omega_{c,x}, Moon(t=0)$ $\omega_{c,y}, Moon(t=0)$ $\omega_{c,z}, Moon(t=0)$

B.2 Topographic coupling at CMB

This section provides the dynamical model equations relevant to the degree-3 topographic coupling at the CMB, used in Section 6.1.2. The spherical harmonic coefficients of the lunar fluid core are given as $C_{n,m}$, $S_{n,m}$ and the angular velocity vector as $\omega_{(x,m/f)}$. The subscript indicates the component (x) for the mantle (m) or the fluid core (f). Fig. B.8 shows the correlation between the non-zero degree-3 spherical harmonic coefficients of the lunar fluid core.

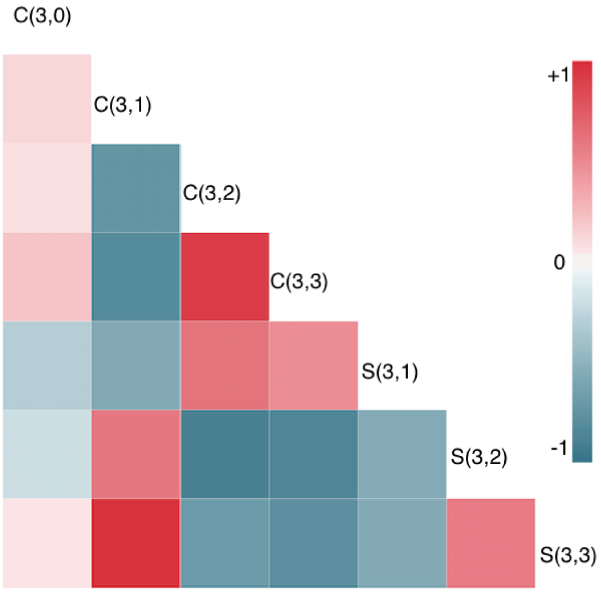

Figure B.8: Correlation between core degree-3 spherical harmonics arising from the topographic coupling at the core-mantle boundary of the Moon.

The following is the expression for the torque arising from the degree-3 topo-

graphic coupling at the core-mantle boundary (Rambaux, 2017):

$$
\begin{aligned}
N_{x,topo} = (\pi R_f)^2 \Bigg\{ & (-\frac{107}{224}) \cdot C_{(2,0)} \cdot S_{(2,1)} \cdot \omega^2_{(z,m)} \\
& (-\frac{45}{32})[C_{(2,1)} \cdot S_{(2,2)} \cdot \omega^2_{(z,m)} - C_{(2,2)} \cdot S_{(2,1)} \cdot \omega^2_{(z,m)}] \\
& (-\frac{1665}{3584}) \cdot C_{(3,0)} \cdot S_{(3,1)} \cdot \omega^2_{(z,m)} \\
& (-\frac{10093}{3584})[C_{(3,1)} \cdot S_{(3,2)} \cdot \omega^2_{(z,m)} - C_{(3,2)} \cdot S_{(3,1)} \cdot \omega^2_{(z,m)}] \\
& (-\frac{39475}{1792})[C_{(3,2)} \cdot S_{(3,3)} \cdot \omega^2_{(z,m)} - C_{(3,3)} \cdot S_{(3,2)} \cdot \omega^2_{(z,m)}] \\
& (+\frac{3}{8})[C_{(2,0)} \cdot \omega_{(y,m)}\omega_{(z,m)} + C_{(2,0)} \cdot \omega_{(z,m)}\omega_{(y,f)}] \\
& (+\frac{3}{4})[C_{(2,2)} \cdot \omega_{(y,m)}\omega_{(z,m)} + C_{(2,2)} \cdot \omega_{(z,m)}\omega_{(y,f)}] \\
& (-\frac{3}{4})[S_{(2,2)} \cdot \omega_{(x,m)}\omega_{(z,m)} + S_{(2,2)} \cdot \omega_{(z,m)}\omega_{(x,f)}] \\
& (-\frac{11}{8}) \cdot S_{(2,1)} \cdot \omega_{(z,m)}\omega_{(z,f)} \\
& (-\frac{11}{16}) \cdot S_{(2,1)} \cdot \omega^2_{(z,m)} \Bigg\} \\
N_{y,topo} = (\pi R_f)^2 \Bigg\{ & (-\frac{3}{8})[C_{(2,0)} \cdot \omega_{(z,m)}\omega_{(x,m)} + C_{(2,0)} \cdot \omega_{(z,m)}\omega_{(x,f)}] \\
& (+\frac{11}{8}) \cdot C_{(2,1)} \cdot \omega_{(z,m)}\omega_{(z,f)} \\
& (+\frac{3}{4})[C_{(2,2)} \cdot \omega_{(z,m)}\omega_{(x,m)} + C_{(2,2)} \cdot \omega_{(z,m)}\omega_{(x,f)} \\
& + S_{(2,2)} \cdot \omega_{(x,m)}\omega_{(y,m)} + S_{(2,2)} \cdot \omega_{(x,m)}\omega_{(y,f)}] \\
& (+\frac{11}{16}) \cdot C_{(2,1)} \cdot \omega^2_{(z,m)} \\
& (+\frac{107}{224}) \cdot C_{(2,0)}C_{(2,1)} \cdot \omega^2_{(z,m)} \\
& (+\frac{45}{32})[C_{(2,1)}C_{(2,2)} \cdot \omega^2_{(z,m)} + S_{(2,1)}S_{(2,2)} \cdot \omega^2_{(z,m)}] \\
& (+\frac{1665}{3584}) \cdot C_{(3,0)}C_{(3,1)} \cdot \omega^2_{(z,m)} \\
& (+\frac{10093}{3584})[C_{(3,1)}C_{(3,2)} \cdot \omega^2_{(z,m)} + S_{(3,1)}S_{(3,2)} \cdot \omega^2_{(z,m)}] \\
& (+\frac{39475}{1792})[C_{(3,2)}C_{(3,3)} \cdot \omega^2_{(z,m)} + S_{(3,2)}S_{(3,3)} \cdot \omega^2_{(z,m)}] \Bigg\} \\
N_{z,topo} = (\pi R_f)^2 \Bigg\{ & (-\frac{3}{8})[C_{(2,1)} \cdot \omega_{(z,m)}\omega_{(y,m)} + C_{(2,1)} \cdot \omega_{(z,m)}\omega_{(y,f)} \\
& - S_{(2,1)} \cdot \omega_{(z,m)}\omega_{(x,m)} - S_{(2,1)} \cdot \omega_{(z,m)}\omega_{(x,f)}] \Bigg\}
\end{aligned}
\tag{B.1}
$$

Appendix C

Article submitted to A&A: under revision

Astronomy & Astrophysics manuscript no. Viswanathan_AA_lettre_submit
September 18, 2017

Letter to the Editor

Possible degree-3 geometry of the lunar fluid core constrained with GRAIL and LLR

V. Viswanathan[1,2], A. Fienga[1,2], N. Rambaux[2], H. Manche[2], J. Laskar[2], M. Gastineau[2]

[1] Observatoire de la Côte d'Azur, CNRS-UMR Géoazur, Valbonne France
[2] IMCCE, CNRS/UMR8028, Observatoire de Paris, Paris, France

September 18, 2017

ABSTRACT

We use the INPOP planetary and lunar ephemeris and fit 48 years (1969-2017) of lunar laser ranging (LLR) data to our model. After a first validation of our models and procedures by following the DE430 JPL lunar ephemeris, we show that by fitting the integrated orbit and orientation parameters of the Moon to the LLR observations, we obtain residuals that contain a 6-year signature associated with a departure of the harmonic degree-3 components of the gravity field of the Moon from the model (GL0660b) derived from GRAIL observations. More specifically, in the equation of conservation of the angular momentum of the Moon fluid core, we take into account harmonic-3 degree torques from the Earth, which enables us to estimate the Stokes coefficients $C_{32} = (-5.63 \pm 0.02) \times 10^{-8}$ and $S_{32} = (5.1 \pm 0.1) \times 10^{-8}$ of the gravitational potential of the fluid core. The new solution is compatible with both the GRAIL-derived gravity field (GL0660b), as well as the LOLA-derived vertical displacement lunar Love number (h_2).

Key words. Moon, LLR, asymmetric fluid core, numerical ephemeris, INPOP

1. Introduction

The Earth-Moon system is an ideal laboratory for exploring the mechanism of evolution for the solar system bodies, in particular from the point of view of the dynamics, the rotation and the internal structure. Questions related to the scenario of the formation of the Moon by collision between the Earth and a Mars-like object - such as the amount of impactor material that could have formed the internal structure of the present Moon - are still unsolved. A characterization of the inner structure of the Moon would bring key answers to these questions.

With the exploration of the Moon by the US and the Russian missions, retro-reflector arrays were installed at the near-side. Centimetric measurements of the Earth-Moon distances by lunar laser ranging (LLR) have then been obtained for the last 48 years using laser tracking (Bender et al. (1973); Samain et al. (1998); Murphy (2013)). Moreover, seismological profiles were obtained during the APOLLO missions and re-analyzed recently by Weber et al. (2011); Garcia et al. (2011).

The characterization of the inner structure of the Moon can be investigated by the study of its gravity field and its rotational and orbital dynamics using dedicated space missions like GRAIL (Zuber et al. (2013); Konopliv et al. (2013)) and LLR measurements (Williams et al. (2014)). Recent results about tidal dissipation (Williams & Boggs (2015); Matsuyama et al. (2016)) were obtained from the construction of lunar ephemerides (Folkner et al. (2014); Pavlov et al. (2016)).

Since 2006, INPOP (e.g. Fienga et al. (2016)) has become a reference for space navigation and for scientific research in the solar system dynamics and in fundamental physics. This letter gives the main result in term of the degree-3 components of the gravitational potential of the lunar fluid core obtained with this new modeling.

2. Lunar Dynamical Model for an Asymmetric Fluid Core

A description of the dynamical model with the orbit interactions, frame and moment of inertia tensor definitions are provided in Appendix A. Meyer & Wisdom (2011) proposed a fluid core flattening parameter $f_c = 2.09 \times 10^{-4}$ computed theoretically for a hydrostatic fluid core with a non-hydrostatic mantle. The value of $f_c = (2.0 \pm 2.3) \times 10^{-4}$ from the LLR analysis by Williams (2009)) suggests a small deviation from the hydrostatic value, but with large error bars. Previously, this deviation was associated to the marginal detection of f_c and a possible correlation with other parameters during the estimation from the LLR observations. However, with an improved time span of quality LLR datasets (Murphy (2013); Courde et al. (2017)) and constraints provided by the analysis of GRAIL observations (Konopliv et al. (2013)) on the lunar gravity field and potential Love number (k_2), recent studies (Williams et al. (2014); Pavlov et al. (2016)) show stronger detection of f_c ($(2.47 \pm 0.04) \times 10^{-4}$ and $(2.46 \pm 1.4) \times 10^{-4}$, respectively). These estimated values continue to suggest a small but non-ignorable departure of f_c from its hydrostatic value.

The impact of the C_{22} parameter is very weak for the lunar fluid core (Goldreich (1967)). By using a density profile from Dumberry & Wieczorek (2016) and extending their approach to a triaxial fluid core case, we estimate a theoretical value of C_{22} for the fluid core equal to 6.10^{-9}, while the corresponding C_{20} value of the fluid core is 10 times greater. In using equations for a triaxial fluid core from Rambaux et al. (2007) and fixing the theoretical value of C_{22}, an undetectable variation of about 0.5 mm is induced on the Earth-Moon distance (below the current LLR data accuracy of $\approx$ 5 mm). Hence, for the scope of this study, we equate the equatorial moments within the lunar fluid core inertia tensor, while limiting our discussion to the departure

of the lunar fluid core from a purely ellipsoidal shape, from that followed by Folkner et al. (2014) and Pavlov et al. (2016).

The effects of a non-hydrostatic core-mantle boundary (CMB) topography on the Earth nutations were often ignored, being considered as of the second order (Dehant & Mathews (2015)). The impact of considering this departure from a hydrostatic case, has been studied by Wu & Wahr (1997), which introduces a net external gravitational torque on the fluid core within the dynamical model. This additional torque from the point mass Earth on the figure of the fluid core ($N_{c,figc-pmA}$) is modeled through Eqn. 28 from Folkner et al. (2014), which appears on the right hand side of Eqn. (1), as :

$$\frac{dL_c}{dt} + \omega_m \times L_c = -N_{CMB} + N_{c,figC-pmA} \quad (1)$$

It was noticed that among the degree-3 and degree-4 spherical harmonics of the lunar fluid core, only C_{32} and S_{32} induce perturbations detectable by the LLR data. Moreover, this additional torque is only computed from the point mass Earth while neglecting other bodies. For the purpose of comparison only solution S2 (Section 3.4) takes this additional torque into account, while other solutions (S0a, S0b and S1) neglect this effect.

3. Results

The lunar part of the INPOP ephemeris is generated by fitting numerically integrated orbit and orientation parameters of the Moon to the LLR observations. A weighted least square (WLS) regression procedure is used for the fit including weighting scheme, data filtering and bias estimations described in Appendix B. Table D.2 gives the list of the adjusted parameters of interest to this study. The reduction model for the LLR data analysis follows the IERS 2010 recommendations (Petit & Luzum (2010)), while using KEOF Earth orientation parameters (Ratcliff & Gross (2015)) as recommended by a recent study (Pavlov et al. (2016)). We consider three cases:

- The Solutions 0 with an axisymmetric core fitted to the LLR observations serves as a validation of our lunar model and analysis procedure, against the DE430 JPL planetary and lunar ephemeris analysis described in Folkner et al. (2014) and EPM IAA RAS ephemeris in Pavlov et al. (2016). Only 532 nm wavelength LLR data are used for matching with the DE430 and EPM ephemeris. Two different versions were considered:
  a. Solution 0a (S0a) with coefficients C_{32}, S_{32} and C_{33} as fitted parameters, like in Folkner et al. (2014); Pavlov et al. (2016);
  b. Solution 0b (S0b) with coefficients C_{32}, S_{32} and C_{33} fixed to values from GL0660b (Konopliv et al. (2013)) derived from GRAIL observations.
- The Solution 1 (S1) refers to the addition of two years of IR LLR observations (Courde et al. (2017)) following the same specification as of S0a.
- The Solution 2 (S2) introduces the modeling of an asymmetric fluid core with the additional harmonic-3 degree torques from the Earth included in the equation of conservation of the angular momentum of the lunar fluid core (Eqn. 1).

Solutions by Williams et al. (2014) and Pavlov et al. (2016) additionally solve for three coefficients to correct for periodic terms in the integrated physical longitude librations. This approach is guided by a semianalytical theory (Williams et al. (2001)). None of our integrated solutions follow this approach.

3.1. S0a: Validation

In S0a, we aim at validating our lunar dynamical model by comparing our lunar parameter estimates and LLR residuals, with that provided by Folkner et al. (2014) and Pavlov et al. (2016). In Folkner et al. (2014), Pavlov et al. (2016) and S0a, gravity field coefficients up-to degree and order 6 are used for the Moon (GL0660b (Konopliv et al. (2013))) and the Earth (GGM05C (Ries et al. (2016))). Coefficients C_{32}, S_{32} and C_{33} are then included in the fit parameters as they improve the overall post-fit residuals. For S0a, the improvement of the uncertainty compared to Pavlov et al. (2016), especially in the estimation of the parameter k_v/C_T, continues to indicate a strong dissipation mechanism within the Moon, through viscous torques at the fluid core-mantle boundary.

Differences between GL0660b values and fitted C_{32}, S_{32} and C_{33} from Folkner et al. (2014), Pavlov et al. (2016) or in S0a, are several orders of magnitude greater than the mean GRAIL uncertainties (see Konopliv et al. (2013)). These results suggest that some significant effects impacting the LLR observations, are absorbed by the adjustment of the degree-3 of the full Moon gravity field.

3.2. S0b: Asymmetric fluid core and fixed GRAIL gravity field coefficients

S0b is similar to S0a, but the coefficients of spherical harmonics (including C_{32}, S_{32} and C_{33}) are fixed to the GL0660b values. Post-fit residuals obtained with S0a and S0b are provided within Fig. 1. On constraining our analysis to GL0660b values, we noticed a strong 6-year libration period on all reflectors (except weakly on A15) with an amplitude of ±5 mm on the post-fit residuals of S0b (see Fig. 1). Such a degradation of the post-fit residuals affected by the described 6-year signature can be proposed to be due to the absence of a higher degree figure - point mass torque in the angular momentum balance equation for the fluid core, from the assumption of hydrostatic equilibrium within the dynamical model. We find through S0b that the deviation from GRAIL degree-3 spherical harmonics impact distinctly the dissipation terms (τ and k_v/C_T) estimated through LLR analyses, as well as the vertical displacement Love number (h_2) (see Table D.3). More generally, S0a and S0b provide fitted values consistent with Folkner et al. (2014) and Pavlov et al. (2016) (see tables within Appendix D).

3.3. S1: Addition of the new IR LLR data from Grasse

S1 includes additionally 1707 normal points (7% of the total LLR data till date) to the solution specifications of S0a. This new dataset is obtained from 2 years of operation in IR (1064 nm) wavelength at the ILRS station in Grasse. The new IR LLR data from Grasse is made publicly available on http://www.geoazur.fr/astrogeo/?href=observations/donnees/luneRG/brutes. A review of the technical developments, accuracy and the homogeneity in the distribution (both spatial and temporal) of this new dataset can be found in Courde et al. (2017). This dataset is weighted at the same level as the APOLLO station normal points within the estimation procedure (see Appendix B).

3.4. S2: Degree-3 components for the fluid core

Eckhardt (1973) has shown the influence of lunar physical librations of the Moon through its third and fourth degree harmonics

Table 1. Comparison between solutions: Extended body parameters for the Moon. Uncertainties are obtained from a 5% jackknife (JK) test, the least squares 1-σ uncertainties being either consistent or smaller than the JK estimations.* stands for values fixed to model (GL0660b) values from GRAIL. ‡ indicates that the h_2 reference value is extracted from Mazarico et al. (2014).

Parameter	S0a	S2
$(C_T/(m_M R^2) - 0.393140) \times 10^6$	7.3 ± 0.2	5.0 ± 0.2
$(C_{32} - 4.8404981 \times 10^{-6}) \times 10^9$	4.1 ± 0.3	0.0*
$(S_{32} - 1.6661414 \times 10^{-6}) \times 10^8$	1.704 ± 0.006	0.0*
$(C_{33} - 1.7116596 \times 10^{-6}) \times 10^8$	-1.19 ± 0.04	0.0*
$(\tau_M - 9 \times 10^{-2}) \times 10^4$ [d]	-2 ± 5	-56 ± 5
$(\frac{k_v}{C_T} - 1.6 \times 10^{-8}) \times 10^{10}$ [d^{-1}]	10.2 ± 0.4	17.9 ± 0.4
$(f_c - 2.1 \times 10^{-4}) \times 10^6$	41 ± 3	47 ± 3
$(C_{32}(Core) + 5.6 \times 10^{-8}) \times 10^{10}$	-	-3.0 ± 2
$(S_{32}(Core) - 5.0 \times 10^{-8}) \times 10^{10}$	-	5 ± 10
$(k_{2,M} - 0.024059) \times 10^3$	0.0*	0.0*
$(h_2 - 3.71 \times 10^{-2})^\ddagger \times 10^3$	6.6 ± 0.2	2.3 ± 0.2
$l_{2,m} - 1.07 \times 10^{-2}$	0.0*	0.0*
$Q_{27.212} - 45$ (derived)	3.2 ± 0.5	6.6 ± 0.3

from point mass interactions of the Earth with multiple effects on the lunar orbital and orientation parameters. S2 tests our hypothesis of a possible departure of the fluid core flattening from a purely hydrostatic value, by the inclusion of a net external gravitational torque acting on the degree-3 components (C_{32} and S_{32}) of the core.

A first result from S2, through the introduction of the figure of the fluid core, is the removal of the 6-year signature and the slight reduction of the residual dispersion (see Fig. 1). Only the coefficients C_{32} and S_{32} for the fluid core were fitted (along with other parameters in S0b), due to the large formal uncertainty on the other degree-3 and degree-4 harmonics from the estimation procedure. The other degree-3 and degree-4 components of the fluid core were fixed to 0.

Table 1 provides few of the parameters relevant to the fit of the lunar dynamical model. We find that the fitted value of vertical displacement Love number (h_2) in S2 becomes more compatible with the one obtained through the Lunar Orbiter Laser Altimeter (LOLA) derived value (Mazarico et al. (2014)). The dissipation quality factor $Q_{27.212}$ derived from the tidal time delay (27.212 days/$(2\pi\tau_M)$) notices a small increase from S0a, however, they remain within the error bar of Williams et al. (2014). The post-fit residuals obtained with S2 can be found in Appendix C. A list of the relevant fitted dynamical parameters can be found within tables provided in Appendix D.

4. Discussion

By considering an additional torque on the lunar fluid core as described in Section 2, we are able to absorb a 6-year signature in the LLR residuals, while remaining strictly to GRAIL-derived (GL0660b) gravity field coefficients and obtaining the same dispersion of the post-fit residuals (see Fig. 1). The additional torque has a degree-3 geometry. In this letter, it is modeled as an external gravitational torque on the lunar fluid core. An alternate origin might also be the pressure torque acting on the degree-3 interface at the core-mantle boundary. We consider two additional test solutions (S2b and S2c) for evaluating the robustness of our model and the reliability of our fit. Estimates from these two test solutions are provided in Table D.2.

S2b includes the potential Love number k_2 as a fitted parameter to the solution specifications of S2. The resulting estimates show a larger deviation of f_c away from its hydrostatic value, while the estimates from the other fitted parameters show a consistency within their respective uncertainties. However, this additional deviation is due to the correlation between f_c, k_2 and the fluid core moment of inertia (Williams et al. (2014)). This indicates that it is advisable to fix the value of k_2 to a spacecraft determined value for reducing the propagation of error to correlated parameters. For this reason, all our solutions (except S2b) uses GRAIL-derived k_2 for a higher reliability.

S2c follows the same solution specifications as S2, except that the degree-3 components of the gravitational potential (C_{32} and S_{32}) of the Moon are included as fitted parameters. On comparing the LLR estimates of C_{32} and S_{32}, it is noticed that the differences in percentages to GRAIL values are reduced by a factor 20 for C_{32} and a factor 10 for S_{32}. These results indicate that the fit of the lunar dynamical model to LLR observations seems to favor a departure from hydrostatic equilibrium for the fluid core through its degree-3 figure, in the direction of a better consistency with the GRAIL-derived gravity field. A larger deviation is noticed on the estimated fluid core degree-3 components (C_{32} and S_{32}) induced by its weak correlation with that of the full Moon (correlation coefficient of < 0.2). The uncertainty on the LLR estimated harmonic degree-3 components of the gravity field of the Moon remains at-least 3 order of magnitude greater than the uncertainty provided within the GL0660b model. Hence, it is advisable to fix the Moon gravity field to model values to avoid weakly determined parameters as well as correlations during the fit.

S2b and S2c give consistent estimations of parameters related to the fluid core departure from hydrostatic equilibrium, in favor of the assumptions used for the S2 construction and related to the correlation between GRAIL-derived gravity field harmonic degree-3 components, potential Love number k_2 and the fluid core harmonic degree-3 components (C_{32} and S_{32}).

5. Conclusion and future work

In this study, we have tested a possible estimation of the harmonic degree-3 component of the gravitational potential of the lunar fluid core through the introduction of the associated extended figure torques into the lunar fluid core's angular momentum balance differential equation within the INPOP ephemeris. This was done with a strictly GRAIL-derived (GL0660b) gravity field of the Moon. We have shown through our post-fit residuals (see Fig. 1) that the resulting 6-year signature from the degree-3 components of the gravitational potential of the lunar fluid core is absorbed, compared to previous LLR analyses by Folkner et al. (2014) and Pavlov et al. (2016), which preferred to fit the degree-3 harmonics of the Moon as well as correct for periodic terms in the integrated physical longitude librations, for better post-fit residuals.

We have verified that the degree-3 coefficients of the fluid core and that of the Moon have a maximum correlation coefficient of 0.2 over the entire time span of the LLR dataset. The signature induced on the Earth-Moon distance from these two set of harmonic coefficients (degree-3 of the lunar fluid core and that of the Moon) do not have the same effect. The test case S2c (provided within Appendix D) which fits both these sets of harmonic coefficients show that the deviation from GRAIL-derived (GL0660b) values are reduced by a factor of 20 for C_{32} and a factor of 10 for S_{32}.

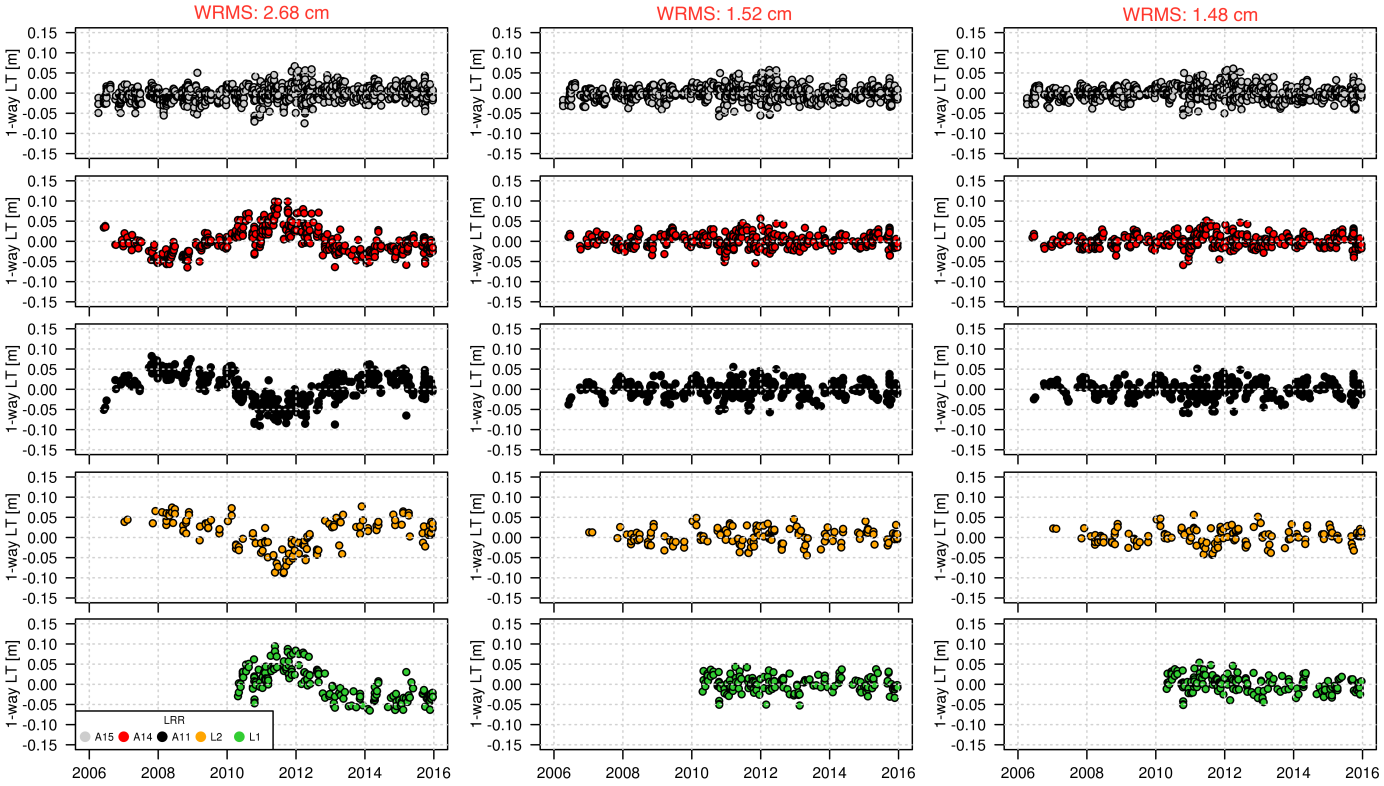

Fig. 1. Post-fit residuals (5-σ filtered 1-way light time (m)) obtained with the APOLLO station data vs time (years). Left: S0b with C_{32}, S_{32} and C_{33} fixed to GRAIL-derived GL0660b values; Center: S0a with C_{32}, S_{32} and C_{33} as fit parameters resulting in deviation from GL0660b values; Right: S2 with C_{32}, S_{32} and C_{33} fixed to GRAIL-derived GL0660b values, to solve for degree 3 shape of the fluid core.

Estimation of the fluid core flattening (f_c) is significantly constrained with the synergy between the LLR observations and a spacecraft-determined gravity field. On constraining our numerical model with a full Moon GRAIL-derived gravity field model (GL0660b), we show that a small but non-ignorable departure of the fluid core from an ellipsoidal shape can reconcile the LLR residuals, GRAIL-derived gravity field measurements and the LRO-LOLA estimations. Future work will address the problem of the frequency dependencies of the tidal dissipation effects by a direct integration in the Louville or Poincaré equations rather than a semi-analytical approach.

Acknowledgements. V.Viswanathan extends his sincere gratitude to: all the observers and engineers at Calern, APOLLO, McDonald, Matera and Haleakala for providing timely and accurate LLR measurements over the past 48 years; Y.Rogister for his comments on the letter and related discussions; A.Memin for the analysis of geodetic techniques at Calern to characterize the local hydrology loading; J.M.Torre and G.Kirchner for discussions on the normal point computation algorithm; J.C.Marty and S.Loyer for providing the developmental access to the CNES POD software (GINS).

References

Bender, P. L., Currie, D. G., Poultney, S. K., et al. 1973, Science, 182, 229
Courde, C., Torre, J., Samain, E., et al. 2017, Astronomy & Astrophysics
Dehant, V. & Mathews, P. 2015, Precession, Nutation and Wobble of the Earth (Cambridge University Press), 554
Dumberry, M. & Wieczorek, M. A. 2016, Journal of Geophysical Research: Planets, 121, 1264
Eckhardt, D. H. 1973, The Moon, 6, 127
Fienga, A., Laskar, J., Manche, H., & Gastineau, M. 2016, Astronomy & Astrophysics, 587, L8
Folkner, W. M., Williams, J. G., Boggs, D. H., Park, R. S., & Kuchynka, P. 2014, Interplanetary Network Progress Report, 196, C1
Garcia, R. F., Gagnepain-Beyneix, J., Chevrot, S., & Lognonné, P. 2011, Physics of the Earth and Planetary Interiors, 188, 96
Goldreich, P. 1967, Journal of Geophysical Research, 72, 3135
Konopliv, A. S., Park, R. S., Yuan, D.-N. N., et al. 2013, Journal of Geophysical Research: Planets, 118, 1415
Lyard, F., Lefevre, F., Letellier, T., & Francis, O. 2006, Ocean Dynamics, 56, 394
Manche, H. 2011, Theses, Observatoire de Paris
Matsuyama, I., Nimmo, F., Keane, J. T., et al. 2016, Geophys. Res. Lett., 43, 8365
Mazarico, E., Barker, M. K., Neumann, G. A., Zuber, M. T., & Smith, D. E. 2014, Geophysical Research Letters, 41, 2282
Meyer, J. & Wisdom, J. 2011, Icarus, 211, 921
Murphy, T. W. 2013, Reports on Progress in Physics, 76, 076901
Pavlov, D. A., Williams, J. G., & Suvorkin, V. V. 2016, Celestial Mechanics and Dynamical Astronomy, 126, 61
Petit, G. & Luzum, B. 2010, IERS Technical Note, 36
Rambaux, N., Van Hoolst, T., Dehant, V., & Bois, E. 2007, Astronomy & Astrophysics, 468, 711
Ratcliff, J. T. & Gross, R. S. 2015, Combinations of Earth Orientation Measurements: SPACE2014, COMB2014, and POLE2014, Tech. rep.
Ries, J., Bettadpur, S., Eanes, R., et al. 2016, The Combined Gravity Model GGM05C, Tech. rep.
Samain, E., Mangin, J. F., Veillet, C., et al. 1998, Astronomy & Astrophysics Supplement Series, 130, 235
Standish, E. 2003, JPL planetary ephemeris DE410 Interoffice Memorandum 312, Tech. rep., N-03-109
Viswanathan, V., Fienga, A., Manche, H., et al. 2016, in 20th International Workshop on Laser Ranging
Weber, R. C., Lin, P.-y., Garnero, E. J., Williams, Q., & Lognonné, P. 2011, Science, 331, 309
Williams, J. 2009, Lunar and Planetary Science Conference, 91109, 1452
Williams, J. G. & Boggs, D. H. 2015, Journal of Geophysical Research: Planets, 120, 689
Williams, J. G. & Boggs, D. H. 2016, Celestial Mechanics and Dynamical Astronomy, 126, 89
Williams, J. G., Boggs, D. H., Yoder, C. F., Ratcliff, J. T., & Dickey, J. O. 2001, Journal of Geophysical Research, 106, 27933
Williams, J. G., Konopliv, A. S., Boggs, D. H., et al. 2014, Journal of Geophysical Research: Planets, 119, 1546
Wu, X. & Wahr, J. M. 1997, Geophysical Journal International, 128, 18
Zuber, M. T., Smith, D. E., Watkins, M. M., et al. 2013, 339, 2011

Appendix A: Dynamical model description

Appendix A.1: Lunar orbit interactions:

In our model, we include the following accelerations perturbing the Moon's orbit:

1. Point mass mutual interactions from the Sun, planets and asteroids (through Eqn. 27 Folkner et al. (2014))
2. Point mass mutual interactions from the extended bodies (through Eqn. 28 Folkner et al. (2014)) which include :
   - the interaction of the zonal harmonics of the Earth through degree-6;
   - the interaction between the zonal, sectoral, and tesseral harmonics of the Moon through degree-6 and the point mass Earth, Sun, Jupiter, Saturn, Venus and Mars;
   - the interaction of the degree-2 zonal harmonic of the Sun.
3. Interaction from the Earth tides (through Eqn. 32 Folkner et al. (2014))
   The tidal acceleration from the tides due to the Moon and the Sun are separated into three frequency bands (zonal, diurnal and semi-diurnal). Each band is represented by a potential Love number $k_{2m,E}$ with a matching pair of time delays $\tau_{Xm,E}$ (where subscript X is either associated with the daily Earth rotation $\tau_{Rm,E}$ or orbital motion $\tau_{Om,E}$) to account for frequency dependent phase shifts from an anelastic Earth with oceans. Here the time delay represents the phase lag induced by the tidal components. Although the time delay method inherently assumes that the real component of $k_{2m,E}$ varies linearly with frequency, it reduces the complexity of the dynamical model. The diurnal $\tau_{R1,E}$ and semi-diurnal $\tau_{R2,E}$ are included as solution parameters in the LLR analysis, while model values for potential Love numbers for a solid Earth are fixed to that from Table 6.3 in Petit & Luzum (2010) followed by corrections from the ocean model FES2004 (Lyard et al. (2006)). A detailed explanation about the most influential tides relevant to the Earth-Moon orbit integration can be found in Table 6 in Williams & Boggs (2016).

Appendix A.2: Lunar orientation and inertia tensor:

1. Lunar frame and orientation.
   The mantle coordinate system is defined by the principal axes of the undistorted mantle, whose moments of inertia matrix are diagonal. The time varying mantle Euler angles ($\phi_m(t)$,$\theta_m(t)$,$\psi_m(t)$) define the orientation of the principal axis (PA) frame with respect to the inertial ICRF2 frame (see Folkner et al. (2014) for details). The time derivatives of the Euler angles are defined through Eqn. 14 Folkner et al. (2014).
2. Lunar moment of inertia tensor.
   The undistorted total moment of inertia of the Moon $\tilde{\mathrm{I}}_T$ is given by:

$$\tilde{I}_T = \frac{\tilde{C}_T}{m_M R_M^2}\begin{bmatrix}1&0&0\\0&1&0\\0&0&1\end{bmatrix}+\begin{bmatrix}\tilde{C}_{2,0,M}-2\tilde{C}_{2,2,M}&0&0\\0&\tilde{C}_{2,0,M}+2\tilde{C}_{2,2,M}&0\\0&0&0\end{bmatrix} \tag{A.1}$$

   where $\tilde{C}_{n,m,M}$ is the unnormalized degree-n, order m of the Stokes coefficient $C_{n,m}$ for the spherical harmonic model of the undistorted Moon and $\tilde{C}_T$ is the undistorted polar moment of inertia of the Moon normalized by it's mass m_M and radius squared R_M^2. Through Eqn. (A.1), we are able to directly use the undistorted value of C_{22} (Manche (2011)) from GRAIL-derived spherical harmonic model of Konopliv et al. (2013). The moment of inertia of the fluid core I_c is given by:

$$I_c = \alpha_c \tilde{C}_T \begin{bmatrix}1-f_c&0&0\\0&1-f_c&0\\0&0&1\end{bmatrix} = \begin{bmatrix}A_c&0&0\\0&B_c&0\\0&0&C_c\end{bmatrix} \tag{A.2a}$$

   where α_c is the ratio of the fluid core polar moment of inertia C_c to the undistorted polar moment of inertia of the Moon C_T, A_c and B_c are the equatorial moments of the fluid core and f_c is the fluid core flattening given as:

$$f_c\alpha_c = [C_c - \frac{A_c+B_c}{2}]/C_T \tag{A.2b}$$

   The moment of inertia of the mantle I_m has a rigid-body contribution $\tilde{I}_m$ and two time varying contributions due to the tidal distortion of the Earth and spin distortion as given in Eqn. 41 of (Folkner et al. (2014)). The undistorted moment of inertia of the mantle is obtained using the tide free second degree gravity field coefficients from GRAIL, given by:

$$\tilde{I}_m = \tilde{I}_T - I_c \tag{A.2c}$$

   The single time delay model (characterized by τ_M) allows for dissipation when flexing the Moon (Williams et al. (2001), Standish (2003), Folkner et al. (2014)).
3. Lunar angular momentum and torques.
   The time derivative of the angular momentum vector is equal to the sum of torques (N) acting on the body. In the rotating mantle frame, the angular momentum differential equation for the mantle is given by:

$$\frac{d}{dt}I_m\omega_m + \omega_m \times I_m\omega_m = N \tag{A.2d}$$

   where N is the sum of torques on the lunar mantle from the point mass body A ($N_{M,figM-pmA}$), figure-figure interaction between the Moon and the Earth ($N_{M,figM-figE}$) and the viscous interaction between the fluid core and the mantle (N_{CMB}).
   The motion of the uniform fluid core is controlled by the mantle interior, with the fluid core moment of inertia (I_c) constant in the frame of the mantle. The angular momentum differential equation of the fluid core in the mantle frame is then given by:

$$\frac{d}{dt}I_c\omega_c + \omega_m \times I_c\omega_c = -N_{CMB} \tag{A.2e}$$

   with

$$N_{CMB} = k_v(\omega_c - \omega_m) + (C_c - A_c)(\hat{z}_m \cdot \omega_c)(\hat{z}_m \times \omega_c) \tag{A.2f}$$

   where k_v is the coefficient of viscous friction at the CMB and $\hat{z}_m$ is a unit vector aligned with the polar axis of the mantle frame. The second part on the right-hand side of Eqn. (A.2f) is the inertial torque on an axis-symmetric fluid core.

Appendix B: Reduction model and fitting procedure

The reduction model for the LLR data analysis has been implemented within a precise orbit determination and geodetic software: GINS (Viswanathan et al. (2016)) maintained by space geodesy teams at GRGS/OCA/CNES and written in Fortran90. The modeling follows the recommendations of IERS 2010 (Petit

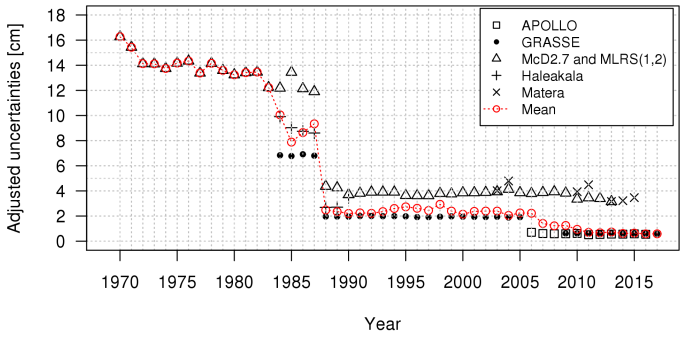

Fig. B.1. Annual mean of weights from different LLR stations after adjustments to the uncertainties present within the LLR observation (converted to 1-way LT [cm]).

& Luzum (2010)). A detailed description of the reduction model used for this study is provided in Manche (2011).

The observations are weighted after adjustments to the uncertainties present within the LLR observations. The annual weights used for the observations from each of the LLR stations can be found in Figure B.1.

A filtering scheme is enforced during the iterative fit of the parameters based on a 3-σ filter (σ recomputed at each iteration). Changes in the ground station introduce biases in the residuals. These biases correspond either with a known technical development at the station (new equipment, change of optical fiber cables) or systematics. Any estimated bias can be correlated with a corresponding change in the ground station, provided the incidents have been logged.

Appendix C: Post-fit residuals

Appendix D: Solution estimates comparison

Table C.1. LLR observations from ILRS ground stations with corresponding time span and number of normal points available, with the new IR dataset from Grasse in bold.

Code	Station	Time span	Normal points		S2 WRMS
		[yyyy/mm/dd]	Available	Used	[cm]
70610	Apache Point, NM, USA (group A)	2006/04/07 - 2010/10/30	941	929	1.27
70610	Apache Point, NM, USA (group B)	2010/12/01 - 2012/04/05	506	486	1.95
70610	Apache Point, NM, USA (re-group C)	2012/04/07 - 2013/09/01	361	345	1.52
70610	Apache Point, NM, USA (group D)	2013/09/30 - 2016/11/25	832	800	1.15
01910	Grasse, FR (693.8 nm Ruby laser)	1984/04/07 - 1986/06/12	1187	1151	14.19
01910	Grasse, FR (532.0 nm Nd:YAG laser)	1986/03/22 - 2005/07/30	8312	8110	3.22
01910	Grasse, FR (532.0 nm MeO laser)	2009/11/11 - 2017/02/07	1898	1831	1.42
01910	Grasse, FR (1064.0 nm Nd:YAG laser)	1989/09/23 - 1992/02/08	13	13	2.27
01910	**Grasse, FR (1064.2 nm MeO laser)**	**2015/03/11 - 2017/02/19**	**1707**	**1673**	**1.43**
56610	Haleakala, HI, USA	1984/11/13 - 1990/08/30	770	728	4.96
07941	Matera, IT	2003/02/22 - 2015/06/25	113	64	2.63
71110	McDonald, TX, USA	1969/08/20 - 1985/06/30	3604	3392	18.96
71111	MLRS1, TX, USA	1983/08/02 - 1988/01/27	631	513	20.44
71112	MLRS2, TX, USA	1988/02/29 - 2015/03/25	3670	3108	3.52
	TOTAL	**1969/08/20 - 2017/02/19**	**24545**		

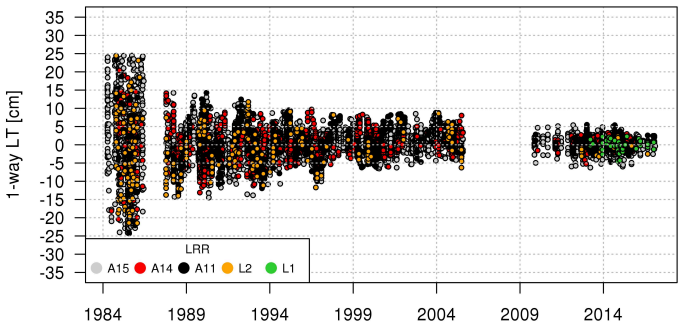

a) GRASSE station with the 532 nm wavelength

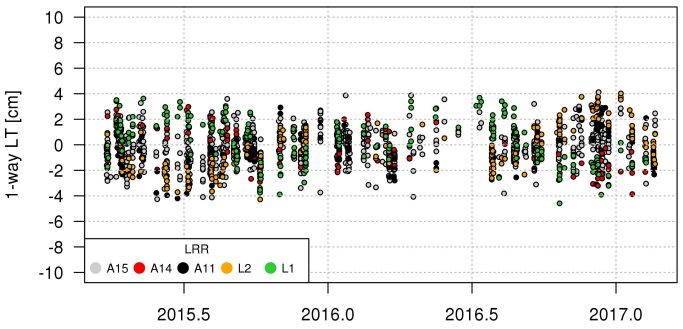

b) GRASSE station with the 1064 nm wavelenth

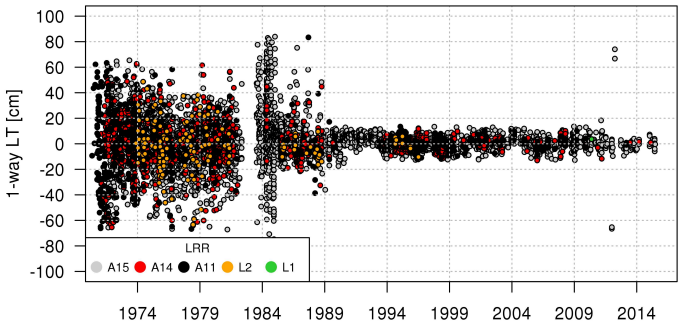

c) McDonald, MLRS1, MLRS2, Haleakala and Matera stations

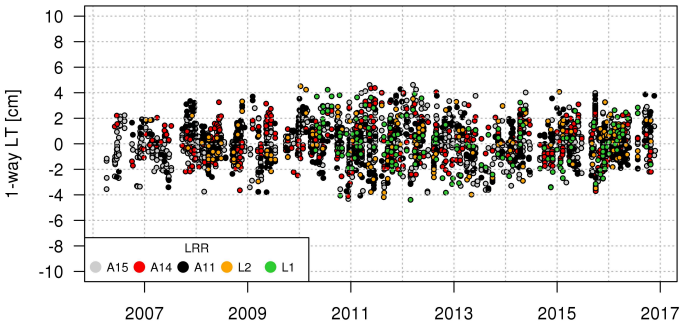

c) APOLLO station

Fig. C.1. Post-fit residuals in (cm) vs time (year) obtained with Solution 2 (S2) specification (Section 3.4) for : a) GRASSE station with the 532 nm wavelength, b) GRASSE station with the 532 nm wavelength, c) McDonald, MLRS1, MLRS2, Haleakala and Matera stations, d) APOLLO station. Post-fit residuals are filtered at 5-σ.

Table D.1. Fixed parameters for the Earth-Moon system.

Parameter	Units	S0a	DE430	EPM
$(EMRAT^{\dagger} - 81.300570) \times 10^6$		1	-1	-1
$(R_E - 6378.1366) \times 10^4$	km	0.0	-3	0.0
$(\dot{J}_{2E} - 2.6 \times 10^{-11})$	year^{-1}	0.0	0.0	0.0
$(k_{20,E} - 0.335)$		0.0	0.0	0.0
$(k_{21,E} - 0.32)$		0.0	0.0	0.0
$(k_{22,E} - 0.30102)$		-0.01902	0.01898	-0.01902
$(\tau_{O0,E} - 7.8 \times 10^{-2}) \times 10^2$	day	0.0	-1.4	0.0
$(\tau_{O1,E} + 4.4 \times 10^{-2})$	day	0.0	0.0‡	0.0
$\tau_{O2,E} + 1.13 \times 10^{-1}) \times 10^1$	day	0.0	0.13	0.0
$(R_M - 1738.0)$	km	0.0	0.0	0.0
$(\alpha_C - 7.0 \times 10^{-4})$		0.0	0.0	0.0
$(k_{2,M} - 0.024059)$		0.0	0.0	0.0
$(l_2 - 0.0107)$		0.0	0.0	0.0

†: EMRAT is fit during the joint analysis between the lunar and planetary part.
‡: $\tau_{O1,E}$ in Folkner et al. (2014) given as -0.0044 is a typographical error.

Table D.2. Extended body parameters for the Earth and the Moon. Uncertainties for S0a (1-σ) are obtained from a 5% jackknife (JK), while other solutions (DE430 and EPM) are assumed as (1-σ) formal uncertainties. †: C_{32}, S_{32} and C_{33} are reference values from the GRAIL analysis by Konopliv et al. (2013). ‡: h_2 reference value from LRO-LOLA analysis by Mazarico et al. (2014).

Parameter	Units	S0a	DE430	EPM
$(GM_{EMB} - 8.99701140 \times 10^{-10}) \times 10^{19}$	AU^3/day^2	-2 ± 1	-10	10 ± 5
$(\tau_{R1,E} - 7.3 \times 10^{-3}) \times 10^5$	day	1 ± 4	6 ± 30	57 ± 5
$(\tau_{R2,E} - 2.8 \times 10^{-3}) \times 10^5$	day	9.3 ± 0.4	-27 ± 2	5.5 ± 0.4
$(C_T/(m_M R^2) - 0.393140) \times 10^6$		7.3 ± 0.2	2 (derived)	2 (derived)
$(C_{32} - 4.8404981 \times 10^{-6\dagger}) \times 10^9$		4.1 ± 0.3	4.4	4.4 ± 0.1
$(S_{32} - 1.6661414 \times 10^{-6\dagger}) \times 10^8$		1.704 ± 0.006	1.84	1.84 ± 0.02
$(C_{33} - 1.7116596 \times 10^{-6\dagger}) \times 10^8$		-1.19 ± 0.04	-3.6	-4.2 ± 0.2
$(\tau_M - 9 \times 10^{-2}) \times 10^4$	day	-2 ± 5	58.0 ± 100	60 ± 10
$(\frac{k_v}{C_T} - 1.6 \times 10^{-8}) \times 10^{10}$	day^{-1}	10.2 ± 0.4	4.0 ± 10.0	3.0 ± 2.0
$(f_c - 2.1 \times 10^{-4}) \times 10^6$		41 ± 3	36 ± 28	37 ± 4
$(h_2 - 3.71 \times 10^{-2\ddagger}) \times 10^3$		6.6 ± 0.2	11.0 ± 6	6 ± 1
$Q_{27.212} - 45$ (derived)		3.2 ± 0.5	0 ± 5	0 ± 1

Table D.3. Comparison between solutions: Extended body parameters for the Earth, Moon and mass parameters for the Earth-Moon system. Uncertainties (1-σ) are obtained from a 5% jackknife (JK). †: C_{32}, S_{32} and C_{33} are reference values from the GRAIL analysis by Konopliv et al. (2013). ‡: h_2 reference value from LRO-LOLA analysis by Mazarico et al. (2014).

Parameter	Units	S0b	S1	S2	S2b	S2c
$(GM_{EMB} - 8.99701140 \times 10^{-10}) \times 10^{19}$	AU^3/day^2	7 ± 4	4 ± 2	6.0 ± 0.5	7.2 ± 0.5	6.1 ± 0.5
$(\tau_{R1,E} - 7.3 \times 10^{-3}) \times 10^5$	day	-7 ± 7	6 ± 3	3 ± 9	-12 ± 14	6 ± 4
$(\tau_{R2,E} - 2.80 \times 10^{-3}) \times 10^5$	day	16.0 ± 0.8	8.7 ± 0.3	10.0 ± 0.9	11.5 ± 0.9	9.6 ± 0.3
$(C_T/m_M R_M^2 - 3.93140 \times 10^{-1}) \times 10^6$		-0.6 ± 0.2	8.2 ± 0.2	5.0 ± 0.2	9.0 ± 0.5	5.1 ± 0.2
$(C_{32} - 4.8404981 \times 10^{-6\dagger}) \times 10^9$		fixed	3.9 ± 0.3	fixed	fixed	0.2 ± 0.3
$(S_{32} - 1.6661414 \times 10^{-6\dagger}) \times 10^8$		fixed	1.664 ± 0.006	fixed	fixed	0.189 ± 0.006
$(C_{33} - 1.7116596 \times 10^{-6\dagger}) \times 10^8$		fixed	-2.39 ± 0.04	fixed	fixed	fixed
$(\tau_M - 9 \times 10^{-2}) \times 10^4$	day	298 ± 7	-34 ± 3	-56 ± 5	-17 ± 7	-56 ± 5
$(\frac{k_v}{C_T} - 1.6 \times 10^{-8}) \times 10^{10}$	day^{-1}	-33 ± 1	14.9 ± 0.5	17.9 ± 0.4	14 ± 1	18.1 ± 0.2
$(f_c - 2.1 \times 10^{-4}) \times 10^6$		36 ± 5	42 ± 3	47 ± 3	97 ± 6	48 ± 3
$(h_2 - 3.71 \times 10^{-2\ddagger}) \times 10^3$		3.6 ± 0.5	6.8 ± 0.2	2.3 ± 0.2	1.4 ± 0.1	2.7 ± 0.2
$(k_{2,M} - 0.024059) \times 10^3$		fixed	fixed	fixed	-1 ± 1	fixed
$(C_{32}(Core) + 5.6 \times 10^{-8}) \times 10^{10}$		NA	NA	-3 ± 2	-3 ± 2	61 ± 40
$(S_{32}(Core) - 5.0 \times 10^{-8}) \times 10^{10}$		NA	NA	5 ± 10	23 ± 10	-33 ± 60
$Q_{27.212} - 45$ (derived)		-8.9 ± 0.2	5.0 ± 0.2	6.6 ± 0.3	4 ± 0.25	6.6 ± 0.3

Appendix D

Article submitted to MNRAS

MNRAS **000**, 1–13 (2018) Preprint 7 February 2018 Compiled using MNRAS LATEX style file v3.0

The new lunar ephemeris INPOP17a and its application to fundamental physics

V. Viswanathan,[1,2]★ A. Fienga,[1,2] O. Minazzoli,[3,4] L. Bernus,[2] J. Laskar,[2] M. Gastineau[2]
[1]*AstroGéo, Géoazur - CNRS UMR 7329 - Observatoire de la Côte d'Azur, 250 Rue Albert Einstein, 06560 Valbonne*
[2]*ASD, IMCCE - CNRS UMR 8028 - Observatoire de Paris, 61 Avenue de l'Observatoire, 75014 Paris*
[3]*Centre Scientifique de Monaco, 8 Quai Antoine Ier, MC 98000, Monaco*
[4]*Artemis - CNRS UMR 7250 - Observatoire de la Côte d'Azur, 96 Boulevard de l'Observatoire, 06300 Nice*

Accepted 09-Jan-2018. Received 25-Oct-2017

ABSTRACT
We present here the new INPOP lunar ephemeris, INPOP17a. This ephemeris is obtained through the numerical integration of the equations of motion and of rotation of the Moon, fitted over 48 years of Lunar Laser Ranging (LLR) data. We also include the 2 years of infrared (IR) LLR data acquired at the Grasse station between 2015 and 2017. Tests of the universality of free fall are performed. We find no violation of the principle of equivalence at the (-3.8 ± 7.1) × 10^{-14} level. A new interpretation in the frame of dilaton theories is also proposed.

Key words: Moon, ephemerides, gravitation

1 INTRODUCTION

The Earth-Moon system is an ideal tool for carrying out tests of general relativity and more particularly the test of the universality of free fall (Nordtvedt 1968a; Anderson et al. 1996). Since 1969, the lunar laser ranging (LLR) observations are obtained on a regular basis by a network of laser ranging stations (Faller et al. 1969; Bender et al. 1973), and currently with a millimeter-level accuracy (Samain et al. 1998; Murphy 2013). Thanks to this level of accuracy at the solar system scale, the principle of the universality of free fall (UFF) can in theory be tested. However, at these accuracies (of 1 cm or below), the tidal interactions between the Earth and the Moon are complex to model, especially when considering that the inner structure of the Moon is poorly known (Wieczorek 2007; Williams & Boggs 2015). This explains why the UFF test is only possible after an improvement of the dynamical modeling of the Earth-Moon interactions.

Recently, thanks to the GRAIL mission, an unprecedented description of the shape of the lunar gravity field and its variations were obtained for the 6 months of the duration of the mission (Konopliv et al. 2014; Lemoine et al. 2014). This information is crucial for a better understanding of the dissipation mechanism over longer time span (Matsumoto et al. 2015; Williams & Boggs 2015; Matsuyama et al. 2016). Furthermore, since 2015, the Grasse station which produces more than 50 % of the LLR data, has installed a new detection path at 1064 nm (IR) ranging wavelength leading to a significant increase of the number of observations and of the signal to noise ratio (Courde et al. 2017).

Together with these new instrumental and GRAIL developments, the Moon modeling of the INPOP planetary ephemeris was improved. Since 2006, INPOP has become a reference in the field of the dynamics of the solar system objects and in fundamental physics (Fienga et al. 2011, 2016).

The INPOP17a version presented here also benefits some of the planetary improvements brought by the use of updated Cassini deduced positions of Saturn. The planetary and lunar Chebyshev polynomials built from INPOP17a have been made available on the INPOP website[1] together with a detailed technical documentation (Viswanathan et al. 2017).

Since 2010, thanks to the millimeter-level accuracy of the LLR measurements and the developments in the dynamical modeling of the Earth-Moon tidal interactions, differences in acceleration of Earth and Moon in free fall towards the direction of the Sun could reach an accuracy of the order of 10^{-14} (Merkowitz 2010; Williams et al. 2012). With the improvement brought by GRAIL, addition of IR LLR observations and the recent improvement of the dynamical modeling of INPOP17a, one can expect to confirm or improve this limit.

In this paper, we first present (see section 2.1) the statistics related to the IR dataset obtained at the Grasse station since 2015. In section (2.2), we introduce the updated dynamical model of the Moon as implemented in the INPOP planetary ephemeris including contributions from the shape of the fluid core. In section (2.4), we explain how we use the IR data to fit the lunar dynamical model parameters with the GRAIL gravity field coefficients as a supplementary constraint for the fluid core description.

Finally in section (3) we describe how we test the UFF and give new constraints. In addition, we present a generalization of the interpretation in terms of gravitational to inertial mass ratios of

★ E-mail: viswanathan@geoazur.unice.fr

[1] Available at: http://www.imcce.fr/inpop

UFF constraints, based on recent developments in dilaton theories (Hees & Minazzoli 2015; Minazzoli & Hees 2016). Hinged on this generalization, we deduce that from a pure phenomenological point of view, one cannot interpret UFF violation tests in the Earth-Moon system as tests of the difference between gravitational and inertial masses only.

2 LUNAR EPHEMERIDES

The new INPOP planetary ephemerides INPOP17a (Viswanathan et al. 2017) is fitted to LLR observations from 1969 to 2017, including the new IR LLR data obtained at the Grasse station.

2.1 Lunar Laser Ranging

The principle of the LLR observations is well documented (Murphy et al. 2012; Murphy 2013). Besides the lunar applications, the laser ranging technique is still intensively used for tracking Earth orbiting satellites, especially for very accurate orbital (Peron 2013; Lucchesi et al. 2015) and geophysical studies (Jeon et al. 2011; Matsuo et al. 2013).

Non-uniform distributions in the dataset are one contributor to correlations between solution parameters (Williams et al. 2009). Like one can see on Fig. (1), Fig. (2) and Fig. (3), about 70 % of the data are obtained after reflection on A15 reflector and on an average 40 % of the data are acquired within 30° of the quarter Moons.

In this study, we show how the IR LLR observations acquired at the Grasse station between 2015 and 2017 (corresponding to 7 % of the total LLR observations obtained between 1969 and 2017 from all known ILRS ground stations) can help to reduce the presence of such heterogeneity.

2.1.1 *Spatial distribution*

Statistics drawn from the historical LLR dataset (1969-2015) show an observer bias to range to the larger Apollo reflector arrays (mainly Apollo 15). This trend (see Fig. 1 and Fig. 3) is also present on statistics taken during time periods after the re-discovery of Lunokhod 1 by Murphy et al. (2011). This is due to the higher return rate and thermal stability over a lunar day on the Apollo reflectors, thereby contributing to the higher likelihood of success.

With the installation of the 1064 nm detection path (see Fig. 3), as explained in Courde et al. (2017), the detection of photon reflected on all reflectors is facilitated, especially for Lunokhod 2 (L2): about 17 % of IR data are obtained with L2 when only 2 % were detected at 532 nm.

Owing to the spatial distribution of the reflectors on the Moon, Apollo 11 and 14 give sensitivity to longitude librations, Apollo 15 gives sensitivity to latitude librations and the Lunokhod reflectors give sensitivity both in the latitude and longitude libration of the Moon. The heterogeneity in the reflector distribution of LLR data affects then the sensitivity of the lunar modeling adjustment (Viswanathan et al. 2016). By acquiring a better uniformity in the reflector sampling, IR contributes to improve the adjustment of the Moon dynamical and rotational modeling (see section 2.5).

2.1.2 *Temporal distribution*

The full and new Moon periods are the most favorable for testing gravity, as the gravitational and tidal effects are maximum. This was partially demonstrated by Nordtvedt (1998). On Fig. (2) are plotted the distributions of normal points relative to the synodic angle for APOLLO (in capitals, abbreviation for Apache Point Observatory Lunar Laser-ranging Operation, while Apollo refers to the US manned lunar missions) and Grasse station obtained at 532 nm and 1064 nm. About 25 % of the APOLLO data sample and almost 45 % of the Grasse 532 nm data sample are obtained within 30° of the quarter Moons. This can be explained by two factors:

(i) New Moon phase
As the pointing of the telescope onto the reflectors is calibrated with respect to a nearby topographical feature on the surface of the Moon, the pointing itself becomes a challenge when the reference points lie in the unlit areas of the Moon. Also, as the New Moon phase occurs in the daylight sky, the noise floor increases and the detector electronics become vulnerable due to ranging at a very close angle to the Sun (Williams et al. 2009; Courde et al. 2017).

(ii) Full Moon phase
During this phase, thermal distortions remain as the primary challenge, arising due to the over-head Sun heating of the retro-reflector arrays. This induces refractive index gradients within each corner cube causing a spread in the return beam, which makes detection more difficult. The proportion of this effect is partially linked to the thermal stability of the arrays. Since the A11, A14 and A15 arrays have a better thermal stability compared to the L1 and L2 arrays (Murphy et al. 2014), observations to the latter become sparse during the full Moon phase (where A and L indicates Apollo and Lunokhod retro-reflectors, respectively).

Despite these challenges, LLR observations during the above mentioned phases of the Moon have been acquired with the IR detection.

After the first two years of 1064 nm detection path at the Grasse station, the observations obtained within the 30° of the quarter Moons are reduced to 32 %, effectively increasing by around 10 % the portion of data sample close from the most favorable periods (new and full Moon) for tides and UFF studies.

This is primarily achieved due to the improved signal to noise ratio resulting from an improved transmission efficiency of the atmosphere at the IR wavelength of 1064 nm. In addition, high precision data have also been acquired on the two Lunokhod reflector arrays during full Moon phase.

In section (3), we will see how the IR LLR data help to improve the results related to the UFF tests.

2.1.3 *Observational Accuracy of the LLR observations*

APOLLO observations are obtained with a 3.5 m telescope (under time sharing) at the Apache Point Observatory, while Grasse observations are obtained with a 1.5 m telescope dedicated for SLR and LLR. A larger aperture is beneficial for statistically reducing the uncertainty of the observation (Murphy 2013), which translates to millimeter level accuracies for APOLLO. One can notice in Fig. (4) that the current lunar ephemerides have a post-fit residual scatter (RMS) of about 1-2 cm for the recent observations while the LLR normal point accuracy is given to be at least two times smaller. This calls for an improvement of the Earth-Moon dynamical models within highly accurate numerically integrated ephemerides (see section 2.5).

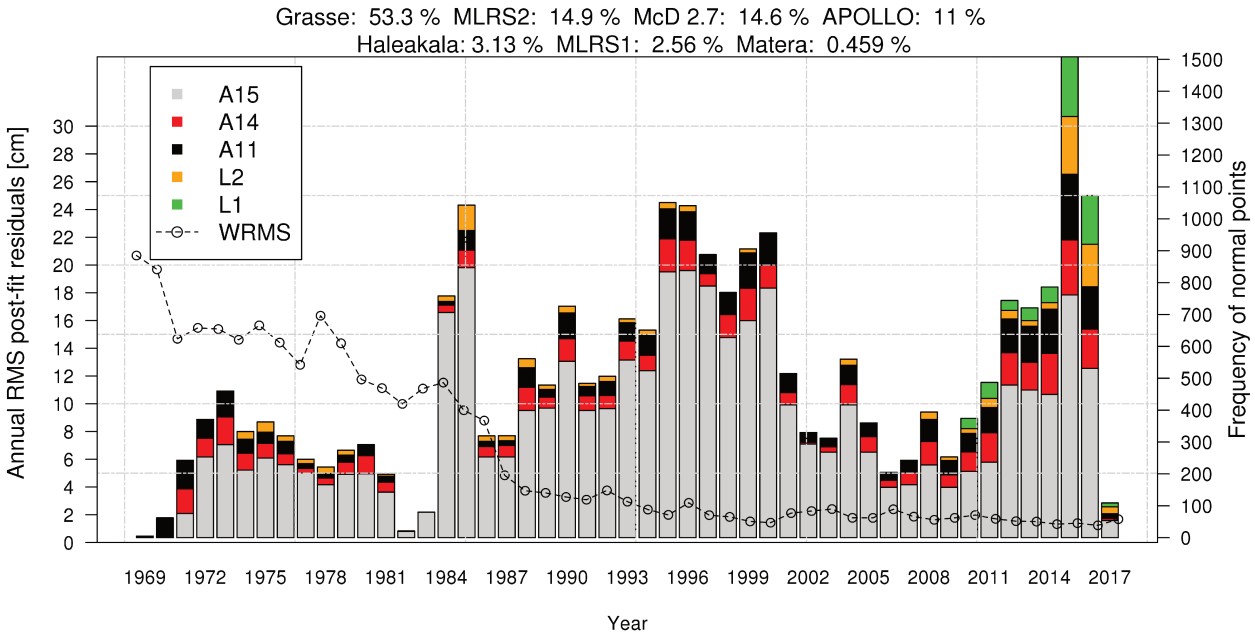

Figure 1. Histogram of annual frequency of LLR data with relative contribution from each LRR array including Grasse IR (1064 nm) observations. Points indicate the annual mean of post-fit residuals (in cm) obtained with INPOP17a. The dominance of range observations to A15 is evident. A change can be noticed after 2014 due to the contribution from IR at Grasse. The values in percentage indicate the LLR data contribution from each participating station.

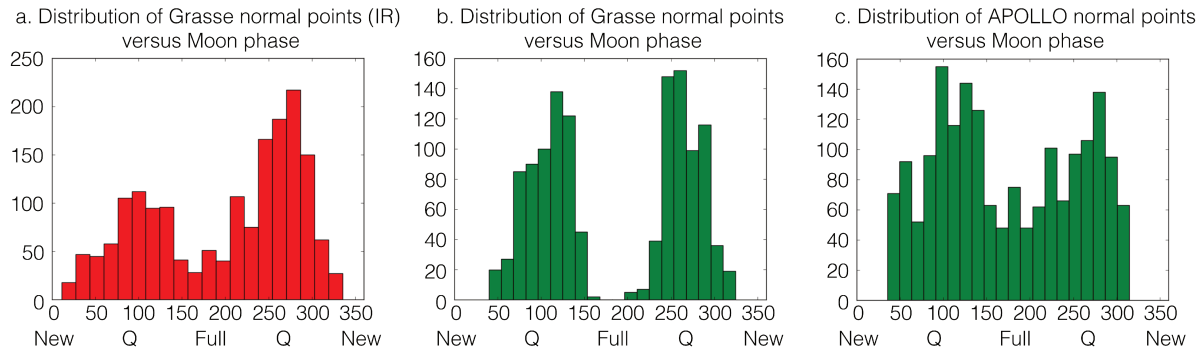

Figure 2. Histogram of synodic distribution of normal points obtained at Apache Point (c), at the Grasse station from 2012 from 2014 at 542 nm (b) and from 2014 to 2016 at 1064 nm (a). Q indicates the quarter Moon phase.

2.2 Lunar Dynamical Model

2.2.1 Lunar orbit interactions

In our model, we include the following accelerations perturbing the Moon's orbit:

(i) Point mass mutual relativistic interactions, in the parametrized post-Newtonian formalism, from the Sun, planets and asteroids through Folkner et al. (2014, Eqn. 27);
(ii) Extended bodies mutual interactions, through Folkner et al. (2014, Eqn. 28), which include :

- the interaction of the zonal harmonics of the Earth through degree 6;
- the interaction between zonal, sectoral, and tesseral harmonics of the Moon through degree 6 and the point mass Earth, Sun, Jupiter, Saturn, Venus and Mars;
- the interaction of degree 2 zonal harmonic of the Sun.

(iii) Interaction from the Earth tides, through Folkner et al. (2014, Eqn. 32)

The tidal acceleration from the tides due to the Moon and the Sun are separated into three frequency bands (zonal, diurnal and semi-diurnal). Each band is represented by a potential Love number $k_{2m,E}$ with a matching pair of time delays $\tau_{Xm,E}$ (where subscript X is either associated with the daily Earth rotation $\tau_{Rm,E}$ or orbital motion $\tau_{Om,E}$) to account for frequency dependent phase shifts

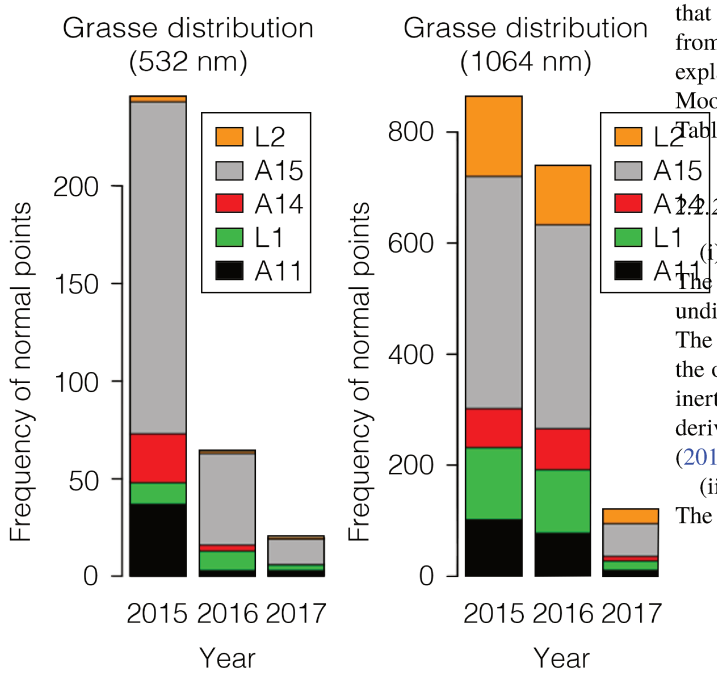

Figure 3. Grasse LLR data retro-reflector distribution at 532 nm and 1064 nm from 2015 to 2017. A and L indicate Apollo and Lunokhod retro-reflectors, numbered by their respective lunar missions.

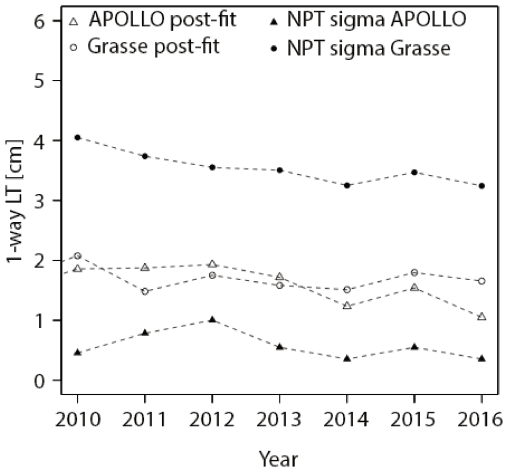

Figure 4. APOLLO and Grasse LLR observations in terms of i) observational accuracy as given by the annual mean of normal point uncertainty (converted from ps to 1-way light time (LT) in cm) and ii) annual weighted root mean square of post-fit residuals (1-way LT in cm) obtained with INPOP17a.

from an anelastic Earth with oceans. Here the time delay represents the phase lag induced by the tidal components. Although the time delay method inherently assumes that the imaginary component of $k_{2m,E}$ varies linearly with frequency, it reduces the complexity of the dynamical model. The diurnal $\tau_{R1,E}$ and semi-diurnal $\tau_{R2,E}$ are included as solution parameters in the LLR analysis, while model values for potential Love numbers for a solid Earth are fixed to that from Petit & Luzum (2010, Table 6.3) followed by corrections from the ocean model FES2004 (Lyard et al. 2006). A detailed explanation about the most influential tides relevant to the Earth-Moon orbit integration can be found in Williams & Boggs (2016, Table 6).

2.2.2 *Lunar orientation and inertia tensor*

(i) Lunar frame and orientation

The mantle coordinate system is defined by the principal axes of the undistorted mantle, whose moments of inertia matrix are diagonal. The time varying mantle Euler angles ($\phi_m(t)$,$\theta_m(t)$,$\psi_m(t)$) define the orientation of the principal axis (PA) frame with respect to the inertial ICRF2 frame (see Folkner et al. (2014) for details). The time derivatives of the Euler angles are defined through Folkner et al. (2014, Eqn. 14).

(ii) Lunar moment of inertia tensor

The undistorted total moment of inertia of the Moon $\tilde{I}_T$ is given by:

$$\tilde{I}_T = \frac{\tilde{C}_T}{m_M R_M^2}\begin{bmatrix}1&0&0\\0&1&0\\0&0&1\end{bmatrix} + \begin{bmatrix}\tilde{C}_{2,0,M}-2\tilde{C}_{2,2,M}&0&0\\0&\tilde{C}_{2,0,M}+2\tilde{C}_{2,2,M}&0\\0&0&0\end{bmatrix} \quad (1)$$

where $\tilde{C}_{n,m,M}$ is the unnormalized degree n, order m of the Stokes coefficient $C_{n,m}$ for the spherical harmonic model of the undistorted Moon and $\tilde{C}_T$ is the undistorted polar moment of inertia of the Moon normalized by it's mass m_M and radius squared R_M^2. Through Eqn. (1), we are able to directly use the undistorted value of C_{22} (Manche 2011) from GRAIL derived spherical harmonic model of Konopliv et al. (2013).

The moment of inertia of the fluid core I_c is given by:

$$I_c = \alpha_c \tilde{C}_T \begin{bmatrix}1-f_c&0&0\\0&1-f_c&0\\0&0&1\end{bmatrix} = \begin{bmatrix}A_c&0&0\\0&B_c&0\\0&0&C_c\end{bmatrix} \quad (2a)$$

where α_c is the ratio of the fluid core polar moment of inertia C_c to the undistorted polar moment of inertia of the Moon C_T, f_c is the fluid core polar flattening and, A_c and B_c are the equatorial moments of the fluid core. This study assumes an axis-symmetric fluid core with $A_c = B_c$.

The moment of inertia of the mantle I_m has a rigid-body contribution $\tilde{I}_m$ and two time varying contributions due to the tidal distortion of the Earth and spin distortion as given in Folkner et al. (2014, Eqn. 41). The single time delay model (characterized by τ_M) allows for dissipation when flexing the Moon (Standish & Williams 1992; Williams et al. 2001; Folkner et al. 2014).

$$\tilde{I}_m = \tilde{I}_T - I_c \quad (2b)$$

(iii) Lunar angular momentum and torques

The time derivative of the angular momentum vector is equal to the sum of torques (N) acting on the body. In the rotating mantle frame, the angular momentum differential equation for the mantle is given by:

$$\frac{d}{dt} I_m \omega_m + \omega_m \times I_m \omega_m = N \quad (2c)$$

where N is the sum of torques on the lunar mantle from the point mass body A ($N_{M,figM-pmA}$), figure-figure interaction between

the Moon and the Earth ($N_{M,figM-figE}$, using Folkner et al. (2014, Eqn. 44)) and the viscous interaction between the fluid core and the mantle (N_{CMB}).

The motion of the uniform fluid core is controlled by the mantle interior, with the fluid core moment of inertia (I_c) constant in the frame of the mantle. The angular momentum differential equation of the fluid core in the mantle frame is then given by:

$$\frac{d}{dt} I_c \omega_c + \omega_m \times I_c \omega_c = -N_{CMB} \tag{2d}$$

$$N_{CMB} = k_v (\omega_c - \omega_m) + (C_c - A_c)(\hat{z}_m \cdot \omega_c)(\hat{z}_m \times \omega_c) \tag{2e}$$

where k_v is the coefficient of viscous friction at the CMB and $\hat{z}_m$ is a unit vector aligned with the polar axis of the mantle frame. The second part on the right-hand side of Eqn. (2e) is the inertial torque on the axis-symmetric fluid core.

2.3 Reduction model

The reduction model for the LLR data analysis has been implemented within a precise orbit determination and geodetic software: GINS (Marty et al. 2011; Viswanathan et al. 2015) maintained by space geodesy teams at GRGS/OCA/CNES and written in Fortran90. The subroutines for the LLR data reduction within GINS is vetted through a step-wise comparison study conducted among the LLR analysis teams in OCA-Nice (this study), IMCCE-Paris and IfE-Hannover, by using simulated LLR data and DE421 (Folkner et al. 2009) as the planetary and lunar ephemeris. The modeling follows the recommendations of IERS 2010 (Petit & Luzum 2010). To avoid any systematics in the reduction model, the upper-limit on the discrepancy between the teams was fixed to 1 mm in one-way light time.

From each normal point, the emission time (in UTC) and the round trip time (in seconds) are used to iteratively solve for the reflection time in the light-time equations. A detailed description is available in Moyer (2003, Section 8 & 11) for a precise round-trip light-time computation.

A detailed description of the reduction model used for this study is provided in Manche (2011).

2.4 Fitting procedure

For APOLLO station observations, scaling the uncertainties of the normal points depending on the change of equipments, or a change in the normal point computation algorithm, is advised (see `http://physics.ucsd.edu/~tmurphy/apollo/151201_notes.txt`). Unrealistic uncertainties present in observations from Grasse, McDonald MLRS2 and Matera between time periods 1998-1999, 1996 and 2010-2012 respectively, are rescaled.

During the fitting procedure, bounds are used (Stark & Parker 1995) for limiting the variability of the estimated parameters, while considering the parameter correlation and variance within the normal matrix. For the gravity field coefficients (including $C_{2,0,M}$ and $C_{2,2,M}$), the bounds are placed using the uncertainties provided by GRAIL (after scaling the formal uncertainties by a factor 40, following the recommendation by Konopliv et al. (2013)) with their values centered on the GRAIL gravity field estimates.

Additional details of the weighting scheme and the fitting procedure used for the construction of INPOP17a solution can be found in Viswanathan et al. (2017). A filtering scheme is enforced during the iterative fit of the parameters. At each iteration, the residuals

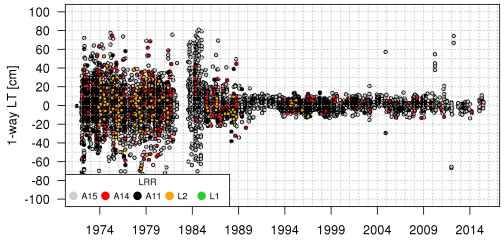

Figure 5. Post-fit residuals in (cm) vs time (year) obtained with $\text{INPOP}_{\text{G+IR}}$ specification (sec. 2.5) for McDonald, MLRS1, MLRS2, Haleakala and Matera stations

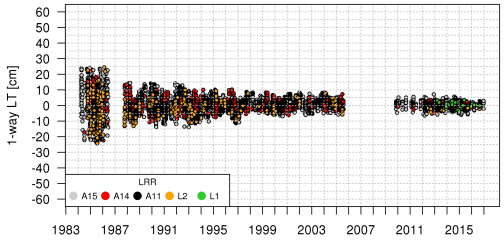

Figure 6. Post-fit residuals in (cm) vs time (year) obtained with $\text{INPOP}_{\text{G+IR}}$ specification (sec. 2.5) for GRASSE station with the Green wavelength

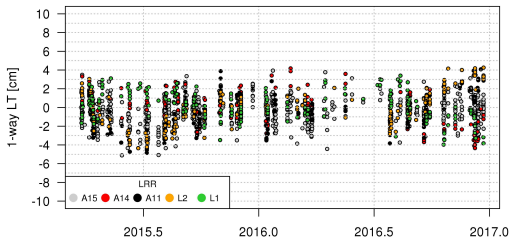

Figure 7. Post-fit residuals in (cm) vs time (year) obtained with $\text{INPOP}_{\text{G+IR}}$ specification (sec. 2.5) for GRASSE station with the IR wavelength

are passed through a 3-σ filter (where σ is recomputed at each iteration).

2.4.1 *Biases*

Changes in the ground station introduces biases in the residuals. These biases correspond either with a known technical development at the station (new equipment, change of optical fiber cables) or systematics. Any estimated bias can be correlated with a corresponding change in the ground station, provided the incidents have been logged. A list of known and detected biases are given in Viswanathan et al. (2017).

2.5 Results

Table (5) gives the list of the adjusted parameters related to the lunar interior when Table (4) provides a list of the fixed parameters. The fitted coordinates of the Moon reflectors and of the LLR stations can be found in Viswanathan et al. (2017). As the LLR observations are not included in the construction of the ITRF (Altamimi et al. 2016), small corrections to the LLR station coordinates help for the improvement of LLR residuals during the construction of the

Table 1. Comparison of post-fit residuals of LLR observations from ground stations with corresponding time span, number of normal points available, number of normal points used in each solution after a 3-σ rejection filter. The WRMS (in cm) is obtained with solutions INPOP13c (1969-2013) and INPOP17a (1969-2017). INPOP13c statistics are drawn from Fienga et al. (2014).

Code	Station	Time span	Available	INPOP13c		INPOP17a	
				Used	WRMS	Used	WRMS
					[cm]		[cm]
70610	APOLLO, NM, USA (group A)	2006 - 2010	941	940	4.92	929	1.27
70610	APOLLO, NM, USA (group B)	2010 - 2012	506	414	6.61	486	1.95
70610	APOLLO, NM, USA (re-group C)	2012 - 2013	361	359	7.62	345	1.52
70610	APOLLO, NM, USA (group D)	2013 - 2016	832	-	-	800	1.15
01910	Grasse, FR	1984 - 1986	1187	1161	16.02	1161	14.01
01910	Grasse, FR	1987 - 1995	3443	3411	6.58	3407	4.11
01910	Grasse, FR	1995 - 2006	4881	4845	3.97	4754	2.86
01910	Grasse, FR	2009 - 2013	999	990	6.08	982	1.41
01910	Grasse, FR	2013 - 2017	3351	-	-	3320	1.51
56610	Haleakala, HI, USA	1984 - 1990	770	739	8.63	728	4.80
07941	Matera, IT	2003 - 2013	83	70	7.62	37	2.37
07941	Matera, IT	2013 - 2015	30	-	-	28	2.93
71110	McDonald, TX, USA	1969 - 1983	3410	3302	31.86	3246	18.87
71110	McDonald, TX, USA	1983 - 1986	194	182	20.60	148	16.77
71111	MLRS1, TX, USA	1983 - 1984	44	44	29.43	44	32.73
71111	MLRS1, TX, USA	1984 - 1985	368	358	77.25	356	62.58
71111	MLRS1, TX, USA	1985 - 1988	219	207	7.79	202	11.07
71112	MLRS2, TX, USA	1988 - 1996	1199	1166	5.36	1162	3.81
71112	MLRS2, TX, USA	1996 - 2012	2454	1972	5.81	1939	3.72
71112	MLRS2, TX, USA	2012 - 2015	17	-	-	15	2.59
	TOTAL	**1969 - 2017**	**25289**	**20160**		**24089**	

Table 2. Grasse LLR data retro-reflector statistics computed using post-fit residuals obtained with INPOP_G and $\text{INPOP}_\text{G+IR}$, within the fit intervals 01/01/2015 to 01/01/2017 (with a 3-σ filter), with the WRMS in m (RMS weighted by the number of normal points from each reflector).

Grasse				
LRRR	**INPOP_G**	**$\text{INPOP}_\text{G+IR}$**	**% change**	**NPTs**
A15	0.0183	0.0181	1.1	1018
A14	0.0203	0.0177	12.8	172
A11	0.0267	0.0239	10.5	215
L1	0.0215	0.0166	**22.8**	265
L2	0.0246	0.0215	12.6	256
WRMS	0.0207	0.0189	9.5	1926

Table 3. APOLLO LLR data retro-reflector statistics computed using post-fit residuals obtained with INPOP_G and $\text{INPOP}_\text{G+IR}$, within the fit intervals 01/01/2015 to 01/01/2017 (with a 3-σ filter), with the WRMS in m (RMS weighted by the number of normal points from each reflector).

APOLLO				
LRRR	**INPOP_G**	**$\text{INPOP}_\text{G+IR}$**	**% change**	**NPTs**
A15	0.0127	0.0127	0.2	344
A14	0.0192	0.0177	7.8	176
A11	0.0185	0.0169	8.7	164
L1	0.0186	0.0157	**15.6**	89
L2	0.0136	0.0137	-0.7	64
WRMS	0.0159	0.0149	6.7	837

lunar ephemerides. The Earth Orientation parameters (EOP) and the modeling of the Earth rotation are however kept fixed to the IERS convention (see section 2.3).

The solution INPOP_G with an axis-symmetric core fitted to LLR observations serves as a validation of our lunar model and analysis procedure, against the DE430 JPL planetary and lunar ephemeris analysis described in Folkner et al. (2014) and EPM IAA RAS ephemeris in Pavlov et al. (2016). Only 532 nm wavelength LLR data are used for matching with the DE430 and EPM ephemeris. In Folkner et al. (2014); Pavlov et al. (2016)

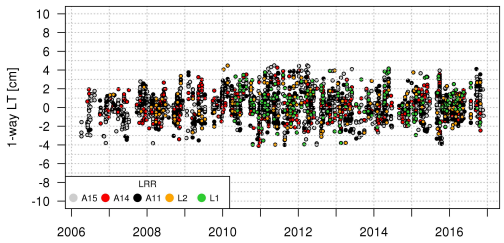

Figure 8. Post-fit residuals in (cm) vs time (year) obtained with INPOP$_{G+IR}$ specification (sec. 2.5) for APOLLO station

and INPOP$_G$, gravity field coefficients up-to degree and order 6 are used for the Moon (GL0660b from Konopliv et al. (2013)) and the Earth (GGM05C from Ries et al. (2016) for INPOP17a ephemeris and EGM2008 from Pavlis et al. (2012, 2013) for DE/EPM ephemerides). Coefficients C_{32}, S_{32} and C_{33} are then included in the fit parameters as they improve the overall post-fit residuals. For INPOP$_G$, the improvement of the formal uncertainty compared to Pavlov et al. (2016), especially in the estimation of parameter k_v/C_T indicates a strong dissipation mechanism within the Moon, through viscous torques at the fluid core-mantle boundary. Overall, INPOP uncertainties are consistent with EPM (Pavlov et al. 2016) published values. DE (Williams et al. 2013; Folkner et al. 2014) uncertainties are greater than INPOP and EPM, and should therefore be considered as more realistic.

Differences between GL0660b values and fitted C_{32}, S_{32} and C_{33} from Folkner et al. (2014), Pavlov et al. (2016) or in INPOP$_G$, are several orders of magnitude greater than the mean GRAIL uncertainties (see Konopliv et al. (2013)). These results suggest that some significant effects impacting the LLR observations, are absorbed by the adjustment of the degree-3 of the full Moon gravity field.

The solution INPOP$_{G+IR}$ refers to the addition of two years of IR LLR observations (Courde et al. 2017) described in section (2.1) and built in following the same specification as of INPOP$_G$.

This dataset is weighted at the same level as the APOLLO station normal points within the estimation procedure (see section 2.4).

The first outcome from the introduction of the IR data sets is the improvement of the post-fit residuals obtained for L1 reflector as one can see on Tables (2 and 3) and on Figures (5 to 8). This is due to the increase of normal points obtained for this reflector as discussed in section (2.1.1).

The second conclusion is that because of only two years on data, the improvement brought by the addition of IR data on the estimated parameters characterizing the Moon and its inner structure is significant, especially for those quantifying the dissipation mechanism such as $Q_{27.212}$ and τ_M with a decreasing uncertainty or $\frac{k_v}{C_T}$ and f_c with a significant change in the fitted value (see Table 5).

A significant global improvement is noticeable when one compares post-fit residuals obtained with INPOP$_G$ and with INPOP$_{G+IR}$ with those obtained with INPOP13c as presented in Fienga et al. (2014) or in Tables 2 and 3. Finally one should notice in Table (1) the 1.15 cm obtained for the post-fit weighted RMS obtained for the 3 years of the last period of the APOLLO data (group D) as well as that for the IR Grasse station.

3 TEST OF THE EQUIVALENCE PRINCIPLE

3.1 Context

Among all possibilities to test General Relativity (GR), the tests of the motion of massive bodies as well as the propagation of light in the solar system, were historically the first ones, and still provide the highest accuracies for several aspects of gravity tests (see Joyce et al. (2015); Berti et al. (2015); Yunes et al. (2016) for recent overviews of constraints on alternative theories from many different types of observations). This is in part due to the fact that the dynamics of the solar system is well understood and supported by a long history of observational data.

In GR, not only do test particles with different compositions fall equally in a given gravitational field, but also extended bodies with different gravitational self-energies. While a deviation from the former case would indicate a violation of the Weak Equivalence Principle (WEP), a deviation from the latter case would be a sign of a violation of the Strong Equivalence Principle (SEP) (Will (2014)). Violations of the Equivalence Principles are predicted by a number of modifications of GR, often intending to suggest a solution for the problems of Dark Energy and Dark Matter Capozziello & de Laurentis (2011); Joyce et al. (2015); Berti et al. (2015) and/or to put gravity in the context of Quantum Field Theory Kostelecký (2004); Woodard (2009); Donoghue (2017). The Universality of Free Fall (UFF), an important part of the Equivalence Principle, is currently tested at a level of about 10^{-13} with torsion balances (Adelberger et al. 2003) and LLR analyses (Williams et al. 2012).

As the Earth and the Moon both fall in the gravitational field of the Sun — and because they neither have the same compositions, nor the same gravitational self-energies — the Earth-Moon system is an ideal probe of both the WEP and the SEP, while torsion balance (Adelberger et al. 2003) or MICROSCOPE (Liorzou et al. 2014) are only sensitive to violations of the WEP.

In this paper, we implemented the equations given in Williams et al. (2012) and introduce in the INPOP fit, the differences between the accelerations of the Moon and the Earth.

The aim of this work is first to give the most general constraint in terms of acceleration differences without assuming metric theories or other types of alternative theories (section 3.3). In a second step (section 3.4), we propose two interpretations : one following the usual formalism proposed by Nordtvedt (see, e.g., (Nordtvedt 2014) and references therein), and the other following the dilaton theory (Damour & Polyakov 1994; Hees & Minazzoli 2015; Minazzoli & Hees 2016).

3.2 Method

In order to test possible violations of GR in terms of UFF, a supplementary acceleration is introduced in the geocentric equation of motion of the Moon, such that the UFF violation related difference between the Moon and the Earth accelerations reads (Nordtvedt 1968b):

$$\Delta \boldsymbol{a}^{\overline{UFF}} \equiv (\boldsymbol{a}_M - \boldsymbol{a}_E)^{\overline{UFF}} = \boldsymbol{a}_E \Delta_{ESM} \tag{3}$$

Δ_{ESM} is estimated in the LLR adjustment together with the other parameters of the lunar ephemerides given in Table (5). In what follows, we shall name Δ_{ESM} "UFF violation parameter". ESM stands for the three bodies involved, namely the Earth, the Sun and the Moon respectively. As we shall see in Sec. 3.4.2, some theoretical models induce a dependence of the UFF violation parameter on the composition of the Sun, in addition to the "more usual" depen-

dence on the compositions and on the gravitational binding energies of the Moon and the Earth.

In order to estimate Δ_{ESM} with the appropriate accuracy, one should correct for supplementary effects such as the solar radiation pressure and thermal expansion of the retro-reflectors (Vokrouhlický 1997; Williams et al. 2012). An empirical correction on the radial perturbation (Δr_{EM}) induced by the UFF test has to be applied. For instance, with some simplifying approximations (Nordtvedt (2014)), one can show that the UFF additional acceleration would indeed lead to an additional radial perturbation (Δr_{EM}) of the Moon's orbit towards the direction of the Sun given by:

$$\Delta r_{EM} = S\Delta_{ESM}\cos D, \tag{4}$$

where S is a scaling factor of about -3×10^{10} m (Williams et al. 2012) and D is the synodic angle. A correction $\Delta r = 3.0\pm0.5$ mm (Vokrouhlický 1997; Williams et al. 2012) is then applied in order to correct for solar radiation pressure and thermal radiation of the retro-reflectors, and a new corrected value of Δ_{ESM} is then deduced (see Table 6).

3.3 Results

Fits were performed including in addition to the previous fitted parameters presented in Table (5), the UFF violation parameter Δ_{ESM} given in Eqn. (3). Two different fits were considered including 532 nm and 1064 nm data sets (solution labeled $\mathrm{INPOP_{G+IR}}$), or just the 532 nm data sets (solution labeled $\mathrm{INPOP_G}$). A supplementary adjustment was also performed for a better comparison to the previous determination from other LLR analysis groups, which were limited to a data sample up to 2011 (labeled as limited data). Results are given in Table (6).

The additional acceleration of the Moon orbit in the direction of the Sun correlates with a coefficient of 0.95 and 0.90 with $\mathrm{GM_{EMB}}$ and the Earth-Moon mass ratio (EMRAT), respectively. In all the solutions w.r.t LLR EP estimation, the gravitational mass of the Earth Moon barycenter ($\mathrm{GM_{EMB}}$) remains as a fit parameter due its high correlation with the EP parameter (Δ_{ESM}). EMRAT was estimated from a joint planetary solution and kept fixed during LLR EP tests (for all INPOP solutions in Table 6) due to its weak determination from LLR.

A test solution that fitted EMRAT, with $\mathrm{GM_{EMB}}$ as a fixed parameter, gives an estimate of $\Delta_{ESM} = (8\pm7.0)\times10^{-14}$. However, the value of EMRAT estimated from an LLR only solution has an uncertainty of one order of magnitude greater than that obtained from the joint planetary fit. This is also consistent with a similar result by Williams et al. (2009). As a result, EMRAT was not included as a fit parameter for the estimates provided in Table (6), as it resulted in a degraded fit of the overall solution.

Williams et al. (2012) show that including annual nutation components of the Earth pole direction in space, to the list of fitted parameters during the estimation of LLR EP solution, increases the uncertainty of the estimated UFF violation parameter (Δ_{ESM}) by 2.5 times. Moreover, it is to be noted that within Table (6), the solutions by Williams et al. (2009, 2012); Müller et al. (2012) use the IERS2003 (McCarthy & Petit 2004) recommendations within the reduction model, while all INPOP17 solutions use IERS 2010 (Petit & Luzum 2010) recommendations. The notable difference between the two IERS models impacting the LLR EP estimation is expected to be from the precession-nutation of the celestial intermediate pole (CIP) within the ITRS-GCRS transformation Petit & Luzum (2010, p. 8).

Eqn. (4) shows the dependence of Δ_{ESM} w.r.t the cosine of the lunar orbit synodic angle, synonymous with the illumination cycle of the lunar phases. Due to the difficulties involved with ranging to the Moon during the lunar phases with the extreme values of cos D (New and Full Moon) as described in section (2.1.2), the LLR observations during these phases remain scarce. The availability of IR LLR observations from Grasse, contributes to the improvement of this situation, as shown in Fig. (2). This is reflected in the improvement of the uncertainty of the estimated value of Δ_{ESM} by 14 %, with solutions including the IR LLR data.

Using both IR and green wavelength data, and empirically correcting for the radial perturbation for effects related to solar radiation pressure and thermal expansion, our final result on the UFF violation parameter is given by (see, also, Table 6)

$$\Delta_{ESM} = (-3.8\pm7.1)\times10^{-14} \tag{5}$$

The continuation of the IR observational sessions at Grasse will help to continue the improvement in the Δ_{ESM} estimations.

An observable bias in the differential radial perturbation of the lunar orbit w.r.t the Earth, towards the direction of the Sun, if significant and not accounted for within the dynamical model, would result in a false indication of the violation of the principle of equivalence estimated with the LLR observations. Oberst et al. (2012) show the distribution of meteoroid impacts with the lunar phase. Peaks within the histogram in Oberst et al. (2012, p 186) indicate a non-uniform temporal distribution with a non-negligible increase in both small and large impacts during the New and Full Moon phase. Future improvements to the LLR EP estimation must consider the impact of such a bias that could potentially be absorbed during the fit by the LLR UFF violation parameter Δ_{ESM}.

3.4 Theoretical interpretations

3.4.1 *Nordtvedt's interpretation: gravitational versus inertial masses*

Although equations of motion are developed at the post-Newtonian level in INPOP (Moyer 2003), violations of the UFF can be cast entirely in the Newtonian equation of motion with sufficient accuracy. As described by Nordtvedt (Nordtvedt 1968b), a difference of the inertial (m^I) and gravitational (m^G) masses would lead to an alteration of body trajectories in celestial mechanics according to the following equation:

$$\boldsymbol{a}_T = -\left(\frac{m^G}{m^I}\right)_T \sum_{A\neq T}\frac{Gm_A^G}{r_{AT}^3}\boldsymbol{r}_{AT}, \tag{6}$$

where $\boldsymbol{r}_{AT} = \boldsymbol{x}_T - \boldsymbol{x}_A$ and G is the constant of Newton.

Following Williams et al. (2012), the relative acceleration at the Newtonian level between the Earth and the Moon due to the attraction of the Sun reads

$$\begin{aligned}\boldsymbol{a}_M - \boldsymbol{a}_E = &-\frac{G\mu}{r_{EM}^3}\boldsymbol{r}_{EM} + Gm_S^G\left[\frac{\boldsymbol{r}_{SE}}{r_{SE}^3} - \frac{\boldsymbol{r}_{SM}}{r_{SM}^3}\right] + \\ &+Gm_S^G\left[\frac{\boldsymbol{r}_{SE}}{r_{SE}^3}\left(\left(\frac{m^G}{m^I}\right)_E - 1\right) - \frac{\boldsymbol{r}_{SM}}{r_{SM}^3}\left(\left(\frac{m^G}{m^I}\right)_M - 1\right)\right],\end{aligned} \tag{7}$$

with $\mu \equiv m_M^G + m_E^G + \left(\left(\frac{m^G}{m^I}\right)_E - 1\right)m_M^G + \left(\left(\frac{m^G}{m^I}\right)_M - 1\right)m_E^G$. $\left(\frac{m^G}{m^I}\right)_E$ and $\left(\frac{m^G}{m^I}\right)_M$ are the ratios between the gravitational and the inertial masses of the Earth and Moon respectively.

With ephemerides, the first term of Eqn. (7) does not lead to a sensitive test of the UFF, because it is absorbed in the fit of the

parameter $m_M^G + m_E^G$ (Williams et al. 2012, e.g.), while the last term, does. At leading order, one can approximate both distances appearing in this last term as being approximately equal. One gets

$$\begin{aligned}\Delta\boldsymbol{a}^{\overline{UFF}} &\equiv (\boldsymbol{a}_M - \boldsymbol{a}_E)^{\overline{UFF}} \\ &\approx Gm_S^G\left[\frac{\boldsymbol{r}_{SE}}{r_{SE}^3}\left(\left(\frac{m^G}{m^I}\right)_E - 1\right) - \frac{\boldsymbol{r}_{SM}}{r_{SM}^3}\left(\left(\frac{m^G}{m^I}\right)_M - 1\right)\right] \\ &\approx \boldsymbol{a}_E\left[\left(\left(\frac{m^G}{m^I}\right)_E - 1\right) - \left(\left(\frac{m^G}{m^I}\right)_M - 1\right)\right] \\ &\equiv \boldsymbol{a}_E\Delta_{ESM} \end{aligned} \tag{8}$$

with

$$\Delta_{ESM} = \left[\left(\frac{m^G}{m^I}\right)_E - \left(\frac{m^G}{m^I}\right)_M\right]. \tag{9}$$

One recovers Eqn. (3). Therefore, in this context, constraints on Δ_{ESM} can be interpreted as constraints on the difference of the gravitational to inertial mass ratios between the Earth and the Moon.

Furthermore, the LLR test of UFF captures a combined effect of the SEP, from the differences in the gravitational self-energies, and the WEP due to compositional differences, of the Earth-Moon system. In general, one has:

$$\Delta_{ESM} = \Delta_{ESM}^{WEP} + \Delta_{ESM}^{SEP} \tag{10}$$

In order to separate the effects of WEP, we rely on results from laboratory experiments that simulate the composition of the core and the mantle materials of the Earth-Moon system. One such estimate is provided by Adelberger (2001), that translates to the following mass ratios difference:

$$\begin{aligned}\Delta_{ESM}^{WEP} &= \left[\left(\frac{m^G}{m^I}\right)_E - \left(\frac{m^G}{m^I}\right)_M\right]_{WEP} &(11)\\ &= (1.0 \pm 1.4)\times 10^{-13} &(12)\end{aligned}$$

It is also possible to deduce the Nordtvedt parameter (η) defined as:

$$\begin{aligned}\Delta_{ESM}^{SEP} &= \eta_{SEP}\left[\left(\frac{|\Omega|}{m\,c^2}\right)_E - \left(\frac{|\Omega|}{m\,c^2}\right)_M\right] &(13)\\ &\approx \eta_{SEP}\times(-4.45\times 10^{-10}) &(14)\end{aligned}$$

where Ω and mc^2 are the gravitational binding and rest mass energies respectively for the Earth and the Moon (subscripts E and M respectively). The value of -4.45×10^{-10} is obtained from Williams et al. (2009, Eqn. 7).

However, all metric theories lead to a violation of the SEP only. Therefore, for metric theories, it is irrelevant to try to separate violation effects of the WEP and SEP, as the WEP is intrinsically respected.

3.4.2 *Dilaton theory and a generalization of the Nordtvedt interpretation*

Starting from a general dilaton theory, a more general equation governing celestial mechanics than (6) has been found to be (Hees & Minazzoli 2015; Minazzoli & Hees 2016)

$$\boldsymbol{a}_T = -\sum_{A\neq T}\frac{Gm_A^G}{r_{AT}^3}\boldsymbol{r}_{AT}\,(1+\delta_T+\delta_{AT}), \tag{15}$$

The coefficients δ_T and δ_{AT} parametrize the violation of the UFF. In this expression the inertial mass m_A^I writes in terms of the gravitational mass m_A^G as $m_A^G = (1+\delta_A)m_A^I$ (Hees & Minazzoli 2015; Minazzoli & Hees 2016). Of course, since $m_A^G/m_A^I = 1+\delta_A$, one recovers Eqn. (6) when $\delta_{AB} = 0$ for all A and B. From Eqn. (15), one can check that the gravitational force in this context still satisfies Newton's third law of motion:

$$m_A^I\boldsymbol{a}_A = \frac{Gm_A^Im_B^I}{r_{AB}^3}\boldsymbol{r}_{AB}\,(1+\delta_A+\delta_B+\delta_{AB}) = -m_B^I\boldsymbol{a}_B. \tag{16}$$

In the dilaton theory, the δ coefficients are functions of "dilatonic charges" and of the fundamental parameters of the theory (Damour & Donoghue 2010; Hees & Minazzoli 2015; Minazzoli & Hees 2016). However, in what follows, we will consider the phenomenology based on the δ parameters independently of its theoretical origin, as a similar phenomenology may occur in a different theoretical framework.

In general, δ_T can be decomposed into two contributions: one from a violation of the WEP and one from a violation of the SEP:

$$\delta_T = \delta_T^{WEP} + \delta_T^{SEP}, \qquad \text{with} \qquad \delta_T^{SEP} = \eta\frac{|\Omega_T|}{m_T\,c^2}, \tag{17}$$

The quantity δ_T^{SEP} depends only on the gravitational energy content of the body T. On the other hand, δ_T^{WEP} depends on the composition of the falling body T (Damour & Donoghue (2010); Hees & Minazzoli (2015); Minazzoli & Hees (2016)). In some theoretical situations (see e.g. Damour & Donoghue (2010)), if $\delta_T^{WEP} \neq 0$, then $\delta_T^{WEP} \gg \delta_T^{SEP}$, such that one can have either a clean WEP violation, or a clean SEP violation.

Like the parameter δ_T^{WEP}, δ_{AT} depends on the composition of the falling bodies. However, unlike δ_T^{WEP}, it also depends on the composition of the body A that is source of the gravitational field in which the body T is falling (Hees & Minazzoli (2015); Minazzoli & Hees (2016)). As a consequence, the relative acceleration of two test particles with different composition cannot only be related to the ratios between their gravitational to inertial masses in general (i.e. $m_A^G/m_A^I = 1+\delta_A$). This contrasts with the usual interpretation (see for instance Williams et al. (2012)). However, with some theoretical models, δ_T^{WEP} is much greater than δ_{AT} (Damour & Donoghue (2010); Hees & Minazzoli (2015); Minazzoli & Hees (2016)).

At the Newtonian level, the relative acceleration between the Earth and the Moon reads

$$\begin{aligned}\boldsymbol{a}_M - \boldsymbol{a}_E = &-\frac{G\mu}{r_{EM}^3}\boldsymbol{r}_{EM} + Gm_S^G\left[\frac{\boldsymbol{r}_{SE}}{r_{SE}^3} - \frac{\boldsymbol{r}_{SM}}{r_{SM}^3}\right] \\ &+Gm_S^G\left[\frac{\boldsymbol{r}_{SE}}{r_{SE}^3}(\delta_E+\delta_{SE}) - \frac{\boldsymbol{r}_{SM}}{r_{SM}^3}(\delta_M+\delta_{SM})\right],\end{aligned} \tag{18}$$

with $\mu \equiv m_M^G + m_E^G + (\delta_E+\delta_{EM})m_M^G + (\delta_M+\delta_{EM})m_E^G$. As discussed already in the previous subsection, the first term of Eqn. (18) does not lead to a sensitive test of the UFF, because it can be absorbed in the fit of the parameter $m_M^G + m_E^G$ (e.g. Williams et al. 2012), while the last term, does. At leading order, one can approximate both distances appearing in this last term as being approximately equal. One therefore has

$$\begin{aligned}\Delta\boldsymbol{a}^{\overline{UFF}} &\equiv (\boldsymbol{a}_M - \boldsymbol{a}_E)^{\overline{UFF}} \\ &\approx Gm_S^G\left[\frac{\boldsymbol{r}_{SE}}{r_{SE}^3}(\delta_E+\delta_{SE}) - \frac{\boldsymbol{r}_{SM}}{r_{SM}^3}(\delta_M+\delta_{SM})\right] \\ &\approx \boldsymbol{a}_E\left[(\delta_E+\delta_{SE}) - (\delta_M+\delta_{SM})\right] \\ &\equiv \boldsymbol{a}_E\Delta_{ESM}\end{aligned} \tag{19}$$

where $\Delta\boldsymbol{a}^{\overline{UFF}}$ is the part of the relative acceleration between the

Earth and the Moon that violates the UFF. Once again, one recovers Eqn. (3) — although its theoretical interpretation is different compared to the previous subsection.

When $\delta_{SM} = \delta_{SE}$, and especially when $\delta_{SM} = \delta_{SE} = 0$, one recovers the usual Eqn. (9). But it is not the case in general because the composition of the Sun may affect the dynamics in some cases as well. Therefore, in a more general context than in section (3.4.1), constraints on Δ_{ESM} cannot be uniquely interpreted as constraints on the difference of the gravitational to inertial mass ratios between the Earth and the Moon.

As a consequence, from a pure phenomenological point of view — or, equivalently, from an agnostic point of view — one shouldn't interpret Δ_{ESM} in terms of gravitational to inertial mass ratios only. Indeed, a more general expression of the UFF violating parameter is given by

$$\Delta_{ESM} = [(\delta_E + \delta_{SE}) - (\delta_M + \delta_{SM})], \quad (20)$$

where one can see that the Sun's composition may affect the dynamics as well, through the coefficients δ_{SE} and δ_{SM}.

(Otherwise, see a discussion on how to decorrelate the dilaton parameters from planetary ephemeris in (Minazzoli et al. 2017)).

4 DISCUSSION

As emphasized in section (3.4.1), metric theories lead to a violation of the SEP only. Hence, it is tempting to use Eqn. (13) in order to convert the result on Δ_{ESM} in Eqn. (5) into a constraint on the Nordtvedt parameter η_{SEP} — when considering a metric theory prior.

However, such a conversion would not give a clean constraint on the actual Nordtvedt parameter η_{SEP}. The reason is that, since η_{SEP} depends on the post-Newtonian (pN) parameters, one should also fit the extra pN parameters in the Einstein-Infeld-Hoffmann (EIH) equations of motion, at the same time in both the Lunar and the planetary ephemeris — because the latter is used in the derivation of the former. Hence, unless a global fit of the various pN parameters and Δ_{ESM} is done at the same time for the whole solar system solution, the conversion of Δ_{ESM} into η_{SEP} through Eqn. (13) does not give a constraint on the actual Nordtvedt parameter η_{SEP}, but on another parameter that we shall call η instead – and that is simply defined by Eqn. (13).

Despite this fact, the result on Δ_{ESM} that is given in Eqn. (5) can nevertheless be interpreted in terms of fundamental physics, because a whole subset of theories predict a large domination of the WEP over the SEP in Δ_{ESM} (Damour & Donoghue 2010; Minazzoli & Hees 2016) — meaning that one would have a violation of the UFF while the pN parameters would be either equal to their value in general relativity, or their difference with respect to their value in general relativity would be negligible at the present level of experimental accuracy.

However, in order to separate the SEP and WEP contributions to Δ_{ESM} in a general case — or to determine the Nordtvedt parameter η_{SEP} when considering a metric theory prior — one would need to consider the whole solar system simultaneously in a consistent parametrized pN framework. This interesting study is left for a future work.

Nevertheless, an internal test on the impact of the extra pN parameters γ and β in the EIH equations under their known limits (taken from Bertotti et al. (2003) and Fienga et al. (2015), respectively) show no significant impact on our results, due to the little sensitivity of these parameters to the LLR data. Hence, η represents a good quantitative approximation of the Nordtvedt parameter η_{SEP}, as deduced from testing the UFF with LLR data only. Moreover, since UFF constraints are often reported in terms of η, this quantity can still be used in order to compare the sensitivity of the various Lunar ephemeris solutions with respect to testing the UFF. The estimates of η are reported in Table (6).

5 CONCLUSIONS AND FUTURE WORK

In this paper, we present an improvement in the lunar dynamical model of INPOP ephemeris (version 17a) compared to the previous release (version 13c). The model is fitted to the LLR observations between 1969-2017, following the model recommendations from IERS 2010 (Petit & Luzum 2010). The lunar parameter estimates obtained with the new solution are provided in Table (5) with comparisons to that obtained by other LLR analyses groups. The improvement brought by the new IR LLR data from Grasse station on the parameter estimates is characterized. The post-fit LLR residuals obtained with INPOP17a are between 1.15 cm to 1.95 cm over 10 years of APOLLO data and 1.47 cm over 2 years of the new IR LLR data from Grasse (Viswanathan et al. 2017). Our solution benefits also of the better spatial and temporal distribution of the IR Grasse data with an improvement of 14% of the UFF tests and better estimations of the Moon dissipation parameters.

We take advantage of the lunar ephemeris improvements to perform new tests of the universality of free fall. A general constraint is obtained using INPOP, in terms of the differences in the acceleration of the Earth and the Moon towards the Sun. In addition to the Nordtvedt interpretation of Nordtvedt (1968b) (provided in section 3.4.1), we propose an alternative interpretation and a generalization of the usual interpretation from the point of view of the dilaton theory (Damour & Polyakov 1994; Hees & Minazzoli 2015; Minazzoli & Hees 2016) (provided in section 3.4.2). We obtain an estimate of the UFF violating parameter $\Delta_{ESM} = (-3.8 \pm 7.1) \times 10^{-14}$, showing no violation of the principle of equivalence at this level. Future work may further allow to separate between the SEP and the WEP contributions to Δ_{ESM} by studying the whole solar system simultaneously in a consistent parametrized pN framework — see discussion in Sec. 4.

Thermal expansion of the retro-reflectors and solar radiation pressure are currently employed as empirical corrections following Vokrouhlický (1997); Williams et al. (2009). Future LLR analysis will consider an implementation of these effects within the reduction procedure, so as to improve the uncertainty of the EP test. Oberst et al. (2012) show the distribution of meteoroid impacts with the lunar phase, indicating a non-uniform temporal distribution during the New and Full Moon phase which could impact the test of EP. The impact of this effect needs to be characterized during the EP test, to be considered as negligible at the present LLR accuracy.

The use of a strictly GRAIL-derived gravity field model (Konopliv et al. 2013) highlights longitude libration signatures well above the LLR noise floor, arising from unmodeled effects in lunar ephemeris (Viswanathan 2017). Other LLR analyses groups (Folkner et al. 2009, 2014; Pavlov et al. 2016) prefer to fit the degree-3 components away from GRAIL-derived gravity field coefficients. Extra periodic terms on the longitude libration present in the DE430 lunar model are not considered within this paper. Instead, a work is in progress to further improve the lunar dynamical model and to identify the cause of the low-degree spacecraft-derived lunar gravity field inconsistency with that from the analysis of LLR data.

ACKNOWLEDGMENTS

The authors extend their sincere gratitude to all the observers and engineers at Grasse, APOLLO, McDonald, Matera and Haleakala LLR stations for providing timely and accurate observations over the past 48 years.

Table 4. Fixed parameters for the Earth-Moon system.

Parameter	Units	INPOP	DE430	EPM
$(EMRAT^{\dagger} - 81.300570) \times 10^6$		1.87	-0.92	-0.92
$(R_E - 6378.1366) \times 10^4$	km	0.0	-3	0.0
$(\dot{J}_{2E} - 2.6 \times 10^{-11})$	year^{-1}	0.0	0.0	0.0
$(k_{20,E} - 0.335)$		0.0	0.0	0.0
$(k_{21,E} - 0.32)$		0.0	0.0	0.0
$(k_{22,E} - 0.30102)$		-0.01902	0.01898	-0.01902
$(\tau_{O0,E} - 7.8 \times 10^{-2}) \times 10^2$	day	0.0	-1.4	0.0
$(\tau_{O1,E} + 4.4 \times 10^{-2})$	day	0.0	0.0‡	0.0
$\tau_{O2,E} + 1.13 \times 10^{-1}) \times 10^1$	day	0.0	0.13	0.0
$(R_M - 1738.0)$	km	0.0	0.0	0.0
$(\alpha_C - 7.0 \times 10^{-4})$		0.0	0.0	0.0
$(k_{2,M} - 0.024059)$		0.0	0.0	0.0
$(l_2 - 0.0107)$		0.0	0.0	0.0

†: EMRAT is fitted during the joint analysis between the lunar and planetary part.
‡: $\tau_{O1,E}$ in Folkner et al. (2014) given as -0.0044 is a typographical error.

Table 5. Extended body parameters for the Earth and the Moon. Uncertainties for INPOP_{G} and $\text{INPOP}_{\text{G+IR}}$ (1-σ) are obtained from a 5 % jackknife (JK), while other solutions (DE430 and EPM) are assumed as (1-σ) formal uncertainties. †: C_{32}, S_{32} and C_{33} are reference values from the GRAIL analysis by Konopliv et al. (2013). ‡: h_2 reference value from LRO-LOLA analysis by Mazarico et al. (2014). * : derived quantity

Parameter	Units	INPOP_{G}	$\text{INPOP}_{\text{G+IR}}$	DE430	EPM
$(GM_{\text{EMB}} - 8.997011400 \times 10^{-10}) \times 10^{19}$	AU^3/day^2	4 ± 2	4 ± 2	-10	10 ± 5
$(\tau_{R1,E} - 7.3 \times 10^{-3}) \times 10^5$	day	0 ± 4	6 ± 3	6 ± 30	57 ± 5
$(\tau_{R2,E} - 2.8 \times 10^{-3}) \times 10^5$	day	9.2 ± 0.4	8.7 ± 0.3	−27 ± 2	5.5 ± 0.4
$(C_T/(m_M R^2) - 0.393140) \times 10^6$		6.9 ± 0.2	8.2 ± 0.2	2*	2*
$(C_{32} - 4.8404981 \times 10^{-6\dagger}) \times 10^9$		4.1 ± 0.3	3.9 ± 0.3	4.4	4.4 ± 0.1
$(S_{32} - 1.6661414 \times 10^{-6\dagger}) \times 10^8$		1.707 ± 0.006	1.666 ± 0.006	1.84	1.84 ± 0.02
$(C_{33} - 1.7116596 \times 10^{-6\dagger}) \times 10^8$		−1.19 ± 0.04	-2.40 ± 0.04	−3.6	−4.2 ± 0.2
$(\tau_M - 9 \times 10^{-2}) \times 10^4$	day	−14 ± 5	-35 ± 3	58.0 ± 100	60 ± 10
$(\frac{k_V}{C_T} - 1.6 \times 10^{-8}) \times 10^{10}$	day^{-1}	12.7 ± 0.4	15.3 ± 0.5	4.0 ± 10.0	3.0 ± 2.0
$(f_c - 2.1 \times 10^{-4}) \times 10^6$		37 ± 3	42 ± 3	36 ± 28	37 ± 4
$(h_2 - 3.71 \times 10^{-2\ddagger}) \times 10^3$		6.3 ± 0.2	6.8± 0.2	11.0 ± 6	6 ± 1
$Q_{27.212} - 45$ (derived)		3.9 ± 0.5	5.0 ± 0.2	0 ± 5	0 ± 1

Table 6. Comparison of results for the value of Δ_{ESM} (Column 4) estimated with the solution INPOP17A fitted to LLR dataset between: 1) 1969-2011 (for comparison with Williams et al. (2012); Müller et al. (2012); 2) 1969-2017 with data obtained only in Green wavelength, 3) 1969-2017 with data obtained with both Green and IR wavelength. Column 5 empirically corrects the radial perturbation from effects related to solar radiation pressure and thermal expansion of retro-reflectors using Eqn. (4), with a value $\Delta r = 3.0 \pm 0.5$ mm (Williams et al. 2012). Column 6 contains the value of Δ_{ESM} after applying the corrections of Column 5. Column 7 contains the parameter η obtained using Eqn. (13). See discussion in Sec. 4.

Reference	Data time span [Year]	Uncertainty	estimated Δ_{ESM} [$\times 10^{-14}$]	corrected cos D [mm]	corrected Δ_{ESM} [$\times 10^{-14}$]	Parameter $\eta^{\ddagger}$ [$\times 10^{-4}$]
Williams et al. (2009)†	1969-2004	N/A	3.0 ± 14.2	2.8 ± 4.1	-9.6 ± 14.2	2.24 ± 3.14
Williams et al. (2012)	1969-2011	N/A	0.3 ± 12.8	2.9 ± 3.8	-9.9 ± 12.9	2.25 ± 2.90
Müller et al. (2012)*†	1969-2011	3-σ	-14 ± 16	-	-	-
INPOP17A (limited data)	1969-2011	3-σ	-3.3 ± 17.7	4.0 ± 5.2	-13.5 ± 17.8	3.03 ± 4.00
Hofmann & Müller (2016)†	1969-2016	3-σ	-	-	-3.0 ± 6.6	0.67 ± 1.48
INPOP17A (Green only)	1969-2017	3-σ	5.2 ± 8.7	1.5 ± 2.6	-5.0 ± 8.9	1.12 ± 2.00
INPOP17A (Green and IR)	1969-2017	3-σ	6.4 ± 6.9	1.1 ± 2.1	-3.8 ± 7.1	0.85 ± 1.59

*: SRP correction not applied
†: Thermal expansion correction not applied
‡: derived using $\frac{|\Omega_E|}{m_E\ c^2} - \frac{|\Omega_M|}{m_M\ c^2}$ = -4.45×10^{-10} (Williams et al. 2012, Eqn. 6)

REFERENCES

Adelberger E. G., 2001, Classical and Quantum Gravity, 18, 2397
Adelberger E. G., Fischbach E., Krause D. E., Newman R. D., 2003, Physical Review D, 68, 062002
Altamimi Z., Rebischung P., Métivier L., Collilieux X., 2016, Journal of Geophysical Research (Solid Earth), 121, 6109Ð6131
Anderson J. D., Gross M., Nordtvedt K. L., Turyshev S. G., 1996, ApJ, 459, 365
Bender P. L., et al., 1973, Science, 182, 229
Berti E., et al., 2015, Classical and Quantum Gravity, 32, 243001
Bertotti B., Iess L., Tortora P., 2003, Nature, 425, 374
Capozziello S., de Laurentis M., 2011, Physics Reports, 509, 167
Courde C., et al., 2017, Astronomy & Astrophysics
Damour T., Donoghue J. F., 2010, Physical Review D, 82, 084033
Damour T., Polyakov A. M., 1994, Nuclear Physics B, 423, 532
Donoghue J. F., 2017, Scholarpedia, 12, 32997
Faller J., Winer I., Carrion W., Johnson T. S., Spadin P., Robinson L., Wampler E. J., Wieber D., 1969, Science, 166, 99
Fienga A., Laskar J., Kuchynka P., Manche H., Desvignes G., Gastineau M., Cognard I., Theureau G., 2011, Celestial Mechanics and Dynamical Astronomy, 111, 363
Fienga A., Manche H., Laskar J., Gastineau M., Verma A., 2014, INPOP new release: INPOP13c, https://www.imcce.fr/recherche/equipes/asd/inpop/download13c
Fienga A., Laskar J., Exertier P., Manche H., Gastineau M., 2015, Celestial Mechanics and Dynamical Astronomy, 123, 325
Fienga A., Laskar J., Manche H., Gastineau M., 2016, preprint, (arXiv:1601.00947)
Folkner W. M., Williams J. G., Boggs D. H., 2009, Interplanetary Network Progress Report, 178, 1
Folkner W. M., Williams J. G., Boggs D. H., Park R. S., Kuchynka P., 2014, Interplanetary Network Progress Report, 196, 1
Hees A., Minazzoli O., 2015, preprint, (arXiv:1512.05233)
Hofmann F., Müller J., 2016, in 20th International Workshop on Laser Ranging. https://cddis.nasa.gov/lw20/docs/2016/presentations/30-Hofmann_presentation.pdf
Jeon H. S., Cho S., Kwak Y. S., Chung J. K., Park J. U., Lee D. K., Kuzmicz-Cieslak M., 2011, Ap&SS, 332, 341
Joyce A., Jain B., Khoury J., Trodden M., 2015, Physics Reports, 568, 1
Konopliv A. S., et al., 2013, Journal of Geophysical Research E: Planets, 118, 1415
Konopliv A. S., et al., 2014, Geophys. Res. Lett., 41, 1452
Kostelecký V. A., 2004, Physical Review D, 69, 105009
Lemoine F. G., et al., 2014, Geophysical Research Letters, 41, 3382
Liorzou F., Boulanger D., Rodrigues M., Touboul P., Selig H., 2014, Advances in Space Research, 54, 1119
Lucchesi D. M., Anselmo L., Bassan M., Pardini C., Peron R., Pucacco G., Visco M., 2015, Classical and Quantum Gravity, 32, 155012
Lyard F., Lefevre F., Letellier T., Francis O., 2006, Ocean Dynamics, 56, 394
Manche H., 2011, Phd dissertation, Observatoire de Paris, https://tel.archives-ouvertes.fr/tel-00689852
Marty J., et al., 2011, in 3rd International Colloquium Scientific and Fundamental Aspects of the Galileo Programme, ESA Proceedings WPP326. http://hpiers.obspm.fr/combinaison/documentation/articles/GINS_Marty.pdf
Matsumoto K., Yamada R., Kikuchi F., Kamata S., Ishihara Y., Iwata T., Hanada H., Sasaki S., 2015, Geophys. Res. Lett., 42, 7351
Matsuo K., Chao B. F., Otsubo T., Heki K., 2013, Geophys. Res. Lett., 40, 4662
Matsuyama I., Nimmo F., Keane J. T., Chan N. H., Taylor G. J., Wieczorek M. A., Kiefer W. S., Williams J. G., 2016, Geophys. Res. Lett., 43, 8365
Mazarico E., Barker M. K., Neumann G. A., Zuber M. T., Smith D. E., 2014, Geophysical Research Letters, 41, 2282
McCarthy D. D., Petit G., 2004, IERS Technical Note, 32
Merkowitz S. M., 2010, Living Reviews in Relativity, 13, 7
Minazzoli O., Hees A., 2016, Physical Review D, 94, 064038
Minazzoli O., Bernus L., Fienga A., Hees A., Laskar J., Viswanathan V., 2017, preprint, (arXiv:1705.05244)
Moyer T. D., 2003, Formulation for Observed and Computed Values of Deep Space Network Data Types for Navigation. Vol. 2, John Wiley & Sons, Inc., Hoboken, NJ, USA, doi:10.1002/0471728470
Müller J., Hofmann F., Biskupek L., 2012, Classical and Quantum Gravity, 29, 184006
Murphy T. W., 2013, Reports on Progress in Physics, 76, 076901
Murphy T. W., et al., 2011, Icarus, 211, 1103
Murphy T. W., Adelberger E. G., Battat J. B. R., Hoyle C. D., Johnson N. H., McMillan R. J., Stubbs C. W., Swanson H. E., 2012, Classical and Quantum Gravity, 29, 184005
Murphy T. W., McMillan R. J., Johnson N. H., Goodrow S. D., 2014, Icarus, 231, 183
Nordtvedt K., 1968a, Physical Review, 169, 1017
Nordtvedt K., 1968b, Physical Review, 170, 1186
Nordtvedt K., 1998, Classical and Quantum Gravity, 15, 3363
Nordtvedt K., 2014, Scholarpedia, 9, 32141
Oberst J., et al., 2012, Planetary and Space Science, 74, 179
Pavlis N. K., Holmes S. A., Kenyon S. C., Factor J. K., 2012, Journal of Geophysical Research: Solid Earth, 117, n/a
Pavlis N. K., Holmes S. A., Kenyon S. C., Factor J. K., 2013, Journal of Geophysical Research: Solid Earth, 118, 2633
Pavlov D. A., Williams J. G., Suvorkin V. V., 2016, Celestial Mechanics and Dynamical Astronomy, 126, 61
Peron R., 2013, MNRAS, 432, 2591
Petit G., Luzum B., 2010, IERS Technical Note, 36
Ries J., et al., 2016, GFZ Data Services
Samain E., et al., 1998, Astronomy and Astrophysics Supplement Series, 130, 235
Standish E. M., Williams J. G., 1992, Explanatory supplement to the astronomical almanac, pp 279–323
Stark P., Parker R., 1995, Computational Statistics, 10, 129ŏ013141
Viswanathan V., 2017, Phd dissertation (submitted), Observatoire de Paris
Viswanathan V., Fienga A., Laskar J., Manche H., Torre J.-M., Courde C., Exertier P., 2015, IAU General Assembly, 22, 2228567
Viswanathan V., et al., 2016, EGU General Assembly Conference Abstracts, 18, 13995
Viswanathan V., Fienga A., Gastineau M., Laskar J., 2017, Notes Scientifiques et Techniques de l'Institut de Mécanique Céleste, 108, 1
Vokrouhlický D., 1997, Icarus, 126, 293
Wieczorek M., 2007, in Schubert G., ed., , Treatise on Geophysics. Elsevier, Amsterdam, pp 165 – 206, doi:10.1016/B978-044452748-6.00156-5
Will C. M., 2014, Living Reviews in Relativity, 17, 4
Williams J. G., Boggs D. H., 2015, Journal of Geophysical Research: Planets, 120, 689
Williams J. G., Boggs D. H., 2016, Celestial Mechanics and Dynamical Astronomy, 126, 89
Williams J. G., Boggs D. H., Yoder C. F., Ratcliff J. T., Dickey J. O., 2001, Journal of Geophysical Research, 106, 27933
Williams J., Turyshev S., Boggs D., 2009, International Journal of Modern Physics D, 18, 1129
Williams J. G., Turyshev S. G., Boggs D. H., 2012, Classical and Quantum Gravity, 29, 184004
Williams J., Boggs D., Folkner W., 2013, Technical report, DE430 Lunar Orbit, Physical Librations, and Surface Coordinates, JPL IOM 335-JW, DB. WF-20130722-016, July 22
Woodard R. P., 2009, Reports on Progress in Physics, 72, 126002
Yunes N., Yagi K., Pretorius F., 2016, Physical Review D, 94, 084002

Bibliography

Abbot, R. I., Shelus, P. J., Mulholland, J. D., and Silverberg, E. C. (1973). Laser observations of the Moon: Identification and construction of normal points for 1969-1971. *The Astronomical Journal*, 78(8):784.

Acton, C. H. (1996). Ancillary data services of NASA's Navigation and Ancillary Information Facility. *Planetary and Space Science*, 44(1):65–70.

Adelberger, E. G. (2001). New tests of Einstein's equivalence principle and Newton's inverse-square law. *Classical and Quantum Gravity*, 18(13):2397–2405.

Adelberger, E. G., Heckel, B. R., and Nelson, A. E. (2003). Tests of the Gravitational Inverse-Square Law. *Annual Review of Nuclear and Particle Science*, 53:77–121.

Altamimi, Z., Collilieux, X., Legrand, J., Garayt, B., and Boucher, C. (2007). ITRF2005: A new release of the International Terrestrial Reference Frame based on time series of station positions and Earth Orientation Parameters. *Journal of Geophysical Research*, 112(B9):B09401.

Anderson, J. D., Keesey, M. S., Lau, E. L., Standish, E. M., and Newhall, X. (1978). Tests of general relativity using astrometric and radio metric observations of the planets. *Acta Astronautica*, 5(1):43–61.

Andrews-Hanna, J. C., Asmar, S. W., Head, J. W., Kiefer, W. S., Konopliv, A. S., Lemoine, F. G., Matsuyama, I., Mazarico, E., McGovern, P. J., Melosh, H. J., Neumann, G. A., Nimmo, F., Phillips, R. J., Smith, D. E., Solomon, S. C., Taylor, G. J., Wieczorek, M. A., Williams, J. G., and Zuber, M. T. (2013). Ancient Igneous Intrusions and Early Expansion of the Moon Revealed by GRAIL Gravity Gradiometry. *Science*, 339(6120):675–678.

Ash, M. E. (1965). Generation of the lunar ephemeris on an electronic computer. Technical report, Massachusetts Institute of Technology, Lexinton Lincoln Laboratory.

Avsyuk, Y. N. (1977). On the tidal force. *Soviet Astronomy Letters*, 3:96–99.

Azzalini, A. and Capitanio, A. (1999). Statistical applications of the multivariate skew normal distribution. *Journal of the Royal Statistical Society: Series B (Statistical Methodology)*, 61(3):579–602.

Bender, P. L., Currie, D. G., Poultney, S. K., Alley, C. O., Dicke, R. H., Wilkinson, D. T., Eckhardt, D. H., Faller, J. E., Kaula, W. M., Mulholland, J. D., Plotkin, H. H., Silverberg, E. C., and Williams, J. G. (1973). The Lunar Laser Ranging Experiment: Accurate ranges have given a large improvement in the lunar orbit and new selenophysical information. *Science*, 182(4109):229–238.

Berg, E., Carter, J., Harris, D., Laurila, S., Schenck, B., Sutton, G., Wolfe, J., and Cushman, S. (1978). High-precision laser distance measurement in support of lunar laser ranging at haleakala, maui, 1976-1977.

Bergé, J., Touboul, P., Rodrigues, M., and MICROSCOPE Team (2015). Status of MICROSCOPE, a mission to test the Equivalence Principle in space. In *Journal of Physics Conference Series*, volume 610 of *Journal of Physics Conference Series*, page 012009.

Bertotti, B., Iess, L., and Tortora, P. (2003). A test of general relativity using radio links with the Cassini spacecraft. *Nature*, 425(6956):374–376.

Bevis, M., Alsdorf, D., Kendrick, E., Fortes, L. P., Forsberg, B., Smalley, R., and Becker, J. (2005). Seasonal fluctuations in the mass of the amazon river system and earth's elastic response. *Geophysical Research Letters*, 32(16):n/a–n/a. L16308.

Binder, A. B. (1998). Lunar Prospector: Overview. *Science*, 281(5382):1475–1476.

Blewitt, G., Lavallée, D., Clarke, P., and Nurutdinov, K. (2001). A new global mode of earth deformation: Seasonal cycle detected. *Science*, 294(5550):2342–2345.

Bois, E., Wytrzyszczak, I., and Journet, A. (1992). Planetary and figure-figure effects on the moon's rotational motion. *Celestial Mechanics and Dynamical Astronomy*, 53:185–201.

Bouquillon, S., Francou, G., Manche, H., Torre, J., Féraudy, D., Le Poncin-Lafitte, C., and Lhotka, C. (2013). Lunar laser ranging: Recent activities of the paris observatory lunar analysis center.

Burkhardt, C. (2014). Isotopic Composition of the Moon and the Lunar Isotopic Crisis. In *Encyclopedia of Lunar Science*, pages 1–13. Springer International Publishing, Cham.

Busing, F.-M., Meijer, E., and Van der Leeden, R. (1999). Delete-m jackknife for unequal m. *Statistics and Computing*, 9:3.

Canup, R. M. (2004). Simulations of a late lunar-forming impact. *Icarus*, 168(2):433–456.

Canup, R. M. (2008). Lunar-forming collisions with pre-impact rotation. *Icarus*, 196(2):518–538.

Canup, R. M. and Asphaug, E. (2001). Origin of the Moon in a giant impact near the end of the Earth's formation. *Nature*, 412(6848):708–712.

Cappallo, R. J. (1980). *The Rotation of the Moon.* PhD thesis, Massachusetts Institute of Technology.

Chapront, J., Chapront-Touzé, M., and Francou, G. (2002). A new determination of lunar orbital parameters, precession constant and tidal acceleration from LLR measurements. *Astronomy & Astrophysics*, 387:700–709.

Chapront-Touze, M. and Chapront, J. (1983). The lunar ephemeris ELP 2000. *Astronomy & Astrophysics*, 124:50–62.

Ciocci, E., Martini, M., Contessa, S., Porcelli, L., Mastrofini, M., Currie, D., Delle Monache, G., and Dell'Agnello, S. (2017). Performance analysis of next-generation lunar laser retroreflectors. *Advances in Space Research*.

Cook, R. D. and Weisberg, S. (1982). *Residuals and Influence on regression.* Champman and Hall, New York, USA.

Courde, C., Torre, J., Samain, E., Martinot-Lagarde, G., Aimar, M., Albanese, D., Exertier, P., Feraudy, D., Fienga, A., Mariey, H., Metris, G., Viot, H., and Viswanathan, V. (2017). Lunar laser ranging in infrared at the Grasse laser station. *Astronomy & Astrophysics*.

Ćuk, M., Hamilton, D. P., Lock, S. J., and Stewart, S. T. (2016). Tidal evolution of the Moon from a high-obliquity, high-angular-momentum Earth. *Nature*, pages 1–19.

Ćuk, M. and Stewart, S. T. (2012). Making the Moon from a Fast-Spinning Earth: A Giant Impact Followed by Resonant Despinning. *Science*, 338(6110):1047–1052.

Currie, D. G. and Prochazka, I. (2014). Atmospheric effects and ultimate ranging accuracy for lunar laser ranging. page 92240C.

Dai, W. and Song, X. (2008). Detection of motion and heterogeneity in Earth's liquid outer core. *Geophysical Research Letters*, 35(16):1–5.

Damour, T. (1996). Testing the equivalence principle: why and how? *Classical and Quantum Gravity*, 13(11A):A33–A41.

Damour, T. (2012). Theoretical aspects of the equivalence principle. *Classical and Quantum Gravity*, 29(18):184001.

Damour, T. and Donoghue, J. F. (2010). Equivalence principle violations and couplings of a light dilaton. *Physical Review D*, 82(8):084033.

Damour, T., Piazza, F., and Veneziano, G. (2002). Violations of the equivalence principle in a dilaton-runaway scenario. *Physical Review D*, 66(4):046007.

Damour, T. and Polyakov, A. M. (1994). String theory and gravity. *General Relativity and Gravitation*, 26:1171–1176.

Damour, T. and Vokrouhlický, D. (1996). Equivalence principle and the Moon. *Physical Review D*, 53(8):4177–4201.

Darwin, G. H. (1892). The tides and kindred phenomena in the solar system. *Nova*, 60(1):213.

de Marchi, F. and Congedo, G. (2017). Space tests of the strong equivalence principle: BepiColombo and the Sun-Earth Lagrangian points opportunity. *International Journal of Modern Physics D*, 26:1741021.

Dehant, V., Park, R., Dirkx, D., Iess, L., Neumann, G., Turyshev, S., and Van Hoolst, T. (2017). Survey of Capabilities and Applications of Accurate Clocks: Directions for Planetary Science. *Space Science Reviews*, 212(3-4):1433–1451.

Dell'Agnello, S., Delle Monache, G., Porcelli, L., Boni, A., Contessa, S., Ciocci, E., Martini, M., Tibuzzi, M., Intaglietta, N., Salvatori, L., et al. (2017). Inrri-edm/2016: the first laser retroreflector on the surface of mars. *Advances in Space Research*, 59(2):645–655.

Desai, S. D. (2002). Observing the pole tide with satellite altimetry. *Journal of Geophysical Research*, 107(C11):3186.

Dumberry, M. and Wieczorek, M. A. (2016). The forced precession of the Moon's inner core. *Journal of Geophysical Research: Planets*, 121(7):1264–1292.

Dvali, G., Gabadadze, G., and Shifman, M. (2003). Diluting the cosmological constant in infinite volume extra dimensions. *Physical Review D*, 67(4):044020.

Dvali, G., Gruzinov, A., and Zaldarriaga, M. (2003). The accelerated universe and the Moon. *Physical Review D*, 68(2):1–17.

Einstein, A. (2015). *Relativity: The special and the general theory*. Princeton University Press.

Ewing, M. (1976). Scientific Applications of Lunar Laser Ranging. *Journal of Geodesy*, 50(3):255–267.

Falcon, N. (2011). MoND with Einstein's Cosmological Term as alternative to Dark Matter. In *Revista Mexicana de Astronomia y Astrofisica Conference Series*, volume 40 of *Revista Mexicana de Astronomia y Astrofisica, vol. 27*, pages 11–12.

Faller, J., Winer, I., Carrion, W., Johnson, T. S., Spadin, P., Robinson, L., Wampler, E. J., and Wieber, D. (1969). Laser Beam Directed at the Lunar Retro-Reflector Array: Observations of the First Returns. *Science*, 166(3901):99–102.

Farrell, W. E. (1972). Deformation of the Earth by surface loads. *Reviews of Geophysics*, 10(3):761.

Fay, R. E. (1985). A Jackknifed Chi-Squared Test for Complex Samples. *Journal of the American Statistical Association*, 80:148–157.

Fienga, A. (1999). *Observations Astrometriques des Planetes et Ajustement des Theories Analytiques de leur Mouvement*. PhD thesis, Observatoire de Paris.

Fienga, A., Laskar, J., Exertier, P., Manche, H., and Gastineau, M. (2015). Numerical estimation of the sensitivity of INPOP planetary ephemerides to general relativity parameters. *Celestial Mechanics and Dynamical Astronomy*, 123:325–349.

Fienga, A., Laskar, J., Kuchynka, P., Manche, H., Desvignes, G., Gastineau, M., Cognard, I., and Theureau, G. (2011). The INPOP10a planetary ephemeris and its applications in fundamental physics. *Celestial Mechanics and Dynamical Astronomy*, 111(3):363–385.

Fienga, A., Laskar, J., Kuchynka, P., Manche, H., Gastineau, M., and Somenzi, L. (2009). Evolution of INPOP planetary ephemerides. In Soffel, M. and Capitaine, N., editors, *Journées Systèmes de Référence Spatio-temporels 2008*, pages 65–68.

Fienga, A., Laskar, J., Manche, H., and Gastineau, M. (2016a). Constraints on the location of a possible 9th planet derived from the Cassini data. *Astronomy & Astrophysics*, 587:L8.

Fienga, A., Laskar, J., Manche, H., and Gastineau, M. (2016b). Tests of GR with INPOP15a planetary ephemerides: estimations of possible supplementary advances of perihelia for Mercury and Saturn. *arXiv: 1601.00947v1 [gr-qc]*, (criteria 1):5–6.

Fienga, A., Manche, H., Laskar, J., and Gastineau, M. (2008). INPOP06: a new numerical planetary ephemeris. *Astronomy & Astrophysics*, 477:315–327.

Fienga, A., Manche, H., Laskar, J., Gastineau, M., and Verma, A. (2014). INPOP new release: INPOP13b. *ArXiv e-prints*.

Fienga, A., Manche, H., Laskar, J., Gastineau, M., and Verma, A. (2014). INPOP new release: INPOP13c. Available at http://www.imcce.fr/fr/presentation/equipes/ASD/inpop/inpop13c.pdf.

Folkner, W., Williams, J., and Boggs, D. (2009). The planetary and lunar ephemeris DE 421. *IPN Progress Report 42-178*, 005:1–34.

Folkner, W. M., Charlot, P., Finger, M. H., Williams, J. G., Sovers, O. J., Newhall, X., and Standish, Jr., E. M. (1994). Determination of the extragalactic-planetary frame tie from joint analysis of radio interferometric and lunar laser ranging measurements. *Astronomy & Astrophysics*, 287:279–289.

Folkner, W. M., Iess, L., Anderson, J. D., Asmar, S. W., Buccino, D. R., Durante, D., Feldman, M., Gomez Casajus, L., Gregnanin, M., Milani, A., Parisi, M., Park, R. S., Serra, D., Tommei, G., Tortora, P., Zannoni, M., Bolton, S. J., Connerney, J. E. P., and Levin, S. M. (2017). Jupiter gravity field estimated from the first two Juno orbits. *Geophysical Research Letters*, 44(10):4694–4700.

Folkner, W. M., Williams, J. G., Boggs, D. H., Park, R. S., and Kuchynka, P. (2014). The Planetary and Lunar Ephemerides DE430 and DE431. *Interplanetary Network Progress Report*, 196:C1.

Fu, Y., Freymueller, J. T., and Jensen, T. (2012). Seasonal hydrological loading in southern alaska observed by gps and grace. *Geophysical Research Letters*, 39(15):n/a–n/a. L15310.

Garcia, R. F., Gagnepain-Beyneix, J., Chevrot, S., and Lognonné, P. (2011). Very preliminary reference Moon model. *Physics of the Earth and Planetary Interiors*, 188(1-2):96–113.

Gastineau, M., Laskar, J., Manche, H., and Fienga, A. (2015). CALCEPH: Planetary ephemeris files access code. *Astrophysics Source Code Library, record ascl:1505.001*.

Gilli, E., Boudin, F., Longuevergne, L., Florsch, N., Walch, J.-J., Gomez, A., Depeyre, J., and Marie, J.-C. (2010). Neotectonics and current hydrologically-induced karst deformation. Case study of the Plateau de Calern (Alpes-Maritimes, France). *Geodinamica Acta*, 23(1-3):49–64.

Goldreich, P. (1967). Precession of the Moon's core. *Journal of Geophysical Research*, 72(12):3135–3137.

Goodrow, S. D. and Murphy, T. W. (2012). Effects of thermal gradients on total internal reflection corner cubes. *Applied Optics*, 51(36):8793.

Goswami, J. and Annadurai, M. (2009). Chandrayaan-1: India's first planetary science mission to the moon. *Current Science*, pages 486–491.

Gupta, M. R. and Chen, Y. (2011). Theory and use of the em algorithm. *Foundations and Trends® in Signal Processing*, 4(3):223–296.

Hartmann, T. and Wenzel, H.-G. (1995). The HW95 tidal potential catalogue. *Geophysical Research Letters*, 22(24):3553–3556.

Hees, A., Hestroffer, D., Le Poncin-Lafitte, C., and David, P. (2015). Tests of gravitation with GAIA observations of Solar System Objects. In Martins, F., Boissier, S., Buat, V., Cambrésy, L., and Petit, P., editors, *SF2A-2015: Proceedings of the Annual meeting of the French Society of Astronomy and Astrophysics*, pages 125–131.

Hofmann, F. and Müller, J. (2016). Update of the ife llr analysis model and new fit of relativistic parameters. In *20th International Workshop on Laser Ranging*.

Hofmann, F., Müller, J., and Biskupek, L. (2010). Lunar laser ranging test of the Nordtvedt parameter and a possible variation in the gravitational constant. *a&a*, 522:5–7.

Hood, L. (1986). Geophysical constraints on the lunar interior. In *Origin of the Moon*, pages 361–410.

Hood, L. L., Mitchell, D. L., Lin, R. P., Acuna, M. H., and Binder, A. B. (1999). Initial measurements of the lunar induced magnetic dipole moment using lunar prospector magnetometer data. *Geophysical Research Letters*, 26(15):2327–2330.

Hulley, G. C. and Pavlis, E. C. (2007). A ray-tracing technique for improving Satellite Laser Ranging atmospheric delay corrections, including the effects of horizontal refractivity gradients. *Journal of Geophysical Research: Solid Earth*, 112(6):1–19.

IAU SOFA Board. SOFA Tools for Earth Attitude. Available at http://www.iausofa.org/2017_0420_F/sofa/sofa_pn_f.pdf.

Iess, L., Stevenson, D. J., Parisi, M., Hemingway, D., Jacobson, R. A., Lunine, J. I., Nimmo, F., Armstrong, J. W., Asmar, S. W., Ducci, M., and Tortora, P. (2014). The Gravity Field and Interior Structure of Enceladus. *Science*, 344(6179):78–80.

Kato, M., Sasaki, S., Tanaka, K., Iijima, Y., and Takizawa, Y. (2008). The japanese lunar mission selene: Science goals and present status. *Advances in Space Research*, 42(2):294–300.

Kaula, W., Schubert, G., Lingenfelter, R., Sjogren, W., and Wollenhaupt, W. (1972). Analysis and interpretation of lunar laser altimetry. In *Lunar and Planetary Science Conference Proceedings*, volume 3, page 2189.

Kenneth R Lang (2011). *The Cambridge guide to the solar system*. Cambridge ; New York ; Cambridge University Press.

Konopliv, A. S., Asmar, S. W., Carranza, E., Sjogren, W. L., and Yuan, D. N. (2001). Recent gravity models as a result of the Lunar Prospector mission. *Icarus*, 150:1–18.

Konopliv, A. S., Park, R. S., Yuan, D.-N. N., Asmar, S. W., Watkins, M. M., Williams, J. G., Fahnestock, E., Kruizinga, G., Paik, M., Strekalov, D., Harvey, N., Smith, D. E., and Zuber, M. T. (2013). The JPL lunar gravity field to spherical harmonic degree 660 from the GRAIL Primary Mission. *Journal of Geophysical Research: Planets*, 118(7):1415–1434.

Kucharski, D., Kirchner, G., Otsubo, T., and Koidl, F. (2015). A method to calculate zero-signature satellite laser ranging normal points for millimeter geodesy - a case study with Ajisai. *Earth, Planets and Space*, 67(1):34.

Kuchynka, P., Laskar, J., Fienga, A., and Manche, H. (2010). A ring as a model of the main belt in planetary ephemerides. *Astronomy & Astrophysics*, 514:A96.

Laneuville, M., Wieczorek, M. A., Breuer, D., Aubert, J., Morard, G., and Rückriemen, T. (2014). A long-lived lunar dynamo powered by core crystallization. *Earth and Planetary Science Letters*, 401:251–260.

Laneuville, M., Wieczorek, M. A., Breuer, D., and Tosi, N. (2013). Asymmetric thermal evolution of the Moon. *Journal of Geophysical Research: Planets*, 118(7):1435–1452.

Laskar, J., Fienga, A., Gastineau, M., and Manche, H. (2011). La2010: a new orbital solution for the long-term motion of the Earth. *Astronomy & Astrophysics*, 532:A89.

Laskar, J., Joutel, F., and Robutel, P. (1993). Stabilization of the earth's obliquity by the moon. *Nature*, 361(6413):615–617.

Laskar, J., Robutel, P., Joutel, F., Gastineau, M., Correia, A. C. M., and Levrard, B. (2004). A long-term numerical solution for the insolation quantities of the Earth. *Astronomy & Astrophysics*, 428:261–285.

Laureijs, R., Amiaux, J., Arduini, S., Augueres, J.-L., Brinchmann, J., Cole, R., Cropper, M., Dabin, C., Duvet, L., Ealet, A., et al. (2011). Euclid definition study report. *arXiv preprint arXiv:1110.3193*.

Lawrence, D. J. (1998). Global Elemental Maps of the Moon: The Lunar Prospector Gamma-Ray Spectrometer. *Science*, 281(5382):1484–1489.

Lawson, C. L. and Hanson, R. J. (1995). *Solving Least Squares Problems*. Society for Industrial and Applied Mathematics.

Le Bars, M., Wieczorek, M. a., Karatekin, O., Cébron, D., and Laneuville, M. (2011). An impact-driven dynamo for the early Moon. *Nature*, 479(7372):215–8.

Lemoine, F. G., Goossens, S., Sabaka, T. J., Nicholas, J. B., Mazarico, E., Rowlands, D. D., Loomis, B. D., Chinn, D. S., Caprette, D. S., Neumann, G. A., Smith, D. E., and Zuber, M. T. (2013). High-degree gravity models from GRAIL primary mission data. *Journal of Geophysical Research: Planets*, 118(8):1676–1698.

Lemoine, F. G., Goossens, S., Sabaka, T. J., Nicholas, J. B., Mazarico, E., Rowlands, D. D., Loomis, B. D., Chinn, D. S., Neumann, G. A., Smith, D. E., and Zuber, M. T. (2014). GRGM900C: A degree 900 lunar gravity model from GRAIL primary and extended mission data. *Geophysical Research Letters*, 41(10):3382–3389.

Liorzou, F., Boulanger, D., Rodrigues, M., Touboul, P., and Selig, H. (2014). Free fall tests of the accelerometers of the MICROSCOPE mission. *Advances in Space Research*, 54:1119–1128.

Lue, A. and Starkman, G. (2003). Gravitational leakage into extra dimensions: Probing dark energy using local gravity. *Phys. Rev. D*, 67:064002.

Lyard, F., Lefevre, F., Letellier, T., and Francis, O. (2006). Modelling the global ocean tides: modern insights from FES2004. *Ocean Dynamics*, 56(5-6):394–415.

Ma, C., Arias, E. F., Bianco, G., Boboltz, D. A., Bolotin, S. L., Charlot, P., Engelhardt, G., Fey, A. L., Gaume, R. A., Gontier, A.-M., Heinkelmann, R., Jacobs, C. S., Kurdubov, S., Lambert, S. B., Malkin, Z. M., Nothnagel, A., Petrov, L., Skurikhina, E., Sokolova, J. R., Souchay, J., Sovers, O. J., Tesmer, V., Titov, O. A., Wang, G., Zharov, V. E., Barache, C., Boeckmann, S., Collioud, A., Gipson, J. M., Gordon, D., Lytvyn, S. O., MacMillan, D. S., and Ojha, R. (2009). The Second Realization of the International Celestial Reference Frame by Very Long Baseline Interferometry. *IERS Technical Note*, 35.

Manche, H. (2011). *Construction of the INPOP ephemeris: dynamical model and adjustments to Lunar Laser Ranging data*. Thesis, Observatoire de Paris.

Martinot-Lagarde, G., Aimar, M., Albanèse, D., Courde, C., Exertier, P., Fienga, A., Mariey, H., Métris, G., Rigard-Cerison, R., Samain, E., Torre, J.-M., and Viot, H. (2016). Laser enhancements for Lunar Laser Ranging at 532nm. *Results in Physics*, 6:329–336.

Marty, J., Loyer, S., Perosanz, F., Mercier, F., Bracher, G., Legresy, B., Portier, L., Capdeville, H., Fund, F., Lemoine, J., et al. (2011). Gins: the cnes/grgs gnss scientific software. In *3rd International Colloquium Scientific and Fundamental Aspects of the Galileo Programme, ESA Proceedings WPP326*, volume 31.

Matsuyama, I., Nimmo, F., Keane, J. T., Chan, N. H., Taylor, G. J., Wieczorek, M. A., Kiefer, W. S., and Williams, J. G. (2016). GRAIL, LLR, and LOLA constraints on the interior structure of the Moon. *Geophysical Research Letters*.

Mazarico, E., Barker, M. K., Neumann, G. A., Zuber, M. T., and Smith, D. E. (2014). Detection of the lunar body tide by the Lunar Orbiter Laser Altimeter. *Geophysical Research Letters*, 41(7):2282–2288.

McCarthy, D. D. and Petit, G. (2004). *IERS conventions (2003)*.

Melosh, H. J. (2014). New approaches to the Moon's isotopic crisis. *Philosophical Transactions of the Royal Society A: Mathematical, Physical and Engineering Sciences*, 372(2024):20130168–20130168.

Melosh, H. J., Freed, A. M., Johnson, B. C., Blair, D. M., Andrews-Hanna, J. C., Neumann, G. A., Phillips, R. J., Smith, D. E., Solomon, S. C., Wieczorek,

M. A., and Zuber, M. T. (2013). The Origin of Lunar Mascon Basins. *Science*, 340(6140):1552–1555.

Mémin, A., Viswanathan, V., Fienga, A., Santamarìa-Gómez, A., Boy, J.-P., Cavalié, O., Deleflie, F., and Exertier, P. (2016). Multi-geodetic characterization of the seasonal signal at the CERGA geodetic reference station. In *AGU General Assembly Conference Abstracts*, volume 1, page 1.

Mendes, V. B. and Pavlis, E. C. (2004). High-accuracy zenith delay prediction at optical wavelengths. *Geophysical Research Letters*, 31(14):1–5.

Mendes, V. B., Prates, G., Pavlis, E. C., Pavlis, D. E., and Langley, R. B. (2002). Improved mapping functions for atmospheric refraction correction in SLR. *Geophysical Research Letters*, 29(10):53–54.

Merkowitz, S. M. (2010). Tests of gravity using lunar laser ranging. *Living Reviews in Relativity*, 13.

Michelsen, E. L. (2010). *Normal point generation and first photon bias correction in APOLLO lunar laser ranging*. PhD thesis, University of California, San Diego.

Moore, E. H. On the reciprocal of the general algebraic matrix. *Bulletin of the American Mathematical Society*, 26:394–395.

Moyer, T. D. (2003). *Formulation for Observed and Computed Values of Deep Space Network Data Types for Navigation*, volume 2. John Wiley & Sons, Inc., Hoboken, NJ, USA.

Mulholland, J. D., Burk, C. A., and Silverberg, E. C., editors (1977). *Scientific Applications of Lunar Laser Ranging*, volume 62 of *Astrophysics and Space Science Library*. Springer Netherlands, Dordrecht.

Müller, J., Hofmann, F., and Biskupek, L. (2012). Testing various facets of the equivalence principle using lunar laser ranging. *Classical and Quantum Gravity*, 29(18):184006.

Müller, J., Williams, J. G., Turyshev, S. G., and Shelus, P. J. (2005). Potential Capabilities of Lunar Laser Ranging for Geodesy and Relativity. *ArXiv General Relativity and Quantum Cosmology e-prints*.

Muller, P. M. and Sjogren, W. L. (1968). Mascons: lunar mass concentrations. *Science*, 161(3842):680–684.

Munghemezulu, C., Combrinck, W., Botai, J., and Botha, R. (2016). Design of the timing system for the new lunar laser ranger proposed for the matjiesfontein space geodetic observatory in the great karoo, south africa: preliminary results. *South African Journal of Geology*, 119(1):91–98.

Munk, W. H. and MacDonald, G. J. F. (1960). The rotation of the earth; a geophysical discussion.

Murphy, T. W. (2013). Lunar laser ranging: the millimeter challenge. *Reports on Progress in Physics*, 76(7):076901.

Murphy, T. W., Adelberger, E. G., Battat, J. B. R., Carey, L. N., Hoyle, C. D., LeBlanc, P., Michelsen, E. L., Nordtvedt, K., Orin, A. E., Strasburg, J. D., Stubbs, C. W., Swanson, H. E., Williams, E., The, U. O. F., and The, O. O. F. (2008). The Apache Point Observatory Lunar Laser-ranging Operation: Instrument Description and First Detections. *Publications of the Astronomical Society of the Pacific*, 120(863):20–37.

Murphy, T. W., Adelberger, E. G., Battat, J. B. R., Hoyle, C. D., Johnson, N. H., McMillan, R. J., Michelsen, E. L., Stubbs, C. W., and Swanson, H. E. (2011). Laser ranging to the lost Lunokhod 1 reflector. *Icarus*, 211(2):1103–1108.

Murphy, T. W., Adelberger, E. G., Battat, J. B. R., Hoyle, C. D., Johnson, N. H., McMillan, R. J., Stubbs, C. W., and Swanson, H. E. (2012). APOLLO: millimeter lunar laser ranging. *Classical and Quantum Gravity*, 29(18):184005.

Murphy, T. W., McMillan, R. J., Johnson, N. H., and Goodrow, S. D. (2014). Lunar eclipse observations reveal anomalous thermal performance of Apollo reflectors. *Icarus*, 231:183–192.

Neumann, G. A., Zuber, M. T., Wieczorek, M. A., Head, J. W., Baker, D. M. H., Solomon, S. C., Smith, D. E., Lemoine, F. G., Mazarico, E., Sabaka, T. J., Goossens, S. J., Melosh, H. J., Phillips, R. J., Asmar, S. W., Konopliv, A. S., Williams, J. G., Sori, M. M., Soderblom, J. M., Miljković, K., Andrews-Hanna, J. C., Nimmo, F., and Kiefer, W. S. (2015). Lunar impact basins revealed by Gravity Recovery and Interior Laboratory measurements. *Science Advances*, 1(9):e1500852–e1500852.

Newhall, X., Standish, E., and Williams JG (1983). DE 102-A numerically integrated ephemeris of the moon and planets spanning forty-four centuries. *Astronomy & Astrophysics*, 125:150–167.

Nordtvedt, K. (1968). Testing Relativity with Laser Ranging to the Moon. *Physical Review*, 170(5):1186–1187.

Nordtvedt, K. (1998). Optimizing the observation schedule for tests of gravity in lunar laser ranging and similar experiments. *Classical and Quantum Gravity*, 15:3363–3381.

Nordtvedt, K. L., Mueller, J., and Soffel, M. (1995). Cosmic acceleration of the Earth and Moon by dark matter. *Astronomy & Astrophysics*, 293:73–74.

Nozette, S., Rustan, P., Pleasance, L. P., Kordas, J. F., Lewis, I. T., Park, H. S., Priest, R. E., Horan, D. M., Regeon, P., Lichtenberg, C. L., Shoemaker, E. M., Eliason, E. M., McEwen, A. S., Robinson, M. S., Spudis, P. D., Acton, C. H., Buratti, B. J., Duxbury, T. C., Baker, D. N., Jakosky, B. M., Blamont, J. E., Corson, M. P., Resnick, J. H., Rollins, C. J., Davies, M. E., Lucey, P. G., Malaret, E., Massie, M. A., Pieters, C. M., Reisse, R. A., Simpson, R. A., Smith, D. E., Sorenson, T. C., Breugge, R. W. V., and Zuber, M. T. (1994). The Clementine Mission to the Moon: Scientific Overview. *Science*, 266(5192):1835–1839.

Oberst, J., Christou, A., Suggs, R., Moser, D., Daubar, I., McEwen, A., Burchell, M., Kawamura, T., Hiesinger, H., Wünnemann, K., Wagner, R., and Robinson, M. (2012). The present-day flux of large meteoroids on the lunar surface—A synthesis of models and observational techniques. *Planetary and Space Science*, 74(1):179–193.

Ouyang, Z., Li, C., Zou, Y., Zhang, H., Lü, C., Liu, J., Liu, J., Zuo, W., Su, Y., Wen, W., et al. (2010). Primary scientific results of chang'e-1 lunar mission. *Science China Earth Sciences*, 53(11):1565–1581.

Pahlevan, K. and Morbidelli, A. (2015). Collisionless encounters and the origin of the lunar inclination. *Nature*, 527(7579):492–494.

Pavlis, N. K., Holmes, S. A., Kenyon, S. C., and Factor, J. K. (2008). The EGM2008 Global Gravitational Model. *AGU Fall Meeting Abstracts*, pages G22A–01.

Pavlov, D. A., Williams, J. G., and Suvorkin, V. V. (2016). Determining parameters of Moon's orbital and rotational motion from LLR observations using GRAIL and IERS-recommended models. *Celestial Mechanics and Dynamical Astronomy*, 126(1-3):61–88.

Peale, S. J., Margot, J.-L., Hauck, S. A., and Solomon, S. C. (2016). Consequences of a solid inner core on Mercury's spin configuration. *Icarus*, 264:443–455.

Pearlman, M., Degnan, J., and Bosworth, J. (2002). The International Laser Ranging Service. *Advances in Space Research*, 30(2):135–143.

Pearson, K. (1895). Note on Regression and Inheritance in the Case of Two Parents. *Proceedings of the Royal Society of London (1854-1905)*, 58(-1):240–242.

Penrose, R. and Todd, J. A. (1955). A generalized inverse for matrices. *Mathematical Proceedings of the Cambridge Philosophical Society*, 51(03):406.

Petit, G. and Luzum, B. (2010). IERS Conventions (2010). *IERS Technical Note*, 36.

Pitjeva, E. (2005). High-precision ephemerides of planets—epm and determination of some astronomical constants. *Solar System Research*, 39(3):176–186.

Pitjeva, E. (2013). Updated iaa ras planetary ephemerides-epm2011 and their use in scientific research. *Solar System Research*, 47(5):386–402.

Poincaré, H. (1910). Sur la précession des corps déformables. *Bulletin Astronomique, Serie I*, 27:321–356.

Press, W. H., Teukolsky, S. A., Vetterling, W. T., and Flannery, B. P. (2007). *Numerical Recipes 3rd Edition: The Art of Scientific Computing*. Cambridge University Press, New York, NY, USA, 3 edition.

Qin, C. (2015). Determination of Tidal Response of the Moon with Fully Three-dimensional Elastic and Density Structures Using a Perturbation Method.

Rambaux, N. (2017). personal communication.

Rambaux, N., Van Hoolst, T., Dehant, V., and Bois, E. (2007). Inertial core-mantle coupling and libration of Mercury. *Astronomy & Astrophysics*, 468(2):711–719.

Rambaux, N. and Williams, J. G. (2011). The Moon's physical librations and determination of their free modes. *Celestial Mechanics and Dynamical Astronomy*, 109(1):85–100.

Ratcliff, J. T. and Gross, R. S. (2015). Combinations of Earth Orientation Measurements: SPACE2014, COMB2014, and POLE2014.

Ray, R. D. and Ponte, R. M. (2003). Barometric tides from ECMWF operational analyses. *Annales Geophysicae*, 21(8):1897–1910.

Ries, J., Bettadpur, S., Eanes, R., Kang, Z., Ko, U., McCullough, C., Nagel, P., Pie, N., Poole, S., Richter, T., Save, H., and Tapley, B. (2016). The Combined Gravity Model GGM05C.

Rufu, R., Aharonson, O., and Perets, H. B. (2017). A multiple-impact origin for the Moon. *Nature Geoscience*, 10(2):89–94.

Samain, E. (1995). *Le laser lune millimetrique et nouvelles methodes de datation optique*. PhD thesis.

Samain, E., Mangin, J. F., Veillet, C., Torre, J. M., Fridelance, P., Chabaudie, J. E., Féraudy, D., Glentzlin, M., Pham Van, J., Furia, M., Journet, A., and Vigouroux, G. (1998). Millimetric Lunar Laser Ranging at OCA (Observatoire de la Côte d'Azur). *Astronomy & Astrophysics Supplement Series*, 130(2):235–244.

Sasao, T. and Wahr, J. M. (1981). An excitation mechanism for the free ' core nutation '. pages 129–146.

Scheinberg, A., Soderlund, K., and Schubert, G. (2015). Magnetic field generation in the lunar core: The role of inner core growth. *Icarus*, 254:62–71.

Schwiderski, E. W. (1980). On charting global ocean tides. *Reviews of Geophysics*, 18(1):243–268.

Shapiro, I. I. (1964). Fourth Test of General Relativity. *Physical Review Letters*, 13(26):789–791.

Shelus, P. J. (1985). Mlrs: A lunar/artificial satellite laser ranging facility at the mcdonald observatory. *IEEE transactions on geoscience and remote sensing*, (4):385–390.

Shimizu, H., Matsushima, M., Takahashi, F., Shibuya, H., and Tsunakawa, H. (2013). Constraint on the lunar core size from electromagnetic sounding based on magnetic field observations by an orbiting satellite. *Icarus*, 222(1):32–43.

Standish, E. (1998). Jpl planetary and lunar ephemerides, de405/le405, jpl iom 312.f-98-048. Technical report, JPL Memo, August 26.

Standish, E. (2006). Jpl planetary ephemeris de414. *JPL IOM 343R-06-002*.

Standish, E., Keesey, M. S., and Newhall, X. (1976). Jpl development ephemeris number 96. *NASA-CR-147923*.

Standish, E. M., Williams, J. G., and Ephemerides, F. (2003). Orbital Ephemerides of the Sun, Moon, and Planets. *Tensor*, pages 1–33.

Standish Jr, E. (1990). The observational basis for jpl's de 200, the planetary ephemerides of the astronomical almanac. *Astronomy & Astrophysics*, 233:252–271.

Stark, P. B. and Parker, R. (1995). Bounded-variable least-squares: an algorithm and applications. *Computational Statistics*, 10(2):129–141. n/a.

Tapley, B. D., Born, G. H., and Schutz, B. E. (2010). *Statistical orbit determination*. Elsevier Academic Press.

Tian, Z., Wisdom, J., and Elkins-Tanton, L. (2017). Coupled orbital-thermal evolution of the early Earth-Moon system with a fast-spinning Earth. *Icarus*, 281:90–102.

Torre, J. (2013). First LLR Observations of Lunokhod 1 with MéO Instrument (Calern, France).

Touma, J. and Wisdom, J. (1998). Resonances in the Early Evolution of the Earth-Moon System. *The Astronomical Journal*, 115(4):1653–1663.

Van Hoolst, T. (2007). The Rotation of the Terrestrial Planets. In *Treatise on Geophysics*, volume 10, pages 123–164. Elsevier.

Varghese, T. K., Decker, W. M., Crooks, H. A., and Bianco, G. (1993). Matera laser ranging observatory (mlro): an overview.

Vasilyev, M. V., Yagudina, E. I., Grishin, E. A., Ivlev, O. A., and Grechukhin, I. A. (2016). On the accuracy of lunar ephemerides using the data provided by the future russian lunar laser ranging system. *Solar System Research*, 50(5):361–367.

Veillet, C. (1987). La distance Terre-Lune {à} quelques centim{è}tres pr{è}s. *La Recherche*, 186.

Veillet, C., Mangin, J. F., Chabaubie, J. E., Dumolin, C., Feraudy, D., and Torre, J. M. (1993). Lunar Laser Ranging at CERGA for the ruby period (1981–1986). In *Contributions of Space Geodesy to Geodynamics: Technology*, pages 189–193. Wiley-Blackwell.

Verma, A., Fienga, A., Laskar, J., Issautier, K., Manche, H., and Gastineau, M. (2013). Electron density distribution and solar plasma correction of radio signals using mgs, mex, and vex spacecraft navigation data and its application to planetary ephemerides. *Astronomy & Astrophysics*, 550:A124.

Viswanathan, V., Fienga, A., Courde, C., Torre, J.-M., Exertier, P., Samain, E., Feraudy, D., Albanese, D., Aimar, M., Mariey, H., Others, Viot, H., and Martinot-Lagarde, G. (2016). LLR data analysis and impact on lunar dynamics from recent developments at OCA LLR Station. In *EGU General Assembly Conference Abstracts*, volume 18, page 13995.

Viswanathan, V., Fienga, A., Gastineau, M., and Laskar, J. (2017). INPOP17a planetary ephemerides. *Notes Scientifiques et Techniques de l'Institut de Mécanique Céleste*, 108:1–39.

Viswanathan, V., Fienga, A., Laskar, J., Manche, H., Torre, J.-M., Courde, C., and Exertier, P. (2015). Utilizing the Lunar Laser Ranging datasets alongside the radioscience data from the Lunar Reconnaissance Orbiter to improve the dynamical model of the Moon. *IAU General Assembly*, 22:28567.

Viswanathan, V., Fienga, A., Minazzoli, O., Bernus, L., Laskar, J., and Gastineau, M. (2018). The new lunar ephemeris INPOP17a and its application to fundamental physics. *Monthly Notices of the Royal Astronomical Society*.

Vokrouhlický, D. (1997). A Note on the Solar Radiation Perturbations of Lunar Motion. *Icarus*, 126(2):293–300.

Wahr, J. and de Vries, D. (1989). The possibility of lateral structure inside the core and its implications for nutation and Earth tide observations. *Geophysical Journal International*, 99(3):511–519.

Wahr, J. M. (1981). Body tides on an elliptical, rotating, elastic and oceanless earth. *Geophysical Journal*, 64:677–703.

Wahr, J. M. (1985). Deformation induced by polar motion. *Journal of Geophysical Research*, 90(B11):9363.

Ward, W. R. and Canup, R. M. (2000). Origin of the Moon's orbital inclination from resonant disk interactions. *Nature*, 403(6771):741–743.

Weber, R. C., Lin, P.-Y., Garnero, E. J., Williams, Q., and Lognonne, P. (2011). Seismic Detection of the Lunar Core. *Science*, 331(6015):309–312.

Wieczorek, M. a. (2006). The Constitution and Structure of the Lunar Interior. *Reviews in Mineralogy and Geochemistry*, 60(1):221–364.

Wieczorek, M. A. (2009). The interior structure of the moon: What does geophysics have to say? *Elements*, 5(1):35–40.

Wieczorek, M. A., Neumann, G. A., Nimmo, F., Kiefer, W. S., Taylor, G. J., Melosh, H. J., Phillips, R. J., Solomon, S. C., Andrews-Hanna, J. C., Asmar, S. W., Konopliv, A. S., Lemoine, F. G., Smith, D. E., Watkins, M. M., Williams, J. G., and Zuber, M. T. (2013). The Crust of the Moon as Seen by GRAIL. *Science*, 339(6120):671–675.

Williams, J. (2009). A larger lunar core? *Lunar and Planetary Science Conference*, 91109:1452.

Williams, J. and Boggs, D. (2015a). The jpl lunar laser range model, jpl iom 335-jgw, dhb-20150701-32. Technical report, California Institute of Technology, July 1.

Williams, J., Boggs, D., and Folkner, W. (2008). De421 lunar orbit, physical librations, and surface coordinates, jpl iom 335-jw, db. Technical report, WF-20080314-001, March 14.

Williams, J., Boggs, D., and Folkner, W. (2013). De430 lunar orbit, physical librations, and surface coordinates, jpl iom 335-jw, db. Technical report, WF-20130722-016, July 22.

Williams, J., Dicke, R., Bender, P., Alley, C., Carter, W., Currie, D., Eckhardt, D., Faller, J., Kaula, W., Mulholland, J., et al. (1976). New test of the equivalence principle from lunar laser ranging. *Physical Review Letters*, 36(11):551.

Williams, J., XX, N., and Standish, E. (1993). De 245 earth and moon. Technical report, JPL Memo, December 17.

Williams, J. G. (2007). A scheme for lunar inner core detection. *Geophysical Research Letters*, 34(3):2–5.

Williams, J. G., Boggs, D., and Ratcliff, J. (2012a). Lunar Moment of Inertia, Love number and Core. *Lunar and Planetary Institute Science Conference Abstracts*, 91109:10–11.

Williams, J. G. and Boggs, D. H. (2015b). Tides on the Moon: Theory and determination of dissipation. *Journal of Geophysical Research: Planets*, 120(4):689–724.

Williams, J. G. and Boggs, D. H. (2016). Secular tidal changes in lunar orbit and Earth rotation. *Celestial Mechanics and Dynamical Astronomy*, 126(1-3):89–129.

Williams, J. G., Boggs, D. H., and Ratcliff, J. T. (2014a). Free Libration Modes of a Structured Moon. *45th Lunar and Planetary Science ConferenceLunar and Planetary Science Conference*, (1579):10–11.

Williams, J. G., Boggs, D. H., Yoder, C. F., Ratcliff, J. T., and Dickey, J. O. (2001). Lunar rotational dissipation in solid body and molten core. *Journal of Geophysical Research*, 106(E11):27933.

Williams, J. G., Konopliv, A. S., Boggs, D. H., Park, R. S., Yuan, D. N., Lemoine, F. G., Goossens, S., Mazarico, E., Nimmo, F., Weber, R. C., Asmar, S. W., Jay Melosh, H., Neumann, G. A., Phillips, R. J., Smith, D. E., Solomon, S. C., Watkins, M. M., Wieczorek, M. A., Andrews-Hanna, J. C., Head, J. W., Kiefer, W. S., Matsuyama, I., McGovern, P. J., Jeffrey Taylor, G., and Zuber, M. T. (2014b). Lunar interior properties from the GRAIL mission. *Journal of Geophysical Research: Planets*, 119(7):1546–1578.

Williams, J. G., Newhall, X. X., and Dickey, J. O. (1996). Relativity parameters determined from lunar laser ranging. *Physical Review D (Particles*, 53(1):6730–6739.

Williams, J. G., Turyshev, S. G., and Boggs, D. H. (2004). Progress in Lunar Laser Ranging Tests of Relativistic Gravity. *Physical Review Letters*, 93(26):261101.

Williams, J. G., Turyshev, S. G., and Boggs, D. H. (2012b). Lunar laser ranging tests of the equivalence principle. *Classical and Quantum Gravity*, 29(18):184004.

Williams, J. G., Turyshev, S. G., and Boggs, D. H. (2014c). The past and present Earth-Moon system: the speed of light stays steady as tides evolve. *Planetary Science*, 3:2.

Williams, J. G. and Watkins, M. M. (2015). The deep lunar interior from GRAIL. (February):10–12.

Williams, J. G. J., Turyshev, S. G. S., and BOGGS, D. D. H. (2009). Laser Ranging Tests of the Equivalence Principle with the Earth and Moon. *International Journal of Modern Physics D*, 18(07):1129–1175.

Wisdom, J. and Tian, Z. (2015). Early evolution of the Earth–Moon system with a fast-spinning Earth. *Icarus*, 256:138–146.

Young, E. D., Kohl, I. E., Warren, P. H., Rubie, D. C., Jacobson, S. A., and Morbidelli, A. (2016). Oxygen isotopic evidence for vigorous mixing during the Moon-forming giant impact. *Science*, 351(6272):493–496.

Zhang, N., Parmentier, E. M., and Liang, Y. (2013). A 3-D numerical study of the thermal evolution of the Moon after cumulate mantle overturn: The importance of rheology and core solidification. *Journal of Geophysical Research: Planets*, 118(9):1789–1804.

Zhong, S., Qin, C., A, G., and Wahr, J. (2012). Can tidal tomography be used to unravel the long-wavelength structure of the lunar interior? *Geophysical Research Letters*, 39(15):1–5.

Zuber, M. T., Smith, D. E., Watkins, M. M., Asmar, S. W., Konopliv, A. S., Lemoine, F. G., Melosh, H. J., Neumann, G. A., Phillips, R. J., Solomon, S. C., Wieczorek, M. A., Williams, J. G., Goossens, S. J., Kruizinga, G., Mazarico, E., Park, R. S., and Yuan, D.-N. (2013). Gravity Field of the Moon from the Gravity Recovery and Interior Laboratory (GRAIL) Mission. *Science*, 339(6120):668–671.

Résumé

L'objectif principal de ce travail était d'améliorer le modèle dynamique de la Lune dans les éphémérides numériques INPOP et d'exploiter cette amélioration en vu d'une meilleure caractérisation de la structure interne de la Lune et d'effectuer des tests de la relativité générale.

Dans un premier temps, un travail d'analyse des algorithmes nécessaires aux calculs des points normaux utilisés pour la construction des éphémérides lunaires a été effectué. L'importance de l'incertitude du point normal se reflète dans la méthode du moindre carré pondéré utilisée pour l'estimation des paramètres lors de la construction des éphémérides. En particulier, l'absence d'un algorithme standardisé entre les différentes stations LLR introduit des biais dans l'estimation des incertitudes qu'il est important de prendre en compte. La thèse a également bénéficié d'un ensemble de données plus dense en raison des améliorations techniques et du passage de la longueur d'onde à l'infrarouge à la station de Grasse (Courde et al., 2017).

Dans un second temps, afin de permettre des analyses multi-techniques combinant mesures SLR et LLR, la réduction des observations LLR a été introduite dans le logiciel de détermination d'orbites GINS du CNES, suite aux recommandations de IERS 2010. En outre, la correction des effets dus au chargement hydrologique observé à la station Grasse a été mise en œuvre et a fait l'objet d'une première communication poster en 2016 (Mémin et al., 2016). Une version améliorée du modèle de réduction LLR a été intégrée à la dernière version distribuée du logiciel GINS par l'équipe de géodésie spatiale (GRGS) du CNES.

Le modèle dynamique lunaire d'INPOP a d'abord été développé par Manche (2011). Cependant, sans doute en raison de l'absence du noyau fluide dans la version précédente (INPOP13c), les résidus obtenus après ajustement étaient au niveau de 5 cm pour la période moderne (2006). Une comparaison détaillée des équations dynamiques avec les éphémérides JPL DE430 a permis d'identifier les changements requis dans INPOP pour l'activation du noyau liquide lunaire. D'autres modifications ont permis l'utilisation d'un champ de gravité lunaire déterminé par la mission spatiale GRAIL. Un algorithme de moindres carrés sous contraintes a aussi été utilisé afin de maintenir les paramètres connus dans des bornes compatibles avec leurs incertitudes. La solution de l'éphéméride INPOP résultante (INPOP17a) produit alors un résidu de 1,4 à 1,8 cm, compatible avec ceux publiés par Folkner et al. (2014); Pavlov et al. (2016). L'éphéméride INPOP17a est distribuée sur le site de l'imcce (www.imcce.fr/inpop) et une documentation a été publiée (Viswanathan et al., 2017) dans les notes scientifiques de l'IMCCE.

En outre, en fournissant des contraintes plus sévères dans le modèle dynamique sur le champ de gravité lunaire à partir de l'analyse des données GRAIL, une signature caractéristique de libration lunaire avec une période de 6 ans a été révélée avec une amplitude de ± 5 cm. Plusieurs pistes ont été étudiées pour l'identification de cet effet, impliquant des termes de marée et des composants de couple à plus haut degré. Une publication est en cours de révision à ce sujet.

Les résidus au niveau d'un centimètre permettent des tests précis du principe d'équivalence dans le système solaire. La valeur ajustée du paramètre caractérisant l'accélération différentielle de la Terre et de la Lune vers le Soleil a été obtenue. Les résultats sont conformes aux travaux antérieurs de Williams et al. (2009, 2012b); Hofmann et al. (2010); Hofmann and Müller (2016) en améliorant la précision de la détermination. Une interprétation en terme de théorie du dilaton est proposée. Un article sur ce travail est accepté pour publication dans MNRAS (Viswanathan et al., 2018).

Mots Clés

Lune, éphémérides, structure interne de la Lune, principe d'équivalence, Télémétrie laser lune, GRAIL

Abstract

The main goal of this Ph.D thesis was to improve the dynamical model of the Moon within the numerically integrated ephemeris (INPOP) and to derive results of scientific value from this improvement through the characterization of the lunar internal structure and tests of general relativity.

At first, raw binaries of LLR echoes obtained from the Grasse ILRS station were used to analyze the algorithm used by the facility, for the computation of a normal point from the full-rate data. Further analysis shows the dependence of the algorithm on the reported uncertainty contained within the distributed LLR normal points from Grasse. The importance of the normal point uncertainty is reflected in the weighted least square procedure used for parameter estimation, especially in the absence of a standardized algorithm between different LLR ground stations. The thesis also benefitted in terms of a more dense dataset due to technical improvements and the switch of operational wavelength to infrared at the Grasse LLR facility (Courde et al., 2017).

The reduction of the LLR observations was implemented within GINS — the orbit determination software from CNES. The modeling follows the IERS 2010 recommendations for the correction of all known effects on the light-time computation. The subroutines were verified through a step by step comparison study using simulated data, with LLR analysis groups in Paris and Hannover, maintaining any discrepancies in the Earth-Moon distance below 1 mm. Additionally, correction of the effect due to hydrology loading observed at the Grasse station was implemented (Mémin et al., 2016). An improved version of the LLR reduction model was submitted to the space geodesy team of CNES (GRGS).

The lunar dynamical model of INPOP was first developed by Manche (2011). However, due to the absence of the fluid core within the previous version of INPOP (13c), the residuals obtained after a least-square fit were in the level of 5 cm for the modern day period (2006 onwards). A detailed comparison of the dynamical equations with DE430 JPL ephemeris helped to identify required changes within INPOP for the activation of the lunar fluid core. Other modifications allowed the use of a spacecraft determined lunar gravity field within the dynamical model. The use of a bounded value least square algorithm during the regression procedure accounted for variability to well-known parameters from their reported uncertainties. The resulting iteratively fit solution of INPOP ephemeris then produces a residual of 1.4-1.8 cm, on par with that reported by Folkner et al. (2014); Pavlov et al. (2016). The new INPOP ephemeris (INPOP17a) is distributed through the IMCCE website (www.imcce.fr/inpop) with a published documentation (Viswanathan et al., 2017) in the scientific notes of IMCCE.

Furthermore, on providing tighter constraints on the lunar gravity field from GRAIL-data analysis within the dynamical model, a characteristic lunar libration signature with a period of 6 years was revealed with an amplitude of ± 5 cm. Several tracks were investigated for the identification of the unmodeled effect, involving higher degree tidal terms and torque components, and a new modeling is proposed. A publication is under revision on this subject.

Residuals at the level of a centimeter allow precision tests of the principle of equivalence in the solar system. The fitted value of the parameter characterizing the differential acceleration of the Earth and the Moon towards the Sun was obtained with numerically integrated partial derivatives. The results are consistent with the previous work by Williams et al. (2009, 2012b); Hofmann et al. (2010); Hofmann and Müller (2016). An article on this work is accepted for publication in MNRAS (Viswanathan et al., 2018).

Keywords

Moon, ephemerides, lunar interior structure, equivalence principle, Lunar Laser Ranging, GRAIL